



JAEA-Review
2009-045

JAEA-Review

Review of JT-60U Experimental Results in 2007 and 2008

The JT-60 Team

Fusion Research and Development Directorate

February 2010

Japan Atomic Energy Agency

日本原子力研究開発機構

本レポートは独立行政法人日本原子力研究開発機構が不定期に発行する成果報告書です。
本レポートの入手並びに著作権利用に関するお問い合わせは、下記あてにお問い合わせ下さい。
なお、本レポートの全文は日本原子力研究開発機構ホームページ (<http://www.jaea.go.jp>)
より発信されています。

独立行政法人日本原子力研究開発機構 研究技術情報部 研究技術情報課
〒319-1195 茨城県那珂郡東海村白方白根 2 番地 4
電話 029-282-6387, Fax 029-282-5920, E-mail:ird-support@jaea.go.jp

This report is issued irregularly by Japan Atomic Energy Agency
Inquiries about availability and/or copyright of this report should be addressed to
Intellectual Resources Section, Intellectual Resources Department,
Japan Atomic Energy Agency
2-4 Shirakata Shirane, Tokai-mura, Naka-gun, Ibaraki-ken 319-1195 Japan
Tel +81-29-282-6387, Fax +81-29-282-5920, E-mail:ird-support@jaea.go.jp

© Japan Atomic Energy Agency, 2010

Review of JT-60U Experimental Results in 2007 and 2008

The JT-60 Team

Division of Advanced Plasma Research and Division of Tokamak System Technology
Fusion Research and Development Directorate, Japan Atomic Energy Agency
Naka-shi, Ibaraki-ken

(Received November 16, 2009)

Results in JT-60U experiments in 2007 and 2008 are reviewed. In this campaign, which is the final experimental period in JT-60U, development of advanced tokamak plasma was extensively performed toward establishment of physics basis of ITER and DEMO. High integrated performance plasma with high normalized beta ($\beta_N \sim 2.6$) and high confinement enhancement factor ($H_{98(y,2)} \sim 1.0-1.1$), which are comparable to those in the ITER Hybrid Scenario, and at the same time with high bootstrap current fraction ($f_{BS} \sim 40\%$) was sustained for 25 s. High density and high radiation loss fraction plasma was sustained for 12 s by adding argon and neon to a deuterium plasma. The duration of the high-performance plasmas is more than 10 times longer than the current diffusion time, τ_R . In a high beta regime exceeding the ideal MHD limit without conducting wall (no-wall limit), a new instability was observed. By suppressing the instability a high beta plasma was sustained for 5 s, which corresponds to several times longer than τ_R . Performance of reversed shear plasmas was significantly improved by utilizing the stabilizing effect of the conducting wall, and $\beta_N \sim 2.7$ and $f_{BS} \sim 90\%$ were obtained. These results significantly exceed those in the previous experimental campaign. In addition, real-time control system was improved, and ion temperature and current profile were independently or simultaneously controlled in real time. Development of new diagnostics was also continuously performed. For example, profiles of electron density and current were measured using the lithium beam probe diagnostic with high resolution. A number of important results from physics experiments were obtained in the area of transport, confinement, instability, plasma-wall interaction etc. Performance of heating and current drive systems was also extended significantly. In the electron cyclotron wave system, 2.9 MW for 5 s injection and 0.4 MW for 30 s injection to plasma were successfully demonstrated. Power modulation up to 7 kHz in synchronization with neoclassical tearing mode was also successful. In the negative-ion-based neutral beam system, 340 keV, 3 MW, 30 s injection corresponding to the highest injection energy of 80 MJ was successfully performed.

Keywords:

Fusion Reactor, Tokamak, JT-60U, Advanced Tokamak, Steady-State Operation, Normalized Beta, Bootstrap Current, Real-Time Control, Instability, Transport, Plasma-Wall Interaction, Plasma Diagnostic, Electron Cyclotron Heating, Neutral Beam Injection

Editors:

Akihiko ISAYAMA, Naoyuki OYAMA, Takahiro SUZUKI, Kouji SHINOHARA,
Yoshiteru SAKAMOTO, Go MATSUNAGA, Maiko YOSHIDA, Nobuyuki ASAKURA,
Tomohide NAKANO, Kensaku KAMIYA, Kiyoshi ITAMI

The JT-60 Team

N. Aiba¹⁾, H. Akasaka, N. Akino, A. Ando²⁾, V. Antoni³⁾, T. Arai, N. Asakura, N. Ashikawa⁴⁾, H. Azechi⁵⁾, M. Azumi, K.I. Baystrukov⁶⁾, B.Z. Chektybayev⁷⁾, J. Chen⁸⁾, S. Chiba, E. Drapiko⁶⁾, N. Ebisawa, T. Fujii, K. Fujimoto¹⁾, T. Fujita, T. Fukuda⁵⁾, M. Fukumoto⁵⁾, A. Fukuyama⁹⁾, H. Furukawa¹⁰⁾, W. Gao⁸⁾, P. Gohil¹¹⁾, L. Grisham¹²⁾, S. Haga¹⁰⁾, K. Hamamatsu, T. Hamano¹⁰⁾, M. Hanada, K. Hasegawa, T. Hatae, R. Hatakeyama²⁾, N. Hayashi, T. Hayashi, S. Higashijima, U. Higashizono¹³⁾, T. Hino¹⁴⁾, S. Hiranai, Y. Hirano¹⁵⁾, J. Hobirk¹⁶⁾, A. Honda, Masao Honda, Mitsuru Honda¹⁾, H. Horiike⁵⁾, K. Hoshino, N. Hosogane, H. Hosoyama¹⁰⁾, J. Howard¹⁷⁾, D.A. Humphreys¹¹⁾, H. Ichige, T. Ichige¹⁰⁾, M. Ichimura¹³⁾, K. Ida⁴⁾, S. Ide, Y. Idomura, K. Igarashi¹⁰⁾, S. Iio¹⁸⁾, Y. Ikeda, T. Imai¹³⁾, A. Inoue¹⁰⁾, M. Inutake²⁾, A. Isayama, S. Ishida, Y. Ishige¹⁰⁾, Kazuhiro Ishii¹⁰⁾, Keiichi Ishii²⁾, Y. Ishii, K. Itami, K. Itoh⁴⁾, Sanae Itoh¹⁹⁾, Satoshi Itoh¹⁹⁾, S. Kado²⁰⁾, Y. Kagei¹⁾, M. Kamada¹⁾, Y. Kamada, M. Kamikawa¹⁰⁾, A. Kaminaga, K. Kamiya, Y. Kashiwa, M. Kawai, Y. Kawamata, Y. Kawano, H. Kawashima, M. Kazawa, K. Kikuchi¹⁰⁾, M. Kikuchi, H. Kimura, A.V. Kirilenko⁷⁾, Y. Kishimoto⁹⁾, S. Kitamura, K. Kiyono, K. Kizu, T. Kobayashi¹⁾, K. Kobayashi¹⁰⁾, Y. Koide, A. Kojima¹⁾, S. Kokusen¹⁰⁾, M. Komata, A. Komori⁴⁾, K. Komuro¹⁰⁾, T. Kondoh, S. Konishi⁹⁾, S. Konoshima, A. Koyama⁹⁾, H. Kubo, K. Kuramochi¹⁰⁾, K. Kurihara, G. Kurita, Y. Kusama, Y. Li⁸⁾, S.Y. Lin⁸⁾, X. Litaudon²¹⁾, T. Maekawa⁹⁾, K. Masaki, M. Matsukawa, T. Matsumoto, Y. Matsuzawa¹⁰⁾, G. Matsunaga, Y. Miura, N. Miya, A. Miyamoto¹⁰⁾, S. Miyamoto⁵⁾, N. Miyato, Y. Miyo, T. Mizuuchi⁹⁾, K. Mogaki, M. Mori, S. Moriyama, H. Murakami, Y. Nagasaka²²⁾, K. Nagasaki⁹⁾, O. Naito, T. Nakahata²³⁾, N. Nakajima⁴⁾, Y. Nakajima, T. Nakano, Y. Nakashima¹³⁾, H. Ninomiya, T. Nishiyama, K. Noto¹⁰⁾, H. Numata¹⁰⁾, K. Oasa, Y. Ogawa²⁰⁾, N. Ohno²⁴⁾, K. Ohshima¹⁰⁾, A. Oikawa, T. Oikawa, M. Okabayashi¹²⁾, N. Okamoto²⁴⁾, F. Okano, J. Okano, K. Okuno²³⁾, Y. Omori, T. Oshima, Y. Oya²³⁾, N. Oyama, T. Ozeki, V. Parail²⁵⁾, B.J. Peterson⁴⁾, Y. Sakamoto, A. Sakasai, S. Sakata, T. Sakuma¹⁰⁾, S. Sakurai, T. Sasajima, S. Sasaki, M. Sasao²⁾, F. Sato¹⁰⁾, Masayasu Sato, Minoru Sato, T. Sato¹⁰⁾, Y. Sato¹⁰⁾, M. Sawahata, M. Seimiya, M. Seki, G. Serianni³⁾, Y. Shibama, K. Shibata¹⁰⁾, T. Shibata, K. Shimada, R. Shimada¹⁸⁾, K. Shimizu, T. Shimizu¹⁰⁾, K. Shimomura¹⁸⁾, M. Shimonon, K. Shinohara, S. Shinozaki, T. Sugimura¹⁰⁾, A.M. Sukegawa, Y.W. Sun⁸⁾, H. Sunaoshi, M. Suzuki¹⁰⁾, S. Suzuki, Takahiro Suzuki, Takashi Suzuki¹⁰⁾, Yoshio Suzuki, Youzou Suzuki¹⁰⁾, Yutaka Suzuki¹⁰⁾, S. Takamura²⁴⁾, Y. Takase²⁰⁾, M. Takechi, H. Takenaga, T. Takenouchi¹⁰⁾, T. Takizuka, H. Tamai, Y. Tanai¹⁰⁾, T. Tani, H. Terakado¹⁰⁾, M. Terakado, T. Terakado, A. Ti⁸⁾, K. Toi⁴⁾, S. Tokuda, T. Totsuka, N. Tsubota¹⁰⁾, K. Tsuchiya, Y. Tsukahara, K. Tsutsumi¹⁰⁾, T. Tuda, Y. Ueda⁵⁾, K. Uehara, Y. Uesugi²⁶⁾, H. Urano, L. Urso¹⁶⁾, K. Ushigusa, K. Usui, Kazuhiko Wada¹⁰⁾, Kenji Wada¹⁰⁾, K. Watanabe⁴⁾, H. Yagisawa¹⁰⁾, J. Yagyu, T. Yamamoto, K. Yamauchi, K. Yamazaki⁴⁾, K. Yatsu¹³⁾, K. Yokokura,

H. Yoshida⁵⁾, Maiko Yoshida, Masafumi Yoshida¹⁹⁾, N. Yoshida¹⁹⁾, Z. Yoshida²⁰⁾,
A. Yoshikawa²³⁾, J. Zhao⁸⁾, H. Zohm¹⁶⁾, H. Zushi¹⁹⁾

Japan Atomic Energy Agency

- 1) Post-Doctoral Fellow
- 2) Tohoku University, Japan
- 3) Associazione EURATOM-ENEA, Italy
- 4) National Institute for Fusion Science, Japan
- 5) Osaka University, Japan
- 6) Tomsk Polytechnic University, Russia
- 7) National Nuclear Center Republic of Kazakhstan
- 8) Institute of Plasma Physics, Chinese Academy of Sciences, China
- 9) Kyoto University, Japan
- 10) Staff on loan
- 11) General Atomics, USA
- 12) Princeton Plasma Physics Laboratory, USA
- 13) University of Tsukuba, Japan
- 14) Hokkaido University, Japan
- 15) National Institute of Advanced Industrial Science and Technology, Japan
- 16) Max-Planck-Institut für Plasmaphysik, Germany
- 17) Australian National University, Australia
- 18) Tokyo Institute of Technology, Japan
- 19) Kyushu University, Japan
- 20) The University of Tokyo, Japan
- 21) Association EURATOM-CEA, France
- 22) Hiroshima Institute of Technology, Japan
- 23) Shizuoka University, Japan
- 24) Nagoya University, Japan
- 25) EURATOM /UKAEA Association, UK
- 26) Kanazawa University, Japan

JT-60U 実験結果のレビュー (2007 年～2008 年)

日本原子力研究開発機構 核融合研究開発部門
先進プラズマ研究開発ユニット・トカマクシステム技術開発ユニット

JT-60 チーム

(2009 年 11 月 16 日 受理)

2007 年および 2008 年の JT-60U の実験結果をレビューする。JT-60U の最後の実験キャンペーンとなる本期間では、ITER や DEMO の物理基盤の確立に向けて先進トカマクプラズマの開発を継続して推進した。総合性能の高いプラズマの開発を行い、ITER のハイブリッド運転シナリオと同程度の規格化ベータ値($\beta_N \sim 2.6$)、閉じ込め性能($H_{98(y,2)} \sim 1.0-1.1$)を持ち、かつ自発電流割合(f_{BS})が約 40%のプラズマを 25 秒間維持することができた。高密度・高放射損失領域においては、重水素プラズマにアルゴンおよびネオンを注入することにより、電子密度、閉じ込め改善度、放射損失割合が高いプラズマを 12 秒間維持することができた。これらの領域における維持時間は電流拡散時間(τ_R)よりも 10 倍以上長い。さらに、自由境界理想 MHD 限界を超えた領域では、高エネルギー粒子により励起される不安定性を発見するとともにこれを抑制することにより τ_R の数倍(5 秒間)の時間維持することができた。また、導体壁の安定化効果を用いることにより負磁気シアプラズマの性能が飛躍的に改善し、 $\beta_N \sim 2.7$ 、 $f_{BS} \sim 90\%$ を達成した。これらの成果は 2005-6 年に達成された成果を大幅に上回るものである。また、先進的な実時間制御システムの開発を進めた結果、イオン温度勾配および電流分布を単独または同時に実時間で制御することに成功した。計測装置の開発も継続して行い、例えばリチウムビームプローブによりプラズマ周辺部の密度分布および電流分布を高分解能で計測することができた。このほか、輸送、閉じ込め、不安定性、プラズマ-壁相互作用等に関する物理研究も進んだ。加熱・電流駆動装置においては、電子サイクロトロン電流駆動装置において 2.9 MW、5 秒間入射、および 0.4 MW、30 秒間入射に成功するとともに、新古典テアリング不安定性の回転に同期して最高 7 kHz でパワーを変調することができた。負イオン源中性粒子ビーム入射装置においては、340 keV、約 3 MW、30 秒間の入射に成功した。

那珂核融合研究所 (駐在) : 〒311-0193 茨城県那珂市向山 801-1

編集 : 諫山 明彦、大山 直幸、鈴木 隆博、篠原 孝司、坂本 宜照、松永 剛、
吉田 麻衣子、朝倉 伸幸、仲野 友英、神谷 健作、伊丹 潔

JT-60 チーム

相羽 信行¹⁾, 赤坂 博美, 秋野 昇, 安藤 晃²⁾, V. Antoni³⁾, 新井 貴, 朝倉 伸幸, 芦川 直子⁴⁾, 疇地 宏⁵⁾, 安積 正史, K.I. Baystrukov⁶⁾, B.Z. Chektybayev⁷⁾, J. Chen⁸⁾, 千葉 真一, E. Drapiko⁶⁾, 海老沢 昇, 藤井 常幸, 藤本 加代子¹⁾, 藤田 隆明, 福田 武司⁵⁾, 福本 正勝⁵⁾, 福山 淳⁹⁾, 古川 弘¹⁰⁾, W. Gao⁸⁾, P. Gohil¹¹⁾, L. Grisham¹²⁾, 芳賀 三郎¹⁰⁾, 濱松 清隆, 濱野 隆¹⁰⁾, 花田 磨砂也, 長谷川 浩一, 波多江 仰紀, 畠山 力三²⁾, 林 伸彦, 林 孝夫, 東島 智, 東園 雄太¹³⁾, 日野 友明¹⁴⁾, 平内 慎一, 平野 洋一¹⁵⁾, J. Hobirk¹⁶⁾, 本田 敦, 本田 正男, 本田 充¹⁾, 堀池 寛⁵⁾, 星野 克道, 細金 延幸, 細山 博己¹⁰⁾, J. Howard¹⁷⁾, D.A. Humphreys¹¹⁾, 市毛 尚志, 市毛 寿一¹⁰⁾, 市村 真¹³⁾, 居田 克巳⁴⁾, 井手 俊介, 井戸村 泰宏, 五十嵐 浩一¹⁰⁾, 飯尾 俊二¹⁸⁾, 池田 佳隆, 今井 剛¹³⁾, 井上 昭¹⁰⁾, 犬竹 正明²⁾, 諫山 明彦, 石田 真一, 石毛 洋一¹⁰⁾, 石井 和宏¹⁰⁾, 石井 啓一²⁾, 石井 康友, 伊丹 潔, 伊藤 公孝⁴⁾, 伊藤 早苗¹⁹⁾, 伊藤 智之¹⁹⁾, 門 信一郎²⁰⁾, 影井 康弘¹⁾, 鎌田 正輝¹⁾, 鎌田 裕, 上川 将章¹⁰⁾, 神永 敦嗣, 神谷 健作, 柏 好敏, 河合 視己人, 川俣 陽一, 河野 康則, 川島 寿人, 梶澤 稔, 菊池 勝美¹⁰⁾, 菊池 満, 木村 晴行, A.V. Kirilenko⁷⁾, 岸本 泰明⁹⁾, 北村 繁, 清野 公広, 木津 要, 小林 貴之¹⁾, 小林 薫¹⁰⁾, 小出 芳彦, 小島 有志¹⁾, 石仙 茂晴¹⁰⁾, 小又 将夫, 小森 彰夫⁴⁾, 小室 健一¹⁰⁾, 近藤 貴, 小西 哲之⁹⁾, 木島 滋, 香山 晃⁹⁾, 久保 博孝, 倉持 勝也¹⁰⁾, 栗原 研一, 栗田 源一, 草間 義紀, Y. Li⁸⁾, S.Y. Lin⁸⁾, X. Litaudon²¹⁾, 前川 孝⁹⁾, 正木 圭, 松川 誠, 松本 太郎, 松沢 行洋¹⁰⁾, 松永 剛, 三浦 幸俊, 宮 直之, 宮本 篤¹⁰⁾, 宮本 斉児⁵⁾, 宮戸 直亮, 三代 康彦, 水内 亨⁹⁾, 藻垣 和彦, 森 雅博, 森山 伸一, 村上 陽之, 長坂 康史²²⁾, 長崎 百伸⁹⁾, 内藤 磨, 中畑 俊彦²³⁾, 中島 徳嘉⁴⁾, 中島 勇太, 仲野 友英, 中嶋 洋輔¹³⁾, 二宮 博正, 西山 友和, 能登 勝也¹⁰⁾, 沼田 寛之¹⁰⁾, 大麻 和美, 小川 雄一²⁰⁾, 大野 哲靖²⁴⁾, 大島 克己¹⁰⁾, 及川 晃, 及川 聡洋, M. Okabayashi¹²⁾, 岡本 征晃²⁴⁾, 岡野 文範, 岡野 潤, 奥野 健二²³⁾, 大森 栄和, 大島 貴幸, 大矢 恭久²³⁾, 大山 直幸, 小関 隆久, V. Parail²⁵⁾, B.J. Peterson⁴⁾, 坂本 宜照, 逆井 章, 坂田 信也, 佐久間 猛¹⁰⁾, 櫻井 真治, 笹島 唯之, 佐々木 駿一, 笹尾 眞實子²⁾, 佐藤 文明¹⁰⁾, 佐藤 正泰, 佐藤 稔, 佐藤 朋樹¹⁰⁾, 佐藤 洋司¹⁰⁾, 澤島 正之, 清宮 宗孝, 関 正美, G. Serianni³⁾, 芝間 祐介, 柴田 一之¹⁰⁾, 柴田 孝俊, 島田 勝弘, 嶋田 隆一¹⁸⁾, 清水 勝宏, 清水 達夫¹⁰⁾, 下村 浩司¹⁸⁾, 下野 貢, 篠原 孝司, 篠崎 信一, 杉村 徹¹⁰⁾, 助川 篤彦, Y.W. Sun⁸⁾, 砂押 秀則, 鈴木 昌栄¹⁰⁾, 鈴木 貞明, 鈴木 隆博, 鈴木 高志¹⁰⁾, 鈴木 喜雄, 鈴木 洋三¹⁰⁾, 鈴木 優¹⁰⁾, 高村 秀一²⁴⁾, 高瀬 雄一²⁰⁾, 武智 学, 竹永 秀信, 竹之内 忠¹⁰⁾, 滝塚 知典, 玉井 広史, 棚井 豊¹⁰⁾, 谷 孝志, 寺門 祐之¹⁰⁾, 寺門 正之, 寺門 恒久, A. Ti⁸⁾, 東井 和夫⁴⁾, 徳田 伸二, 戸塚 俊之, 坪田 直明¹⁰⁾,

土屋 勝彦, 塚原 美光, 堤 和昌¹⁰⁾, 津田 孝, 上田 良夫⁵⁾, 上原 和也,
上杉 喜彦²⁶⁾, 浦野 創, L. Urso¹⁶⁾, 牛草 健吉, 薄井 勝富, 和田 一彦¹⁰⁾,
和田 健次¹⁰⁾, 渡邊 清政⁴⁾, 八木澤 博¹⁰⁾, 柳生 純一, 山本 巧, 山内 邦仁,
山崎 耕造⁴⁾, 谷津 潔¹³⁾, 横倉 賢治, 吉田 英次⁵⁾, 吉田 麻衣子, 吉田 雅史¹⁹⁾,
吉田 直亮¹⁹⁾, 吉田 善章²⁰⁾, 吉河 朗²³⁾, J. Zhao⁸⁾, H. Zohm¹⁶⁾, 関子 秀樹¹⁹⁾

日本原子力研究開発機構

- 1) 博士研究員
- 2) 東北大学
- 3) イタリア原子力・代替エネルギー研究開発委員会(ENEA), イタリア
- 4) 核融合科学研究所
- 5) 大阪大学
- 6) トムスク工科大学, ロシア
- 7) 国立原子力センター, カザフスタン共和国
- 8) 中国科学院プラズマ物理研究所, 中国
- 9) 京都大学
- 10) 業務協力員
- 11) ジェネラルアトミックス社, 米国
- 12) プリンストン大学プラズマ物理研究所, 米国
- 13) 筑波大学
- 14) 北海道大学
- 15) 産業技術総合研究所
- 16) マックスプランクプラズマ物理研究所, ドイツ
- 17) オーストラリア国立大学, オーストラリア
- 18) 東京工業大学
- 19) 九州大学
- 20) 東京大学
- 21) フランス原子力庁(CEA), フランス
- 22) 広島工業大学
- 23) 静岡大学
- 24) 名古屋大学
- 25) 欧州原子力共同体/イギリス原子力公社(UKAEA), イギリス
- 26) 金沢大学

Contents

| | | |
|--|-------|----|
| 1. Introduction | | |
| N. Oyama and A. Isayama | | 1 |
| 2. Overview of Experimental Results | | |
| 2.1 Extension of Operation Regimes | | |
| T. Suzuki | | 3 |
| 2.2 Transport in Core Plasmas | | |
| K. Shinohara | | 3 |
| 2.3 H-mode Confinement and Pedestal | | |
| Y. Sakamoto | | 4 |
| 2.4 MHD Instability and High-Energy Ions | | |
| G. Matsunaga | | 5 |
| 2.5 Plasma Control and Heating/Current Drive Physics | | |
| M. Yoshida | | 7 |
| 2.6 Divertor and SOL Plasmas | | |
| N. Asakura | | 8 |
| 2.7 Plasma-Wall Interactions | | |
| T. Nakano | | 9 |
| 2.8 Diagnostics | | |
| K. Kamiya and K. Itami | | 10 |
| 2.9 Heating Systems | | |
| A. Isayama | | 11 |
| 3. Extension of Operation Regime | | |
| 3.1 Sustainment of High-beta Plasma above Ideal No-wall Beta Limit | | |
| G. Matsunaga et al. | | 12 |
| 3.2 Development of Reversed Shear Plasmas with High Bootstrap Current Fraction towards Reactor Relevant Regime in JT-60U | | |
| Y. Sakamoto et al. | | 13 |
| 3.3 Long-Pulse Hybrid Scenario Development in JT-60U | | |
| N. Oyama et al. | | 14 |
| 3.4 Impurity Seeding Experiments in the Long Pulse Discharges | | |
| N. Asakura et al. | | 15 |
| 3.5 Development of Full-CD Plasma Having Steady Current Profile and High Bootstrap Current Fraction | | |
| T. Suzuki et al. | | 16 |
| 4. Transport in Core Plasmas | | |
| 4.1 Characteristics of Momentum Transport in H-mode Plasmas | | |
| M. Yoshida et al. | | 17 |
| 4.2 Role of ECRF on Toroidal Rotation | | |
| M. Yoshida et al. | | 18 |

| | | |
|------------------------------------|---|----|
| 4.3 | Characteristics of Internal Transport Barrier under Reactor Relevant Condition in JT-60U Weak Shear Plasmas | |
| | H. Takenaga et al. | 19 |
| 4.4 | Fuelling Characteristics of Supersonic Molecular Beam Injection | |
| | H. Takenaga et al. | 20 |
| 4.5 | Effects of Toroidal momentum input on Internal Transport Barrier Formation in JT-60U Reversed Shear Plasmas | |
| | Y. Sakamoto et al. | 24 |
| 4.6 | Effects of Rational Surfaces at q_{\min} on Internal Transport Barrier in JT-60U Reversed Shear Plasmas | |
| | Y. Sakamoto et al. | 28 |
| 4.7 | Effect of toroidal rotation and q profiles on ITB characteristics for JET/JT-60U identity experiment | |
| | Y. Sakamoto et al. | 32 |
| 4.8 | Dependence of Heat Transport on Toroidal Rotation in Conventional H-modes in JT-60U | |
| | H. Urano et al. | 36 |
| 4.9 | Heat Transport of H-mode Plasmas in the Variation of Current Density Profiles in | |
| | H. Urano et al. | 37 |
| 4.10 | Correlation between the Edge and the Internal Transport Barriers and Effect of ELMs in JT-60U | |
| | Y. Kamada et al. | 38 |
| 4.11 | Tungsten Accumulation in H-mode Discharges | |
| | T. Nakano et al. | 39 |
| 4.12 | Experimental Investigation of Particle Transport Associated with Turbulence in LHD Heliotron and JT-60U Tokamak Plasmas | |
| | K. Tanaka et al. | 41 |
| 4.13 | Dynamics of Ion Internal Transport Barrier in LHD Heliotron and JT-60U Tokamak Plasmas | |
| | K. Ida et al. | 42 |
| 5. H-mode Confinement and Pedestal | | |
| 5.1 | Dimensionless Parameter Dependence of H-mode Pedestal Width using Hydrogen and Deuterium Plasmas in JT-60U | |
| | H. Urano et al. | 43 |
| 5.2 | Edge Impurity Ion Dynamics in co-, bal.- and ctr-NBI Heated H-mode Plasmas | |
| | K. Kamiya et al. | 44 |
| 5.3 | L to H-mode Transition Studies | |
| | K. Kamiya et al. | 48 |
| 5.4 | Fast Dynamics of Type I and Grassy ELMs | |
| | A. Kojima et al. | 52 |
| 5.5 | Transport Modeling between ELMs | |
| | N. Hayashi et al. | 53 |

| | | |
|------|--|----|
| 5.6 | Characteristics of QH-mode with Edge Co-rotation in JT-60U Y. Sakamoto et al. | 54 |
| 5.7 | Analysis of Pedestal Characteristics in JT-60U H-mode Plasmas Based on Monte-Carlo Neutral Transport Simulation Y. Nakashima et al. | 58 |
| 5.8 | Effects of Edge Collisionality on ELM Characteristics in Grassy ELM Regime N. Oyama et al. | 59 |
| 5.9 | Effect of Toroidal Rotation on Pedestal and H-mode Performance in JET/JT-60U Similarity Shape N. Oyama et al. | 63 |
| 5.10 | Effect of Edge EC Injection on Type I ELMs N. Oyama et al. | 67 |
| | | |
| 6. | MHD Instability and High-Energy Ions | |
| 6.1 | Observation of Energetic Particle Driven Instability in the Wall-stabilized High- β G. Matsunaga et al. | 71 |
| 6.2 | Observation of RWM Precursor G. Matsunaga et al. | 72 |
| 6.3 | Identification of the Minimum EC-driven Current for Complete Stabilization of an $m/n=2/1$ Neoclassical Tearing Mode A. Isayama et al. | 73 |
| 6.4 | Stabilization of an $m/n=2/1$ NTM Using Modulated ECCD A. Isayama et al. | 74 |
| 6.5 | Fitting of the Modified Rutherford Equation: a Comparison between ASDEX Upgrade and JT-60 Results L. Urso et al. | 75 |
| 6.6 | Triton Burn-up Experiment using Newly Developed Neutron Profile Measurement K. Shinohara et al. | 76 |
| 6.7 | Study of Ion Cyclotron Emissions due to DD Fusion Product Ions on JT-60U M. Ichimura et al. | 80 |
| 6.8 | Study of Current Decay Time during Disruption in JT-60U Tokamak Y. Shibata et al. | 84 |
| | | |
| 7. | Plasma Control and Heating/Current Drive Physics | |
| 7.1 | Integrated Plasma Control using Real-Time Measurements and Control Systems M. Yoshida et al. | 88 |
| 7.2 | Simultaneous Real-time Control of Current and Pressure Profiles T. Suzuki et al. | 92 |

| | | |
|-----------------------------|---|-----|
| 7.3 | Particle Control Study in JT-60U towards Burning Plasma Control H. Takenaga et al. | 96 |
| 7.4 | Demonstration of Real Time Control in Burning Plasma Simulation Experiments H. Takenaga et al. | 97 |
| 7.5 | Off-axis NBCD Measurement T. Suzuki et al. | 101 |
| 7.6 | Plasma Current Start-up Experiment by ECH T. Maekawa et al. | 105 |
| 7.7 | ECH Wall Conditioning Discharges in JT-60U K. Itami et al. | 109 |
| 8. Divertor and SOL Plasmas | | |
| 8.1 | Balance of Ionization and Recombination of Carbon Ions in High Density Peripheral Plasmas of the JT-60U Tokamak T. Nakano et al. | 110 |
| 8.2 | Fluctuation Characteristics of the L-mode and H-mode SOL Plasmas H. Tanaka et al. | 112 |
| 8.3 | Fluctuation Characteristics in the Detached Divertor N. Asakura et al. | 116 |
| 8.4 | SOL Flow and Plasma Profiles in High-Field-Side SOL N. Asakura et al. | 117 |
| 8.5 | Kinetic Simulation of Impurity Transport in Detached Plasma K. Shimizu et al. | 121 |
| 9. Plasma-Wall Interactions | | |
| 9.1 | Particle Balance of Long-Pulse Discharges T. Nakano et al. | 122 |
| 9.2 | Deuterium Depth Profiling in Graphite Tiles not Exposed to Hydrogen Discharges before Air Ventilation T. Hayashi et al. | 126 |
| 9.3 | H+D Retention in the First Wall Graphite Tiles M. Yoshida et al. | 127 |
| 9.4 | Analysis of Residual Gas by High-Resolution Mass Spectrometry during Helium Glow Discharge Cleaning T. Hayashi et al. | 128 |
| 9.5 | Characterization of Re-deposition Layer with Ferritic Steel N. Ashikawa et al. | 129 |
| 9.6 | Localized Tungsten Deposition in Divertor Region Y. Ueda et al. | 130 |
| 9.7 | Modelling of Tungsten Impurity Transport Using IMPGYRO Code K. Hoshino et al. | 131 |
| 9.8 | Tungsten Stripe Coatings on the Lower Divertor Plate T. Nakano et al. | 134 |

| | |
|---------------------|--|
| 10. Diagnostics | |
| 10.1 | Development of a High-Brightness and Low-Divergence Lithium Neutral Beam for a Zeeman Polarimetry A. Kojima et al. 135 |
| 10.2 | Development and Operation of Lithium Beam Probe A. Kojima et al. 136 |
| 10.3 | Zeeman Polarimetry Measurement Using Li-beam Probe K. Kamiya et al. 140 |
| 10.4 | Equilibrium Reconstruction Using the Lithium Beam Probe Data T. Fujita et al. 144 |
| 10.5 | Development of Doppler Reflectometer and Correlation Reflectometer in JT-60U N. Oyama et al. 148 |
| 10.6 | Magnetic Fluctuation Profile Measurement Using Optics of Motional Stark Effect Diagnostics in JT-60U T. Suzuki et al. 152 |
| 10.7 | Two-dimensional Visible Spectrometer for Divertor Plasmas T. Nakano et al. 153 |
| 10.8 | Upgraded Charge Exchange Recombination Spectroscopy on JT-60U Y. Sakamoto et al. 157 |
| 10.9 | Measurements of Carbon Dust by Fast TV Camera and Laser Scattering N. Asakura et al. 161 |
| 10.10 | Development of Polarization Interferometer for Thomson Scattering Diagnostics in T. Hatae et al. 165 |
| 10.11 | A 160 ps Pulse Generation by Stimulated Brillouin Scattering -Phase Conjugation Mirror for advanced Thomson Scattering Diagnostics H. Yoshida et al. 166 |
| 10.12 | Imaging Bolometer Upgrade on JT-60U B.J. Peterson et al. 167 |
| 10.13 | Radiation Temperature of ECE in Bi-Maxwellian Tokamak Plasma M. Sato et al. 168 |
| 10.14 | Fast-Ion Measurement with the Doppler Shifted D-alpha Light on JT-60U M. Osakabe et al. 169 |
| 10.15 | Absolute Calibration of Microfission Chamber T. Hayashi et al. 173 |
| 11. Heating Systems | |
| 11.1 | Development and Achievements on High Power ECRF and LHRF System in JT-60U S. Moriyama et al. 174 |
| 11.2 | Development of Long Pulse Neutral Beam Injector on JT-60U M. Hanada et al. 176 |
| Acknowledgments | 177 |

目 次

| | | |
|---|-------|----|
| 1. 緒言 | | |
| | 大山、諫山 | 1 |
| 2. 実験結果の概要 | | |
| 2.1 運転領域の拡大 | | |
| | 鈴木 | 3 |
| 2.2 コアプラズマにおける輸送 | | |
| | 篠原 | 3 |
| 2.3 Hモード閉じ込めとペDESTAL | | |
| | 坂本 | 4 |
| 2.4 MHD不安定性と高エネルギーイオン | | |
| | 松永 | 5 |
| 2.5 プラズマ制御と加熱/電流駆動物理 | | |
| | 吉田 | 7 |
| 2.6 ダイバータおよびSOLプラズマ | | |
| | 朝倉 | 8 |
| 2.7 プラズマ壁相互作用 | | |
| | 仲野 | 9 |
| 2.8 計測装置 | | |
| | 神谷、伊丹 | 10 |
| 2.9 加熱システム | | |
| | 諫山 | 11 |
| 3. 運転領域の拡大 | | |
| 3.1 壁なし理想ベータ限界を超えた高ベータプラズマの維持 | | |
| | 松永 他 | 12 |
| 3.2 JT-60Uにおける核融合炉相当領域へ向けた高自発電流割合 負磁気シアプラズマの開発 | | |
| | 坂本 他 | 13 |
| 3.3 JT-60Uにおける長パルスハイブリッドシナリオの開発 | | |
| | 大山 他 | 14 |
| 3.4 長パルス放電における不純物注入実験 | | |
| | 朝倉 他 | 15 |
| 3.5 定常電流分布と高自発電流割合を有する完全非誘導電流駆動 プラズマの開発 | | |
| | 鈴木 他 | 16 |

| | |
|--|----|
| 4. コアプラズマにおける輸送 | |
| 4.1 Hモードプラズマにおける運動量輸送の特性 | |
| 吉田 他 | 17 |
| 4.2 トロイダル回転におけるECRFの役割 | |
| 吉田 他 | 18 |
| 4.3 JT-60U弱磁気シアプラズマにおける核融合炉相当条件の下での 内部輸送障壁の特性 | |
| 竹永 他 | 19 |
| 4.4 超音速分子ビーム入射の燃料供給特性 | |
| 竹永 他 | 20 |
| 4.5 JT-60U負磁気シアプラズマにおける内部輸送障壁形成に対する トロイダル方向運動量入力の影響 | |
| 坂本 他 | 24 |
| 4.6 JT-60U負磁気シアプラズマにおける内部輸送障壁に対する 安全係数最小値での有理面の影響 | |
| 坂本 他 | 28 |
| 4.7 JT-60UとJETの比較実験におけるITBに対するトロイダル回転と q分布の効果 | |
| 坂本 他 | 32 |
| 4.8 JT-60UにおけるHモードの熱輸送に対するトロイダル回転依存性 | |
| 浦野 他 | 36 |
| 4.9 JT-60UにおけるHモードプラズマの電流分布による熱輸送への 影響 | |
| 浦野 他 | 37 |
| 4.10 JT-60Uにおける内部輸送障壁と周辺輸送障壁との相関とELMの 影響 | |
| 鎌田 他 | 38 |
| 4.11 Hモード放電におけるタングステンの蓄積 | |
| 仲野 他 | 39 |
| 4.12 LHDヘリオトロンプラズマとJT-60Uトカマクプラズマにおける 乱流に関連する粒子輸送に関する実験研究 | |
| 田中 他 | 41 |
| 4.13 LHDヘリオトロンプラズマとJT-60Uトカマクプラズマにおける イオン系内部輸送障壁のダイナミクス | |
| 居田 他 | 42 |
| 5. Hモード閉じ込めとペデスタル | |
| 5.1 JT-60Uにおける軽水素および重水素プラズマを用いたHモード ペデスタル幅の無次元パラメータ依存性 | |
| 浦野 他 | 43 |

| | | |
|------|---|----|
| 5.2 | Co-, balance-, counter-NBI加熱Hモードプラズマにおける周辺不純物イオンのダイナミクス 神谷 他 | 44 |
| 5.3 | LモードからHモードへの遷移に関する研究 神谷 他 | 48 |
| 5.4 | Type IおよびGrassy ELMの速いダイナミクス 小島 他 | 52 |
| 5.5 | ELM間の輸送のモデリング 林 他 | 53 |
| 5.6 | JT-60Uにおけるco方向回転QHモードの特性 坂本 他 | 54 |
| 5.7 | モンテカルロ中性粒子輸送シミュレーションに基づくJT-60UのHモードプラズマのペデスタル特性の解析 中嶋 他 | 58 |
| 5.8 | Grassy ELM領域におけるELM特性に対する周辺衝突度の影響 大山 他 | 59 |
| 5.9 | JET/JT-60U相似形状の下でのペデスタルおよびHモード性能に対するトロイダル回転の影響 大山 他 | 63 |
| 5.10 | Type I ELMに対する周辺EC入射の影響 大山 他 | 67 |
| 6. | MHD不安定性と高エネルギーイオン | |
| 6.1 | 壁安定化された高ベータプラズマにおける高エネルギー粒子駆動不安定性の観測 松永 他 | 71 |
| 6.2 | RWM前兆振動の観測 松永 他 | 72 |
| 6.3 | $m/n=2/1$ 新古典テアリングモードの完全安定化のための最小EC駆動電流の同定 諫山 他 | 73 |
| 6.4 | 変調ECCDによる $m/n=2/1$ NTMの安定化 諫山 他 | 74 |
| 6.5 | 修正Rutherford式を用いたフィッティング：ASDEX-UpgradeとJT-60Uの結果 ウルソ 他 | 75 |
| 6.6 | 新たに開発した中性子分布計測システムを用いたトリトン燃焼実験 篠原 他 | 76 |

| | | |
|---------------------|---|-----|
| 6.7 | JT-60UにおけるDD核融合生成イオンによる イオンサイクロトロン放射の研究 市村 他 | 80 |
| 6.8 | JT-60Uトカマクにおけるディスラプション時の電流減衰時間 の研究 柴田 他 | 84 |
| 7. プラズマ制御と加熱/電流駆動物理 | | |
| 7.1 | 実時間計測と制御システムを用いた統合プラズマ制御 吉田 他 | 88 |
| 7.2 | 電流分布と圧力分布の同時実時間制御 鈴木 他 | 92 |
| 7.3 | 燃焼プラズマ制御に向けたJT-60Uにおける粒子制御研究 竹永 他 | 96 |
| 7.4 | 燃焼プラズマ模擬実験における実時間制御の実証 竹永 他 | 97 |
| 7.5 | Off-axis NBCD計測 鈴木 他 | 101 |
| 7.6 | ECHによるプラズマ電流立ち上げ実験 前川 他 | 105 |
| 7.7 | JT-60UにおけるECH壁調整放電 伊丹 他 | 109 |
| 8. ダイバータおよびSOLプラズマ | | |
| 8.1 | JT-60Uトカマクの高密度周辺プラズマにおける炭素イオンの 電離と再結合のバランス 仲野 他 | 110 |
| 8.2 | LモードおよびHモードSOLプラズマの揺動特性 田中 他 | 112 |
| 8.3 | 非接触ダイバータにおける揺動特性 朝倉 他 | 116 |
| 8.4 | 高磁場側SOLにおけるSOL流とプラズマ分布 朝倉 他 | 117 |
| 8.5 | 非接触プラズマにおける不純物輸送の運動論効果を含んだ シミュレーション 清水 他 | 121 |

| | |
|--------------|---|
| 9. プラズマ壁相互作用 | |
| 9.1 | 長パルス放電における粒子バランス 仲野 他 122 |
| 9.2 | 大気解放前に軽水素プラズマ放電に晒されていない炭素タイル の重水素深さ分布評価 林 他 126 |
| 9.3 | 第一壁炭素タイルにおけるH+Dリテンション 吉田 他 127 |
| 9.4 | 高分解能質量分析装置を用いたヘリウムグロー放電洗浄中の 残留ガス分析 林 他 128 |
| 9.5 | フェライト鋼の再堆積層の特性 芦川 他 129 |
| 9.6 | ダイバータ領域における局在化したタングステンの堆積 上田 他 130 |
| 9.7 | IMPGYROコードを用いたタングステン不純物輸送のモデリング 星野 他 131 |
| 9.8 | 下側ダイバータ板におけるタングステンストライプコーティング 仲野 他 134 |
| 10. 計測装置 | |
| 10.1 | ゼーマン偏光測定のための高輝度低発散角リチウム中性ビーム の開発 小島 他 135 |
| 10.2 | リチウムビームプローブの開発と運転 小島 他 136 |
| 10.3 | Liビームプローブを用いたゼーマン偏光測定 神谷 他 140 |
| 10.4 | リチウムビームプローブデータを用いた平衡再構成 藤田 他 144 |
| 10.5 | JT-60Uにおけるドップラー反射計と相関反射計の開発 大山 他 148 |

| | | |
|-------|---|-----|
| 10.6 | JT-60Uにおけるモーショナルシュタルク効果計測器の光学系を使った磁場揺動分布測定 鈴木 他 | 152 |
| 10.7 | ダイバータ領域測定のための2次元可視分光装置 仲野 他 | 153 |
| 10.8 | JT-60Uにおける改良荷電交換分光装置 坂本 他 | 157 |
| 10.9 | 高速TVカメラとレーザー散乱による炭素ダストの測定 朝倉 他 | 161 |
| 10.10 | JT-60Uにおけるトムソン散乱計測のための偏光干渉計の開発 波多江 他 | 165 |
| 10.11 | 先進トムソン散乱計測のための誘導ブリュアン散乱位相共役鏡による160psパルス生成 吉田 他 | 166 |
| 10.12 | JT-60Uのイメージングボロメータの改良 ピーターソン 他 | 167 |
| 10.13 | 2成分電子温度マックスウェル分布をもつトカマクプラズマにおけるECE放射温度 佐藤 他 | 168 |
| 10.14 | JT-60UにおけるドップラーシフトしたD α 光を用いた高速イオン計測 長壁 他 | 169 |
| 10.15 | マイクロフィッションチャンバーの絶対較正 林 他 | 173 |
| 11. | 加熱システム | |
| 11.1 | JT-60Uにおける高パワーECRFおよびLHRFシステムの開発と成果 森山 他 | 174 |
| 11.2 | JT-60Uにおける長パルス中性粒子ビーム入射装置の開発 花田 他 | 176 |
| | 謝辞 | 177 |

This is a blank page.

1 Introduction

The JT-60U project has been focused on development of steady-state advanced tokamak (AT) plasmas to realize economical fusion reactor and to establish physics basis for ITER. High confinement, high normalized beta (β_N), high bootstrap current fraction (f_{BS}) and efficient heat/particle handling are important factors to maintain AT plasmas in steady-state. The neutral beam injection (NBI) system and electron cyclotron heating (ECH) system have been improved to provide further flexibility of heating and current drive to develop AT plasmas and to investigate important physics for steady-state AT operation. In positive-ion based NBI (P-NBI) system, the power supply system for three perpendicular-NBI units for central heating has been modified so as to extend the maximum pulse duration up to 30 s, in addition to existing five modified NBI units. Furthermore, 30 s injection of negative-ion based NBI (N-NBI) with heating power of 3 MW (80 MJ) has been achieved. As a result the total input energy of 445 MJ from both P- and N-NBI units has been achieved. In ECH system, four gyrotrons injected high electron cyclotron wave power of 2.9 MW for 5 s, which corresponds to the injected energy of 14.5 MJ. In addition, the power modulation technique up to 7 kHz has been developed for the stabilization of neoclassical tearing modes (NTMs). New diagnostics with high temporal and spatial resolution have improved real-time plasma control scheme for the control of AT plasmas. In the experimental campaign in 2007-2008, further expansion of the operational regime of AT plasmas toward higher β_N regime has been achieved making use of the improved heating systems and diagnostics [1].

In weak magnetic shear plasmas and reversed magnetic shear plasmas, the operational regime has been extended toward higher β_N exceeding the ideal magnetohydrodynamic (MHD) limit without conducting wall ($\beta_N^{\text{no-wall}}$) by resistive wall mode (RWM) stabilization. In long-pulse plasmas with positive magnetic shear, sustainable β_N with high confinement as a development of ITER hybrid scenario, and sustained duration of high density and high radiation loss fraction plasma have been improved. Progress has also been made in physics studies relating to MHD instabilities, internal/edge transport barriers, plasma rotation, current drive, H-mode confinement, impurity transport, SOL/divertor transport and plasma-wall interaction and so on, which also contributed to the development of the AT plasmas. The active NTM stabilization system using modulated electron cyclotron current drive (ECCD), which is synchronized with rotating island, has been developed and the efficiency of modulated ECCD in $m/n = 2/1$ NTM stabilization has been demonstrated (m and n are poloidal and toroidal mode number, respectively). The intrinsic toroidal rotation driven by the ion pressure gradient and by the ECH is confirmed. New fast diagnostics with high spatial and temporal resolutions for ion temperature and electron density reveals the different structure of pedestal pressure between co- and counter-rotating plasma, resulting in different ELM size determined by the radial penetration depth of the ELM crash. The tungsten generation and

accumulation are also studied.

The results from AT research in JT-60U contribute for the development of physics basis for ITER through International Tokamak Physics Activity (ITPA) activities. Various inter-machine experiments have been performed with on-site and/or remote participations. Domestic collaboration with universities and institutes has been expanded. All experiments have been discussed and planned by the joint experimental theme group* including co-leaders for sub-themes with experts from universities and institutes.

Reference

[1] Oyama, N. and the JT-60 Team, to appear in Nuclear Fusion.

* Theme Leaders:

N. Oyama, A. Isayama, and H. Takenagaⁱ⁾

Co-Leaders for Sub-Themes:

T. Suzuki and K. Nagasakiⁱ⁾ for Extension of Operation Regime and Improvement of Performance,

K. Shinohara and K. Ida²⁾ for Transport,

Y. Sakamoto and Y. Nakashima³⁾ for Pedestal,

G. Matsunaga, S. Sakakibara²⁾ and A. Isayamaⁱ⁾ for MHD,

N. Asakura and N. Ohno⁴⁾ for Divertor and SOL,

T. Nakano, Y. Ueda⁵⁾ and H. Kuboⁱⁱ⁾ for Plasma Wall Interaction.

i) until September, 2007

ii) until March, 2007

1) Kyoto University

2) National Institute for Fusion Science

3) University of Tsukuba

4) Nagoya University

5) Osaka University

2. Overview of Experimental Results

2.1 Extension of Operation Regimes

Owing to modification of power supply systems for three perpendicular P-NBs in order to provide a long period of central NB heating up to 30 s, high performance plasma at $\beta_N = 2.6$, $H_{H98(y,2)} > 1$, and $\beta_N H_{H98(y,2)} / q_{95}^2 = 0.25$ at low $q_{95} = 3.2$ (safety factor at 95 % flux surface) has been sustained for 25 s, corresponding to about 14 times the current diffusion time. This plasma has a flat q profile in the central region ($r/a < 0.5$), and such q profile is effective in avoiding the onset of neoclassical tearing modes up to $\beta_N \sim 3$ for a peaked pressure profile. In high β_N regime above $\beta_N^{\text{no-wall}}$, $\beta_N \sim 3$ at high $f_{BS} = 0.5$ has been successfully sustained for about 5 s, which corresponds to 3 times the current diffusion time (~ 1.5 s), by avoiding newly observed MHD instabilities, namely energetic particle driven wall mode (EWM) and resistive wall mode (RWM) precursor. Since the EWM that is destabilized by trapped energetic particles by perpendicular NBs slows down the plasma rotation below a critical velocity and then finally triggers the RWM, the perpendicular NBs are replaced by tangential N-NB in order to avoid EWM. Toward steady-state operation, a fully non-inductive discharge having a relaxed current profile and high $f_{BS} = 0.5$ has been established at reasonably low $q_{95} = 5.8$, $q_{\min} = 2.1$, and $q(0) = 2.4$, where q_{\min} and $q(0)$ are the safety factor at the minimum and the plasma center, respectively. This plasma is free from MHD instabilities at low q (≤ 2) rational surfaces, and the steady current profile at full-CD (fraction of non-inductively driven current to the plasma current $f_{CD} = 1$) is obtained using NBCD and off-axis LHCD. A stability of reversed magnetic-shear plasmas has been largely improved from previous experiment ($\beta_N = 1.7$ - 2.1) to $\beta_N \sim 2.7$ at reasonably low $q_{95} \sim 5.3$, placing the plasma close to the conducting wall under reduced toroidal field ripple by ferritic steel tiles. This β_N well exceeds $\beta_N^{\text{no-wall}} \sim 1.9$, and is close to the ideal wall beta limit $\beta_N^{\text{ideal-wall}}$ at ~ 2.9 (resulting $C_\beta \equiv (\beta_N - \beta_N^{\text{no-wall}}) / (\beta_N^{\text{ideal-wall}} - \beta_N^{\text{no-wall}}) \sim 0.8$). In addition, high integrated performance is achieved at $H_{H98(y,2)} \sim 1.7$, $f_{BS} \sim 0.92$, $f_{CD} \sim 0.94$ and $n_e/n_{GW} \sim 0.87$ under the conditions of $T_e \sim T_i$ and low momentum input. In impurity seeding experiments in positive shear plasmas, good energy confinement ($H_{H98(y,2)} \sim 0.87$ - 0.75), large total radiation fraction ($f_{\text{rad}} \sim 0.77$ - 1), and high density ($f_{GW} = 0.67$ - 0.85) are sustained for 13 s using Ar as core radiator. When seeding Ar and Ne for core and divertor radiations, respectively, better performance has been sustained for 12 s at $H_{H98(y,2)} \sim 0.95$ - 0.85 , $f_{\text{rad}} \sim 0.78$ - 1 and $f_{GW} = 0.68$ - 0.88 , where radiation power at divertor is 50-70 % of the absorbed heating power.

2.2 Transport in Core Plasmas

The formation condition of internal transport barrier (ITB) was compared between balanced and co-neutral beam injections by using modulation CXRS (MCXRS) diagnostic in reversed shear (RS) plasmas. Different characteristics were observed in the location of ITB

foot, final structure of the ion temperature (T_i) and the toroidal rotation (V_t) profiles, and the temporal evolution of ITB formation. The effects of rational surfaces at the minimum q -value, q_{\min} , on ITB were also investigated in RS plasmas by using MCXRS and fast CXRS. The increase in T_i and the rapid change in V_t were observed almost at the same time when q_{\min} crossed an integer. The reduction of T_i and V_t was observed in wide area prior to crossing the integer value of q_{\min} . The correlation between the edge transport barrier (ETB) and the ITB was also investigated. It was found that the ELM affected area was deeper in the order of V_t , T_i and then the electron temperature (T_e).

In the study of momentum transport, the correlation among the toroidal momentum diffusivity (χ_ϕ), the ion thermal diffusivity (χ_i), and the convection velocity (V_{conv}) was investigated in H-mode plasmas with the perturbation technique using modulated NBs. The investigation revealed that the correlation between χ_ϕ and χ_i , and the decrease of $-V_{\text{conv}}$ with increasing χ_ϕ . The ECRF-driven intrinsic rotation was also investigated. It was found that ECRF drove the co-intrinsic rotation inside the EC deposition radius and induced the counter-intrinsic rotation outside the EC deposition radius.

For the study of particle transport, supersonic molecular beam injection (SMBI) was installed in collaboration with CEA-Cadarache for the first time among the large tokamaks. The SMBI could directly affect the plasma parameters at $r/a \sim 0.8$ and also affect through cold pulse propagation inside more. The SMBI contributed to the study of an intermediate fueling method between pellet injection and gas-puffing.

In order to investigate the conditions that tungsten, W, ions accumulate in the plasma core, plasma toroidal rotation scan, EC and NNB injection experiments were performed. The W accumulation became significant with increasing toroidal rotation velocity in the counter-direction. The EC and NNB injections successfully suppressed the W accumulation.

Under the collaboration with LHD, the characteristics of the particle transport in the core region and the ITB formation condition were compared with helical system as another torus system. In the comparison of particle transport, it was found that the collisionality dependence of the density profile was different in LHD when the magnetic axis position was varied by 0.1 m. This dependence was not observed in tokamaks. In the comparison of the ITB formation, it was found that the ITB location moves outward regardless of the sign of magnetic shear in JT-60U while the ITB location tends to expand inward in LHD.

2.3 H-mode Confinement and Pedestal

Dimensionless parameter dependence of H-mode pedestal width has been clarified by comparison of hydrogen and deuterium plasmas. The scaling of the pedestal width is evaluated as $\Delta_{\text{ped}} \propto a_p \rho_{\text{pol}}^*{}^{0.2} \beta_p^{0.5}$, where a_p , ρ_{pol}^* and β_p are plasma minor radius, poloidal gyro-radius and poloidal beta, respectively. The temporal evolution and radial perturbation of

the radial electric field E_r during type-I ELM phase have been investigated by using the data from newly installed fast charge exchange recombination spectroscopy ($\Delta t \sim 2.5$ ms). The E_r -well for the co-NBI discharge seems to be shallower than that for the counter-NBI. On the contrary, the E_r -shear layer for the co-NBI discharge is likely to be wider than that for the counter-NBI. The wider T_i pedestal width seen in the co-NBI discharge than that seen in the counter-NBI discharge may come from the difference in the E_r -shear layer. The dynamics of the density in the type-I and grassy ELMs are also investigated by using newly installed lithium beam probe ($\Delta t \sim 0.5$ ms). Type-I ELM observed in co-rotating plasmas exhibited larger and wider ELM affected area ($\Delta n_{\text{ped}}/n_{\text{ped}} \sim 30\%$, radial extent >15 cm) than ctr-rotating plasmas ($\Delta n_{\text{ped}}/n_{\text{ped}} \sim 20\%$, radial extent ~ 10 cm). The collapse of density pedestal by grassy ELM is smaller ($<20\%$) and narrower (~ 5 cm) than that by type-I ELMs. The transition phenomenology in the H-mode discharge has been studied. It is found that there are two discrete phases with different magnitude of E_r in the ELM-free H-mode phase. One is the intermediate H-phase having the large ion temperature gradients without significant poloidal rotation (and with moderate magnitude of E_r), and the other is the complete H-phase characterized by the large E_r . The ELM energy loss and cycle have been studied by using the TOPICS-IB code. The ELM energy loss increases with decreasing the collisionality and the ELM frequency increases linearly with the input power, as in experiments of type-I ELMs. The transport model with the pedestal neoclassical transport connected to the SOL parallel transport reproduces the inter-ELM transport as observed in experiments. Dedicated ripple experiments have been performed in JET and JT-60U using matched plasma shape. It is observed that larger toroidal rotation in co-direction is favorable to achieve higher pedestal pressure, while the effect of different TF ripple between 1.2% (w/o FST) and 0.5% (with FST) is smaller than the effect of toroidal rotation. Co-NBI QH-mode is partially obtained with co-rotation at the edge, which indicates that ctr-NBI and ctr-rotation are not essential for producing QH-mode. The effects of edge collisionality on grassy ELM characteristics have been investigated. The grassy ELM amplitude increases with increasing the edge collisionality toward unity, which is opposite to type-I ELM regime. As a development of the active ELM control, effects of EC injection to the pedestal have been investigated. The ELM frequency is increased only when EC is injected to the high field side. Fully 3-dimensional neutral transport simulation shows that the density in the region from the pedestal to the SOL has a strong influence of neutral penetration into the core plasma region from the last closed flux surface as well as a significant effect on the ionization zone in this region.

2.4 MHD Instability and High-Energy Ions

In high- β_N plasmas above the ideal β -limit without a conducting wall $\beta_N^{\text{no-wall}}$, two instabilities are newly observed; one is fishbone-like bursts observed in the frequency range

of several kHz, and the other is slowly growing mode with the time scale of several tens milliseconds. These instabilities seem to affect the RWM stability, that is, finally trigger the RWM onset. The former is found to be driven by the trapped energetic particles originating from perpendicular NBs. Since the mode is observed only in wall-stabilized high- β_N plasmas ($\beta_N > \beta_N^{\text{no-wall}}$), we have named it as the energetic particle driven wall mode (EWM). The latter mode strongly affects the plasma rotation profile around $q=2$. In particular, the rotational shear is reduced by this mode, and finally the RWM is appeared. The mode has been named as the RWM precursor; it is sometimes triggered by ELM or EWM.

Regarding ECCD stabilization of $m/n=2/1$ NTM, the minimum EC-driven current has been identified by EC wave power scan. The required ECCD is as follows: $0.20 < j_{EC}/j_{BS} < 0.40$ for the high-field case (3.7 T), and $0.35 < j_{EC}/j_{BS} < 0.46$ for the low-field case (1.7 T). Here, j_{EC} and j_{BS} the EC-driven and bootstrap current densities at the mode rational surface, respectively. In this campaign, modulated ECCD up to ~ 7 kHz became possible. In addition, a new system to synchronize the modulated EC wave with NTM rotation in real time by referring magnetic perturbation signals was developed. By application of the EC wave system against $m/n=2/1$ NTM, it is found that the stabilization effect weakens as the phase of the modulation deviates from that corresponding to O-point ECCD. In contrast, in the case of X-point ECCD, NTM amplitude increased, showing a destabilization effect. Moreover, the modulated ECCD actually has a stronger effect on NTM stabilization than unmodulated ECCD. In order to validate the modified Rutherford equation (MRE) and evaluate the MRE coefficients such as bootstrap and the Glasser-Greene-Johnson effects, a comparison between ASDEX-U and JT-60U for an $m/n=3/2$ NTM was performed.

A new system for neutron profile measurement has been developed. The system is based on the stilbene crystal detector and the fast Flash-ADC with 200 MHz sampling rates, and that has 7 chords so as to cover the whole plasma region. The fast sampling makes it possible to discriminate the neutron and γ signals. Moreover, after this process, the DD- and DT-neutron are discriminated by the pulse height. The measurement has been applied to the NTM experiment with intense NBs injection. On this experiment, the time evolution of DT-neutron is obtained as well as that of the DD-neutron. The experimental results suggest the accumulation and transport of triton.

Ion cyclotron emissions (ICEs) due to DD fusion-product (FP), ^3He , T and P-ions, are measured by using ion cyclotron antennas as pickup loops. It is found that ICE due to T, ICE(T), with lower frequency has larger wave numbers than ICE due to ^3He , ICE(^3He). Moreover, the density dependence for the excitation of the fundamental and the second harmonic ICEs(^3He) is obtained. The fundamental ICE(^3He) appears only in relatively low density region. Also, ICE due to P-ions is identified in relatively high density plasmas. This experimental results suggest that ICE(T) is no longer on the same branch of the fast Alfvén

wave and rather the branch of slow Alfvén wave.

The plasma current decay time during the initial phase of radiation induced disruption has been studied based on the plasma inductance and resistance estimated by experimental data. The area-normalized current decay time derived from the L/R model is not dependent on the electron temperature, and experimental decay time is one order of magnitude smaller than the model-based current decay time in short experimental decay time region (15~30 ms). On the other hand, current decay time derived by a new model, in which the time evolution of the plasma inductance is taken into account, is consistent with the experimental decay time.

2.5 Plasma Control and Heating/Current Drive Physics

Real-time control of the ion temperature gradient at high beta plasmas and of the toroidal rotation (V_t) in ELMy H-mode plasmas was demonstrated using the upgraded charge exchange recombination spectroscopy (CXRS) diagnostic and the real-time control system. The T_i and V_t at 4 radial locations are calculated within 10 ms with low error level (~5%). An integral term was newly introduced in addition to the proportional and differential terms, and the proportional gain was improved to be a function of T_i and the line-integrated electron density. Real-time control of the product of line-integrated electron density and ion temperature gradient, which is regarded as a measure of pressure gradient, was performed in high f_{BS} reversed magnetic shear plasmas to avoid collapse and MHD instabilities. Simultaneous real-time control of current and T_i profiles was demonstrated in high- β_p ELMy H-mode plasmas; the minimum of the safety factor profile representing current profile evaluated by motional Stark effect (MSE) diagnostics and T_i gradient were controlled independently using the off-axis LHCD and on-axis NBs. Burn controllability was investigated using external heating and fuelling with a burning plasma simulation (BPS) scheme. The BPS scheme was developed using 2 groups of NBs, where one simulates alpha particle heating (P^α) and the other simulates external heating. The heating power for the simulation of P^α was calculated with consideration for temperature dependence of the DT fusion reaction rate. In the BPS scheme, good controllability was demonstrated based on the FB control using external heating or gas-puffing. Responses of burning plasmas to fuelling were also investigated using supersonic molecular beam injection (SMBI). It was demonstrated to reduce the simulated fusion gain for keeping the control margin with SMBI due to confinement degradation and flattening of pressure profile. Relation between measured NBCD location by MSE diagnostics and the calculated one by ACCOME code was investigated by systematic scans such as NBCD location, beam energy, heating power and plasma triangularity (δ). For the low δ of 0.25 and low power of ~7 MW case, an increase in current density around $r/a \sim 0.4$ was observed during the off-axis NBCD application. The NBCD location was consistent with that calculated by ACCOME code. The change in the

current density profile measured by MSE was compared to the calculated NB current density by ACCOME in various discharges. The peak location of the change in the total current profile was roughly consistent with the peak location of the calculated NB current density except for the case with the upper ion source of N-NB at high δ and high power case. ECH start-up experiments were demonstrated in which the plasma current reached 21 kA by the microwave pulses of the oblique O-mode polarization from four 110 GHz gyrotrons with the vertical field produced by VT and VR coils. Oblique X-mode injection was also examined with the same discharge condition. The maximum current was lower (13 kA) compared with the oblique O-mode case. Wall conditioning discharges were investigated by using the 110 GHz ECRF system for the development of first wall conditioning scheme in ITER and DEMO. It was found that the horizontal field is crucially important to expand He plasma toward the high-field side from the fundamental ECH resonant surface. The efficiency of H₂ outgas in a minute was as large as 79% of that in He Taylor discharge cleaning. The ECH wall conditioning discharge was applied after the plasma disruption. The following experimental plasma was successfully started up. On the other hand, the plasma without the ECH wall conditioning discharge was not started up. This means that the ECH wall conditioning discharges is effective in the wall recovery.

2.6 Divertor and SOL Plasmas

Line radiation of carbon ions, C³⁺, plays an important role on radiation processes in the high density divertor of JT-60U. Understanding of ionization and recombination processes for the carbon ions has progressed by two-dimensional measurement of the divertor plasma with a visible spectrometer system. During an X-point MARFE, radiation peaks of C³⁺ and C²⁺ ions were identified precisely in the vicinity of the divertor X-point. Analysis of the series of the line intensities applied with a collisional-radiative model showed that the dominant radiator, C³⁺, is produced by ionization of C²⁺ and recombination of C⁴⁺ at similar rates around the radiative zone, and that C²⁺ is the second biggest radiator. The line-radiation power from the ionizing plasma component of C³⁺ and C²⁺ ions corresponds to respectively 60% and 30% of the total radiation power, while the line-radiation power from the recombining plasma component was a few percent.

The intermittent plasma transport, so-called “plasma blobs”, in SOL is recognized as an important mechanism to enhance radial transport of the heat and particle fluxes. Intermittency in the turbulent plasma was determined by statistical analysis as deformation of the probability density function (PDF) from a Gaussian distribution, and it was observed mostly at the Low-Field-Side midplane in the JT-60U L-mode plasma. Determination of a time scale of the intermittent events, i.e. fast rump-up and slow decay, was improved by the VITA (variable-interval time-averaging) method applied to the conditional average (CA). It was

found that, in the outer divertor, large burst events frequently appear near the X-point when detachment of the divertor plasma occurs at the divertor target: peaks in the ion saturation current were 2-5 times larger than the averaged value and the long time scale of 40-80 μs .

The SOL plasma transport along the field lines was investigated in a special plasma configuration with a small separation between the inner-upper wall and the separatrix. The influence of the plasma configuration on the plasma pressure and the SOL flow appeared only at the High-Field-Side: reduction in the plasma pressure was seen on the in-out separated field lines at the HFS SOL, suggesting the parallel convection from the LFS is dominant on the in-out connected field lines at the HFS.

An integrated divertor and SOL simulation code "SONIC" (SOLDOR, NEUT2D and IMPMC codes) has been developed and examined to simulate the SOL and divertor plasmas in the JT-60U with NB heating power of 14 MW and a very strong gas puff of 150 Pam^3/s . Dynamic evolution of the very high density and radiation zone as observed by an X-point MARFE in the experiments was reproduced with the SONIC code. The IMPMC code including a full dissociation modelling for hydrocarbons showed that the private dome with a small sticking coefficient enhances carbon influx to the main plasma.

2.7 Plasma-Wall Interactions

Deuterium retention in the first wall tiles was evaluated. At the topmost surface (depth of $< 0.1 \mu\text{m}$), H was dominant because of isotope exchange of D with H by degassing H-discharges. With increasing depth up to $1 \mu\text{m}$, a D/H ratio increased up to a level higher than that of the outer divertor plates. This is probably due to high-energy deuteron injection into that depth range by the ripple loss. Then, in the depth range deeper than $1 \mu\text{m}$, H was dominant.

The dependence of deuterium inventory on the baking temperature was investigated by a particle balance analysis. In discharges with the outer divertor attached, the deuterium inventory decreased pulse-by-pulse at a baking temperature of 570 K and decreased more gradually at 420 K compared to that at 570 K. In contrast, the deuterium inventory did not change at 350 K. In discharges with the outer divertor detached, the deuterium inventory increased at all the three baking temperatures. Because the CD_4 generation flux increased significantly in the detached divertor, co-deposition of D with C is considered to contribute to the D retention. In discharges with the outer divertor detached at 420 K, $^{13}\text{CH}_4$ was injected from the outer divertor in order to evaluate the number of D in the co-deposition layer with ^{13}C by post mortem analyses. The evaluated D retention will be compared with that evaluated by the particle balance analysis. For further understanding of the co-deposition mechanisms on the inner divertor plate, one CFC tile which gap width continuously changed in both poloidal and toroidal directions was installed.

The deposition profile of Fe originating from the ferritic steel was investigated. The thickness of the deposition layer on the material probe at the P-15 equatorial port was 12 nm and is similar to that before the ferritic tile installation. But after the installation, 45 at.% (atomic percent) of Fe was detected. Although the ferritic tile includes 2 at.% of W, no W was detected on the deposition layer. This means the atomic concentration of the ferritic steel was not kept in the deposition layer. This is due probably to long-term transport process.

The deposition profile of W originating from the W-coated tile at the outer divertor was investigated. The neutron activation method was applied in FNS (Fusion Neutrinos Source) for the first time to evaluate absolute W amount. The highest W concentration of about 1% was found in the co-deposition layer of C on the inner divertor plate. The W deposition on the outer dome wing and the dome top tile was relatively high, and very low W deposition was found on the inner dome wing. The toroidal distribution on the outer dome wing was also investigated; the W deposition was peaked at the P-8 section, where the W-coated tiles were positioned, and the W deposition was very low at the P-5 section (60 degree from the P-8 section in the toroidal direction opposed to the plasma current). In addition, for the purpose of investigation of the prompt redeposition of W, one CFC tile with W stripe coatings was installed as a lower target of the outer divertor.

An impurity Monte-Carlo transport code, which considers gyro-motion, has been developed, in particular, for W transport analysis. Although the peak location of the W deposition profile on the inner divertor plates could not be reproduced, the calculated poloidal distribution of the W deposition was in qualitative agreement with the measured profile.

2.8 Diagnostics

New diagnostic systems, such as modulation charge exchange recombination spectroscopy, beam emission spectroscopy, two-dimensional visible spectroscopic measurement system for divertor plasmas have provided reliable data with high-temporal and high-spatial resolutions.

In addition, substantial development of components for advanced diagnostic systems, such as the fine tuning technique of Zeeman polarimeter, Thomson scattering diagnostics using Fourier transform spectroscopy, a 160 ps YAG laser pulse generation by a stimulated Brillouin scattering-phase conjugation mirror, has been made.

A new lithium beam probe has been developed, whose ion beam is characterized by a low-divergence with a high brightness, enabling the Zeeman polarimetry to measure the edge current density. A new fast-ion diagnostic method using charge exchange recombination spectroscopy has been developed to evaluate fast-ion confinements. In this method, the Doppler shifted deuterium Balmer-alpha lights (D_{α}) are evaluated as signals of fast-ions that are created as a result of charge exchange recombination processes between fast-ions and

injected NBs. The motional Stark effect diagnostic system has been modified to measure spatial correlation between the magnetic fluctuations. A new reflectometer system using synchronized synthesizers, which can sweep the frequency of the incident wave rapidly, has been developed to complement the existing three channels of the O-mode reflectometer with fixed frequencies. Density fluctuation and E_r profile have been measured by Doppler reflectometer technique, and radial correlation has been measured by correlation reflectometer technique. YAG Thomson scattering system has been applied for the detection of dust scattering light, and event number and its distribution in plasmas were investigated after the disruption. An upgraded version of the infrared imaging video bolometer has been installed. This upgrade utilizes a state-of-the-art infrared camera (256 x 360 pixels, 3 ms time resolution) mounted in a neutron/gamma/magnetic shield behind a 3.6 m-long infrared periscope consisting of CaF₂ optics and an aluminum mirror.

2.9 Heating Systems

Development of the ECRF and NB systems toward high-power, long-pulse injection was continuously performed in this experimental campaign. In the ECRF system, 2.9 MW, 5 s injection to plasma using 4 gyrotrons and 0.4 MW, 30 s injection to plasma using 1 gyrotron were demonstrated. Injection to a dummy load with 1.5 MW for 1 s using one gyrotron was also successful. In addition, power modulation up to 7 kHz in synchronization with NTM rotation was performed by modifying the high-voltage circuits for the gyrotrons. In the P-NB system, power supply of 3 perpendicular units was modified to enable 30 s injection, which contributed to central heating for longer time in the long-pulse high-beta experiments. In the N-NB system, modification of the field shaping plate in the negative ion source enabled the reduction of the heat load on the acceleration grid by D^- ions and thus allowed high-power long-pulse injection. As a result, 340 keV, 3 MW injection to plasma for 30 s, which corresponds to the highest injection energy of 80 MJ, was achieved.

3 Extension of Operation Regime

3.1 Sustainment of High-beta Plasma above Ideal No-wall Beta Limit [1]

G. Matsunaga, Y. Sakamoto, N. Aiba, K. Shinohara, M. Takechi, T. Suzuki, A. Isayama, N. Oyama, N. Asakura, Y. Kamada, T. Ozeki and the JT-60 team

For a future fusion reactor with an economical attractiveness, the establishment of the high- β_N operation above the ideal no-wall β_N -limit ($\beta_N^{\text{no-wall}}$) is desirable. However, in such a high- β_N region, the β_N -value is limited by the resistive wall mode (RWM) that grows with the skin time of the resistive wall. Therefore, the RWM stabilization is one of the key issues for future fusion reactors. In previous experimental campaign, it has been found that the required plasma rotation for the RWM stabilization is less than about 1% of Alfvén velocity at a rational surface [2] and the dependence of the required rotation on β_N is weak [3].

In this campaign, we have carried out the demonstration of the high- β_N sustainment with suppressing the RWM by the plasma rotation. However, almost all discharges on the high- β_N region were limited by the RWMs triggered by two newly observed MHD instabilities despite enough plasma rotation for RWM stabilization. One is fishbone-like burst that repeats growth and decay within a few milliseconds. The other is a slowly growing mode with growth time 50 ms with affecting plasma rotation profile around $q=2$. These are named as energetic particle driven wall mode (EWM) and the RWM precursor, respectively. Particularly, we have found the EWM was destabilized by the trapped energetic particles by perpendicular NBs. In order to avoid the EWM as well as the RWM, the perpendicular NBs were replaced to negative-ion based NBs, that are tangentially injected beams, with keeping both β_N and plasma rotation. As a consequence, the high- $\beta_N \approx 3$ above $\beta_N^{\text{no-wall}}$ has been successfully sustained for about 5 s, which corresponds to 3 times the current diffusion time of ~ 1.5 s in this plasma. In this discharge, since $\beta_N^{\text{no-wall}}$ increased with l_i , which is due to plasma current penetration, the time duration of high- β_N above $\beta_N^{\text{no-wall}}$ is limited. According to the ACCOME calculation, large bootstrap current fraction f_{BS} of 50% is also achieved by a weak shear profiles. For a steady-state scenario with high- β_N above $\beta_N^{\text{no-wall}}$, the control of MHD instability should be established.

References

- [1]G. Matsunaga et al., Proc. in 22nd Fusion Energy Conference, EX/5-2 (2008).
- [2]G. Matsunaga et al., Proc. in 33rd EPS Conference on Plasma Physics, Rome, Italy, (2006), 30I, O2.003 (CD-ROM).
- [3]M. Takechi et al., Phys. Rev. Lett. **98**, 055002 (2007)

3.2 Development of Reversed Shear Plasmas with High Bootstrap Current Fraction towards Reactor Relevant Regime in JT-60U [1]

Y. Sakamoto, G. Matsunaga, N. Oyama, T. Suzuki, N. Aiba, H. Takenaga,
A. Isayama, M. Takechi

High fraction of bootstrap current, driven in off-axis region due to the neoclassical effects in high beta plasmas, to plasma current is required for steady-state tokamak operation in order to reduce a circulating power for non-inductive current drivers. Therefore, the bootstrap current fraction $f_{BS} \sim 0.5$ is expected in the ITER steady-state operation scenario, further $f_{BS} > 0.75$ in DEMO reactors. One of the candidates for the operation scenario is the reversed shear plasma that is naturally formed with a high f_{BS} . The DEMO reactors require not only high f_{BS} but also high integrated performance in which high values of HH_{98y2} , β_N , f_{BS} , f_{CD} , fuel purity, f_{rad} and n_e/n_{GW} should be sustained long time. Furthermore, the other reactor relevant conditions are also important in which the operation region of $q_{95} \sim 5-6$, electron temperature nearly equal to ion temperature and low momentum input due to the dominant alpha heating. Although high f_{BS} plasmas were reported from many tokamaks, the operational region is practically limited at high $q_{95} > 8$ region in which f_{BS} is enhanced within the attainable beta limit because of $f_{BS} \propto \beta_p \propto \beta_N q_{95}$.

In 2008 JT-60U experimental campaign, the reversed shear plasmas with high f_{BS} was emphasized in the lower q_{95} regime by utilizing the large volume configuration close to the conductive wall ($d/a \sim 1.3$) for wall stabilization. As a result, high confinement reversed shear plasmas exceeding the no-wall beta limit with high f_{BS} are obtained in the reactor relevant regime in JT-60U, where $\beta_N \sim 2.7$, $\beta_p \sim 2.3$ is achieved in reversed shear plasma at $q_{95} \sim 5.3$. The achieved β_N is much higher than previous experiments of large f_{BS} plasmas with $\beta_N \sim 1.7 - 2.1$ at $d/a \sim 1.5$. However, the discharges were terminated in disruption, where slowly growing RWM ($n = 1$) was observed. The RWM became unstable when toroidal rotation velocities at $q = 3$ surface decreased to the critical toroidal rotation velocity for RWM stabilization [2]. By comparison of balance- and co-injected discharges, the toroidal rotation velocity at outer $q = 3$ surface might play an important role for RWM stabilization. The detail analysis of MHD stability using the MARG2D code based on the experimental profile data indicates that the ideal wall beta limit is $\beta_N \sim 2.9$ and the no-wall beta limit is ~ 1.9 , resulting $C_\beta \sim 0.8$.

In addition to high β_N , high confinement is simultaneously achieved in the reactor relevant conditions. Then high integrated performance is close to or exceeds ITER steady-state scenario (VI), where $HH_{98y2} \sim 1.7$, $\beta_N \sim 2.7$, $f_{BS} \sim 0.92$, $f_{CD} \sim 0.94$ and $n_e/n_{GW} \sim 0.87$ are simultaneously achieved under the conditions of $T_e \sim T_i$, low momentum input and the similar q profile except $q(0)$. It should be mentioned however that JT-60SA would address the remaining issues towards DEMO reactor, especially long sustainment with higher β_N , as a satellite tokamak of ITER.

Reference

- [1] Sakamoto, Y., et al., Proc. IAEA FEC 2008 EX1/1, submitted to Nucl. Fusion.
[2] Takechi, M., et al., Phys. Rev. Lett. **98**, 055002 (2007).

3.3 Long-Pulse Hybrid Scenario Development in JT-60U [1, 2]

N. Oyama, A. Isayama, G. Matsunaga, T. Suzuki, H. Takenaga, Y. Sakamoto, T. Nakano,
Y. Kamada, S. Ide and the JT-60 Team

The ‘hybrid scenario’ is a kind of advanced tokamak (AT) plasma operation scenario proposed for ITER to extend the pulse duration of burning plasma so as to increase neutron fluence. In the previous hybrid scenario development in JT-60U, the sustained duration is limited by the degradation of ITB due to the change in the power deposition profile under the condition that several perpendicular NBIs (perp-NBIs) for central heating are replaced with other perp-NBIs for off-axis heating due to the limited pulse duration of NBIs [3]. After the modification of power supply systems for three perp-NBIs provides a long period of central NB heating up to 30 s, the performance and sustained duration of long-pulse discharges have been improved.

In long-pulse hybrid discharges, the peaked density profile in the core plasma can be maintained even when the density at the pedestal increases in the latter phase of the discharge due to the increase in the divertor recycling. Thus, the peaked pressure profile attributed to ITB can be kept constant through the discharge with the peaked power deposition profile. The peaked density profile is not attributed to the central fueling, but is suggested by the lower diffusion at ITB region as observed in other ITB experiments [4]. In these long-pulse discharges, MHD activity with toroidal mode number $n = 1$ is observed in whole plasma region even when neoclassical tearing modes (NTMs) are avoided. When the amplitude of the mode at peripheral region becomes large, the pedestal pressure is degraded. The mode amplitude is sensitive to the toroidal magnetic field (or edge safety factor) and the heating power from perp-NBIs. After the adjustment of toroidal magnetic field so as to reduce the mode amplitude, high normalized beta (β_N) of 2.6 and high thermal confinement enhancement factor ($H_{H98(y,2)} > 1$) are sustained for 25 s ($\sim 14 \tau_R$, where τ_R is the current diffusion time) under the ITER relevant small toroidal rotation condition (~ 1.3 kHz in the plasma center). The peaked pressure profile with flat q profile in the central region ($r/a < 0.5$) at low safety factor plasma (safety factor at 95% flux surface $q_{95} \sim 3.2$) is effective to avoid the onset of NTMs up to $\beta_N \sim 3$ in these plasmas. High $\beta_N H_{H98(y,2)}$ of 2.6 gives high G-factor ($\beta_N H_{H98(y,2)} / q_{95}^2$) of 0.25 and peaked pressure profile gives large bootstrap current fraction ($f_{BS} > 0.43$). Therefore, these long-pulse hybrid discharges are suitable for ‘ITER hybrid scenario’

References

- [1] Oyama, N., *et al.*, Nucl. Fusion **49**, 065026 (2009).
- [2] Suzuki, T., *et al.*, Nucl. Fusion **49**, 085003 (2009).
- [3] Oyama, N., *et al.*, Nucl. Fusion **47**, 689 (2007).
- [4] Takenaga, H., *et al.*, Nucl. Fusion **43**, 1235 (2003).

3.4 Impurity Seeding Experiments in the Long Pulse Discharges [1]

N. Asakura, T. Nakano, N. Oyama, T. Sakamoto, G. Matsunaga, K. Itami

Reduction of heat flux appropriate for heat exhaust of the divertor is crucial for a fusion reactor. Power handling by large radiation power loss with impurity gas seeding such as Ar, Ne and their combination has been studied in the ELMy H-mode plasmas, where $I_p = 1\text{-}1.2$ MA, $B_t = 2.0\text{-}2.6$ T, $P_{NB} = 12\text{-}16$ MW and NBI period of 30 s. Long sustainment of the ELMy H-mode plasmas with high total radiation fraction ($f_{rad}^{tot} = P_{rad}^{tot}/P_{abs} > 0.7$) and high density fraction ($f_n^{GW} = \bar{n}_e/n^{GW} > 0.7$, n^{GW} is the Greenwald density) has been progressed, in particular, through the use of Ar seeding (Case-1) and a combination of Ar and Ne seeding (Case-2).

For the Case-1, the radiation power increased particularly in the main plasma (P_{rad}^{main}), which became comparable to that at the divertor (P_{rad}^{div}). The large radiative loss in the main plasma edge ($P_{rad}^{main} > 3.5$ MW) changed ELM characteristics from Type-I to Type-III, and reduction in ELM energy loss fraction (W_{ELM}/W_{dia}) to 0.15%, which level is acceptable for ITER operation. Both transient and steady-state heat loadings were reduced. Active feedback of the Ar puff rate was applied to maintain a constant level of P_{rad}^{main} , using integrating bolometer signals viewing the main plasma edge. In the Type-III ELMy H-mode, relatively good energy confinement ($H_{H98y2} = 0.87\text{-}0.75$) with high f_{rad}^{tot} ($= 0.77\text{-}1$) and high f_n^{GW} ($= 0.67\text{-}0.85$) was sustained continuously for 13 s until a short stop of two NB injectors. Since ion flux (j_s^{div}) near the outer strike-point decreased with reduction in electron temperature (T_e^{div}) to ~ 5 eV, plasma detachment was also sustained. On the other hand, H-factor ($H_{H98y2} < 0.87$) was lower than that during the Type-I ELM period ($H_{H98y2} = 0.9\text{-}1$ for $f_n^{GW} = 0.6\text{-}0.55$).

For the Case-2, Type-I ELMy H-mode plasma with an ITB was used in order to sustain better energy confinement, where Ar seeding rate was reduced to decrease P_{rad}^{main} ($= 2.5\text{-}3$ MW). The radiation power in the divertor and its fraction were increasing intensively during Ne seeding ($P_{rad}^{div}/P_{abs} = 0.5\text{-}0.7$). Better energy confinement ($H_{H98y2} = 0.95\text{-}0.85$) with high f_{rad} ($= 0.78\text{-}1$) and high f_n^{GW} ($= 0.73\text{-}0.85$) was sustained continuously for 12 s. Investigation of the divertor showed that particle recycling flux in the divertor and global outgassing flux were increasing with rise of the target temperature, and that the increase in P_{rad}^{div} was produced not only by seeding Ne but also by carbon influx from the divertor. In the outer divertor, j_s^{div} near the outer strike-point also increased while the local T_e^{div} was 5-10 eV. Thus, the outer divertor plasma was still attached during the Type-I ELMs. A rate of the rise of the target temperature near the outer strike point ($\Delta T_{target-out} = 13$ °C/s) was 3 times larger than that for Case-1 due to large transient (ELM) and steady-state heat loadings. As a result, radiation regions (main edge and divertor) can be controlled by combination of the different radiators, but enhancement of P_{rad}^{div} will be necessary to form the divertor detachment.

Reference

[1] Asakura, N., et al., 22nd IAEA FEC, Geneva (2008) EX4-4Ra, submitted to Nucl. Fusion.

3.5 Development of Full-CD Plasma Having Steady Current Profile and High Bootstrap Current Fraction [1]

T. Suzuki, N. Oyama, A. Isayama, Y. Sakamoto, T. Fujita, S. Ide, Y. Kamada, O. Naito,
M. Sueoka, S. Moriyama, M. Hanada, and the JT-60 Team

For steady-state operation of tokamak fusion reactors, a discharge fully sustained by non-inductive current drive and having steady current profile and high bootstrap (BS) current fraction ($f_{BS} \geq 0.5$) is required at reasonably low q_{95} regime ($q_{95} < 6$). However, such plasmas have not been realized yet, in spite of worldwide intensive efforts, since the above requirements impose strong constraints on plasma pressure and current profiles. The plasma should have strong pressure gradient enough for $f_{BS} \geq 0.5$, but be free from MHD activity under the steady state current profile with the large BS current and zero inductive current. In order to resolve these issues, we have developed the steady-state operation scenario, making full use of off-axis lower hybrid (LH) current drive (CD) to produce and sustain broad current profile. A weak magnetic shear having the minimum of safety factor $q_{min} > 2$ is formed in the plasma, avoiding low q ($q \leq 2$) MHD.

Fully non-inductive discharge having a relaxed current profile and high bootstrap current fraction $f_{BS} = 0.5$ has been established in the high- β_p ELMy H-mode discharge with weak magnetic-shear having $q_{95} = 5.8$, $q_{min} = 2.1$, and $q(0) = 2.4$, where $q(0)$ is the safety factor at the plasma center. The rest of the plasma current is externally driven by neutral beams (NBs) and LH waves. The safety factor profile evaluated by the motional Stark effect (MSE) diagnostics is kept constant for 0.7 s at the end of the full-CD sustainment for 2 s (1.5 times the current relaxation time). The loop voltage profile is spatially uniform at 0 V at the end of the sustainment. The steady sustainment of full-CD plasma, which is stably controlled by appropriate external current drivers, is demonstrated at high $f_{BS} = 0.5$ and reasonably low $q_{95} = 5.8$ regime for the first time. On the other hand, when the combination of bootstrap current and externally driven current does not match to the steady current profile, slight change in the current profile due to current relaxation resulted in the onset of neo-classical tearing mode (NTM), when low- q rational surface exists. Achieved normalized beta ($\beta_N = 1.6$) was limited by the NB heating power to avoid the increase in the pedestal density due to increase in NB fueling and recycling, because LH waves cannot reach the core region in plasmas with higher pedestal density ($1.4\text{-}1.5 \times 10^{19} \text{ m}^{-3}$) as known by the accessibility condition.

References

[1] Suzuki, T., et al., Nucl. Fusion **49**, 085003 (2009).

4 Transport in Core Plasmas

4.1 Characteristics of Momentum Transport in H-mode Plasmas [1]

M. Yoshida, Y. Kamada, H. Takenaga, Y. Sakamoto, N. Oyama, H. Urano, the JT-60 Team

It is widely recognized that the toroidal rotation velocity (V_t) profiles play one of the most critical roles for plasma transport and MHD stability. The momentum transport is one of the crucial parameter for determination of the rotation profile. Therefore, it is the critical importance to understand the properties of the momentum transport coefficients for the prediction of the rotation in next step devices. In the reference [2], parameter dependences of the toroidal momentum diffusivity (χ_ϕ) and the convection velocity (V_{conv}) in L-mode plasmas were reported using the transient experimental method. However, the dependences of these coefficients were not obtained in H-mode plasmas.

In this campaign, after separating the diffusive and convective terms, the correlations between χ_ϕ , V_{conv} and χ_i in H-mode plasmas are discussed. The relations between χ_ϕ and χ_i in H-mode plasmas are elucidated at constant I_p of 1.2 MA. NB heating power and electron density scans are carried out under otherwise similar conditions ($B_T=2.5\text{-}2.6\text{T}$, $\kappa_x=1.34\text{-}1.38$, $\delta_x=0.32\text{-}0.35$). We consider that the diffusivities χ_ϕ and χ_i at $r/a=0.5$ represent the quality of each global confinement and are used for the understanding of the relation (χ_ϕ and χ_i). Because a good correlation between χ_ϕ and χ_i was observed over a wide range of radii, and χ_i at $r/a=0.5$ has a good correlation with the thermal confinement time ($1/\chi_i \propto \tau_E$). The absorbed power varied over the range $5.6\text{ MW} < P_{\text{ABS}} < 9.1\text{ MW}$, and the electron density varied over the range $\bar{n}_e = 2.0\text{-}3.0 \times 10^{19}\text{ m}^{-3}$ by varying gas puff rate. The χ_ϕ increases with increasing χ_i , and the ratio of χ_ϕ/χ_i varies in the range of $\chi_\phi/\chi_i \sim 0.7\text{-}3$ at $r/a=0.5$. The ratio of χ_ϕ/χ_i at middle of plasma $r/a=0.5$ increases with increasing T_i or T_i gradient. This is because that the growth of χ_ϕ is larger than that of χ_i as a function T_i or T_i gradient. The correlation between V_{conv} and χ_ϕ is also found using the same data set. The inward convection velocity ($-V_{\text{conv}}$) increases with increasing χ_ϕ over a wide range of radii for lower density ($\bar{n}_e = 1.9\text{-}2.2 \times 10^{19}\text{ m}^{-3}$). In the case with higher density ($\bar{n}_e = 2.7\text{-}3.0 \times 10^{19}\text{ m}^{-3}$), reflecting that $-V_{\text{conv}}$ decreases with plasma radius in spite of χ_ϕ increases, the decrease of $-V_{\text{conv}}$ with increasing χ_ϕ is observed. The $-V_{\text{conv}}$ increases with increasing χ_ϕ at the fixed radius $r/a=0.5$, and the value of $-V_{\text{conv}}/\chi_\phi$ is around 0.5 - 2 (1/m) in this data set.

References

- [1] Yoshida M., *et al.*, submitted to Nuclear Fusion.
- [2] Yoshida M., *et al.*, Nucl. Fusion **47** 856 (2007).

4.2 Role of ECRF on Toroidal Rotation [1]

M. Yoshida, Y. Sakamoto, H. Takenaga, S. Ide, N. Oyama,
T. Kobayashi, Y. Kamada, the JT-60 Team

There are some experimental results on the rotation response on electron cyclotron resonance frequency (ECRF) wave in several devices. For example, the ECRF H-mode plasmas in DIII-D exhibit CTR-rotation in the core region and CO-rotation in the outer region [2]. The toroidal rotation velocity (V_t) in TCV increases in the CO-direction by third-harmonic X-mode ECRF together with an increase in the ion temperature (T_i) [3]. Therefore, ECRF offers exciting prospects as a rotation control in future devices such as ITER. However, the rotation mechanism with ECRF is not well understood due to the complexity of the physics governing the V_t profile.

In this study, the role of ECRF on the toroidal rotation velocity profile has been investigated from the viewpoints of momentum transport and intrinsic rotations. The change in momentum transport with ECRF is evaluated an ELMy H-mode discharge ($I_p=1.0$ MA, $B_T=3.8$ T, BAL-NB of $P_{NB}=9.4$ MW, $P_{EC}=2.1$ MW with 1st harmonic O-mode, EC deposition $r/a\sim 0.3$). It is found that both the toroidal momentum diffusivity (χ_ϕ) and the inward convection velocity ($-V_{conv}$) increase with ECRF. However, the χ_ϕ and V_{conv} do not affect V_t profile in the region $0.3 < r/a < 0.65$ because of the low external torque input. The response of V_t profile on ECRF is investigated in positive shear L-mode plasmas without sawtooth oscillations ($I_p=1.0$ MA, $B_T=3.8$ T, $R=3.4$ m, $a=0.95$ m, $q_{95}=5.1$, $\delta=0.33$, $\kappa=1.4$ and $P_{NB}=4.9$ MW). Electron cyclotron wave of 2.1 MW is injected at $r/a\sim 0.6$. The electron density remains almost constant with ECRF. The T_e profile in the region of $r/a < 0.85$ increases with ECRF ($\Delta T_e/T_e\sim 40\%$); on the other hand, the T_i profile hardly varies. The measured V_t in the region $0.3 < r/a < 0.6$ changes in the CO-direction; on the other hand, the measured V_t in the region $0.6 < r/a < 0.8$ changes in the CTR-direction. Because the ion pressure gradient ($\text{grad}P_i$) does not vary with ECRF in this discharge, the change in the intrinsic rotation by the change in $\text{grad}P_i$ is negligible small [4]. These results indicate that ECRF drives the CO-intrinsic rotation inside the EC deposition radius and induces the CTR-intrinsic rotation outside the EC deposition radius.

References

- [1] Yoshida M., *et al.*, Physical Rev. Lett. **103**, 065003 (2009).
- [2] deGrassie J. S., *et al.*, Phys. Plasmas **11** (2004) 4323.
- [3] Porte L., *et al.*, Nucl. Fusion **47** (2007) 952.
- [4] Yoshida M., *et al.*, Phys. Rev. Lett. **100** (2008) 105002.

4.3 Characteristics of Internal Transport Barrier under Reactor Relevant Condition in JT-60U Weak Shear Plasmas [1]

H. Takenaga, N. Oyama, H. Urano, Y. Sakamoto, N. Asakura, K. Kamiya, Y. Miyo, T. Nishiyama, T. Sasajima, K. Masaki, A. Kaminaga, H. Ichige, J. Bucalossi¹⁾, V. Marty¹⁾, S. Ide, Y. Koide, Y. Kamada and the JT-60 Team

1) Association Euratom-CEA, CEA Cadarache

Advanced tokamak plasmas have been developed with internal transport barrier (ITB) for establishment of a steady-state operation scenario in fusion reactors such as ITER and DEMO. In order to understand applicability of these plasmas to fusion reactor plasmas, ITB characteristics were investigated under reactor relevant condition with edge fuelling and electron heating in JT-60U weak shear plasmas. A new edge fuelling tool of supersonic molecular beam injection (SMBI) was installed in collaboration with CEA-Cadarache [2] for investigation of edge fuelling effects with dedicated fuelling profile scan by combining pellet injection and gas-puffing. High confinement was sustained at high density with edge fuelling by shallow pellet injection from high-field-side or SMBI with relatively low frequency and low background pressure. On the other hand, confinement was degraded by high frequency SMBI and gas-puffing. The pellet penetration depth was estimated to be $\lambda/a=0.1-0.3$, which is wider than the pedestal width. Light from the SMBI measured using fast TV mainly emitted outside the separatrix. However, the edge ion temperature (T_i) quickly decreased at $r/a\sim 0.8$. The central T_i inside the ITB decreased due to cold pulse propagation even with edge fuelling by pellet injection and SMBI. By optimizing the injection frequency and the penetration depth, the decreased central T_i was recovered and good ITB was sustained with enhanced pedestal pressure. The T_i -ITB also degraded significantly with electron cyclotron heating (ECH), when stiffness feature was strong in the electron temperature (T_e) profile. The ion thermal diffusivity (χ_i) in the ITB region increased with the electron thermal diffusivity, indicating existence of clear relation between ion and electron thermal transport. On the other hand, T_i -ITB unchanged or even grew, when stiffness feature was weak in the T_e profile. Density fluctuation level at ITB seemed to be unchanged during ECH. However, correlation length became longer in the T_i -ITB degradation case and shorter in the T_i -ITB unchanging case. Although dependence of χ_i on correlation length might not be simple, these results indicate that ion thermal transport was modified by changing fluctuation property through electron heating using ECH.

References

- [1] Takenaga H., *et al.*, Nucl. Fusion, **49**, 075012 (2009).
 [2] Takenaga H., *et al.*, Section 4.4 in this JAEA-Review.

4.4 Fuelling Characteristics of Supersonic Molecular Beam Injection

H. Takenaga, Y. Miyo, J. Bucalossi¹⁾, V. Marty¹⁾, H. Urano, N. Asakura

1) Association Euratom-CEA, CEA Cadarache

1. Introduction

In order to investigate effects of fuelling on pedestal characteristics, supersonic molecular beam injection (SMBI) was installed in collaboration with CEA-Cadarache. In JT-60U weak shear plasmas, high confinement of $H_{89PL} \sim 2$ has been achieved at high density ($\bar{n}_e/n_{GW} \sim 0.7$) with enhanced pedestal pressure using high-field-side (HFS) pellet injections [1]. On the other hand, confinement and pedestal pressure decreased to the same level as those in standard ELMy H-mode plasmas with gas-puffing. The fuelling profile of the SMBI is expected to be shallower than that of HFS pellet injection and deeper than that of gas-puffing. Thus, the SMBI allows dedicated fuelling profile scan by combining pellet injection and gas-puffing. In this section, development of the SMBI system and its fuelling characteristics are discussed.

2. System Description of the SMBI

Figure 1 shows schematic drawing of the SMBI system, which is the same as that used in Tore Supra [2]. The SMBI is operated as frequent pulses with an injection frequency (f) of less than 10 Hz and a duration of ~ 2 ms/pulse. The compressor works for each pulse and a pressure wave produced by the compressor travels inside the tube towards the injection head. It accelerates an internal piston inside the injector head that strikes the valve. The valve is closed by a strong spring and the impact of the accelerated internal piston shortly opens the valve (1-2 ms). Then, some fraction of the gas is lost throughout the nozzle due to the valve aperture. The SMBI speed is expected to be 2.2 km/s at the wall temperature of 150°C and background pressure of $P_{BK} = 5$ bar.

The injector heads were installed both on HFS at $Z = 59.0$ cm and LFS at $Z = 10.8$ cm, which are selected by the valves (V1a and V2a are opened for HFS and V1b and V2b are

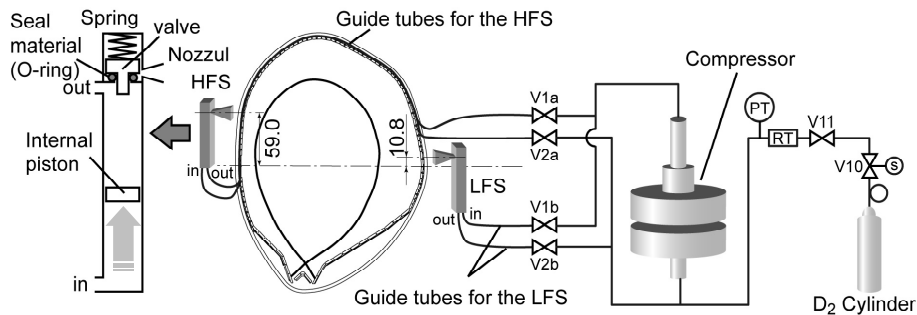


Fig. 1 Schematic drawing of the SMBI system.

opened for LFS). The inner diameter of the guide tubes is 6 mm and the length of the guide tube is about 10 m for the HFS and 5 m for the LHS, respectively.

3. Development of Vacuum Seal inside the Injector Head

In the experimental campaign 2005-2006, the vacuum seal material used inside the injector head was damaged owing to long baking (~ month) at high temperature of 300°C. Therefore, the SMBI operation was not available due to the leak of working gas at the valve inside the injector head. The SMBI system was only available for gas fuelling same as the standard gas-puffing by opening the valve located outside the vacuum vessel (V1a or V1b) in a short period. In order to investigate effect of HFS gas fuelling on the confinement degradation, the HFS gas fuelling was carried out using the SMBI system in the 2005-2006 experimental campaign [3]. Confinement degradation was also observed with the HFS gas fuelling as well as the LFS gas fuelling.

To be able to operate the SMBI during the 2007-2008 experimental campaign, it was decided to make further tests with the reference seal and to test new ones from different companies in order to find a suitable solution for JT-60U operating conditions. First, baking tests were performed for four seal materials, where temperature of the seal materials (T^m) gradually increased inside the vacuum chamber and the chamber pressure was measured. Figure 2 shows temperature dependence of the chamber pressure. For the reference material used in 2005-2006 campaign, the chamber pressure increased from $T^m = 260$ -270°C, indicating that gas release from the seal material started from this temperature range. This result is consistent with the fact that the seal material was damaged due to long baking at 300°C. The new materials have higher critical temperature for gas release as shown in Fig. 2. Especially for the material C, the chamber pressure increased from $T^m \geq 290$ °C.

Next, the SMBI operation tests were performed with the new materials after the high temperature baking at ~ 280-300°C for several weeks. When the feeding gas was not filled in the injector head during the baking, the seal materials were destroyed or damaged after several tens pulses even at operation temperature of 150°C, although the number of pulses was different for different materials and test conditions, i.e. baking temperature, background pressure and so on. On the other hand, when the feeding gas was filled in the injector head during the baking at 300°C (injector head temperature 290-295°C), the seal material C was not damaged and was intact even after more than hundred pulses. The feeding gas pressure in the injector head, which tends to reduce the stresses on the

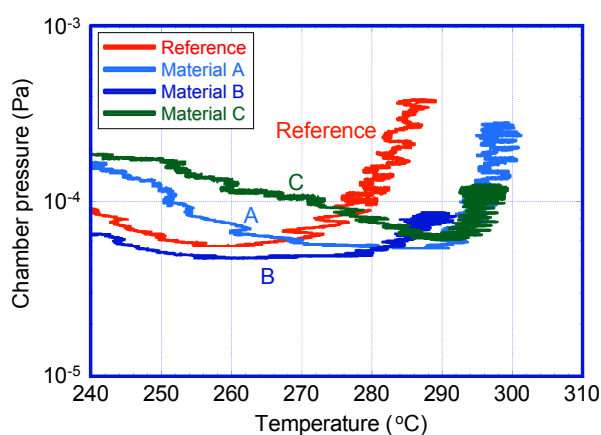


Fig. 2 Temperature dependence of chamber pressure in the baking tests.

seal during the baking, could play a role. Therefore, we decided (1) used of the material C, (2) reduction of the baking temperature to 280°C, (3) feeding gas at 5 bar in the injector head during the baking and (4) operation at only $\leq 150^\circ\text{C}$. After \sim one month baking at 280°C, the SMBI was successfully operated at 150°C.

4. Results on Injection into JT-60U Vacuum Vessel

Fuelling rate per pulse was measured from pressure increase in the JT-60U vacuum vessel after the SMBI pulses.

Figure 3 shows fuelling rate per pulse as a function of background pressure. Here, the volume of the JT-60U vacuum vessel was assumed to be $\sim 120 \text{ m}^3$. Fuelling rate was estimated to be $\sim 1.1 \text{ Pa}\cdot\text{m}^3/\text{pulse}$ at $P_{\text{BK}} = 5 \text{ bar}$ for the HFS injector head. For the LFS injector head, fuelling rate was estimated to be $\sim 0.9 \text{ Pa}\cdot\text{m}^3/\text{pulse}$ at $P_{\text{BK}} = 5 \text{ bar}$. This fuelling rate is comparable with the number of particles fuelled by a pellet injection in JT-60U. The fuelling rate almost linearly decreases with decreasing difference between background pressure and atmospheric pressure.

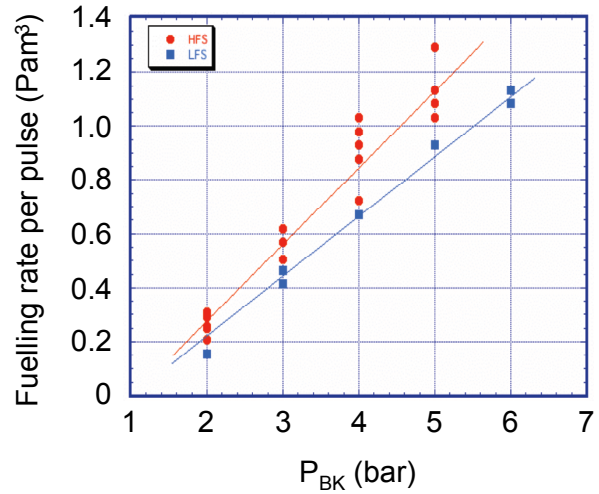


Fig. 3 Fuelling rate per pulse as a function of background pressure.

5. Results on Injection into JT-60U Plasmas

After long baking and operation at $\sim 280^\circ\text{C}$, the SMBI was successfully operated at 150°C. Figure 4 shows typical waveforms of the line averaged electron density, the NB heating power and the stored energy in a weak shear plasma. In this discharge, the SMBI was operated with the LFS injector head at $P_{\text{BK}} = 4 \text{ bar}$ and $f = 10 \text{ Hz}$. The frequent density jumps associated with the SMBI pulses were observed as shown in Fig. 4. The fuelling efficiency is estimated to be larger by a factor of 3-5 than that of gas-puffing.

Figure 5 shows pictures of fast TV camera (right hand side figures) viewing tangentially the plasma (see left hand side figure) with a time resolution of 1/6000 s. Light from the HFS SMBI mainly emitted outside the separatrix even with $P_{\text{BK}} = 6 \text{ bar}$, indicating that SMBI was almost ionized in the scrape-off layer. The SMBI speed estimated from the fast TV camera was lower than expected. Ionization front could move slowly towards plasma boundary. The profiles of the edge ion temperature (T_i) before and just after ($dt = 5 \text{ ms}$) the SMBI at $P_{\text{BK}} = 6$ and 2 bar are shown in Fig. 6 (a) and (b), respectively. Just after the SMBI, pedestal T_i significantly decreased at $P_{\text{BK}} = 6 \text{ bar}$ as shown in Fig. 6 (a), although light from the SMBI was almost emitted outside the separatrix. Similar behavior was observed for the LFS SMBI. Therefore, this behavior was not ascribed to the radial movement toward LFS of

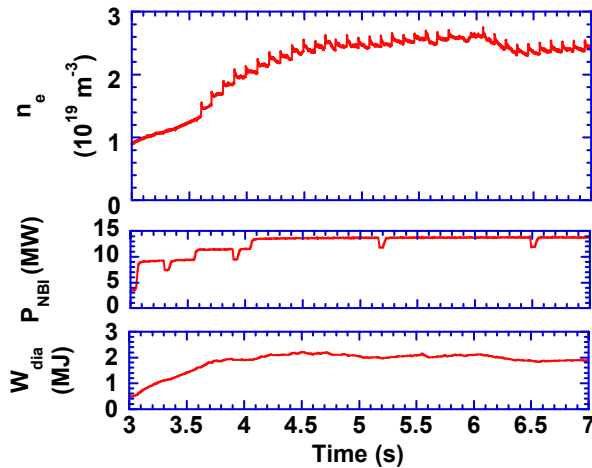


Fig. 4 Typical waveforms of electron density, NB heating power and plasma stored energy with SMBI.

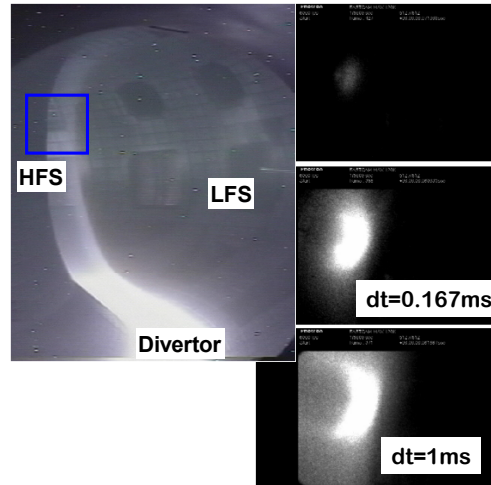


Fig. 5 (Right) Pictures of Fast TV camera. (Left) Box shows field of fast TV camera.

ablation material observed for the pellet injection. Similar response in T_i was observed at $P_{BK} = 4$ bar, however, response became smaller at $P_{BK} = 2$ bar. The emitted area was smaller and farther from the separatrix at $P_{BK} = 2$ bar than at $P_{BK} = 6$ bar. The T_i decrease also became smaller at $P_{BK} = 2$ bar than at $P_{BK} = 6$ bar as shown in Fig. 6 (b). In the T_e profile, clear response was not observed even at $P_{BK} = 6$ bar. Cold pulse induced in the edge region by the SMBI propagated toward the central region. The SMBI could directly affect the plasma parameters at $r/a \sim 0.8$ and also affect through cold pulse propagation inside more.

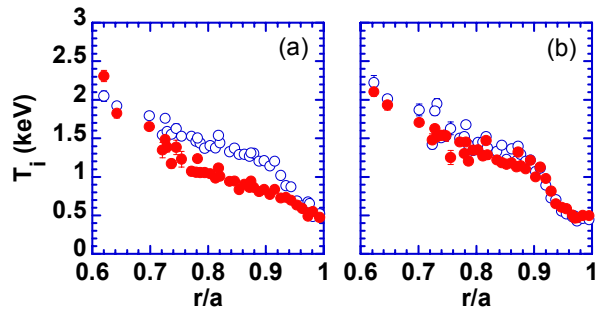


Fig. 6 Profiles of edge ion temperature before (open circles) and 5 ms after (closed circles) the SMBI in the case of (a) $P_{BK}=6$ bar and (b) $P_{BK}=2$ bar, respectively.

6. Summary

The new fuelling tool of the SMBI was successfully operated after development of vacuum seal inside the injector head. Light from the SMBI mainly emitted outside the separatrix even with $P_{BK} = 6$ bar. However, quick T_i decrease was observed at $r/a \sim 0.8$, indicating that the SMBI could directly affect the plasma parameters at $r/a \sim 0.8$ and also affect through cold pulse propagation inside more.

References

- [1] Takenaga, H. and the JT-60 Team, Phys. Plasmas **8** (2001) 2217.
- [2] Bucalossi, J., *et al.*, Proc. 19th IAEA Fusion Energy Conf. (Lyon, 2002) EX/P4-04.
- [3] Takenaga, H., *et al.*, JAEA-Review 2008-045 (2008).

4.5 Effects of Toroidal momentum input on Internal Transport Barrier Formation in JT-60U Reversed Shear Plasmas

Y. Sakamoto, K. Ida¹⁾, M. Yoshida, T. Suzuki

1) NIFS

1. Introduction

Burning plasmas in a fusion reactor are characterized by self-organizing or self-regulating system in which plasma parameters are linking each other and the dominant alpha heating is determined by temperature and density profiles. For that reason, initial temporal evolution of plasma profiles could affect to the steady state of burning plasma. In this study, effect of toroidal momentum input on internal transport barrier (ITB) formation and its evolution in reversed shear plasmas has been investigated. Detail profiles of ion temperature and toroidal rotation velocity are measured with modulation CXRS [1] which has radial measurement points of 270 every 50ms. This powerful diagnostic enables us to clarify the evolution of ITB structure in detail.

2. Comparison of ITB formation between CO and BAL injections

The experiments were performed in reversed shear plasma with plasma current of 1.0 MA and toroidal field of 3.7 T. Figure 1 shows the waveform of discharges with balanced- and co- injection. The low power of tangential NB (~ 4 MW) was injected just after the start

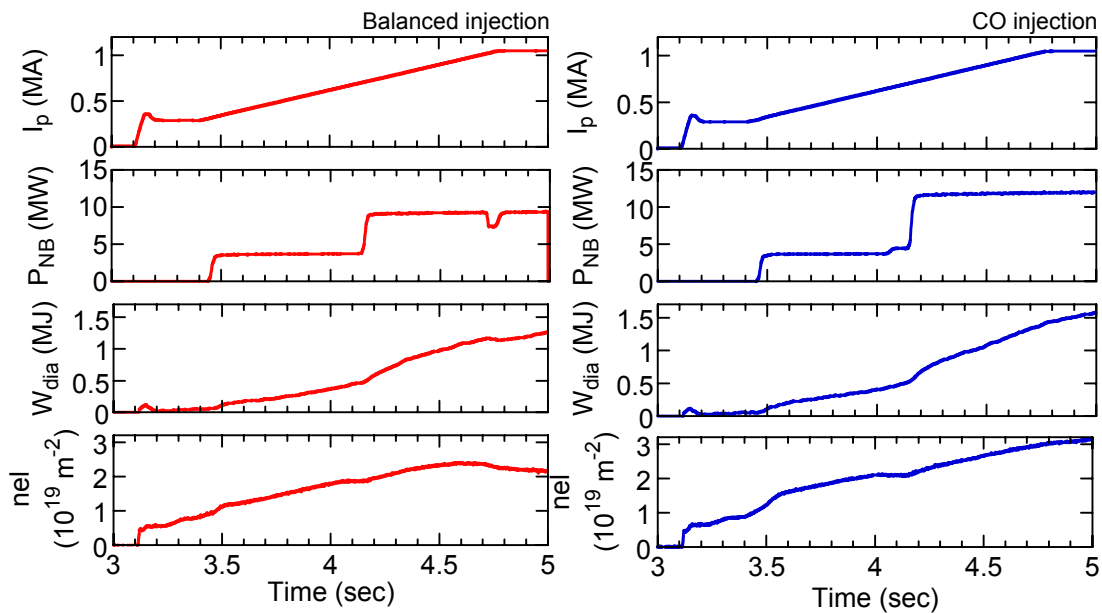


Fig. 1. Waveforms of discharges with balanced injection (left side) and co injection (right side).

of ramp-up of plasma current, which delays the penetration of inductive current, in order to produce reversed shear configuration. In addition to the tangential NB injection, the higher power of perpendicular NB was injected from $t = 4.1$ s for ITB formation. The total injection power of ~ 10 MW produced the ITB in balanced injection case, while no ITB formation in co-injection case. Higher total injection power of ~ 12 MW was required to produce ITB in co-injection case. The characteristics of ITB formation between different toroidal momentum injections are compared under the slightly different heating power.

2.1 Profile evolution of ITB during BAL injection

Figure 2 shows temporal evolutions of ion temperature, toroidal rotation and safety factor (q) profiles in the case of balanced injection. The profiles are shown every 100 ms from just after the perpendicular NB injection to the flat-top of plasma current. Significant change of toroidal rotation profile was observed just after the perpendicular NB injection, where the toroidal rotation increases in counter direction around a half of minor radius and the notched structure with strong toroidal rotation shear is formed at $t = 4.265$ s. After that, ion temperature starts to increase near the location of minimum q (q_{min}), where the gradient of toroidal rotation is positive. The ITB width becomes wider with increasing ion temperature. The interesting feature of evolution of ion temperature profile is that the location of ITB shoulder moves inward

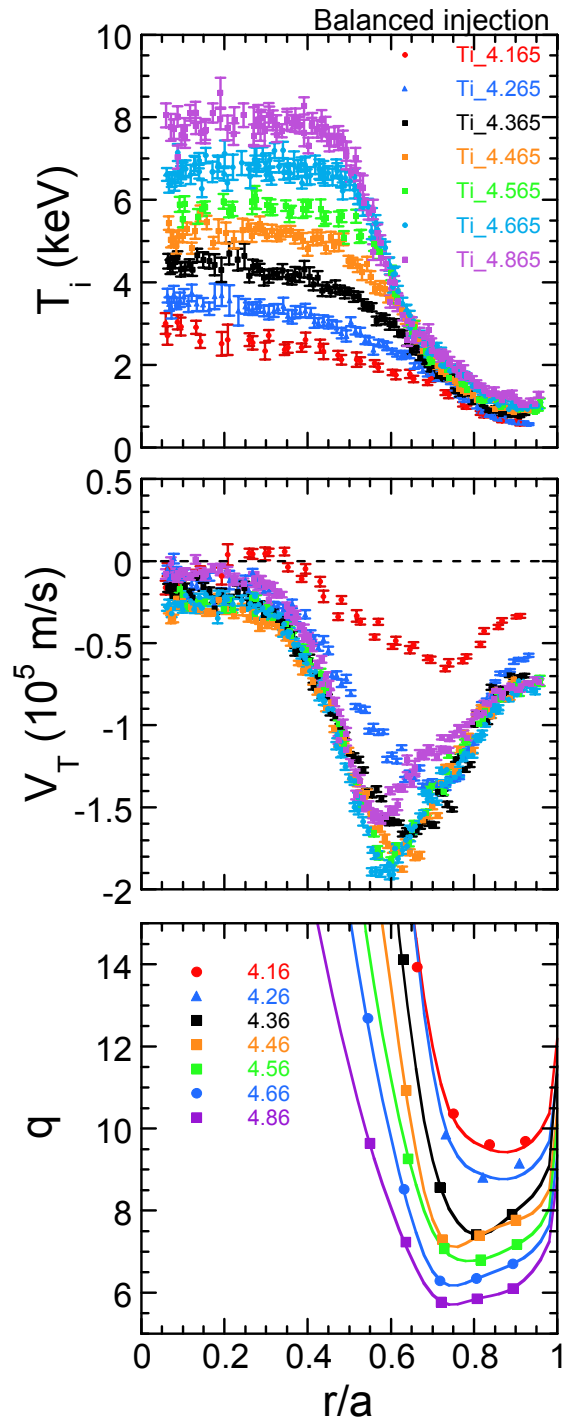


Fig.2. Temporal evolution of ion temperature (top), toroidal rotation velocity (middle), and q (bottom) profiles in balanced injection.

while the location of ITB foot is almost fixed. Finally, the ITB foot locates at q_{min} , and the center of ITB at the location of minimum toroidal rotation or at notch tip. The flat profile region in ion temperature ($r/a < 0.45$) is wider than that in toroidal rotation ($r/a < 0.25$). It should be noted that the change in toroidal rotation profile after the ITB formation is small in comparison with the change in ion temperature profile.

2.2 Profile evolution of ITB during CO injection

Figure 3 shows temporal evolutions of ion temperature, toroidal rotation and q profiles in the case of co-injection. The profiles are shown every 100 ms from just after the perpendicular NB injection to the flat-top of plasma current. As similar to balanced injection case, significant change of toroidal rotation profile was observed just after the perpendicular NB injection. Contrary to balanced injection, no strong-notched structure was observed in toroidal rotation profile, where negative gradient is large while positive gradient is small. Ion temperature starts to increase at the steep toroidal rotation shear, where the gradient of toroidal rotation is negative. It should be mentioned that the ITB foot at the emergence is not near the q_{min} in the co-injection case. The ITB width becomes wider with increasing ion temperature. The interesting feature of evolution of ion temperature profile is that the location of ITB foot moves outward while the location of ITB shoulder is almost fixed. Finally, the ITB foot locates at q_{min} , and the center of ITB at the location of maximum toroidal rotation shear. The flat profile region

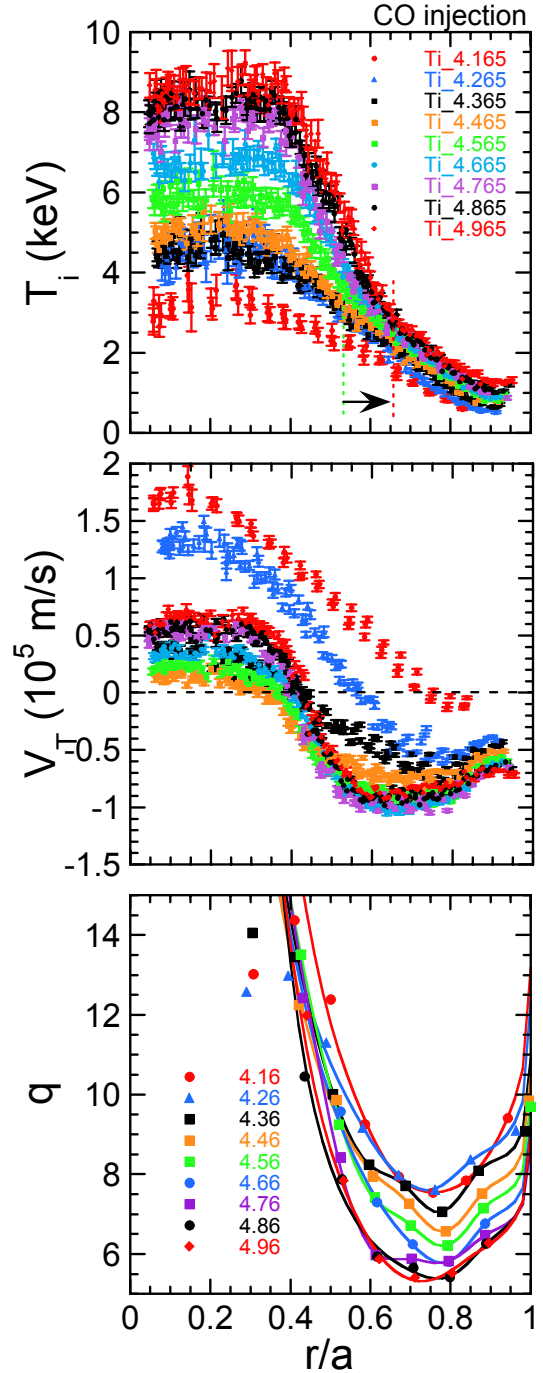


Fig.3. Temporal evolution of ion temperature (top), toroidal rotation velocity (middle), and q (bottom) profiles in co-injection.

in ion temperature ($r/a < 0.35$) is slightly wider than in toroidal rotation ($r/a < 0.3$). As similar to balanced injection case, the change in toroidal rotation profile after the ITB formation is small in comparison with the change in ion temperature profile.

3. Summary

Temporal evolution of ITB structure was measured with modulation CXRS diagnostic, which can measure ion temperature and toroidal rotation velocity at 270 radial points every 50ms, in reversed shear plasmas with different toroidal momentum injections. Comparison of ITB formation and evolution between balanced and co- injections can be summarized as following table.

| | Balanced injection | Co injection |
|--------------------------------|--|---|
| ITB foot at emergence in T_i | Positive grad. region in V_t | Negative gradient in V_t |
| Temp. evolution of ITB | ITB foot moves outward | ITB shoulder moves inward |
| Final structure of T_i | Box type: ITB foot at q_{min} , ITB center at min. of V_t or at notch tip | Box type: ITB foot at q_{min} , ITB center at max. grad. in V_t |
| Final structure of V_t | Notch | Almost monotonic |
| Flat profile region | $T_i \gg V_t$ | $T_i > V_t$ |

Table: Comparison of ITB formation and evolution between balanced and co- injections.

References

[1] Ida, K., et al., Rev. Sci. Instrum. **79** 053506, (2008).

4.6 Effects of Rational Surfaces at q_{\min} on Internal Transport Barrier in JT-60U Reversed Shear Plasmas

Y. Sakamoto, K. Ida¹⁾, M. Yoshida, T. Suzuki

1) NIFS

1. Introduction

Understanding of transition mechanism of improved confinement is crucial to establish the formation of an internal transport barrier (ITB) in fusion reactors. The role of rational surfaces on ITB formation has been discussed in many tokamaks [1-3]. In this study, effects of rational surfaces at the minimum value of safety factor (q_{\min}) on ITBs have been investigated in JT-60U reversed shear plasmas. Detailed profiles of ion temperature and toroidal rotation velocity are measured with modulation CXRS [4] which has radial measurement points of 270 every 50 ms. In addition to modulation CXRS, recently, fast CXRS system has been installed in JT-60U with fast time resolution up to 2.5 ms with radial measurement points of 30 [5]. These powerful diagnostics enable us to clarify the detail change in ITB structure, especially relation between ion temperature and toroidal rotation shear, at q_{\min} being rational surfaces.

2. Observation of ITB transition near integer q_{\min} surfaces

Temporal evolution of ion temperature and toroidal rotation velocity at each radial location are shown in figure 1 together with waveforms of plasma current and NB injection power, which is measured by fast CXRS with time resolution of 2.5 ms. Plasma current is changed as shown in the

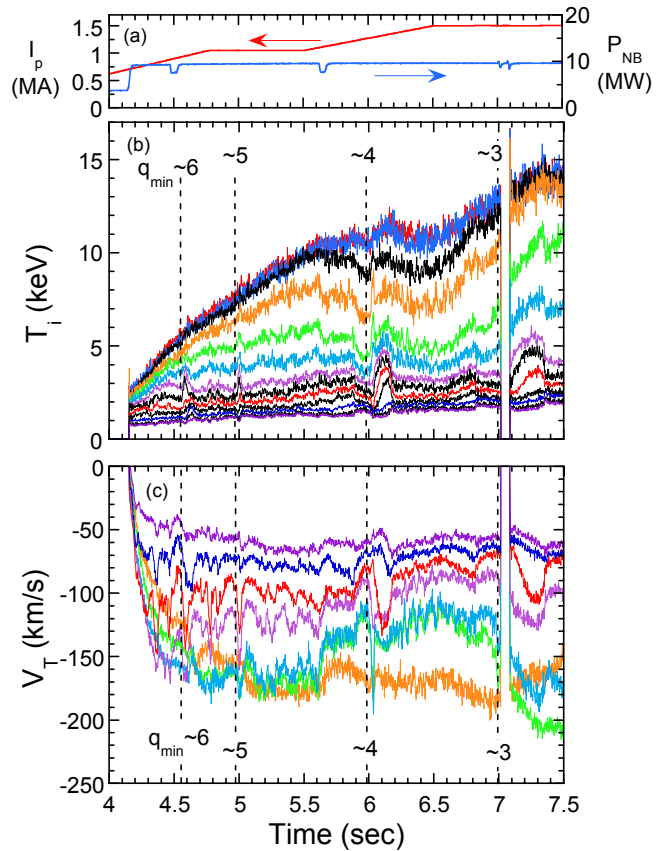


Fig.1. (a) Waveforms of plasma current and NB injection power. Temporal evolutions of (b) ion temperature and (c) toroidal rotation velocity at each radial position.

figure while NB heating power is constant after $t = 4.2$ s. The early NB heating during the ramp-up phase of plasma current makes the penetration of inductive current delay, and then reversed magnetic shear q profile is produced. The ITB was formed just after the main heating ($t = 4.2$ s). In this discharge, the value of q_{\min} decreases continuously from more than six to less than three with increasing plasma current and penetrating inductive current. The location of q_{\min} moves inward to the small radius from $r/a \sim 0.8$ to 0.65. At each time when integer value of the q_{\min} is crossed, the rapid increase in ion temperature and the change in toroidal rotation velocity near the q_{\min} location (ITB foot location) was observed. The change in ion temperature (at foot position) at q_{\min} crossing rational surface becomes large in lower integer value as can be seen in the figure.

Figure 2 shows the enlarged view of temporal evolution of ion temperature and toroidal rotation velocity near the q_{\min} crossing four. When q_{\min} crosses four, the ion temperature inside of q_{\min} increases rapidly, afterward that decreases. In addition, the increase in ion temperatures outside of q_{\min} is observed and it expands outward, afterward ion temperatures decrease. The timescale of the change in ion temperature outside of q_{\min} is slower than that inside of q_{\min} . Furthermore, the excursion in toroidal rotation velocity was observed just inside q_{\min} location, which occurred with the increase in ion temperature almost at the same time. The excursion in toroidal rotation produces large rotation shear near q_{\min} , where the ion thermal diffusivity is reduced. It should be mentioned that no strong excursion in poloidal rotation velocity was observed at the transition phenomena. Moreover the reduction of ion temperature and toroidal rotation velocity was observed in wide area prior to ITB transition phenomena ($t=5.88-6.0$ s). Actually, the ion temperature

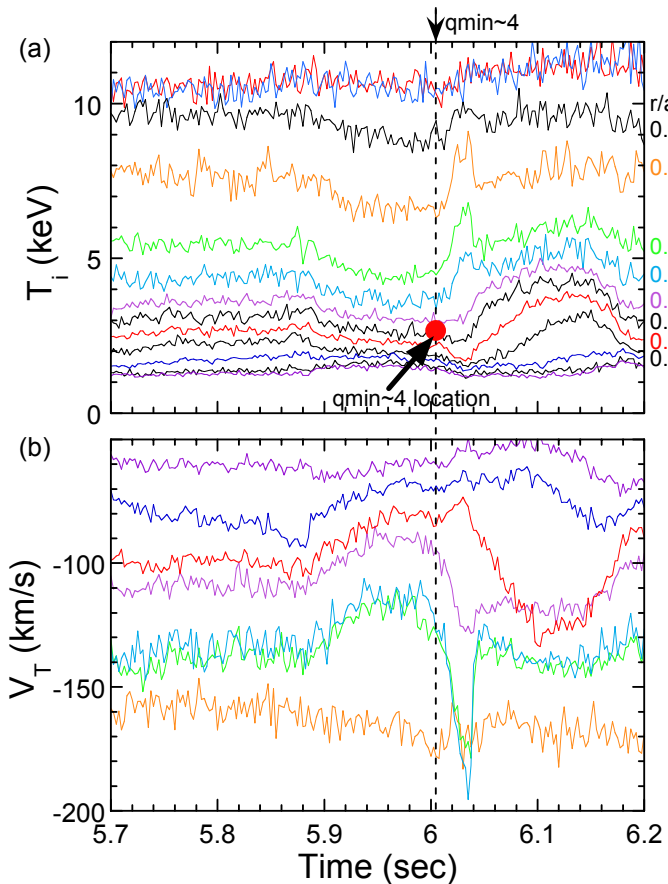


Fig. 2. Temporal evolutions of (a) ion temperature (b) toroidal rotation velocity at q_{\min} crossing 4.

decreases by $\sim 20\%$ and the region is $0.47 < r/a < 0.74$ including the outside of ITB.

The detailed profiles of ion temperature and toroidal rotation velocity before and after q_{\min} crossing three were successfully measured by modulation CXRS, which requires the quasi-steady state phase longer than 50 ms for each profile measurement, as shown in figure 3. Strong ITB was already formed before q_{\min} being three, corresponding to $t = 6.965$ s, where steep ion temperature gradient is located at the notch in toroidal rotation profile. The ITB foot ($r/a \sim 0.58$) is located at just inside of q_{\min} location ($r/a \sim 0.63$). After the transition at q_{\min} being three ($t = 7.26$ s), ion temperatures at both ITB layer and outside of ITB increase, and then the double ITB structure can be seen in ion temperature profile, where the ion temperature gradient is gentle at q_{\min} location. As shown in Fig. 3(a) outer ITB foot seems to be located at outer $q = 3$ surface ($r/a \sim 0.72$), while inner ITB foot ($r/a \sim 0.58$) at slightly inside of q_{\min} ($r/a \sim 0.62$). The MHD activity appeared after $t = 7.3$ s, however, and then outer ITB disappeared. Although outer ITB is lost, inner ITB is sustained in stronger level as shown in the figure. In addition to the double ion ITB structure, double notch structure is clearly formed in toroidal rotation profile.

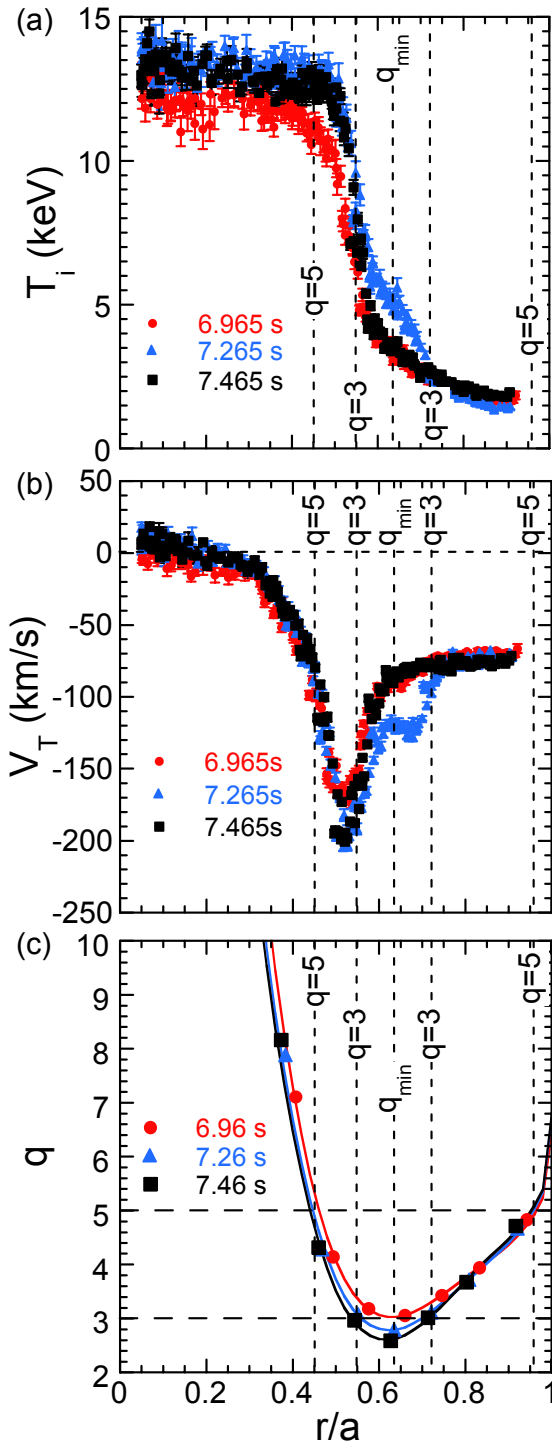


Fig.3. Radial profiles of (a) ion temperature, (b) toroidal rotation velocity and (c) safety factor.

3. Summary

Detailed temporal evolution and radial profiles of ion temperature and toroidal rotation velocity at q_{\min} crossing integer have been measured with modulation CXRS and fast CXRS with high accuracy. The increase in ion temperature and the excursion of toroidal rotation were observed almost at the same time when an integer value of q_{\min} is crossed. The reduction of ion temperature and toroidal rotation velocity was observed in wide area prior to the crossing of the integer q_{\min} .

References

- [1] Koide, Y., et al., Phys. Rev. Lett. **72**, 3662 (1994).
- [2] Joffrin, E., et al., Plasma Phys. Control. Fusion **44**, 1739 (2002).
- [3] Austin, M.E., et al., Phys. Plasma **13**, 082502 (2006).
- [4] Ida, K., et al., Rev. Sci. Instrum. **79**, 053506, (2008).
- [5] Sakamoto, Y., et al., this issue 10.8.

4.7 Effect of toroidal rotation and q profiles on ITB characteristics for JET/JT-60U identity experiment

Y. Sakamoto, X. Litaudon¹⁾, P. C. de Vries²⁾, N. Oyama, T. Suzuki, K. Shinohara, T. Fujita, G. Matsunaga, M. Takechi, N. Hayashi, H. Takenaga, T. Takizuka, H. Urano, M. Yoshida

1) CEA, IRFM, F-13108 St-Paul-Lez-Durance, France.

2) EURATOM/UKAEA Association, Culham Science Centre, OX14 3DB, Abingdon, UK.

1. Introduction

A variety of triggering mechanisms and structures of internal transport barriers (ITBs) has been observed for various operation scenarios in various devices. In order to shed light on the physics behind ITBs, identity experiments in JET and JT-60U have been performed. Because of their similar size, the dimensionless parameters between both devices are the same except for the Mach number of plasma rotation due to the different Neutral Beam Injection (NBI) configurations. These experiments were performed with near identical magnetic configurations, heating waveforms and normalized quantities such as safety factor, magnetic shear, normalized Larmor radius, normalized collision frequency, beta, temperatures ratio etc. Similarities of the ITB triggering mechanism and the ITB strength have been observed when a proper match is achieved of the most relevant profiles of the normalized quantities. The first

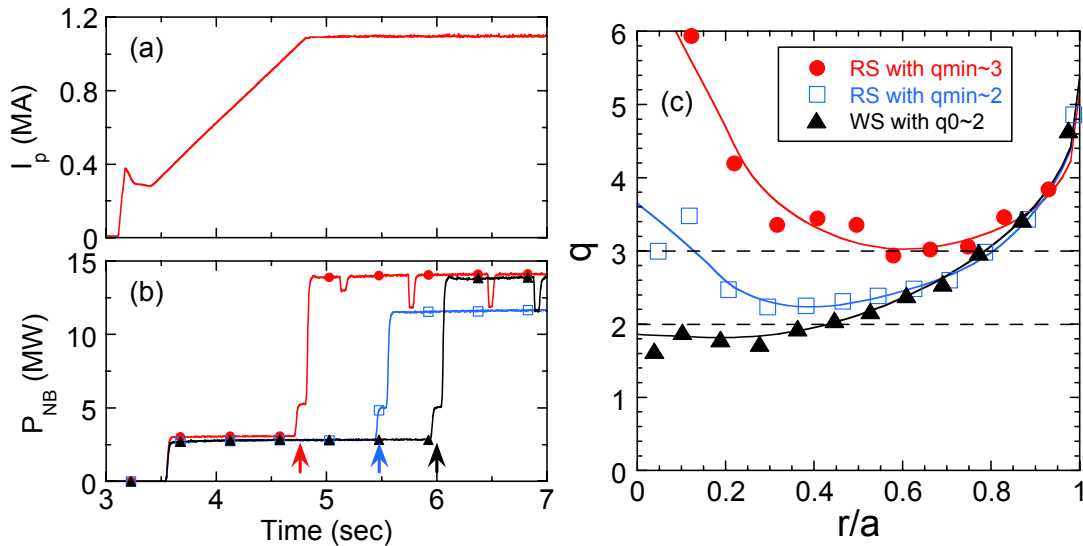


Fig. 1. The three heating scenarios for reversed shear with $q_{min} \sim 3$, $q_{min} \sim 2$, and weak magnetic shear plasma with $q(0) \sim 2$. Waveforms of (a) plasma current and (b) injected NBI power. (c) q profile just before main heating.

overview of the identity experiments in JET and JT-60U has been presented in [1]. This report describes the experiments performed in JT-60U for JET/JT-60U identity experiment to study the effect of toroidal rotation and safety factor (q) profiles on ITB characteristics.

2. Experimental results

2.1 Experimental conditions

In the series of experiments, ITBs were produced with various target q profiles, such as reversed magnetic shear (RS) with $q_{\min}=3$, $q_{\min}=2$, and weak positive magnetic shear (WS) with $q(0)\sim 2$, by adjusting the start time of the main heating, as shown in figure 1. The same waveform of plasma current (I_p) is used in the series of experiments, where the ramp-up rate of I_p is 0.5MA/s. Toroidal magnetic field and plasma current are 2.26T and 1.1MA respectively, resulting $q_{95}\sim 4.2$. Low power NB heating (~ 3 MW) was applied as the pre-heating during I_p ramp-up phase not only to delay the penetration of inductive current but also to avoid ITB formation during I_p ramp-up phase, though the ITBs are produced during I_p ramp-up phase with higher heating power in the usual JT-60U ITB scenario of RS. The NB power was raised to ~ 14 MW just after I_p ramp-up phase ($t=4.7$ s) in the case of the RS scenario with $q_{\min}=3$, while after 0.8 s from the start of I_p flat-top in RS scenario with $q_{\min}=2$ ($t=5.5$ s), and after further 0.5 s in WS with $q(0)\sim 2$ ($t=6.0$ s), as shown in figure 1(b). The

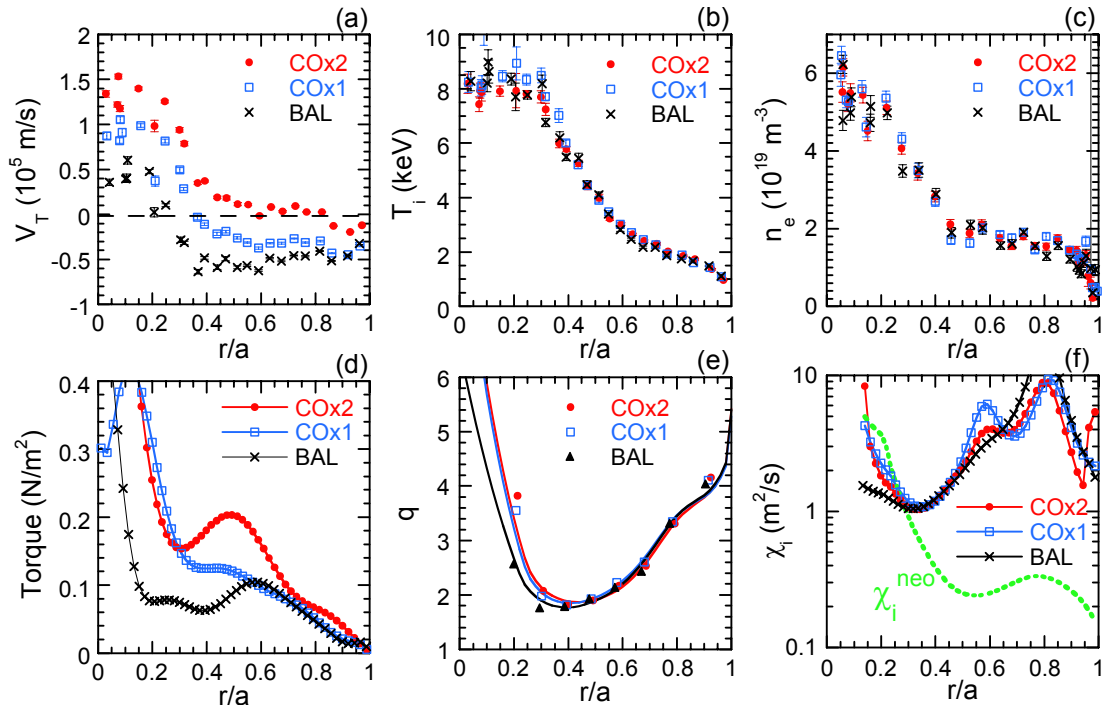


Fig. 2. Radial profiles of (a) toroidal rotation, (b) ion temperature, (c) electron density, (d) torque from NBI, (e) safety factor and (f) thermal diffusivity together with neo-classical one for the cases of two units of CO-NBI (COx2), one unit of CO (COx1) and BAL injections in RS scenario with $q_{\min}=3$.

target q profiles (just before main heating) for each scenario are shown in figure 1 (c). The position of q_{\min} in RS with $q_{\min}=2$ is narrower than that in RS with $q_{\min}=3$. It is noted that the toroidal rotation profiles were scanned only in the case of RS with $q_{\min}=3$ in order to find the closest match in rotation.

2.2 Results of torque scan and q -profile scan

The JT-60U has eleven units of positive ion based NBI. These units are divided into seven nearly-perpendicular injection to the plasma current, two co-tangential (CO) injection, and two counter-tangential injection. In the present experiment, the combination of tangential NBIs was varied, shot by shot, from two units of CO to one unit of CO, and then balanced (BAL) injection, whereas the heating profiles are almost the same. Since the only co-current tangential injection can be applied in JET, the torque scan in the direction of co-current was performed in JT-60U in the detailed manner in order to match the Mach number profile. Note that HH factor of 1.05 and high poloidal beta of 1.6 (bootstrap current fraction of $\sim 70\%$) are obtained at $n_e/n_{GW} \sim 0.5$ with ELMy H-mode edge condition. Figure 2 shows the results of torque scan experiment performed in RS scenario with $q_{\min}=3$. The calculated torque profiles

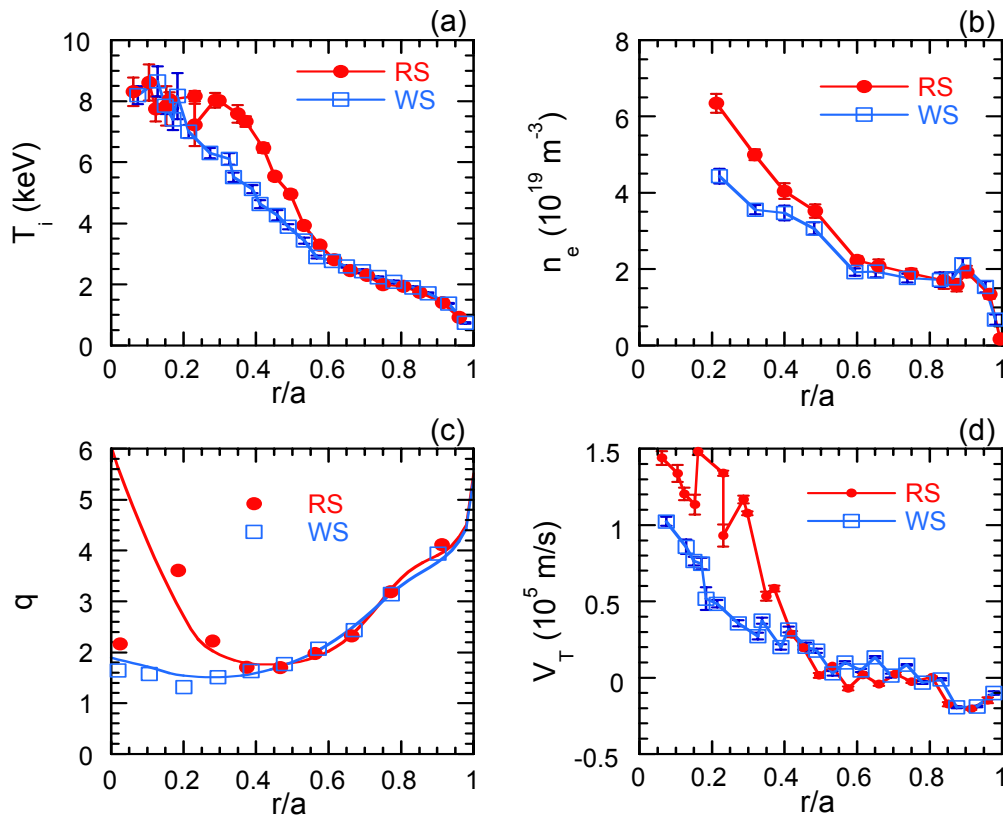


Fig. 3. Comparison of radial profiles of (a) ion temperature, (b) electron density, (c) safety factor and (d) toroidal rotation between RS scenario with $q_{\min}=2$ and WS scenario with $q(0)\sim 2$.

of these three cases are shown in figure 2(d). The different toroidal rotation profiles are obtained, whereas the ion temperature, electron density and q profiles are very similar as shown in figure 2. The thermal diffusivity profiles evaluated from TOPICS are also very similar. Although the toroidal rotation profiles differ, the gradient of toroidal rotation in the core region ($r/a > 0.5$) is similar to three cases. The position of ITB foot for ion temperature is not clear, but it might be around a half of the minor radius, which is wider than the position of q_{\min} ($r/a \sim 0.45$). On the other hand, the clear ITB for the electron density was observed and its foot position is close to the position of q_{\min} or $q=2$.

Figure 3 shows the comparison of the profiles obtained in RS with $q_{\min}=2$ and WS with $q(0)\sim 2$ scenarios. These profiles were obtained at quasi-steady state phase. In these discharges, two units of co-tangential NBI and a half units of counter-tangential NBI for MSE measurement and 4 or 3 units of nearly perpendicular NBI are injected for the WS or the RS plasmas, resulting total injection power is ~ 14 MW (WS) or ~ 12 MW (RS). As can be seen in the figure, the ITBs in the case of RS is stronger than those in WS. Since the injected NBI power in RS case is smaller than that in WS as shown in figure 1 (b), the thermal diffusivity in RS should be lower than that in WS. The ITB foot for both cases are located at $r/a \sim 0.6$ which is very close to the position of $q=2$ surface.

3. Summary

This report describes the experimental results, performed in JT-60U, for JET/JT-60U identity experiments. Because of similar size of JET and JT-60U, implementation of the identity experiments is suitable for both devices in order to shed light on the physics behind ITBs. In the series of JT-60U experiments, we carried out q -profile scan such as RS plasmas with $q_{\min}=3$, $q_{\min}=2$ and WS plasma with $q(0)\sim 2$, and toroidal torque scan in RS plasma with $q_{\min}=3$. The series of JT-60U dataset have been obtained. Detailed comparison of transport properties between JET and JT-60U is being undertaken.

Reference

[1] P.C. de Vries et al., Proc. 36th EPS conf. on Plasma Physics (Sofia, Bulgaria) I5.078.

4.8 Dependence of Heat Transport on Toroidal Rotation in Conventional H-modes in JT-60U [1]

H. Urano, H. Takenaga, T. Fujita, Y. Kamada, Y. Koide, N. Oyama,
M. Yoshida and the JT-60 Team

Temperature gradients are a key element in driving turbulent convection and causing anomalous heat transport in plasmas. The property of the turbulence driven by temperature gradient is believed to be provided by a strong increase of heat conduction which sustains a self-similar profile when the temperature profile exceeds a threshold in the temperature gradient (TG) scale length. Therefore, understanding the response of temperature profiles to variations in magnetic and velocity shear profiles and heat flux profiles is indispensable for predicting and designing a future fusion reactor.

In this study, relation between heat transport in the plasma core and toroidal rotation as well as characteristics of the pedestal structure were examined in conventional ELMy H-mode plasmas in JT-60U. Conducting the experiments on power scan with a variety of toroidal momentum source generating the plasma rotation direction to co, balanced and counter with respect to the plasma current, dependence of the heat transport properties in the plasma core on toroidal rotation profiles was investigated. Energy confinement improvement was observed with toroidal rotation which increases in co-direction. Heat transport in the plasma core varies while sustaining self-similar temperature profile in the variations of toroidal rotation profiles. Pressure at the H-mode pedestal became larger weakly with toroidal rotation in co-direction. Thus, energy confinement enhanced with co-toroidal rotation is determined by increased pedestal and reduced transport brought on by profile resilience. In other words, heat transport in the plasma core is mainly determined by the saturation of temperature profile and is not strongly influenced locally by toroidal rotation. When the pedestal temperature was fixed between the cases of co and counter-NBI by adjusting the plasma density, the identical temperature profiles were obtained in spite of totally different toroidal rotation profiles. In H-mode plasmas where the ion channel is heated dominantly through the accelerating energy with positive ion-based neutral beams, the saturation of ion temperature gradient governs the heat transport in the plasma core. As a result, large increase in heat conduction imposes the resilient profile of ion temperature, under which local effect of toroidal rotation profile on the scale length of ion temperature gradient is very weak.

Reference

[1] Urano H et al., Nucl. Fusion **48** 085007 (2008)

4.9 Heat Transport of H-mode Plasmas in the Variation of Current Density Profiles in JT-60U [1]

H. Urano, Y. Sakamoto, T. Suzuki, T. Fujita, K. Kamiya, A. Isayama, Y. Kamada, H. Takenaga, N. Oyama, G. Matsunaga, S. Ide, Y. Idomura and the JT-60 Team

Tokamaks are a system in which magnetized plasmas are confined by a poloidal magnetic field generated by the plasma current I_p in combination with the toroidal magnetic field. It has been therefore presumed that the heat transport in the plasma core could depend on the current density profile $j(r)$. Understanding the response of temperature profiles to variations in current density profiles and heat flux profiles is indispensable for predicting and designing a future fusion reactor. However, little is known about the effect of the current density profile on the H-mode characteristics.

In this study, conducting the I_p ramp experiments in JT-60U, the dependence of heat transport on the current density profiles was examined. Higher energy confinement is obtained in higher l_i H-mode. The profiles of the core electron density and electron temperature tends to be peaked. The H-factor evaluated for the core plasma of H-mode ($H_{89\text{core}}$) depends strongly on l_i with the relation of $H_{89\text{core}} \propto l_i^{0.8}$ in case of $l_i < 1$. However, at $l_i > 1$, the existence of strong sawtooth prevents from the increase of the core H-factor at higher l_i regime ($H_{89\text{core}} \sim 1.5$ at $l_i > 1$). In order to evaluate the thermal energy confinement properties in the variation of the current density profiles, the power scan was conducted. It is found at higher l_i that larger W_{th} is obtained at a given P_{abs} . On the other hand, no clear difference in W_{ped} is observed between the cases of high and low l_i plasmas. Thus, the increase of W_{th} at higher l_i is attributed mainly to the energy confinement improvement in the core plasma. The changes in χ_i in the power scan are similar between the low and high l_i cases. On the contrary to the ions, the T_e profiles are peaked at the center in the high l_i H-mode plasmas, resulting in the reduction in χ_e . In spite of the similar edge pedestal profiles in the I_p ramp experiments, a clear difference is observed in ELM activity. The ELM frequency f_{ELM} at higher l_i becomes higher at a given P_{sep} . The edge pedestal pressure is not significantly changed by the I_p ramp technique. While the change in W_{ped} is small in the variation of the current density profiles when I_p is given, W_{ped} is increased explicitly with increasing I_p . As the I_p is raised, the pedestal temperature T_i^{ped} is raised while the pedestal width Δ_{ped} tends to shrink. With the increase of I_p , the pedestal β_p decreases.

Reference

- [1] Urano H et al., Nucl. Fusion **49** 095006 (2009)

4.10 Correlation between the Edge and the Internal Transport Barriers and Effect of ELMs in JT-60U [1]

Y. Kamada, M. Yoshida, Y. Sakamoto, Y. Koide, N. Oyama, H. Urano, K. Kamiya
T. Suzuki, A. Isayama, and the JT-60 Team

The world tokamaks have been developing the advanced operation modes characterized by the edge transport barrier (ETB) and the internal transport barrier (ITB). Since radial shapes of the kinetic parameters play the central roles for all of the above performances, it is critical to understand the physics processes determining the radial profiles. For both ETB and ITB, their radial structure and evolution have been studied significantly [2,3]. However, the 'correlation' between these two transport barriers remains still as an open issue. The correlation, if it is strong, determines the whole radial profiles and then determines the dynamics of the advanced tokamak plasma system. In order to address this issue, correlation between the edge transport barrier (ETB) and the internal transport barrier (ITB) has been studied in JT-60U for Type I ELMing plasmas.

We found that the edge pedestal beta, $\beta_{p\text{-ped}}$, increases almost linearly with the total β_p over a wide range of the plasma current for the type I ELMing H-mode, and the dependence becomes stronger with increasing triangularity. This dependence is not due to the profile stiffness. However, with increasing the stored energy inside the ITB radius (W_{ITB}), the total thermal stored energy (W_{th}) increases and then the pedestal stored energy (W_{ped}) increases. With increasing W_{ped} , the ELM penetration depth expands more inward and finally reaches the ITB-foot radius. At this situation, the ITB radius cannot move outward and the ITB strength becomes weak. Then the fractions of W_{ITB} and W_{ped} to W_{th} become almost constant. We also found that the type I ELM expels/decreases edge toroidal momentum larger than ion thermal energy. The ELM penetration radius for toroidal rotation tends to be deeper than that for ion temperature, and can exceed the ITB radius. The ELM affected area is deeper for CO rotating plasmas than CTR rotating ones. The ELM affected area is deeper in the order of the toroidal rotation (V_t), the ion temperature (T_i) and then the electron temperature (T_e). The L-H transition also changes the V_t -profile more significantly than the T_i -profile. After the L-H transition, in the ELM-free phase, the pedestal V_t shifts into the CTR direction deeply and suddenly, and after that the pedestal V_t and T_i evolves in the similar timescale. The change in V_t by ELM and L-H transition may affect degradation / evolution of ITBs.

Reference

[1] Kamada, Y. et al., Nucl. Fusion **49**, 095014 (2009).

4.11 Tungsten Accumulation in H-mode Discharges [1]

T. Nakano, H. Kubo and N. Asakura.

Tungsten is one of the most promising materials for plasma facing components in future fusion devices such as ITER because of advantages particularly such as low sputtering yield and low hydrogen retention. The lower sputtering yield of tungsten, compared to that of carbon, leads to longer lifetime of the plasma facing components. Further the effective sputtering yield becomes lower than the congenital sputtering yield in the magnetic configuration of tokamaks due to prompt redeposition. The lower hydrogen retention of tungsten, compared to that of carbon, suppresses the increase of the tritium inventory, leading to long successive operation without tritium degassing. This is a significant advantage in a deuterium-tritium fusion device, where the amount of tritium inside the device is limited by safety reasons. By these reasons, in particular by the latter reason, tungsten is supposed to be used as the divertor tiles in the deuterium-tritium operation phase of ITER. However, because of the high charge of tungsten ions in high temperature fusion plasmas, the radiation loss efficiency is very high, and therefore allowable tungsten concentration for an ignited plasma is estimated to be lower than 1×10^{-3} against the electron density [2]. Furthermore, it is expected that accumulation in the core plasma becomes significant with increasing atomic number.

In order to investigate the conditions that tungsten ions accumulate in the plasma core, plasma toroidal rotation scan experiments, additional electron cyclotron wave (EC) and negative-ion-source based neutral beam (N-NB) injection experiments were performed. The discharge conditions were as follows; H-mode plasma with a plasma current of 1.5 - 1.6 MA, a toroidal magnetic field of 3.2 - 3.9 T and an neutral beam heating power of 15 MW with the outer strike point on the upper divertor plates, 12 plates of which were coated by tungsten with a thickness of 50 μm . As shown in Fig. 1, The rotation scan experiments indicated that with increasing plasma toroidal rotation velocity in the direction opposite to the plasma current, the sawtooth activity became moderate and the W accumulation became significant. Here W accumulation level is defined as the W XLVI intensity from the core plasma divided by the line-averaged electron density and the W I intensity from the divertor plasma. In order to reduce the statistical errors of the spectroscopic measurements, the data were time-averaged for 0.5 - 1.0

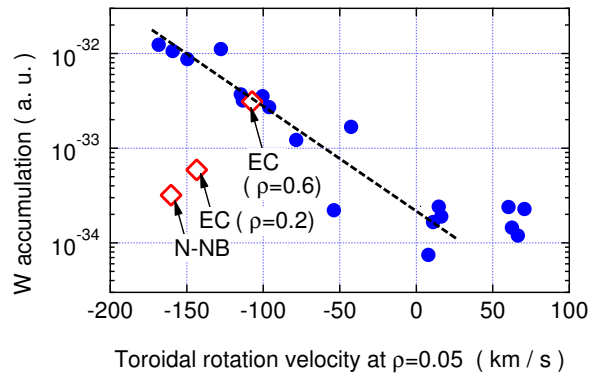


Fig. 1: *W* accumulation level as a function of the toroidal rotation velocity at $\rho = 0.05$. The broken line is to guide readers' eyes.

s. The EC wave and the N-NB injections successfully suppressed the W accumulation in the plasma core even without sawteeth and even at high negative toroidal rotation velocity. However, the electron cyclotron wave injection at the plasma edge kept the W accumulation level high stably.

Although the experimental method to avoid the tungsten accumulation has been clearly shown, mechanisms of the tungsten accumulation has not been yet understood sufficiently. Hence theoretical study to investigate the mechanisms is needed. Quantitative evaluation of the accumulation and the atomic number dependence on the accumulation will be a future work.

References

- [1] Nakano, T. *et al.*, *Nucl. Fusion* **49**, 115024 (2009).
- [2] Post D. E. *J. Nucl. Mater.* **220-222**, 143 (1995).

4.12 Experimental Investigation of Particle Transport Associated with Turbulence in LHD Heliotron and JT-60U Tokamak Plasmas [1,2]

K. Tanaka¹⁾, H. Takenaga, K. Muraoka²⁾, C. A. Michael³⁾, L. N. Vyacheslavov⁴⁾,
 M. Yokoyama¹⁾, H. Yamada¹⁾, N. Oyama, H. Urano, Y. Kamada, S. Murakami⁵⁾,
 A. Wakasa⁶⁾, T. Tokuzawa¹⁾, T. Akiyama¹⁾, K. Kawahata¹⁾, M. Yoshinuma¹⁾,
 K. Ida¹⁾, I. Yamada¹⁾, K. Narihara¹⁾, N. Tamura¹⁾

1) National Institute for Fusion Science, 2) Chubu University, 3) UAKEA Fusion Association,
 4) Budker Institute of Nuclear Physics, 5) Kyoto University, 6) Hokkaido University

Comparative studies were carried out in LHD heliotron and JT-60U tokamak plasmas to elucidate the most essential parameter(s) for control of density profiles in toroidal systems. The analysis was carried out for the ELMy H-mode in JT-60U and for the magnetic axis position (R_{ax}) of 3.5 and 3.6 m in LHD. Both global energy confinement scalings for ELMy H-mode (ITER98y2) and for LHD (ISS04) show a Gyro Bohm nature. This suggests that there exists common underlying physics in both operating domains. A difference of density profiles in the collisionality dependence was found between the two devices. In LHD, the density peaking factor decreased with decreasing collisionality at $R_{ax} = 3.6$ m, while the density peaking factor gradually increased with decreasing collisionality at $R_{ax}=3.5$ m. On the other hand, in JT-60U, the density peaking factor clearly increased with decreasing collisionality. The difference in the collisionality dependence between $R_{ax}=3.5$ and $R_{ax}=3.6$ m is likely due to the difference of the contribution of the neoclassical and anomalous effect. At $R_{ax}=3.5$ m, larger anomalous transport caused a similar collisionality dependence with that for JT-60U.

Possible roles of fluctuation were experimentally studied in JT-60U and LHD. The radial correlation of turbulence was measured in JT-60U by correlation reflectometry and spatial profiles of turbulence were measured in LHD by two dimensional phase contrast imaging. In JT-60U, density profiles were varied by the scan of collisionality from the change of NBI power (P_{NB}) and density. An increase of the radial coherence was observed for a higher density peaking profile. This suggests that a stronger fluctuation induced inwardly directed pinch was enhanced more strongly than the effect caused by diffusion. For a magnetic axis positions (R_{ax}) at 3.6 m in LHD, the increase of the fluctuation power with an increase in P_{NB} was observed, resulting in the change in density profiles from a peaked to a hollow ones, which suggests an increase in diffusion due to anomalous processes.

Reference

- [1] K. Tanaka, H. Takenaga, K. Muraoka et al., "Experimental Investigation of Particle Pinch Associated with Turbulence in LHD Heliotron and JT-60U Tokamak Plasmas" Proc. 22nd IAEA Fusion Energy Conference, EX/P5-6.
 [2] H. Takenaga, K. Tanaka, K. Muraoka et al., Nucl. Fusion **48** (2008) 075004.

4.13 Dynamics of Ion Internal Transport Barrier in LHD Heliotron and JT-60U Tokamak Plasmas

K. Ida¹⁾, Y. Sakamoto, M. Yoshinuma¹⁾, H. Takenaga, K. Nagaoka¹⁾, N. Oyama, M. Osakabe¹⁾, M. Yokoyama¹⁾, H. Funaba¹⁾, N. Tamura¹⁾, K. Tanaka¹⁾, Y. Takeiri¹⁾, K. Ikeda¹⁾, K. Tsumori¹⁾, O. Kaneko¹⁾, K. Itoh¹⁾, S. Inagaki²⁾, T. Kobuchi³⁾, A. Isayama, T. Suzuki, T. Fujita, G. Matsunaga, K. Shinohara, Y. Koide, M. Yoshida, Y. Kamada, LHD experimental group and the JT-60 team

1) National Institute for Fusion Sciences, Toki, Gifu 509-5292, Japan

2) Research Institute for Applied Mechanics, Kyushu University, Kasuga, Fukuoka, 816-8580, Japan

3) Department of Quantum Science and Energy Engineering, Tohoku University, Sendai, Miyagi, 980-8679, Japan

A spontaneous transition phenomena between two states of a plasma with an internal transport barrier (ITB) is observed in the steady-state phase of the magnetic shear in the negative magnetic shear plasma in the JT-60U tokamak using modulation charge exchange spectroscopy[1]. These two ITB states are characterized by different profiles of the second radial derivative of the ion temperature inside the ITB region (one has a weak concave shape and the other has a strong convex shape) and by different degrees of sharpness of the interfaces between the L mode and the ITB region[2,3], which suggests strong self-organized mechanism in the plasma with ITB.

In order to study the self-organized process during the ITB formation, dynamics of ion ITB formation is investigated and compared with that in large Helical Device (LHD) heliotron. Significant differences between heliotron and tokamak plasmas are observed [4]. The location of the ITB moves outward during the ITB formation regardless of the sign of magnetic shear in JT-60U, and the ITB becomes more localized in plasmas with negative magnetic shear. In LHD, the low T_e/T_i ratio (< 1) of the target plasma for the high power heating is found to be necessary to achieve the ITB plasma and the ITB location tends to expand inward.

Since the impurity accumulation is a serious problem in the plasma with ITB, because high concentration of impurity in the plasma core causes the dilution of fuel. Therefore it is important to study the impurity transport in the plasma with ITB. Since the convection term of the impurity transport play an important role to determine the concentration of impurity at the plasma center, the sign and magnitude of convection velocity are investigated in the ITB plasmas in JT-60U with a contrast to that in LHD. Associated with the formation of ITB, the carbon density tends to be peaked due to inward convection in JT-60U while the carbon density becomes hollow due to outward convection in LHD. The outward convection observed in LHD contradicts the prediction by neoclassical theory.

References

- [1] Ida, K., et al., Rev. Sci. Instrum. **79**, 053506 (2008).
- [2] Ida, K., et al., Phys. Rev. Lett. **101**, 055003 (2008).
- [3] Ida, K., et al., Nucl. Fusion **49**, 015005 (2009).
- [4] Ida, K., et al., submitted to Nucl. Fusion.

5 H-mode Confinement and Pedestal

5.1 Dimensionless Parameter Dependence of H-mode Pedestal Width using Hydrogen and Deuterium Plasmas in JT-60U [1]

H. Urano, T. Takizuka, Y. Kamada, N. Oyama, H. Takenaga and the JT-60 Team

In H-mode plasmas, it is of primary importance to understand the physical processes determining the edge pedestal structure. However, the dependence of the spatial width of the H-mode edge transport barrier on local and global plasma parameters is not clearly known. Particularly, a knowledge of the pedestal width Δ_{ped} based on dimensionless parameters is of great help for the extrapolation towards a next step device. Successful ITER operation will require both high pressure at the top of the H-mode transport barrier and small ELMs to simultaneously meet the goals of high fusion power output and high efficiency. However a well-validated means of predicting the spatial width of the H-mode transport barrier in ITER is still lacking and remains a major topic of research. Attempts to project a pedestal width for ITER through physics based or empirical scaling from multi-tokamak databases are underway to extend turbulent models through the pedestal region in recent tokamak research.

Although a variety of empirical scalings of Δ_{ped} during the well-developed type-I ELMy H-mode phase have been proposed, these scalings vary from machine to machine. This disagreement of the scalings intermingling ρ_{pol}^* and β_{pol} can be caused by the existing edge stability boundary for ELMs. In this region, ρ_{pol}^* and β_{pol} are linked strongly and thus are hard to separate out in the standard dimensionless parameter scan using a single gas species.

To distinguish these variables, a pair of experiments in hydrogen and deuterium plasmas were conducted in this study. Explicit difference between ρ_{pol}^* and β_{pol} is the mass dependence of ρ_{pol}^* ($\propto m^{0.5}$) in contrast with no mass dependence in β_{pol} . Both the database analysis and the dedicated experiments on the mass scan indicated that the pedestal width depends very weakly on the plasma particle species or ρ_{pol}^* . Identical profiles of the edge T_i which were obtained in the experiments suggested that the pedestal width depended on β_{pol} more strongly than ρ_{pol}^* . The experiment on β_{pol} scan was also performed. Higher β_{pol} plasma had higher pedestal T_i value accompanied by greater pedestal width in spite of the almost identical ρ_{pol}^* at the pedestal. Based on the experiments on the dimensionless parameter scan, the scaling of the pedestal width was evaluated as $\Delta_{\text{ped}} \propto a_p \rho_{\text{pol}}^{*0.2} \beta_{\text{pol}}^{0.5}$.

Reference

- [1] Urano H et al., Nucl. Fusion **48** 045008 (2008)

5.2 Edge Impurity Ion Dynamics in co-, bal.- and ctr-NBI Heated H-mode Plasmas

K. Kamiya, Y. Sakamoto, and K. Ida¹⁾

1) NIFS

1. Introduction

Previous experiment on JT-60U, the ELM mitigation by means of edge plasma toroidal rotation had been demonstrated [1], although it was not well understood what physics determined edge process. In this study, the edge impurity ion dynamics, such as time evolution and radial perturbation to the radial electric field E_r , during a Type-I ELM cycle for different rotating plasmas has been investigated. A new edge phenomenon in JT-60U H-mode plasma having ELMs has been observed by means of CXRS diagnostic upgrades with fast time-resolution up to 400 Hz with high precision.

The radial electric field, pressure gradient and plasma velocity perpendicular to the magnetic field are governed by the radial force balance equation; $E_r = (Z_j e n_j)^{-1} \nabla p_j - V_{\theta j} B_\phi + V_{\phi j} B_\theta$. Here, Z_j is the ion charge, n_j is the ion density, e is the magnitude of the electron charge, $p_j = n_j T_j$ is the ion pressure with T_j the ion temperature, $V_{\theta j}$ and $V_{\phi j}$ are the ion poloidal and toroidal rotation velocities, respectively, and B_θ and B_ϕ are the poloidal and toroidal magnetic fields, respectively. The sign in both B_θ and B_ϕ are negative in the right hand coordinate system (r, θ, ϕ); the B_θ is upward at the outboard median, the B_ϕ clockwise as viewed from the top of the tokamak. The plasma current I_p is in the positive toroidal direction, and the ion (electron) diamagnetic direction is positive (negative).

2. Effect of the edge plasma rotation on the radial electric field structure

We performed the following experiment under the condition of the plasma current, $I_p = 1.6$ MA and toroidal magnetic field and $B_T = 3.9$ T (corresponding safety factor at 95% of flux surfaces, $q_{95} \sim 4.2$), scanning combinations of NBI as shown in figure 1.

Edge impurity ion dynamics for the middle NBI power case of $P_{NBI} \sim 12$ MW are shown in figure 2 and 3. Improved statistics in assessing the temporal behavior of the measurements can be obtained by mapping of multiple, reproducible ELM cycles onto a single time basis, defined by the time of the measurement relative to the ELM. The technique used here is similar to that used in Ref. 2 for analysis of ELM perturbations.

From figure 2, it is evident that the E_r -well at the pre-ELM phase for the co-NBI discharge seems to be shallower than that seen in the counter-NBI. On the contrary, the E_r -shear layer at the pre-ELM phase for the co-NBI discharge is likely to be wider than that seen in the counter-NBI. The balanced-NBI case is found to be intermediate between them.

The wider T_i pedestal width seen in the co-NBI discharge than that seen in the counter-NBI discharge may come from the difference in the E_r -shear layer. On the contrary, the local maximum in the dT_i/dr , which is seen just inside the E_r -well region in each co-, balanced and counter-NBI discharges, seems to be increased according to the increase in the $|dE_r/dr|$ as the direction of the momentum input changes towards counter-parallel to the plasma current.

Since the E_r is observed in a localized region just inside the separatrix of most H -mode plasmas where the E_r shear (and/or sheared $E \times B$ flow) is created and where the fluctuations decrease, the E_r structure seems to affect on the pedestal structures (and hence ELM affected areas). From figure 3, it is found that each $(Z_j e n_j)^{-1} \nabla p_j$, $-V_{\theta j} B_\phi$, $V_{\phi j} B_\theta$ term gradually decrease towards the deeper edge E_r -“well” formation up to the ELM event. At the time of the ELM, each quantity drops significantly and then undergoes a gradual recovery throughout the remainder of the ELM cycle. Although events that occur just after ELM (up to ~ 5 ms) cannot be resolved accurately due probably to unknown effect on the mixing between CXRS signal and background light, the change in the E_r structure due to the ELM was significant, such as shallower E_r -well with narrower E_r -shear layer.

A more detailed comparison among co-, balanced- and counter-NBI discharges, including the effect of the losses of fast ions on the edge E_r structure, is left to future work.

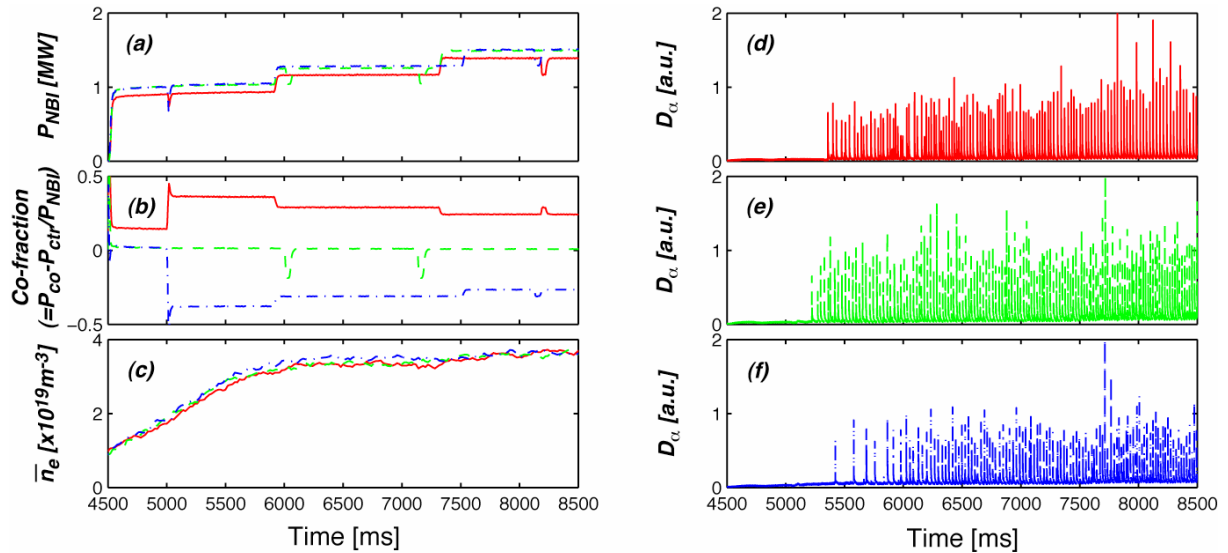


Fig. 1. ELMy H -mode discharges having Type-I ELMs on JT-60U for co- (solid line), balanced- (dotted line), and counter- (dash-dotted line) plus perpendicular-NBI heated plasmas: (a) NBI power (b) Co-fraction of NBI, (c) line-averaged electron density, (d~f) D_α emission from the chord viewing divertor region.

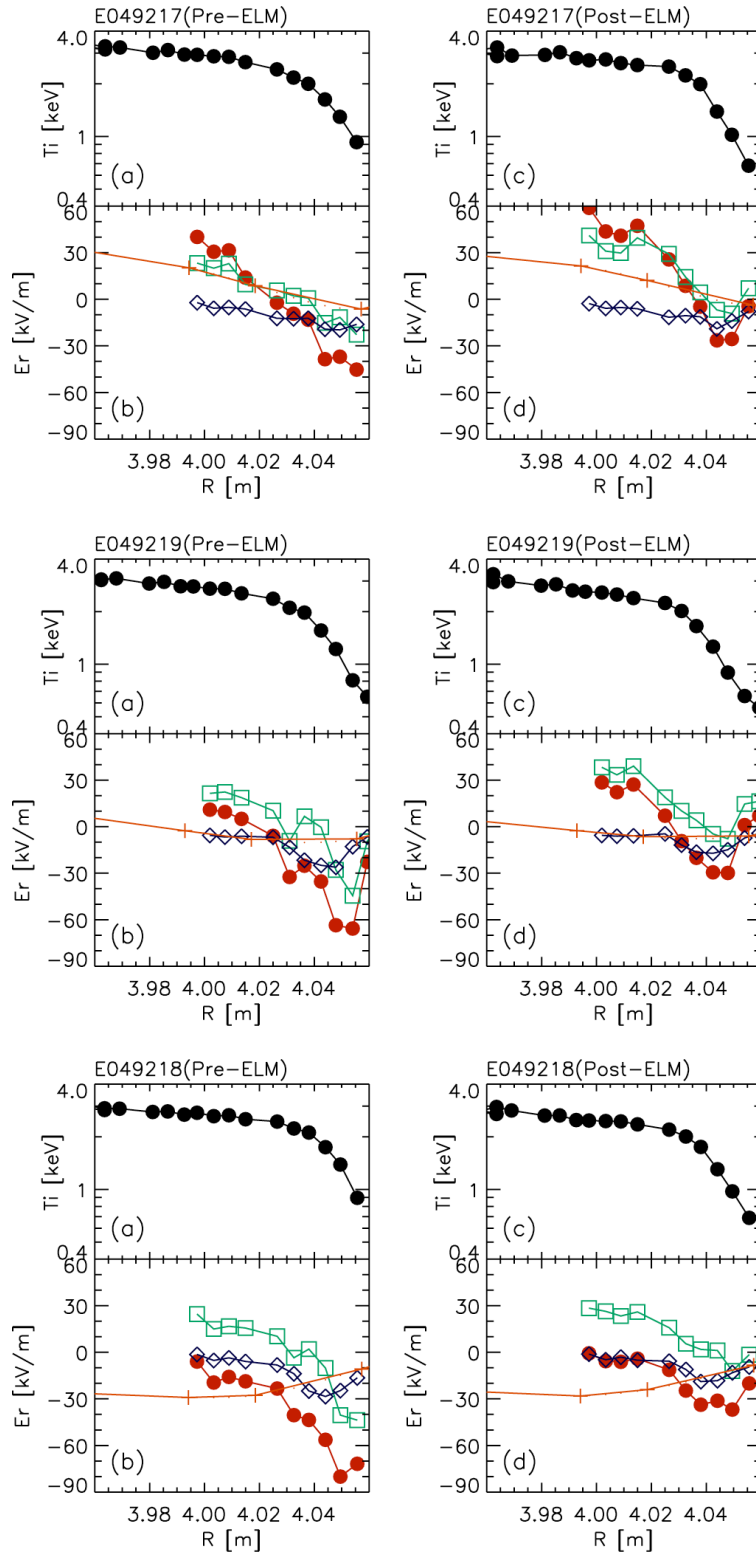


Fig. 2. Radial profiles of (a, c) the ion temperature T_i and (b, d) the E_r (circles), including $V_\phi B_\theta$ (plus symbols) $-V_\phi B_\theta$ (squares) $V_p/(Z_i n_i)$ (diamonds), comparing between pre-ELM (left) and post-ELM (right) for co- (top figures), balanced-NBI discharges (middle figures) and counter- (bottom figures).

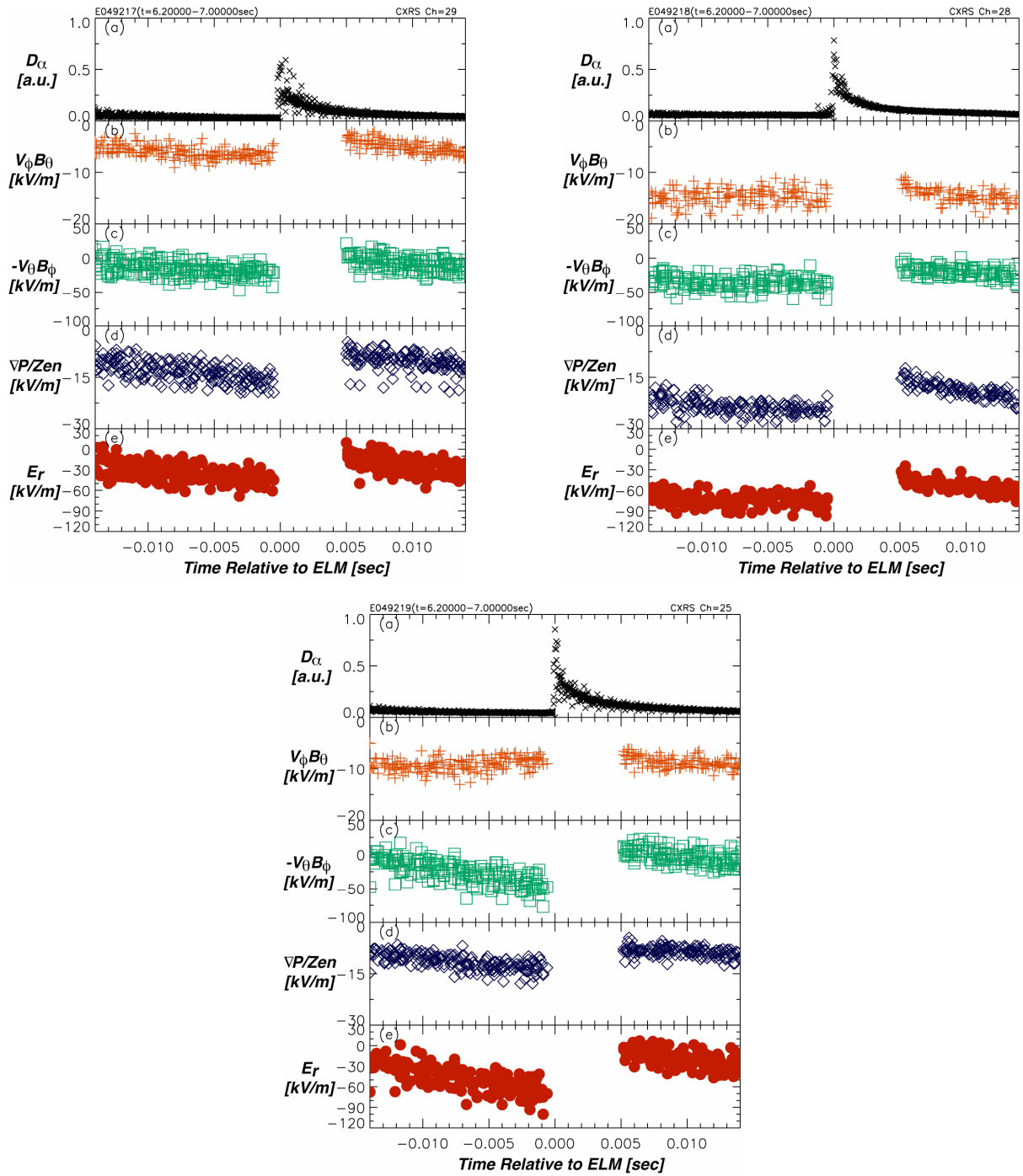


Fig. 3. Temporal evolution of (a) $V_\phi B_\theta$ (b) $-V_\theta B_\phi$ (c) $\nabla p / (Z_i n_i)$ terms in the radial force balance equation for the carbon impurity, (d) E_r , and (e) divertor D_α during ELM cycle constructed by mapping of multiple and reproducible ELM cycles onto a single time basis, defined by the time of the measurement relative to the ELM for co- (left-side for top figures), counter- (right-side for top figures) and balanced-NBI discharges (bottom figures).

References

- [1] Kamiya K., *et al.*, Plasma Phys. Control. Fusion **48**, A131 (2006).
- [2] Wade M., *et al.*, Phys. Plasmas **12**, 056120 (2005).

5.3 L to H-mode Transition Studies

K. Kamiya, K. Ida¹⁾ and Y. Sakamoto

1) NIFS

1. Introduction

The radial electric field has been considered to play a very important role in the decorrelation of the fluctuation and reduction of edge turbulent transport. Although the mechanism of confinement improvement due to suppression of a fluctuation by radial electric field shear has been intensively studied [1], the mechanism of formation and sustainment of radial electric field has not been clarified yet. The radial electric field, pressure gradient and plasma velocity perpendicular to the magnetic field are governed by the radial force balance equation; $E_r = (Z_j e n_j)^{-1} \nabla p_j - V_{\theta j} B_\phi + V_{\phi j} B_\theta$. Here, Z_j is the ion charge, n_j is the ion density, e is the magnitude of the electron charge, $p_j = n_j T_j$ is the ion pressure with T_j the ion temperature, $V_{\theta j}$ and $V_{\phi j}$ are the ion poloidal and toroidal rotation velocities, respectively, and B_θ and B_ϕ are the poloidal and toroidal magnetic fields, respectively. Recently 32 spatial channel charge exchange recombination spectroscopy CXRS with fast time-resolution up to 400 Hz (which corresponds to about ~ 2 ms considering the dead-time of the CCD frame transfer of $\tau_{\text{dead}} \sim 0.5$ ms) has been installed in JT-60U [2]. In this study, the edge impurity ion pressure gradient and rotation velocity are measured with new CXRS in the ELM-free *H*-mode discharge having two steps transition where a jump of ion temperature gradient precedes a jump of impurity poloidal rotation [3]. This review provides new information on the transition phenomenology in the *H*-mode discharge by means of the diagnostic upgrade described above.

2. Transition between intermediate H-phase and complete H-phase in ELM-free H-mode discharge

Figure 1 shows a time evolution of ion temperature gradient and radial electric field measured with the new CXRS system in the two step *H*-mode discharge with balanced neutral beam (NB) injection of $P_{\text{NB}} = 10$ MW on JT-60U (E049219; $I_p \sim 1.6$ MA, $B_\phi \sim 3.9$ T, $q_{95} \sim 4.2$, $\kappa/\delta \sim 1.43/0.34$ at $t \sim 5.0$ s). It is clear that the *L-H* transition occurs spontaneously at $t \sim 4.73$ s, indicating an abrupt drop in the D_α emission in addition to an increase in the time differential in the line-averaged electron density. The ion temperature profile also starts to form the pedestal structure as the E_r changes to be negative. Looking at the electron density and ion temperature profiles comparing between *L*-mode ($t \sim 4.6$ s) and *H*-mode ($t \sim 5.0$ s) phases, a steep gradient was clearly seen at around the E_r -shear region. The most striking feature is the generally expected local drop in the ion thermal diffusivity χ_i between *L*-mode ($t \sim 4.6$ s) and

H -mode ($t \sim 5.0$ s) phases by an order of magnitude. It is noted that the ion thermal diffusivity value of $\chi_i \sim 1$ m²/s at around the E_r -shear region at late phase (e.g. several hundreds millisecond after L - H transition) in the ELM-free H -mode on JT-60U seems to be similar that seen on DIII-D [4].

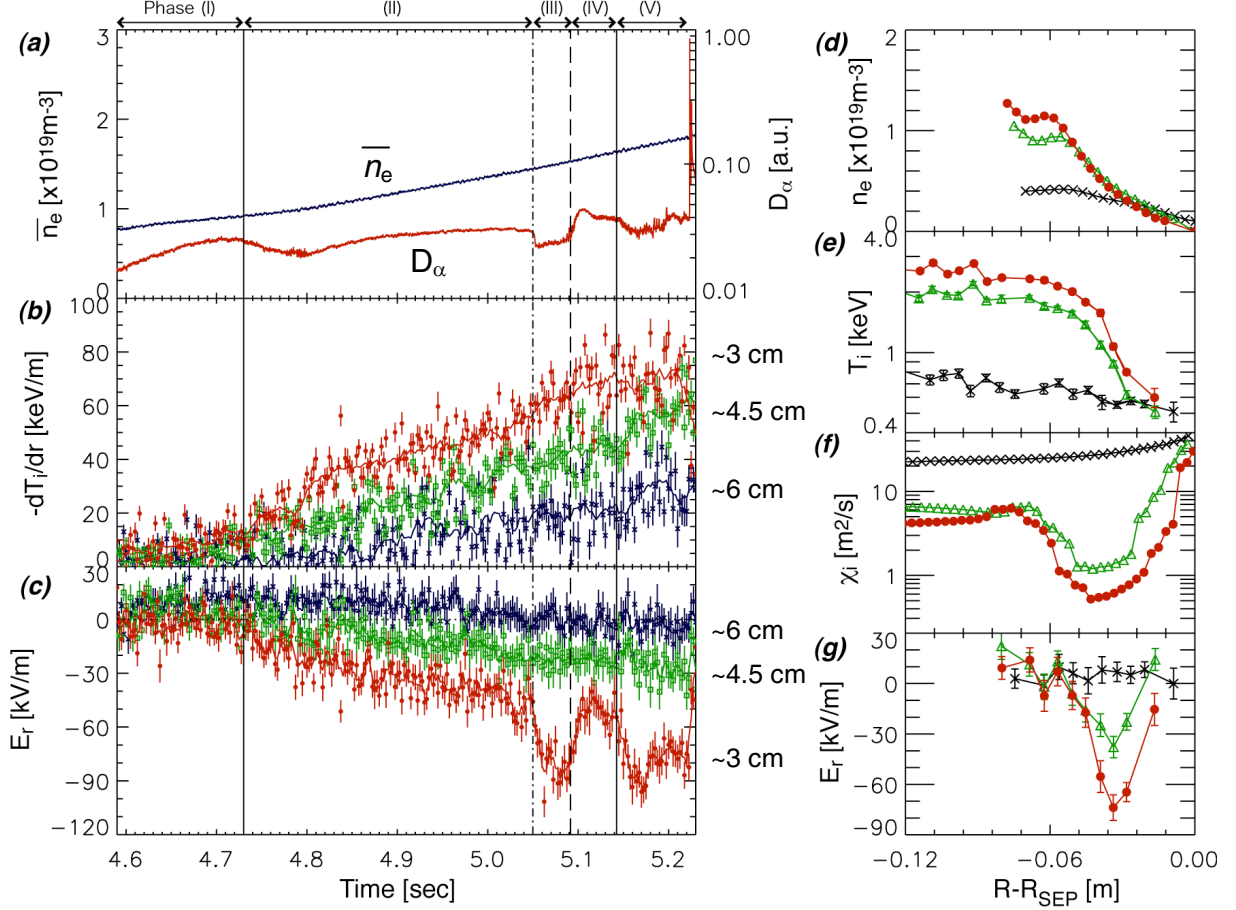


Fig. 1. Temporal evolution of (a) line-averaged electron density and emission, (b) ion temperature gradient $-\nabla T_i$ for ~ 3 cm, ~ 4.5 cm and ~ 6 cm inside the separatrix, (c) radial electric field E_r for ~ 3 cm, ~ 4.5 cm and ~ 6 cm inside the separatrix. The L to H transition, the two steps H -phase transition (H - H) times, including H - H back-transition, and the first ELM times are indicated by vertical lines, respectively. Radial profile of (d) electron density (LiBP), (e) ion temperature (CXRS), (f) ion thermal diffusivity and (g) radial electric field for $t = 4.6$ s (x symbols), 5.0 s (triangles) and 5.07 s (filled circles) are also plotted.

After a L - H transition, the plasma exhibits a smooth transition within a time-scale of about ~ 50 ms as the ion temperature gradient buildup associated with the E_r formation. For the measured carbon impurity ion ($Z_j = 6$), a negative “well” shape of E_r in the edge region is maintained by the both $\nabla p_j / (Z_j n_i)$ and $-V \times B$ terms with an almost similar magnitude of about $\delta E_r \sim 20$ kV/m, respectively (and hence, E_r -well of about -40 kV/m was seen at $t \sim 5.0$ s), as shown in figure 2. It is noted that the both $-V_{\theta j} B_\phi$ term and $V_{\phi j} B_\theta$ term are negative, and the

former is only larger than the latter by approximately a factor of two. The toroidal flow V_{ϕ_j} towards counter direction to the plasma current even in the balanced NBI discharge, which seems to be generated spontaneously, is associated with the change in the $E \times B$ flow direction toward toroidal direction due to lower parallel viscosity during this phase.

A faster and deeper drop in the D_α emission within less than a few millisecond was observed at $t \sim 5.0525s$, exhibiting a rapid change in the E_r -well structure toward more negative direction by approximately a factor of two. As shown in figure 2, the more negative E_r -well formation toward -80 kV/m (or more negative) is maintained by the dominant $-V_{\theta_j}B_\phi$ term for the carbon impurity ion.

This observation shows there are two discrete phases with different magnitude of radial electric field in the H-phase; one is the intermediate H-phase having the large ion temperature gradients without significant poloidal rotation of impurity species (and with moderate magnitude of radial electric field), and the other is the complete H-phase characterized by the large radial electric field. The most important point is that there is a bifurcation branch in terms of the E_r between two discrete H-phases (so-called H-H transition), which indicates not only moderate to large E_r transition (*i.e.* as seen at $t \sim 5.0525s$ and $\sim 5.1425s$) but also large to moderate E_r transition (not to L-mode back-transition as seen at $t \sim 5.09s$).

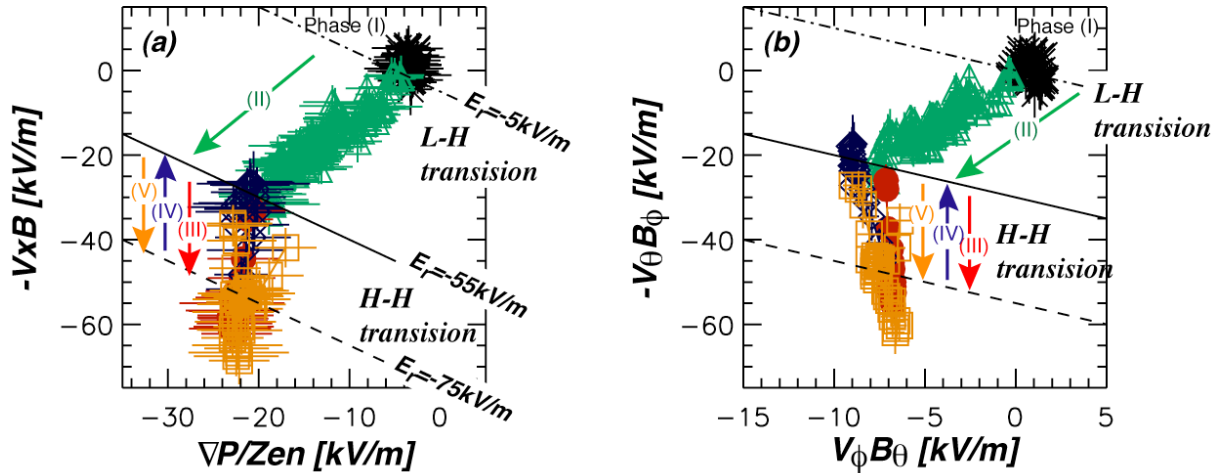


Fig. 2. (a) Contributions of $V \times B (= -V_{\theta_j} B_{\phi} + V_{\phi_j} B_{\theta})$ term to the E_r in the radial force balance equation plotted as a function of $\nabla p_i / (Z_i e n_i)$ term and (b) $V_{\phi_j} B_{\theta}$ term plotted as a function of $-V_{\theta_j} B_{\phi}$ term for carbon impurity ions at ~ 3 cm inside the separatrix. Phase (I)~(V) corresponds to L-mode, intermediate H, complete H, intermediate H, and complete H phases, respectively (see figure 1).

We now focus on the implication of the experimental results for L - H transition theory [5], which gives a clear bifurcation condition as the normalized poloidal Mach number $U_{pm} \ll 1$, in addition to an approximate bifurcation condition as the normalized ion collisionality ν_i^* near unity. Where $U_{pm} = v_{E \times B} / v_{th}(qR/a)$, $\nu_i^* = \nu_{ii} R q / (v_{th} \epsilon^{3/2})$, ν_{ii} is the ion-ion

collision frequency, R is the major radius, q is the safety factor, $v_{th}=(2T/m_i)^{1/2}$ is the ion thermal speed with T_i the ion temperature and m_i the ion mass, and $\varepsilon=a/R$ is the inverse aspect ratio with a the minor radius. As shown in figure 3, the $L-H$ transition occurs at around $v_i^* \sim 1$ as seen in the almost all previous discharges on JT-60U [3]. Although the v_i^* continues to decrease after $L-H$ transition due to plasma heating under the edge transport barriers, the U_{pm} just increase smoothly keeping less than unity even after the pedestal structure developed well in the intermediate H -phase. This observation seems to be different from the conventional tokamak H -mode characteristic [6], in which the H -phase was only one characterized by $U_{pm} \approx 1$ against $U_{pm} < 1$ in the L -phase. However there is a large sudden increase in the U_{pm} toward greater than unity at the $H-H$ transition toward complete H -phase, keeping the critical v_i^* constant, as predicted by a theory (which seems to be more likely to the conventional tokamak H -mode characteristic). After a transition, both density and temperature gradient re-start to increase further, and hence v_i^* decrease, keeping U_{pm} constant greater than unity. In contrast to the $H-H$ transition toward the complete H -phase, both U_{pm} and v_i^* decreased at the $H-H$ transition toward intermediate H -phase, while the 2nd $H-H$ transition from intermediate to complete H -phase at $t \sim 5.1425s$ takes place at almost same point in the $U_{pm} - v_i^*$ space as the 1st $H-H$ transition from intermediate to complete H -phase at $t \sim 5.0525s$.

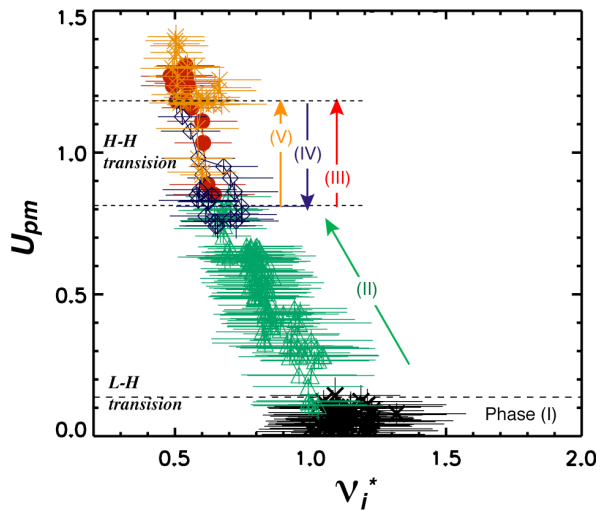


Fig. 3. Poloidal Mach number U_{pm} plotted as a function of v_i^* for bulk ions.

References

- [1] Moyer R. A. et al., Phys. Plasma **2**, (1995) 2397.
- [2] Sakamoto Y. et al., this issue, Sec. 10.8.
- [3] Fukuda T. et al., Plasma Phys. Control. Fusion **36**, A87 (1994).
- [4] Stacey W. M. and Groebner R. J., Phys. Plasma **14**, 012501 (2007).
- [5] Shaing K. C. et al., Phys. Rev. Lett. **63**, 2368 (1989).
- [6] Burrell K. H. et al., Plasma Phys. Control. Fusion **34**, 1859 (1992).

5.4 Fast Dynamics of Type I and Grassy ELMs [1]

A. Kojima, N. Oyama, Y. Sakamoto, Y. Kamada, H. Urano, K. Kamiya, T. Fujita, H. Kubo, N. Aiba and the JT-60 Team

In order to understand the physics of the ELM triggering and determining the ELM size, the fast ELM dynamics of type I and grassy ELMs have been studied in JT-60U H-mode plasmas. The profiles of the pedestal electron density and the pedestal ion temperature are investigated by use of the new fast diagnostics with high spatial and temporal resolutions such as a lithium beam probe ($\Delta t \sim 0.5$ ms) and a charge exchange recombination spectroscopy ($\Delta t \sim 2.5$ ms). Then, the dynamics of the density, the ion temperature and the ion pressure in the ELM cycle are studied.

The behavior of the pedestal density profile during an ELM cycle is obtained in the type I ELM phase. Before the ELM crash, the density profile has the pedestal structure with the density pedestal width of 4-5cm. After the ELM crash, the pedestal structure is collapsed and the ejected particle flux causes the heat load to the divertor target. Then the recycling outflow from the divertor target increases the edge density around the separatrix. The drop of the line-integrated electron density occurs after the density collapse.

The evolution of the pedestal ion pressure profile during an ELM cycle is evaluated for the first time by detailed edge profile measurements. The co- and counter(ctr)-rotating plasmas are compared for the understanding of the toroidal rotation effects. The co-rotating plasmas with the type I ELMs exhibit the larger and wider ELM affected area ($\Delta n_{\text{ped}}/n_{\text{ped}} \sim 30\%$, radial extent >15 cm) than ctr-rotating plasmas ($\Delta n_{\text{ped}}/n_{\text{ped}} \sim 20\%$, radial extent ~ 10 cm). Just before the type I ELM crash, the pedestal ion pressure and its maximum gradient in the co-rotating plasmas are 20% and 12% higher than those in the ctr-rotating plasmas, respectively. It is found that the radial extent of the ion pressure gradient at the pedestal region in the co-rotating plasmas is 14% wider than that in the ctr-rotating plasmas. The experimental results suggest that the ELM size is determined by the structure of the plasma pressure in the whole pedestal region.

As for the dynamics of grassy ELMs, the collapse of density pedestal is smaller ($< 20\%$) and narrower (~ 5 cm) than those of type I ELMs, as observed in the collapse of the pedestal electron temperature. The density pedestal is almost same width and height in the case of the same plasma current. The significant difference between grassy and type I ELMs is the density around the separatrix. In type I ELM, the separatrix density increases due to the enhanced recycling from the divertor. However, grassy ELMs cause no increase of the separatrix density, which is consistent with the small heat load to the divertor plate. It is confirmed that both conductive and convective losses due to grassy ELMs are small. Increasing the frequency of the grassy ELM decreases the ELM size and ELM affected area.

Reference

[1] A. Kojima et al., submitted to Nucl. Fusion.

5.5 Transport Modeling between ELMs [1]

N. Hayashi, T. Takizuka, N. Aiba, N. Oyama, T. Ozeki, S. Wiesen¹⁾, V. Parail²⁾

1) Euratom FZJ Association, 2) Euratom UKAEA Fusion Association

Edge localized modes (ELMs) induce sometimes very large heat load to divertor plates and cause the reduction of plate lifetime. The ELMs, however, are expected to sustain a H-mode plasma without the accumulation of impurities. The ELM cycle consists of two phases: an ELM crash by the MHD instability inducing energy and particle losses from the pedestal plasma and a quiescent phase recovering the pedestal pressure between ELMs (inter-ELM phase). A multi-machine analysis shows that the inter-ELM transport increases with collisionality. Although an effect of the neoclassical transport on the inter-ELM transport have been discussed, the physical understanding and the quantitative evaluation are, however, not fully accomplished so far.

The ELM cycle has been studied by using an integrated core transport code TOPICS-IB. The TOPICS-IB is based on the 1.5D core transport code TOPICS which is extended to the integrated simulation for burning plasmas. For the ELM study, the TOPICS-IB is integrated with a stability code for peeling-ballooning modes MARG2D and a dynamic 5-point model of scrape-off-layer (SOL) and divertor plasmas. The integrated code reproduces a series of ELMs with the following characteristics. The ELM energy loss increases with decreasing collisionality and the ELM frequency increases linearly with the input power, as seen in experiments of type-I ELMs. A transport model with the neoclassical transport in the pedestal connected to the SOL parallel transport reproduces a lowered inter-ELM transport in the case of low collisionality so that the ELM loss power is enhanced as observed in experiments. The inter-ELM energy confinement time evaluated from simulation results agrees with the scaling based on the JT-60U data.

In experiments, the electron transport is reduced to the ion neoclassical level in the pedestal region and thus the electron transport is still governed by the anomalous transport. Since the present model uses the ion neoclassical transport model in the pedestal region not only for ions but also for electrons, the neoclassical-type transport for electrons results in the agreement between the simulation results and the JT-60U scaling of the inter-ELM energy confinement time. Key physics of the JT-60U scaling will be examined by artificially modifying the simulation model.

Reference

[1] N. Hayashi, et al., Proc. 22nd IAEA Fusion Energy Conference, TH/P9-14 (2008); submitted to Nucl. Fusion.

5.6 Characteristics of QH-mode with Edge Co-rotation in JT-60U

Y. Sakamoto, P. Gohil¹⁾, N. Oyama, K. Kamiya, H. Urano

1) General Atomics

1. Introduction

The ELMy H-mode operation is intended as a standard scenario for ITER. However the most significant concern is that the ELMs release high levels of heat and particle fluxes into the scrape-off layer, which would cause rapid erosion of the divertor target plates in next-step devices such as ITER. The quiescent H-mode (QH-mode), discovered in the DIII-D tokamak [1], is one of the alternative H-mode regimes in a low collisionality region, which has a possibility to solve the heat and particle loads on the divertor. The characteristic MHD activity in QH-mode plasmas is multi-harmonic edge MHD activity called edge harmonic oscillations (EHOs), which have usually been observed instead of ELMs. After the discovery in DIII-D, QH-mode was observed in ASDEX-U [2], JET [3] and JT-60U [4]. The original key requirements for producing the QH-mode are neutral beam injection in the direction opposite to the plasma current (CTR-NBI) and a sufficiently large outer mid-plane gap between the separatrix and the first wall on the low field side (GAPOUT). On the other hand, QH-mode without CTR-NBI was observed in JT-60U, though the edge toroidal rotation was in the direction opposite to the plasma current [5]. Most recently, QH-mode with edge co-rotation and its strong shear has been produced in DIII-D [6]. Based on these experimental results, new experiments in JT-60U were performed as one of the ITPA joint experiment with

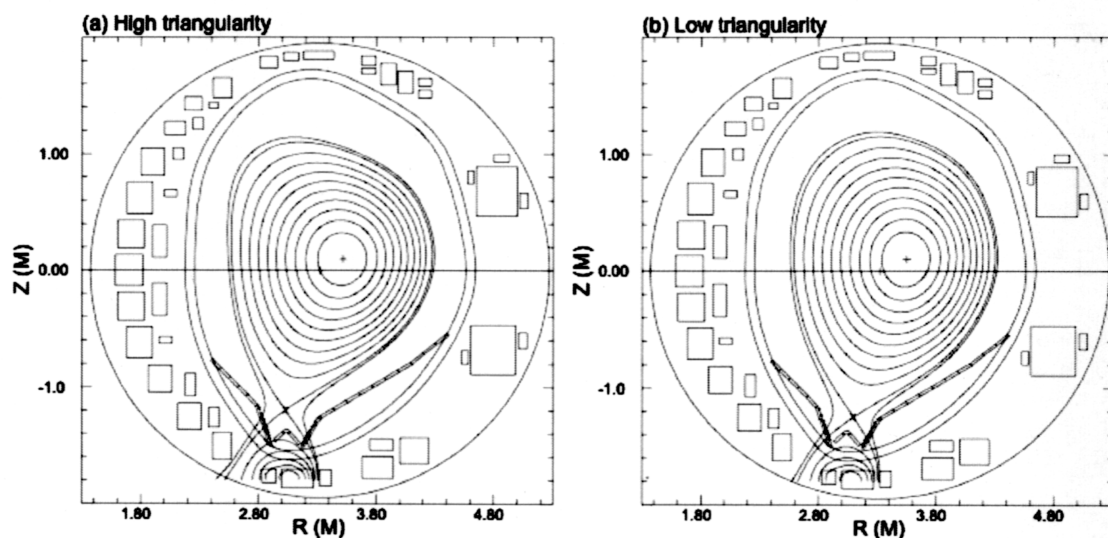


Fig.1 Plasma configuration used for QH-mode experiments in the cases of (a) high triangularity of 0.4 and (b) low triangularity of 0.28.

DIII-D. This report describes the QH-mode experiments performed in JT-60U to examine the effects of triangularity and to obtain QH-mode with co-rotation at the edge.

2. Experimental results

Since the DIII-D experiments indicate that high triangularity configuration enables to expand the operation region of QH-mode into higher pedestal pressure, we have attempted to produce QH-mode plasmas in high triangularity configuration. Figure 1(a) shows the plasma configuration used in the experiment. In order to produce the QH-mode in high triangularity configuration, we have performed GAPOUT scan, torque scan (CO or CTR) and NNB injection for lower particle fueling. As the result, partial QH-mode phase was observed with CTR-NBI, while no QH-mode phase was obtained with CO-NBI. Pedestal pressure in the

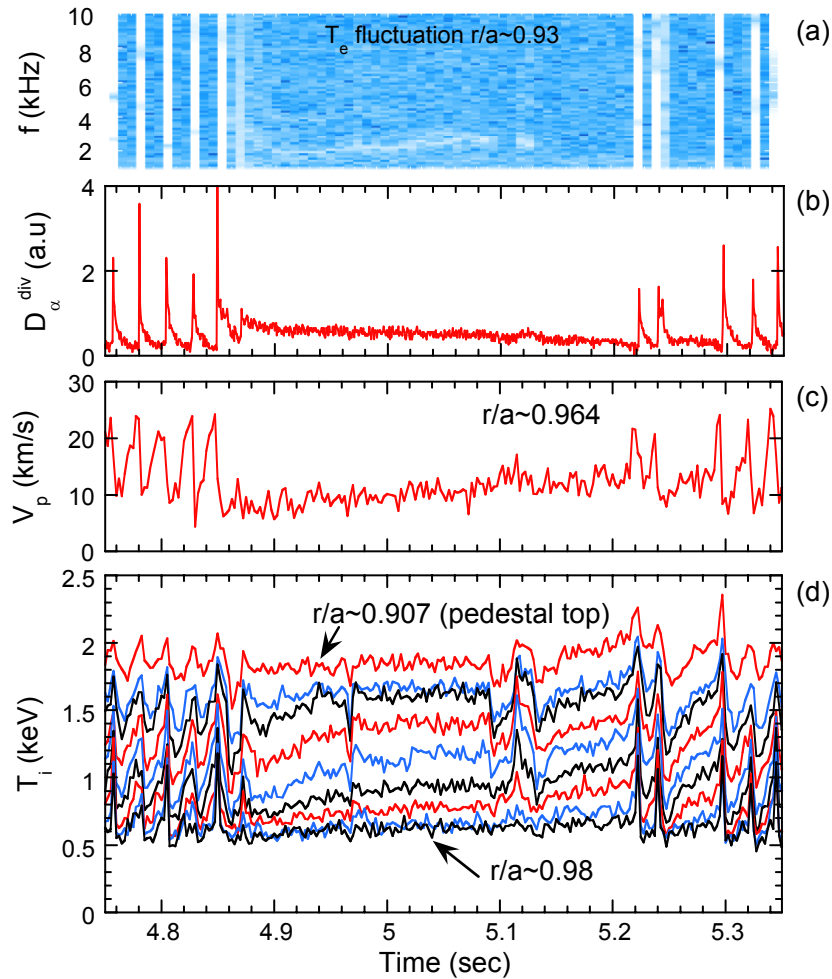


Fig.2 Waveforms of QH-mode produced by CO-NBI. (a) Fluctuation of electron temperature at $r/a \sim 0.93$, which shows EHO during QH-mode phase. (b) D_α signal from divertor region. (c) Poloidal rotation velocity at $r/a \sim 0.964$. (d) Time evolution of ion temperature at the pedestal region.

high triangularity configuration ($\delta \sim 0.4$) is almost similar to or slightly lower than that in the low triangularity configuration ($\delta \sim 0.28$). This result indicates that there is no strong effect of triangularity to pedestal pressure in the δ range from 0.28 to 0.4. Although the reason for the difficulty of getting QH-mode with high triangularity is not fully understood, there is a possibility of an influence of different gaps on getting QH-mode, where high triangularity configuration has wider gap between the separatrix and the first wall near the outer top and near the outer baffle plate, compared to low triangularity configuration, as shown in figure 1.

In the low triangularity configuration, on the other hand, continuous QH-mode was obtained with CTR-NBI as usual. Furthermore, partial QH-mode phase was appeared with CO-NBI. The waveforms of QH-mode with CO-NBI are shown in figure 2. Its duration without ELMs is nearly 0.4s, though clear EHO can be seen at $t=4.87 - 5.13$ s. The ELMy H-mode plasma enters QH-mode just after the ELM at $t=4.87$ s, where the ion temperature at the pedestal decreases together with the appearance of EHO. Then ion temperature gradually increases and saturates. The QH-mode phase was terminated by the appearance of ELM at $t \sim 5.22$ s, where the ion temperature and poloidal rotation rapidly increase just before the ELM. It is noted that the edge toroidal rotation is actually in the direction to the plasma current as shown in figure 3(a). This indicates that both CTR-NBI and counter-rotation are not essential requirements for producing QH-mode. Comparing the DIII-D results, where the strong toroidal rotation shear having difference between the pedestal top and separatrix toroidal rotation of ~ 100 km/s is required for producing QH-mode, the difference of toroidal rotation is much smaller in JT-60U. The interesting features can be seen in the time evolution of poloidal rotation shown in figure 2(c). The poloidal rotation increases in between ELMs with

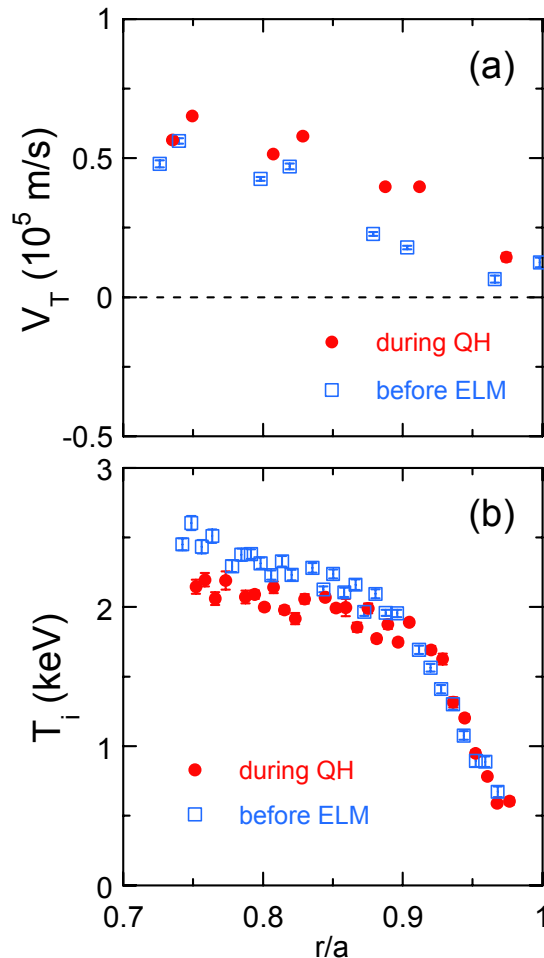


Fig. 3 Radial profiles of (a) toroidal rotation velocity and (b) ion temperature at the pedestal region ($0.7 < r/a < 1$) during QH-mode phase and just before ELM crash.

increasing ion temperature, and has maximum or minimum values just before or after ELM crash. This is reflected in the strong linkage between the radial electric field (E_r) and edge transport barrier (ETB) [7]. Note that the poloidal rotation at the beginning of QH-mode is comparable to that just after ELM crash, and then gradually increased, suggesting that E_r during QH-mode might be smaller than that just before ELM crash. The comparison of ion temperature profiles during QH-mode and just before ELM crash is shown in figure 3(b). Main difference is the width of ETB, which causes the difference of pedestal height. Detailed comparison of the ETB and E_r structure is future work.

3. Summary

QH-mode experiments were performed on JT-60U to examine the effects of triangularity and to obtain QH-mode with predominantly co-injected NBI. The results indicated that the high triangularity ($\delta \sim 0.4$) cases failed to obtain QH-mode with CO-NBI and only reached partial QH-mode with CTR-NBI. The low triangularity ($\delta \sim 0.28$) discharges, however, were able to obtain CO-NBI QH-mode phases for durations of nearly 0.4s. The edge toroidal rotation for this phase was positive and clear EHO activity was observed, though the toroidal rotation shear was not as large as observed in DIII-D.

References

- [1] Burrell, K. H. *et al.*, Bull. Am. Phys. Soc. **44**, 127 (1999).
- [2] Suttrop, W. *et al.*, Plasma Phys. Control. Fusion **45**, 1399 (2003).
- [3] Suttrop, W. *et al.*, Nucl. Fusion **45**, 721 (2005).
- [4] Sakamoto, Y. *et al.*, Plasma Phys. Control. Fusion **44**, A299 (2004).
- [5] Oyama, N. *et al.*, Nucl. Fusion **45**, 871 (2005).
- [6] Burrell, K. H. *et al.*, Phys. Rev. Lett. **102**, 155003 (2009).
- [7] Kamiya, K. *et al.*, Sec. 5.2 in this issue.

5.7 Analysis of Pedestal Characteristics in JT-60U H-mode Plasmas Based on Monte-Carlo Neutral Transport Simulation

Y. Nakashima¹⁾, Y. Higashizono²⁾, H. Kawano¹⁾, H. Takenaga, N. Asakura, N. Oyama, A. Kojima, and Y. Kamada

1) Plasma Research Center, University of Tsukuba,

2) Research Institute for Applied Mechanics, Kyushu University

In H-mode plasmas, neutral particles in the periphery region play a crucial role on pedestal formation near the transport barrier. Neutral transport simulation is one of the useful tools for the above research. The DEGAS ver.63 Monte-Carlo code [1] has been modified for fully three-dimensional simulation in the University of Tsukuba [2] and recently applied to JT-60U plasmas. A fully 3-dimensional neutral transport simulation using DEGAS was performed and the study of physical mechanism of pedestal formation was started [3].

The present mesh model for DEGAS simulation of JT-60U has been developed preserving the consistency with the mesh model of the UEDGE code. The precise mesh structure including main components in the divertor region such as isolated dome, baffle and divertor plates was built-up and the simulation space was extended from the vacuum chamber wall to core plasma region. In this study, a toroidal symmetry of particle source is given in order to focus the objective of the simulation on the characteristics of pedestal structure.

In two different ELMy H-mode plasmas, the plasma parameter dependence on the pedestal structure was investigated and the results were compared from the viewpoint of neutral penetration and ionization region. Comparison of the neutral density profiles between the high and low-density H-mode plasmas showed a noticeable increase in the penetration length of atomic density ($1/e$ scale length of the density at the boundary with far SOL region) is recognized in the low-density case. From the evaluation of the ionization profile near the edge transport barrier region, it is found that the determined ionization width (FWHM value) in the low-density case is wider than those in high-density case by 36 %. The present results on the density survey in pedestal and SOL regions showed that the density in the region from the pedestal to the SOL has a strong influence of neutral penetration into the core plasma region from LCFS as well as a significant effect on the ionization zone in this region.

The result of 3-D simulation carried out with gas puffing showed the considerable localization of neutrals around the gas puffer and the detail of neutral diffusion in toroidal and poloidal directions were clarified. The above-obtained results provide the useful aspect for pedestal physics and this analysis method also gives us important information for the 3-D plasma modeling in near future.

Reference

- [1] Heifetz, D., Post, D., Petravic, M., et al., *J. Comput. Phys.* **46**, 309 (1982).
- [2] Nakashima, Y., et al., *J. Plasma Phys.* **72**, 1123 (2006).
- [3] Nakashima, Y., et al., *Journal of Physics: Conference Series* **123**, 012029 (2008).

5.8 Effects of Edge Collisionality on ELM Characteristics in Grassy ELM Regime

N. Oyama, L.D. Horton¹⁾, A. Kojima, A. Isayama, K. Kamiya, H. Urano, Y. Sakamoto, Y. Kamada, N. Aiba and the JT-60 Team

1) EFDA-CSU Culham, Culham Science Centre

1. Introduction

Establishment of H-mode operation with small ELMs is one of the important and urgent issues for ITER. The grassy ELM regime found in JT-60U has been considered as one candidate for the H-mode operation with small ELMs, since grassy ELMs can be obtained in plasmas with low collisionality and low toroidal rotation [1]. Small ELMs similar to grassy ELMs observed in JT-60U have been reproduced in ASDEX Upgrade (AUG) as inter-machine experiments promoted by ITPA pedestal topical group [2]. As shown in Fig. 1, the grassy ELM like small ELMs in AUG was observed only for edge collisionality lower than unity [2], suggesting an importance of the edge collisionality (ν_e^*) to determine the ELM characteristic. It is noted that type II ELMs, which are other type of small ELMs observed in high density plasmas ($n_e/n_{GW} \sim 0.9$) at $q_{95} \sim 4$ in AUG, appears in higher ν_e^* region [3]. Based on these experimental results, new experiments were performed to understand the meaning of ν_e^* and to investigate the accessibility to type II ELMs in JT-60U.

2. Experimental Condition

The experiments were mainly performed with the toroidal magnetic field of $B_T = 2.5$ T for low q case ($q_{95} \sim 4.3$) and $B_T = 3.9$ T for high q case ($q_{95} > 6$) at the plasma current of 1.0 MA. The plasma triangularity (δ), which is one of the important parameters to obtain grassy ELMs, was higher than 0.5 and well inside the operational regime for grassy ELMs. The typical plasma configuration for ν_e^* scan experiments is shown in Fig. 2. In order to increase the edge ν_e^* , gas puffing of $5\text{-}20 \text{ Pa}\cdot\text{m}^3/\text{s}$ was applied during or before the main heating phase. Since the toroidal rotation in the direction counter to the plasma current is found to be favorable to

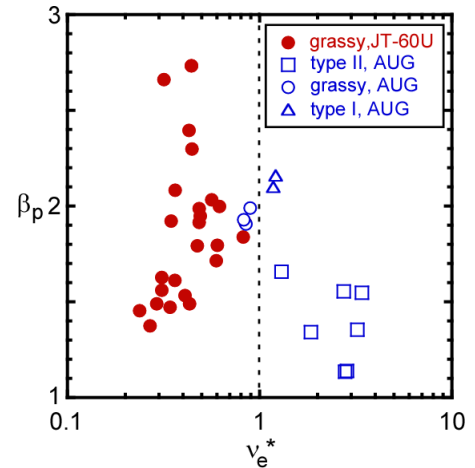


Fig. 1. Operational regime of grassy ELM in JT-60U and its comparison to AUG with double null configuration.

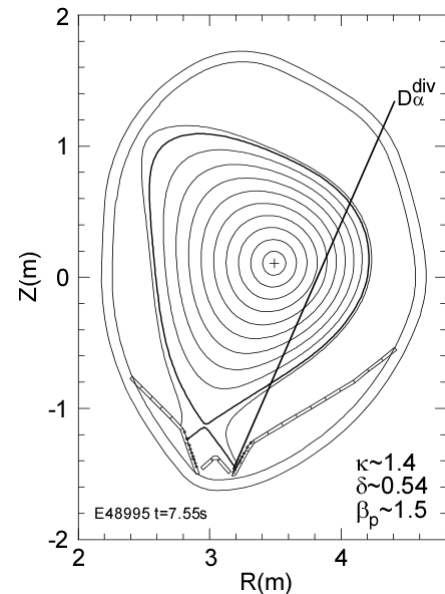


Fig. 2. Typical configuration for grassy ELM experiments.

obtain grassy ELMs, the combination of tangential and perpendicular NBIs was adjusted so as to obtain small toroidal rotation as expected condition in ITER.

3. Experimental Results

The behavior of grassy ELMs between low and high v_e^* is compared in Fig. 3. In the reference discharge at low v_e^* of 0.67 (E48995), typical grassy ELMs with the frequency of 850 Hz were observed in the plasma with $\beta_p \sim 1.5$. In the plasma with higher $v_e^* \sim 1.3$ by higher recycling due to an additional gas puffing (E49040), on the other hand, the amplitude of ELMs increased together with the reduction of the ELM frequency (f_{ELM}) to ~ 500 Hz. As shown in Fig. 3(b) and (d), no detectable losses in the plasma stored energy (W_{dia}) are observed in both cases, suggesting both ELMs are categorized as grassy ELMs with small ELM energy loss. It is noted that the achieved pedestal pressure in both discharges are similar ($P_e^{\text{ped}} \sim 1.9$ kPa in E48995 and 2.1 kPa in E49040). The pedestal temperature in high v_e^* plasmas was lower while the pedestal density was higher than that in low v_e^* plasmas.

In plasmas shown in Fig. 3, the toroidal rotation frequency evaluated at the top of T_i pedestal was not the same, -1.3 kHz in E48995 and -0.79 kHz in E49040. According to the previous experimental results about f_{ELM} dependence on the plasma rotation [1], this small difference of the rotation frequency can cause a difference in f_{ELM} by about 100-200 Hz. However, the observed difference in f_{ELM} was about twice larger than this value and so that it is considered that the difference is not due to the f_{ELM} dependence on the plasma rotation. In addition, when we compare with the other plasma with the same rotation frequency of -1.3 kHz (but, $\beta_p \sim 1.8$ and $v_e^* \sim 0.94$), the f_{ELM} was ~ 620 Hz and the similar ELM characteristics to those in E49040. Although the NB heating power of 18.7 MW in E49040 was higher than that of 13.3 MW in E48995, the ELM frequency was smaller in E49040. These experimental observations suggest that the ELM amplitude of divertor D_α signal in grassy ELM regime

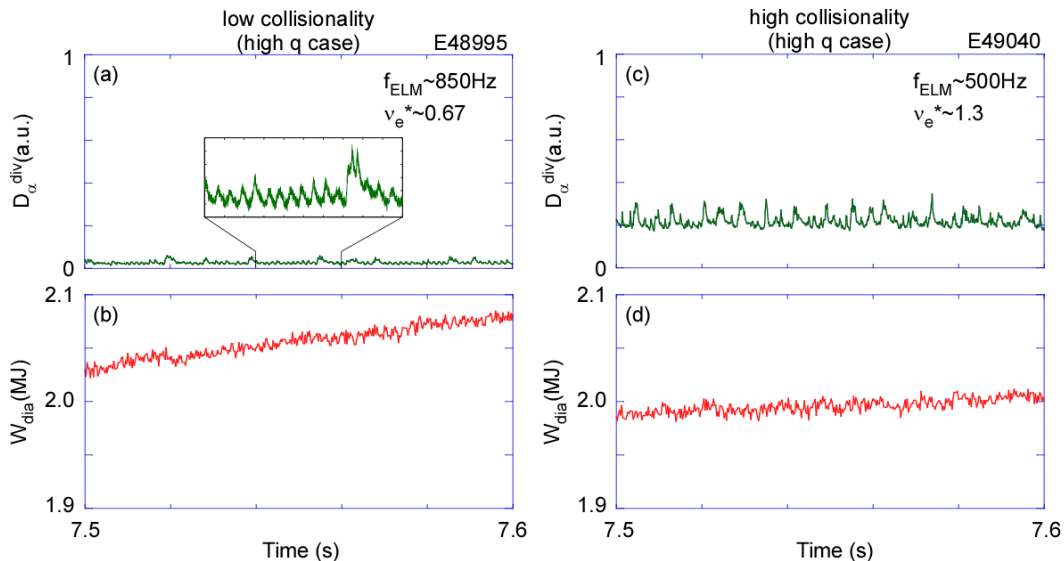


Fig. 3. Comparison of (a),(c) divertor D_α signal at outer strike point (see Fig. 2) and (b),(d) plasma stored energy between low and high collisionality plasmas in high q case.

increases with increasing v_e^* toward unity.

For the comparison between grassy ELMs and high v_e type II ELM observed in AUG, responses of ELMs in $q_{95} \sim 4$ on the v_e^* are also investigated as shown in Fig. 4. In the reference discharge (E49001) at low v_e^* of 0.37, the toroidal rotation frequency of ~ 0 kHz and $\beta_p \sim 1.5$, regular ELMs with $f_{\text{ELM}} \sim 200$ Hz were observed. Although the f_{ELM} was four times smaller than that in high q case, observed difference in f_{ELM} between high and low q_{95} cases can be explained by the ELM frequency dependence on the toroidal rotation frequency. Corresponding to smaller f_{ELM} , the amplitude of ELMs in divertor D_α signal was larger than that in high q case. Even in the ELMs having this level of amplitude no detectable losses in W_{dia} are observed as shown in Fig. 4(b).

In the plasma with higher $v_e^* \sim 1.0$, both ELM frequency and amplitude increased as shown in Fig. 4(d). It is noted that the toroidal rotation frequency, total β_p and the pedestal pressure are the same between high and low v_e^* plasmas shown in Fig. 4. In contrast to other cases, however, clear reduction of the plasma stored energy was observed in some large ELMs as indicated by dotted lines in Fig. 4(e). Since the ELM energy loss in these large ELMs is comparable to those in type I ELMs, these large ELMs seem to be type I ELMs. In between these type I ELMs, grassy ELMs with larger amplitude (but, no detectable loss in W_{dia}) were observed.

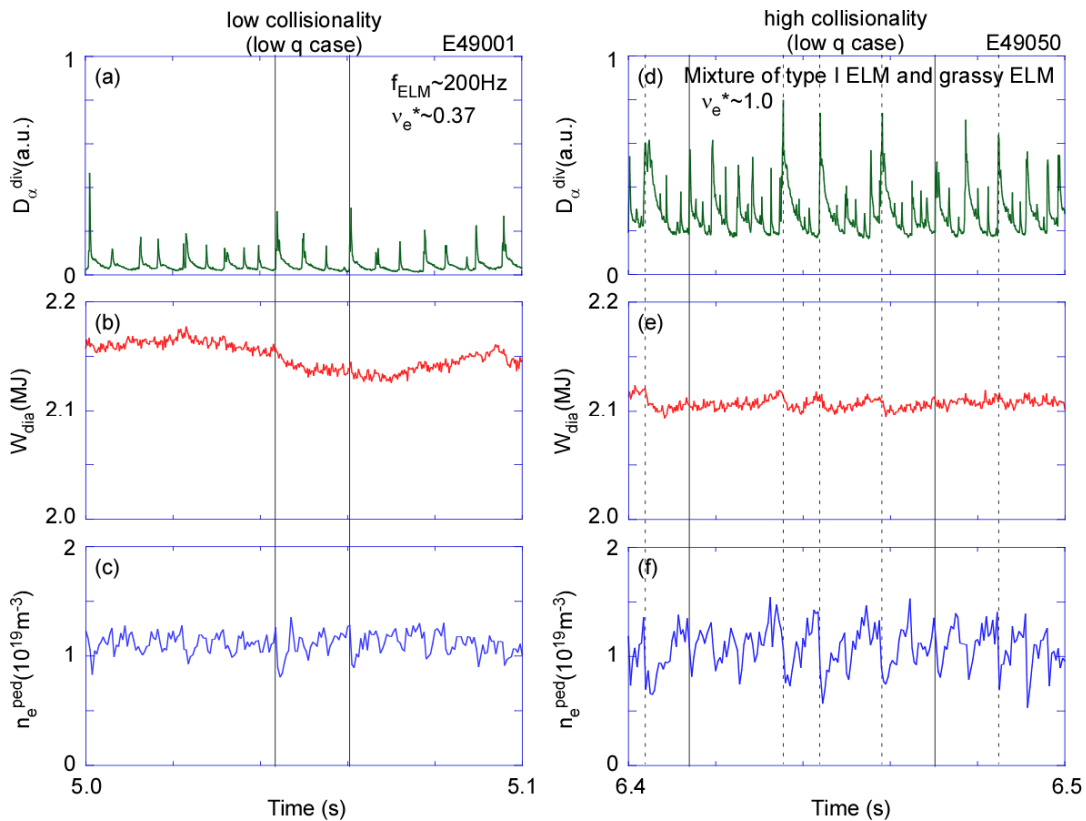


Fig. 4. Comparison of (a),(d) divertor D_α signal at outer strike point (see Fig. 2), (b),(e) plasma stored energy, and (c), (f) electron density at the pedestal between low and high collisionality plasmas in low q case. Note that the location of density measurement is not the top of pedestal. Thin lines show a comparison of some ELMs with similar amplitude of D_α signal.

Since the intensity of divertor D_α signal is only a measure of ELM size, the direct measurements of edge plasma parameters are important for a quantitative evaluation of such small energy losses due to grassy ELMs. In addition to the local temperature measurement using ECE heterodyne radiometer, fast edge density profile measurement using a lithium beam probe has been performed in JT-60U [4]. It is confirmed that the reduction of the electron density at the pedestal (not the top of the pedestal) is related to the intensity of divertor D_α signal. As shown by thin line in Fig. 4, similar density losses were observed in some ELMs having the similar D_α intensity. Therefore, it is considered that the larger D_α intensity observed in higher v_e^* plasmas means the larger ELM energy loss.

The accessibility to type II ELMs was also investigated in a series of v_e^* scan. However, type II like ELMs were not observed so far. When too much gas puffing was applied during the main heating phase, the pedestal pressure was degraded together with the appearance of type III ELMs.

4. Summary and Discussion

The effects of edge collisionality on ELM characteristics have been investigated in grassy ELM regime. Both in high and low q regimes ($q_{95} > 6$ and $q_{95} \sim 4.3$), ELM amplitude increases with increasing the edge collisionality toward unity. This collisionality dependence is opposite to the dependence observed in type I ELM regime, where the ELM amplitude decreases with increasing the edge collisionality. Thus, it can be considered that low edge collisionality is one of the required conditions for grassy ELMs. Further analysis including edge stability analysis will reveal the physics mechanism for the different collisionality dependence of ELM amplitude in grassy ELM regime.

Since low edge collisionality has been expected in next step devices such as ITER, observed collisionality dependence in grassy ELM regime is undoubtedly favorable in terms of the ELM heat loads toward divertor target plates. Therefore, further studies to expand the operational regime of grassy ELMs are strongly encouraged in parallel with the development of active ELM control methods.

Reference

- [1] Oyama, N., *et al.*, Plasma Phys. Control. Fusion **49**, 249 (2007).
- [2] Oyama, N., *et al.*, Plasma Phys. Control. Fusion **48**, A171 (2006).
- [3] Stober, J., *et al.*, Nucl. Fusion **45**, 1213 (2005).
- [4] Kojima, A., *et al.*, submitted to Nucl. Fusion.

5.9 Effect of Toroidal Rotation on Pedestal and H-mode Performance in JET/JT-60U Similarity Shape

N. Oyama, G. Saibene¹⁾, V. Parail²⁾, H. Urano, J. Lönnroth³⁾, Y. Kamada, Y. Sakamoto

1) Fusion for Energy

2) Euratom/UKAEA Fusion Association

3) Association Euratom-Tekes, Helsinki University of Technology, Finland.

1. Introduction

Inter-machine comparison is a very powerful tool to identify the physics mechanism determining the plasma behavior, as well as a way to validate the physics assumptions at the basis of physics based scalings used for the prediction of the plasma parameters of ITER. In 2005-2006 experimental campaign, dedicated ripple experiments have been performed in JET and JT-60U using a matched plasma shape [1]. After the installation of FSTs in JT-60U, the amplitude of the toroidal field (TF) ripple, δr , near the outer midplane was reduced to $\sim 0.5\%$ at the toroidal magnetic field (B_T) of 2.2 T. In JET, on the other hand, δr can be varied by selecting the appropriate differential current between odd and even set of coils out of 32 TF coils, providing in this case four levels of $\delta r = 0.1\%$, 0.5% , 0.75% and 1% . Although the same level of ripple amplitude at the outer midplane was successfully obtained in both devices, the toroidal rotation (V_T) in JET was still higher than that in JT-60U due to a different level of fast ion losses. A series of power and density scans in the previous experiments indicated that plasmas with lower δr and/or larger co- V_T are favorable to achieve higher p^{ped} and H_H factor in both devices. In order to expand the dynamic range of V_T to confirm observed rotation effect in JT-60U, new experiments were performed, since no data from counter-rotating plasmas were obtained in the previous experiments. In addition, effect of negative-ion based NBI on the pedestal performance was also investigated.

2. Experimental Result

The experiments were mainly performed with plasma parameters of $B_T = 2.2$ T and the plasma current of 1.08 MA, where the ripple reduction by ferritic steel tiles (FSTs) are effective. As shown in Fig. 1, the toroidal variation of the toroidal magnetic field strength at the outer midplane indicates δr of about 0.5 % at $B_T = 2.2$ T. Figure 2 shows operational space in electron density and temperature at the top of pedestal during the power scan and

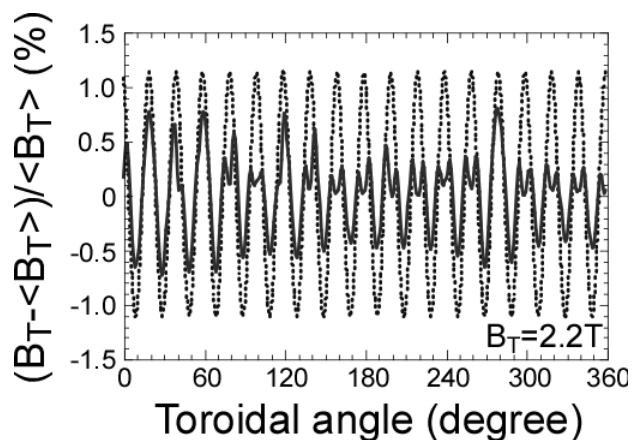


Fig. 1. Toroidal variation of the calculated toroidal magnetic field strength at $R = 4.3$ m and $Z = 0.2$ m. Solid (dotted) line indicates data with (without) FSTs.

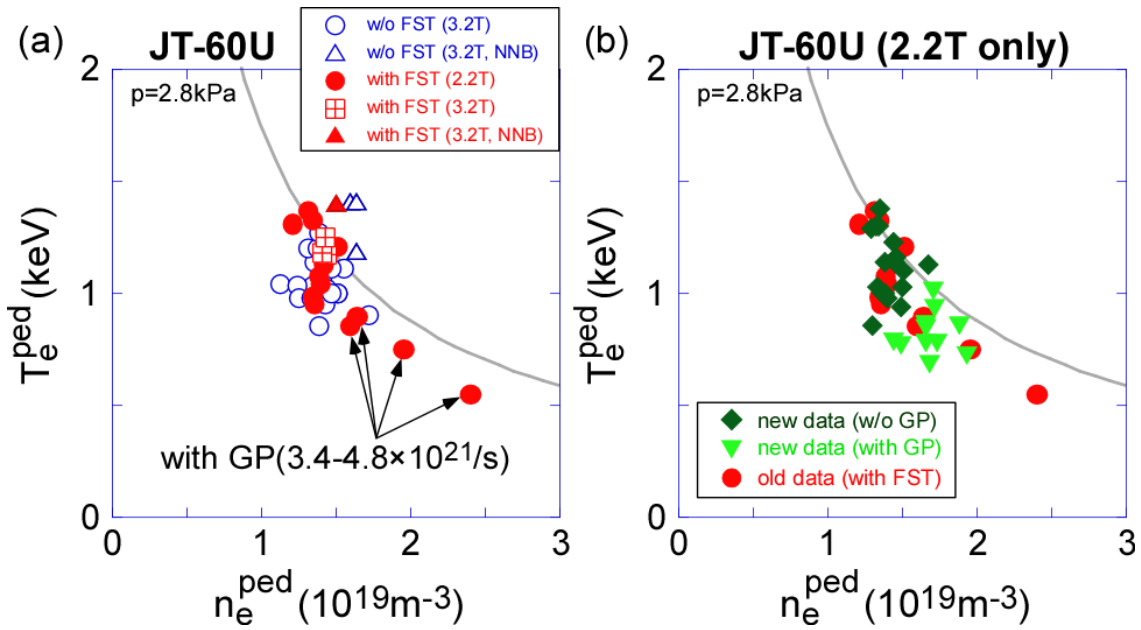


Fig. 2. Comparison of electron density and temperature at pedestal. (a) Previous dataset for comparison between plasmas with and without FSTs. (b) New data and corresponding old data obtained in $B_T = 2.2T$. Triangles show plasmas with gas puffing and/or with high recycling after plasmas with gas puffing.

density scan. The achievable electron pressure of 2.8 kPa was similar to that observed in the previous experiments as shown in Fig. 2(b). In order to increase the pedestal density, continuous gas puffing of $5-7 \text{ Pam}^3/\text{s}$ ($2.4-3.4 \times 10^{21}/\text{s}$) was also applied. The level of degradation with gas puffing was also similar to the previous experiments. Although the global behavior was similar to the previous experiments, ELM frequency was somewhat higher in this experiment.

In order to change the V_T at the top of T_i pedestal, two different ways were used. One is the change in the combination of tangential NBI so as to change the torque input. The other is the change in the number of units of perpendicular-NBI (perp-NBI) to change the loss of fast ions, which acts as an effective torque in the counter direction. Figure 3(a) compares the toroidal rotation profile during torque scan and power scan of perp-NBI. In case with co-NBI dominated case shown by circles, most of the plasma rotates in co-direction and V_T at the pedestal was close to zero. When the combination of tangential NBI was changed to balanced injection, flat and zero rotation was achieved with counter V_T at the pedestal. Then, by adding one perpendicular NBI to plasmas heated by balanced NBI, the plasma rotation profile shifted to further negative (more counter rotation) from edge to core. As the toroidal rotation becomes negative, ion temperature at the pedestal decreases as shown in Fig. 3(b). Corresponding to the reduction of T_i at the pedestal, core T_i is also reduced, suggesting the reduction of core confinement. It is noted that higher heating power plasma shows lowest pedestal temperature.

The total pedestal pressure ($p^{\text{ped}} = n_e^{\text{ped}} T_e^{\text{ped}} + n_i^{\text{ped}} T_i^{\text{ped}}$) evaluated with a spatially constant Z_{eff} is plotted as a function of toroidal rotation frequency in Fig. 4. New data obtained

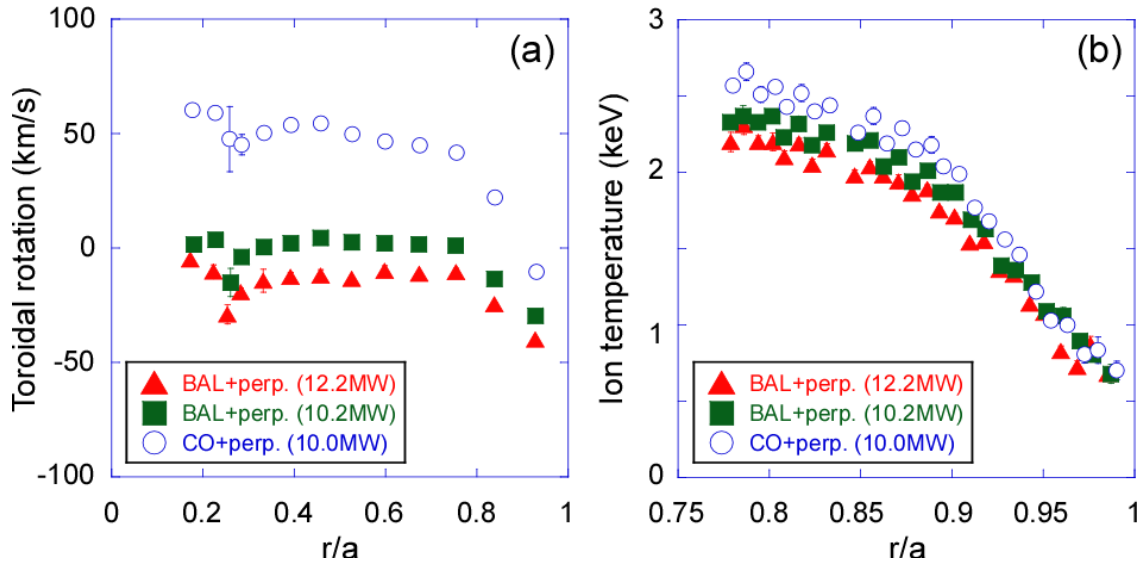


Fig. 3. Comparison of (a) toroidal rotation profile and (b) edge ion temperature profile. Fast ion losses are not subtracted from heating power.

in this experiment shows a clear trend that larger $\text{co-}V_T$ is favorable to achieve higher p^{ped} . It is noted that achieved pedestal pressure in counter rotating plasma ($V_T \sim -1.5\text{kHz}$) is the same between with and without FSTs, suggesting the effect of different TF ripple between 1.2% and 0.5% is smaller than the effect of toroidal rotation. The result is consistent with the dedicated ripple experiments in JT-60U [2].

Another interesting feature can be seen in Fig. 4. Looking at the data with gas puffing, achieved p^{ped} is scattered and does not show a trend that larger $\text{co-}V_T$ is favorable to achieve higher p^{ped} . The experimental result might suggest the role

of other parameter such as edge collisionality in determining the effect of toroidal rotation on the pedestal performance. Further analysis of the pedestal structure and edge turbulence will reveal the relation between gas puffing and V_T dependence.

In the past experiments, higher pedestal pressure was obtained when some perp-NBI units were replaced with N-NBI [3]. In order to understand the physics mechanism of improved pedestal performance with N-NBI, detailed pedestal measurement using new fast CXRS system was performed. In this experiment, however, no clear improvement of pedestal pressure was observed as shown in Fig. 4, while ELM frequency became lower than that in P-NBI heated

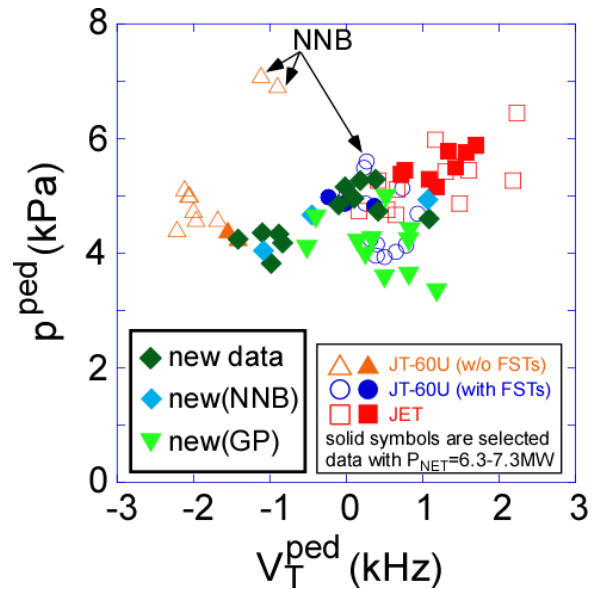


Fig. 4. Comparison of total pedestal pressure as a function of toroidal rotation frequency measured at T_i pedestal.

phase as observed in the previous experiments. So far, the improvement of the pedestal pressure with N-NBI was observed in high q series ($q_{95} \sim 5$). Detailed analysis of edge stability and comparison between high and low q regime will be needed for the further analysis of the effect of N-NBI on the pedestal performance.

3. Summary and Discussion

Dedicated H-mode experiments using a matched plasma shape were performed in JT-60U. The comparison of pedestal pressure between with FSTs ($\delta r \sim 0.5\%$) and without FSTs ($\delta r \sim 1.2\%$) suggests that the change in the TF ripple in this level does not affect pedestal performance significantly. On the other hand, a trend that larger $\text{co-}V_T$ is favorable to achieve higher pedestal p^{ped} is clearly observed. In recent ripple experiment in JET using JT-60U matched shape, no clear difference was observed during ripple scan from 0.08% to 1%. However, from dedicated ripple experiments in JET, no simple correlation between fast ion losses/torque/rotation and confinement explaining the JET results was found. Therefore, further analysis including modeling/simulation of edge transport due to TF ripple will be needed for better understanding of the effect of TF ripple and its extrapolation to ITER.

Reference

- [1] Oyama, N., *et al.*, Journal of Physics: Conference Series **123**, 012015 (2008).
- [2] Urano, H., *et al.*, Nucl. Fusion **47**, 706 (2007).
- [3] Saibene, G., *et al.*, Nucl. Fusion **47**, 969 (2007).

5.10 Effect of Edge EC Injection on Type I ELMs

N. Oyama, A Isayama, Y. Sakamoto, Y. Kamada

1. Introduction

In order to avoid instantaneous heat load transferred to divertor target plates due to ELMs, which has a potential to reduce the lifetime of the divertor material, various active ELM control methods have been proposed and applied in many tokamaks as reviewed in ref [1]. One of the alternative methods, which have not been considered in ITER so far, uses edge ECH. In ASDEX Upgrade, the modulation ECH at the plasma edge can modify the ELM frequency from ~ 150 Hz to the modulation frequency of 100Hz [2]. Although the mechanism of ELM triggering using ECH observed in ASDEX Upgrade has not been understood, similar effects have been observed with pure heating and with current drive, suggesting that the change in the edge pressure gradient term is main term. Since ITER organization recommends to develop new ELM control method, which can be applied to ITER, the effect of edge ECH on type I ELMs has been investigated in JT-60U.

2. Experimental results

2.1 Experimental conditions

Since the mechanism of the change in the ELM frequency observed in ASDEX Upgrade has not been understood, we have decided to increase the ratio of ECH power to NBI power as much as possible. Thus, second harmonic ($2\omega_{ce}$) X-mode ECH has been adopted for the experiment so as to reduce the toroidal magnetic field (B_T) and then to sustain type I ELMy H-mode plasmas with smaller heating power. In the case of low-field side (LFS) deposition, $I_p = 0.8$ MA and $B_T = 2.2$ T ($q_{9.5} \sim 5$) are used. On the other hand, $I_p = 0.95$ MA and $B_T = 1.7$ T ($q_{9.5} \sim 3.2$) are used in the case of high-field side (HFS) deposition.

The modulation frequency of the EC system has been increased from the requirement for NTM control. On the other hand, lowest modulation frequency was also limited to about 400 Hz due to the protection of EC system. The lowest modulation frequency is about 10 times higher than the natural ELM frequency observed in JT-60U in this regime. In the experiment, both continuous wave (CW) injection and modulated wave injection with 400 Hz have examined.

2.2 Edge EC injection at low-field side

The injection angle is determined so as to achieve a localized deposition within the pedestal. As shown in Fig. 1, EC deposition located at the upper-LFS of the plasma. In this condition, 1.6 MW of EC power (CW case) from three gyrotrons is deposited at $r/a = 0.9-1.0$, resulting localized ECCD of 0.9 kA. The bootstrap current at the pedestal is evaluated as 50 kA by ACCOME code.

Figure 2 shows wave forms in the case of edge EC injection at the LFS. Before EC injection,

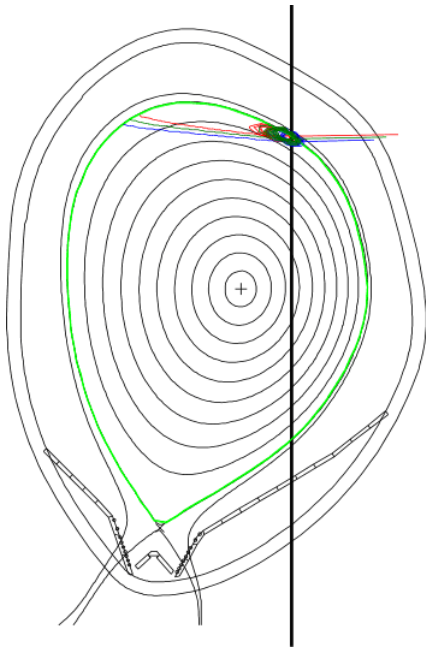


Fig. 1. EC depositions in FS case evaluated by ray tracing code. Three rays from the bottom correspond to EC #1, #2 and #3. Vertical solid line indicates cold resonance for $2 \omega_{ce}$ X-mode ECH.

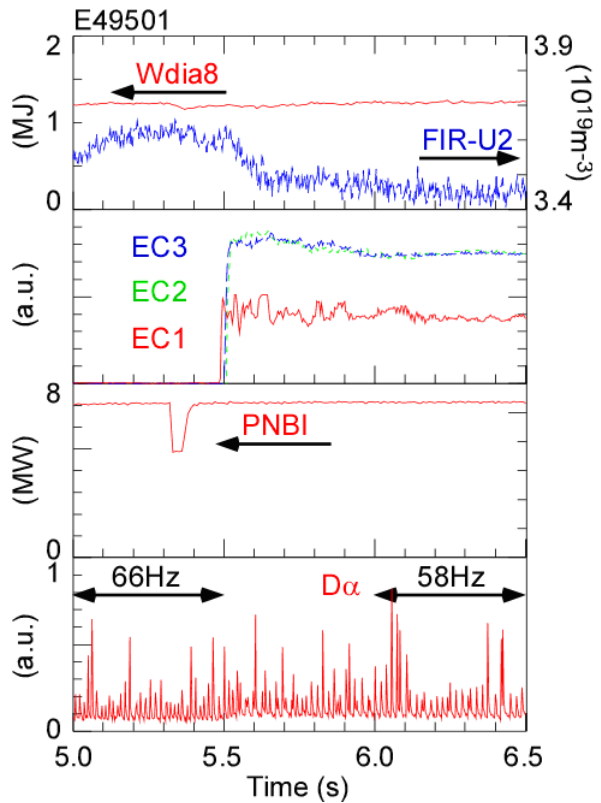


Fig. 2. Waveforms in case of LFS injection.

steady ELMy H-mode plasma with the ELM frequency of 66 Hz is sustained by 7 MW of NB injection power. As a result of EC injection, the line-integrated density measured with the FIR interferometer with central code (FIR-U2) decreases by about 5% taking ~ 150 ms, while keeping the stored energy almost constant. Within 100 ms after EC injection, ELM frequency decreases to 58 Hz in spite of the increase in the total heating power. When the modulated EC wave is applied instead of the CW-EC injection, on the other hand, no clear difference between CW injection and moderated EC wave injection is observed.

2.3 Edge EC injection at high-field side

A higher efficiency of the EC driven current is expected in the case of EC injection at the HFS due to the effect of trapped electrons. Thus, the edge EC injection at the upper-HFS as shown in Fig. 3 is also investigated. In this condition, 1.35 MW of EC power (CW case) from three gyrotrons is deposited at $r/a = 0.9-1.0$, resulting localized ECCD of 2.8 kA. The bootstrap current at the pedestal is evaluated as 60 kA by ACCOME code.

Figure 4 shows wave forms in the case of edge EC injection at the HFS. Before EC injection, steady ELMy H-mode plasma with the ELM frequency of 75 Hz is sustained by 7.2 MW of NB injection power. As a result of EC injection, the line-integrated density measured with FIR-U2 decreases by about 7.5% taking ~ 150 ms and the reduction of the stored energy by 5% together

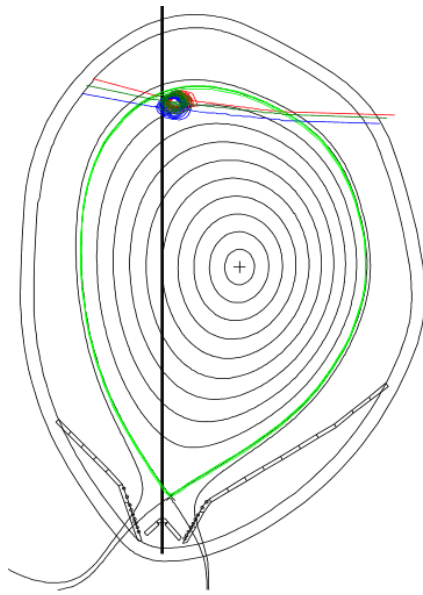


Fig. 3. EC depositions in HFS case evaluated by ray tracing code. Three rays from the bottom correspond to EC #1, #2 and #3. Vertical solid line indicates cold resonance for $2\omega_{ce}$ X-mode ECH.

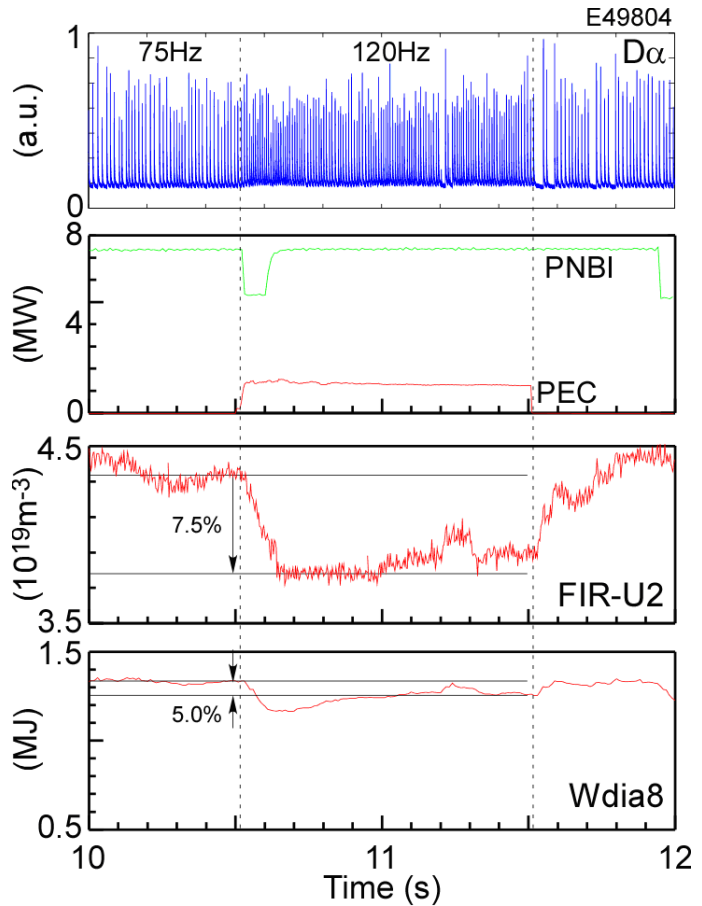


Fig. 4. Waveforms in case of HFS injection.

with the increase in the ELM frequency by 60% (from 75 Hz to 120 Hz).

The ELM frequency increases with the heating power, which is well known as the ELM frequency dependence on the heating power. However, observed change in the ELM frequency with EC injection is not due to the heating power dependence. When the NBI power is increased by 2.2 MW (absorbed power of 1.3 MW), the ELM frequency increased only from ~ 70 Hz to ~ 85 Hz. It is noted that the increase in the ELM frequency by edge EC injection is also observed in high β plasmas with $\beta_N \sim 2.5$.

In JT-60U, it has been observed that the ELM frequency increases as the counter-toroidal rotation velocity increases (or co-toroidal rotation decreases) [3]. On the other hand, the change in the toroidal rotation velocity has also been observed [4]. In E49804, the reduction of co-toroidal rotation by 10 km/s was observed. But, the observed change is too small to explain the change in the observed ELM frequency through the toroidal rotation.

With the change in the ELM frequency by EC injection shown in Fig. 4, the ELM energy loss (ΔW_{ELM}) is decreased from 22 kJ to 16 kJ by about 30%. The change in the ΔW_{ELM} is smaller than that in the ELM frequency, resulting higher ELM energy loss ($P_{ELM} = f_{ELM} \times \Delta W_{ELM}$). On the other hand, the recovery rate of the stored energy after ELM crash is almost constant between before and after EC injection, while the plasma confinement becomes slightly lower with EC

injection as observed in the smaller stored energy. In order to understand the relation among plasma confinement, pedestal performance and ELM characteristics, further analysis will be needed.

3. Summary and discussion

The effect of local heating at the pedestal by EC injection on ELM characteristics has been investigated as a development of an active ELM control method. When the plasma at the top of the pedestal at the HFS is heated by 1.35 MW of EC injection, the ELM frequency is increased from ~75 Hz to ~120 Hz. No response has been observed so far, when EC is injected to the plasma at the top of the pedestal at the LFS and when modulated EC wave (400 Hz) is applied. The increase in ELM frequency is not due to the increase in the heating power, since the increase in the injection power of NBI by 2.2 MW (absorbed power of 1.3 MW) only raised the ELM frequency from ~70 Hz to ~85 Hz. With the increase in the ELM frequency, the ΔW_{ELM} was reduced by ~30%. Thus, the localized EC injection to the pedestal can be considered as a candidate for an active ELM control technique in ITER. However, small reduction of plasma confinement should be considered.

The reason why edge EC injection at the HFS is only effective has not been understood. One possible explanation is that the edge ECCD plays an important role in ELM control, although evaluated ECCD is only 4.5% in HFS case of the bootstrap current at the pedestal region. In order to understand the physics of the change in the ELM characteristics by edge EC injection, inter-machine experiment between ASDEX Upgrade and JT-60U is on going.

References

- [1] Oyama, N., *Journal of Physics: Conference Series* **123**, 012002 (2008).
- [2] Horton, L. D., *et al.*, *Plasma Phys. Control. Fusion* **46**, B511 (2004).
- [3] Kamiya, K., *et al.*, *Plasma and Fusion Research* **2**, 005 (2007).

6. MHD Instability and High-Energy Ions

6.1 Observation of Energetic Particle Driven Instability in the Wall-stabilized High- β Plasmas [1]

G. Matsunaga, Y. Sakamoto, N. Aiba, K. Shinohara, M. Takechi, T. Suzuki, A. Isayama, N. Oyama, N. Asakura, Y. Kamada, T. Ozeki and the JT-60 team

A new instability has been observed in the wall-stabilized high- β_N plasmas above the ideal β -limit without a conducting wall ($\beta_N^{\text{no-wall}}$). This mode behaves like fishbone bursts, that is, it repeats growth and decay within a few milliseconds. Besides, the mode finally triggers the RWM despite enough plasma rotation for RWM stabilization. The radial mode structure measured by ECE is globally extended around the $q=2$ surface. The mode frequency, whose initial value is about 3 kHz, repeatedly chirps down as the mode amplitude increases. The initial frequency is close to the precession frequency of the trapped energetic particles from the perpendicular neutral beams (PERP-NBs) with beam energy of about 85 keV. It is observed that this mode can be stabilized by reducing the PERP-NBs while keeping bulk plasma β_N , indicating that the mode is driven by trapped energetic particles. In order to investigate the stability boundary, $\beta_N^{\text{no-wall}}$ was scanned by changing internal inductance l_i in the range of 0.7-1.0, because $\beta_N^{\text{no-wall}}$ is estimated as $\sim 3l_i$ by the MARG2D code. The mode is observed only in the high- β_N plasmas above $\beta_N^{\text{no-wall}}$, that is, the wall-stabilized high- β_N region, where the ideal kink-ballooning mode (IKBM) and resistive wall mode (RWM) are marginally stable by the conducting wall and/or plasma rotation.

Based on these experimental results, it is concluded that the mode is driven by the trapped energetic particles from the PERP-NBs as the resonance with the precession motion. Namely, it is the kinetic contribution of energetic particles. However, the coupling parity is still unclear. From the fact that the mode is observed only in the high- β_N above $\beta_N^{\text{no-wall}}$, the marginally stable IKBM or RWM are possible candidates. Namely, this mode is considered to be an energetic particle branch with taking into account the kinetic contribution of the energetic particles in the high- β_N MHD dispersion relation. Since the mode is observed in the wall-stabilized high- β_N plasmas, we have named this mode as energetic particle driven wall mode (EWM). The mode behavior is very similar to the so-called fishbone instability associated with the $m/n = 1/1$ internal kink mode. This suggests that α -particle and fast ion contributions to the MHD stability should be paid attention for high- β_N operation above $\beta_N^{\text{no-wall}}$ where the RWM is marginally stable in ITER and fusion reactors.

Reference

- [1] Matsunaga, G. et al., Phys. Rev. Lett. **103**, 045001 (2009).

6.2 Observation of RWM Precursor [1]

G. Matsunaga, N. Aiba, Y. Sakamoto, K. Shinohara, T. Suzuki, A. Isayama, N. Oyama
and the JT-60 team

We have sometimes observed a precursor just before the RWM onset in the high- β_N experiments. The RWM precursor independently appears or is sometimes triggered by the edge localized mode (ELM) or energetic particle-driven wall mode (EWM). This mode has a slow growth time of 10-50 ms which is longer than that of the RWM $\tau_w \sim 10$ ms (the skin time of the resistive wall) and the ideal mode $\tau_A \leq 1 \mu\text{s}$ (the Alfvén time). Rather, this growth time is similar to that of the tearing mode $\tau_{TM} \sim \tau_R^{3/5} \tau_A^{2/5} \sim 50\text{ms}$, where τ_R is a plasma current diffusion time. The mode frequency of the RWM precursor seems to correspond to the plasma rotation just outside the $q=2$ surface. The RWM precursor does not directly affect the plasma confinement, but rather, it can affect the plasma rotation profile around $q=2$. In particular, the rotational shear was strongly reduced while almost keeping the rotation velocity at around the $q=2$ surface. Finally, the $n=1$ magnetic fluctuation rapidly grew, then, a disruption occurred. This rapid growth seems to be the RWM because the growth time is about τ_w .

The waveforms of the RWM precursor, in particular, the growth time is very similar to those of NTM. However, by a comparison of the radial and poloidal mode structures measured by the soft X-ray array and poloidal magnetic probes, it is found that the RWM precursor does not have any clear island structure around the $q=2$ surface. Although the RWM precursor strongly affects the rotation profile around the $q=2$ surface, the poloidal mode structure seems to be $m \sim 3$ at the outside plasma. The RWM precursor has a large amplitude at $q=2$ and is accompanied by $m=3 \sim 4$ poloidal harmonics. Thus, the mode structure of RWM precursor is similar to that of a kink-ballooning mode. These show that the RWM precursor is identified as neither NTM nor tearing mode.

Furthermore, the RWM precursor can reduce the rotation velocity or rotational shear. It is sometimes observed that the RWM was destabilized when the rotational shear was close to zero despite the enough rotation velocity for the RWM stabilization. This result suggests that the rotational shear around the rational surface is important to determine the RWM stability as well as the rotation velocity. At present, this RWM precursor is thought to be essentially the same mode as the RWM and appears at the RWM stability boundary.

Reference

- [1] Matsunaga, G. et al., Proc. 22nd Fusion Energy Conference, EX/5-2 (2008).

6.3 Identification of the Minimum EC-driven Current for Complete Stabilization of an $m/n=2/1$ Neoclassical Tearing Mode [1]

A. Isayama, G. Matsunaga, T. Kobayashi, S. Moriyama, N. Oyama, Y. Sakamoto, T. Suzuki, H. Urano, N. Hayashi, Y. Kamada, T. Ozeki, Y. Hirano, L. Urso¹⁾, H. Zohm¹⁾, M. Maraschek¹⁾, J. Hobirk¹⁾, K. Nagasaki²⁾ and the JT-60 team

1) Max-Planck-Institut für Plasmaphysik, 2) Kyoto University

Stabilizing a neoclassical tearing mode with electron cyclotron current drive (ECCD) is considered to be the most promising method due to its ability of localized current drive. NTM stabilization using electron cyclotron current drive has been extensively performed in JT-60U. However, as in other devices, the NTMs were overstabilized in most cases, and the EC wave power was larger than the minimum required power. Although NTMs should be stabilized with smaller amount of EC wave power in ITER, it remains uncertain how much EC wave power is required as the minimum. Thus, identification of the minimum required EC wave power is an important issue. To clarify the minimum required power, stabilization of an $m/n=2/1$ NTM with reduced EC wave power was performed. Experiments were performed in two different regimes of the different toroidal fields at 3.7 T and 1.7 T. In the experiments, the range of the minimum power was identified as follows: $0.20 < j_{EC}/j_{BS} < 0.40$ with $W_{sat} \sim 0.15$, $W_{marg} \sim 0.08$ and $d_{EC} \sim 0.05$ for the high-field case, and $0.35 < j_{EC}/j_{BS} < 0.46$ with $W_{sat} \sim 0.12$, $W_{marg} \sim 0.06$ and $d_{EC} \sim 0.08$ for the low-field case. Here, j_{EC} and j_{BS} the EC-driven current density and bootstrap current density at the mode rational surface; W_{sat} , W_{marg} and d_{EC} the saturated island width, marginal island width and full width at half maximum of the ECCD deposition profile, respectively. The marginal island width was found to be about 5 times the ion banana width, which is larger than that for an $m/n=3/2$ NTM obtained previously. Detailed analysis using TOPICS-IB code, in which the undetermined coefficients in the modified Rutherford equation are determined by fitting with experimental data, is planned in the near future.

Reference

[1] Isayama, A., et al., Proc. 22nd IAEA Fusion Energy Conf. (2008); Nucl. Fusion **49**, 055006 (2009).

6.4 Stabilization of an $m/n=2/1$ NTM Using Modulated ECCD [1]

A. Isayama, G. Matsunaga, T. Kobayashi, S. Moriyama, N. Oyama, Y. Sakamoto, T. Suzuki, H. Urano, N. Hayashi, Y. Kamada, T. Ozeki, Y. Hirano, L. Urso¹⁾, H. Zohm¹⁾, M. Maraschek¹⁾, J. Hobirk¹⁾, K. Nagasaki²⁾ and the JT-60 team

1) Max-Planck-Institut für Plasmaphysik, 2) Kyoto University

Stabilizing NTMs with modulated electron cyclotron current drive (ECCD) is thought to be more effective than with unmodulated ECCD. Since adding the ability to modulate the EC wave power at several kHz significantly changes the design of gyrotrons, it is important to stabilize the more dangerous $m/n=2/1$ NTM and clarify whether the modulated ECCD is actually more effective and if so by how much. In addition, issues in performing the modulated ECCD need clarifying in order to make the NTM stabilization in ITER more reliable.

In the 2007-8 campaign, significant progress was made in the JT-60U EC wave system. First, the ability to modulate injection power was increased to ~ 7 kHz by modifying the high-voltage circuits of gyrotrons to realize fast power downs; previously the modulation frequency was less than 1 kHz, which was not enough for NTM stabilization experiments. Second, a new system to synchronize the modulated EC wave with NTM rotation was developed, in which the phase of the modulated EC wave is adjusted in real time by referring magnetic perturbation signals. Using the EC wave system, phase scans were then successfully performed, and the effect of the phase shift of the modulated EC wave on stabilization was investigated in detail. The result showed that the stabilization effect weakens as the phase of the modulation deviates from that corresponding to O-point ECCD: τ_{decay} increases by $\sim 50\%$ with a phase shift of $\sim \pm 50^\circ$. Here, the decay time τ_{decay} was obtained by fitting the magnetic perturbation signal with the exponential function $\exp(-t/\tau_{\text{decay}})$. For near X-point ECCD, NTM amplitude increased, showing a destabilization effect. It was also demonstrated that modulated ECCD actually has a stronger effect on NTM stabilization than unmodulated ECCD. The decay time for modulated O-point ECCD is less than 1/3 of that for unmodulated ECCD: $\tau_{\text{decay}}=1.2$ s for modulated ECCD and 4.2 s for unmodulated ECCD. In addition to the stabilization effect, a destabilization effect was observed with ECCD near the island X-point for the first time. This means that the phasing is important to avoid a mode locking caused by $m/n=2/1$ NTM with a large amplitude. Comparison with a theoretical model on ECCD efficiency was also made. It was found that the dependence of the decay time on phase shift with respect to O-point ECCD is similar to that of the inverse of the ECCD efficiency function.

Reference

[1] Isayama, A., et al., Proc. 22nd IAEA Fusion Energy Conf. (2008); Nucl. Fusion **49**, 055006 (2009).

6.5 Fitting of the Modified Rutherford Equation: a Comparison between ASDEX Upgrade and JT-60 Results [1]

L. Urso¹⁾, H. Zohm¹⁾, R. Fischer¹⁾, A. Isayama, Y. Kamada,
the ASDEX Upgrade team and the JT-60 team

1) Max-Planck-Institut für Plasmaphysik, EURATOM-Association, Garching, Germany

Evolution of magnetic island associated with NTMs is described by the modified Rutherford equation (MRE). Since the MRE contains undetermined coefficients for the contribution from different physics such as the effect of bootstrap, the Glasser-Greene-Johnson (GGJ) effect. Determination of the range of the coefficients is important to predict the behavior of NTMs in ITER and establish scenarios for NTM controls. Although fitting of experimental data with the MRE and simulation of NTM stabilization were previously performed independently in JT-60U and ASDEX-U, the form of the MRE was not identical.

To understand the NTM physics in a wider parameter range, comparison of the coefficients between ASDEX-U and JT-60U for an $m/n=3/2$ NTM was performed by using the same form of the MRE and the same analysis method. The MRE used in this comparison is as follows: $\tau_s / r_s (dW/dt) = r_s \Delta' + c_{\text{sat}} (r_s \Delta'_{\text{BS}} + r_s \Delta'_{\text{GGJ}})$. Here, τ_s , r_s and Δ' are the resistive timescale, minor radius at the mode rational surface and the tearing parameter, respectively. Δ'_{BS} and Δ'_{GGJ} stand for contribution from bootstrap current and the GGJ effect, respectively, and they are evaluated by using parameters at the mode rational surface. The coefficients c_{sat} can be estimated by evaluating the full island width at the mode saturation ($dW/dt=0$), i.e., $c_{\text{sat}} = \Delta' / (\Delta'_{\text{BS}} + \Delta'_{\text{GGJ}})$. The plasma parameters in JT-60U are as follows: the plasma current $I_p = 1.5$ MA, toroidal field $B_t = 3.7$ T, major radius $R = 3.24$ m, minor radius $a = 0.76$ m, safety factor at 95% flux surface $q_{95} = 3.8$ and normalized beta at NTM saturation $\beta_N^{\text{sat}} \sim 1.5$, and those in ASDEX-U are $I_p = 0.8$ MA, $B_t = 2.2$ T, $R = 1.65$ m, $a = 0.49$ m, $q_{95} = 4.5$ and $\beta_N^{\text{sat}} \sim 2$. From the comparison, it was found that the value of c_{sat} is about unity while the plasma parameters are quite different in JT-60U and ASDEX-U.

Reference

[1] Urso, L., et al., Proc. 35th EPS Conference on Plasma Phys. **32**, P-2.068 (2008).

6.6 Triton Burn-up Experiment using Newly Developed Neutron Profile Measurement System

K. Shinohara, K. Ishii¹⁾, T. Okuji¹⁾, M. Ishikawa,
M. Baba¹⁾, M. Sasao¹⁾, M. Isobe²⁾

1) Tohoku University, 2) National Institute for Fusion Science

1. Introduction

Tritons with energy of 1.0 MeV are produced in the $D + D \rightarrow p + T$ reaction at approximately the same rate as the DD neutrons with energy of 2.5 MeV from the $D + D \rightarrow n + {}^3\text{He}$ reaction. The study of the behavior of 1 MeV tritons can contribute to predicting the behavior of D-T-produced 3.5 MeV alphas, because 1 MeV tritons and 3.5 MeV alphas have similar Larmor radii. As the 1 MeV triton slows down into the peak of the DT fusion reaction cross-section, it may undergo a DT fusion reaction, $D + T \rightarrow \alpha + n$, emitting a 14 MeV neutron, DT neutrons. Thus, we can investigate the triton behavior by measuring DT neutrons. Additionally, DD neutron gives us the information of DD reaction, namely the source of tritons. Thus, the simultaneous measurement of DD neutrons and DT neutrons is effective for the analysis of triton behavior.

In the previous study[1], 14 MeV neutron detector based on scintillating fibers was used. The detector consists of an array of scintillating fibers, coupled to a magnetic-resistant phototube with a high current output base, enabling count rates up to 100 MHz. This system had excellent time resolution, but crude spatial resolution. The system observed almost whole plasma. This system was only sensitive to neutrons with energy of about 14 MeV. Another measurement using different sight line was required for the DD neutrons of 2.5 MeV.

We have developed a new neutron profile measurement system with 7 chords in order to investigate both DT neutrons and DD neutrons using the same sight lines (Fig. 1). The system is based on the stilbene crystal detector and the fast Flash-ADC (analog-to-digital converter). In this paper, the new neutron profile measurement system is introduced and the preliminary results of triton burn-up measurements using this new system is described.

2. Newly developed neutron profile measurement system

The neutron profile monitor system to measure DD

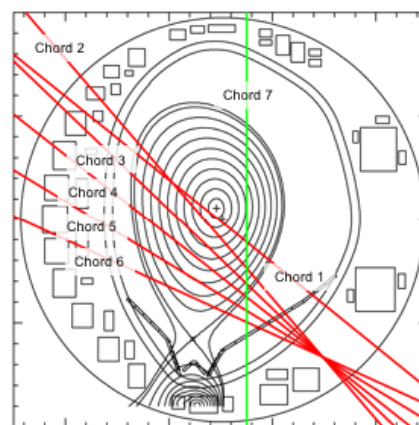


Fig. 1. Plasma configuration for triton burn-up experiment and the sight lines of neutron profile measurement system.

neutrons was installed in 2000, and produced fruitful results[2]. The stilbene detector adopted in this system is sensitive to not only neutrons but also gamma rays. Thus, neutron-gamma ($n-\gamma$) pulse shape discrimination is required. In the original system, built-in analog discrimination circuit was used. This analog circuit limited the maximum count rate below $\sim 1 \times 10^5$ counts/s. This limitation defined the operational window of the system. Namely, the system could not cover a wide range of count rates which was indispensable for research of high performance plasma, including triton burn-up experiments. To increase the count rate, a digital signal processing method was developed[3,4]. In this method, anode signal of phototube coupled to the stilbene detector is directly fed into the Flash-ADC with the sampling rate of 200 MHz. Against the digitized signals, the $n-\gamma$ discrimination is carried out as a post-process in a personal computer with a software using an analogy of a charge comparison method. The neutron and γ signals are discriminated by the difference of the decay time of each single pulse. In the charge comparison method, pulse is integrated for two different time intervals (Δt_F and Δt_S as shown in Fig. 2) and the time scale of pulse is evaluated using these integrated areas of Q_F and Q_S . A typical result of $n-\gamma$ discrimination is shown in Fig. 3 as the two dimensional plot for pulse height vs pulse shape parameter using Q_F and Q_S . After the $n-\gamma$ discrimination, the DD neutrons and DT neutrons are discriminated using the pulse height. This method successfully achieved the counting rate higher than 1×10^5 counts/s and also observation of DT neutrons. As shown in Fig. 4, we can measure the temporal evolution of γ rays, DD neutrons, and DT neutrons in the same sight line. Using this method, it has become possible that the time resolved line-integrated profile measurement of γ rays, DD neutrons, and DT neutrons[5].

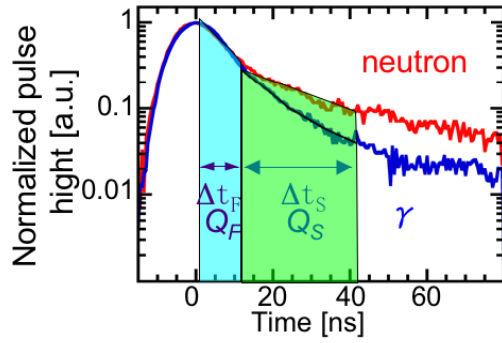


Fig. 2 Waveforms of pulses induced by neutron and gamma. And definition of Δt_F and Δt_S

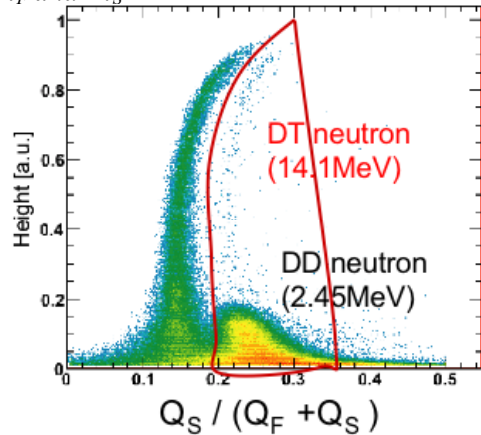


Fig. 3. Two dimensional plot for pulse height vs pulse shape parameter. Pulses enclosed by solid curve come from neutrons.

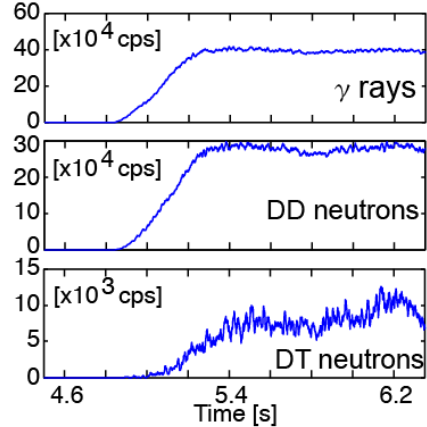


Fig. 4. Measured temporal evolution of emission of γ rays, DD neutrons, DT neutrons in a sight line.

3. Preliminary results of triton burn-up measurements using the new system

The experiments are carried out based on the discharge for the neoclassical tearing mode (NTM) study. For ease of analysis, intense NB was injected as a single pulse. NB was turned off before NTM appearance and there are small MHD activities. Experiments were carried out in $B_t = 3.56 - 3.98\text{T}$ and $I_p = 1.5-1.9\text{MA}$. Figure 5 shows plasma parameters for a discharge in which PNBs were injected with 20 MW and $B_t/I_p = 3.56\text{ T}/1.5\text{ MA}$. ITB is formed for both ion and electron just after intense NB injection. The total neutron emission rate measured by fission chamber (FC) reaches $7 \times 10^{15}\text{ s}^{-1}$. The plasma configuration and sight lines of new profile measurement system are depicted in Fig. 1. The contour corresponds to the volume normalized ρ . The chord 1 goes through $\rho \sim 0.1$ and the chord 6 goes through $\rho \sim 0.8$ at the most inner path. Figure 6 shows the temporal evolution of DD neutron emission and DT neutron emission. The count rate of DT neutron is small, a few 10^3 cps. It is necessary to apply longer counting time interval to raise statistical precision. Thus, the 100 ms averaged value is shown in Fig. 6.

Although the temporal evolution of DD neutron emission is similar to that measured by FC, the difference, which is expected to come from the fast deuterons profile, was observed. We can observe that the start of the increase of DT neutron emission delayed, compared with the start of the increase of DD neutron emission. This is considered to imply the accumulation of tritons. The accumulation process informs the transport of tritons. The decay phase also gives the information of the transport of tritons. We can observe the decay of DT neutron with three time phases, which are indicated as I, II, and III in Fig.6. First phase might be effect of decay of fast deuteron. Interestingly, the plateau phase is observed, however, we do not have an idea what causes this plateau phase at present. The time scale of the decay is $1/2 - 1/3$ of that observed in the previous experiments[1]. The differences are in a plasma current, a plasma configuration, and the first wall shape. In the

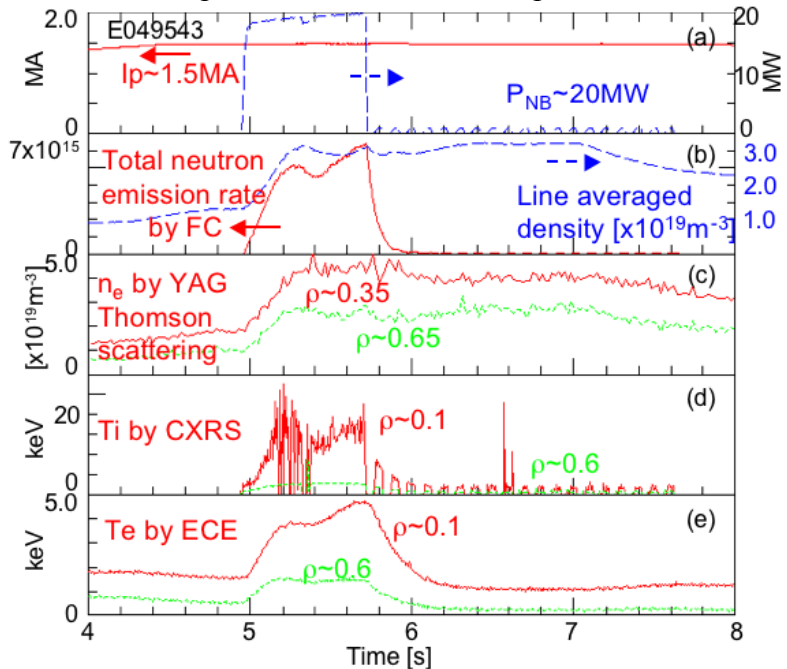


Fig. 5. Waveforms of plasma parameters. (a) plasma current and Power of NB, (b) total neutron emission rate measured by fission chamber and line averaged density measured by FIR interferometer, (c) electron density measured by YAG laser Thomson scattering system, (d) ion temperature measured by charge exchange recombination spectroscopy, (e) electron temperature measured by electron cyclotron emission.

previous experiments, the plasma configuration is highly elongated, and the first wall shape is characterized by the open divertor, namely no baffle structure. These might affect the confinement of the fast ions with a large Larmor radius. We are planning to make the analysis tools which evaluate the classical triton transport, considering the finite orbit size of fast ions by extending OFMC code for the further analysis.

References

- [1] Nishitani T., Hoek M., Harano H., Isobe M., Tobita K., Kusama Y., Wurden G. A., and Chrien R. E., Plasma Phys. Control. Fusion **38**, 355 (1996).
- [2] Ishikawa M., Nishitani T., Morioka A., et. al., Rev. Sci. Instrum. **73**, 4237 (2002).
- [3] Ishikawa M., Itoga T., Okuji T., et. al., Rev. Sci. Instrum. **77**, 10E706 (2006).
- [4] Itoga T., Ishikawa M., Baba M., et. al., Radiat. Prot. Dosimetry **126**, 380 (2007).
- [5] Shinohara K., Okuji T., Ishikawa M., Baba M., Itoga T., Rev. Sci. Instrum. **79**, 10E509 (2008).

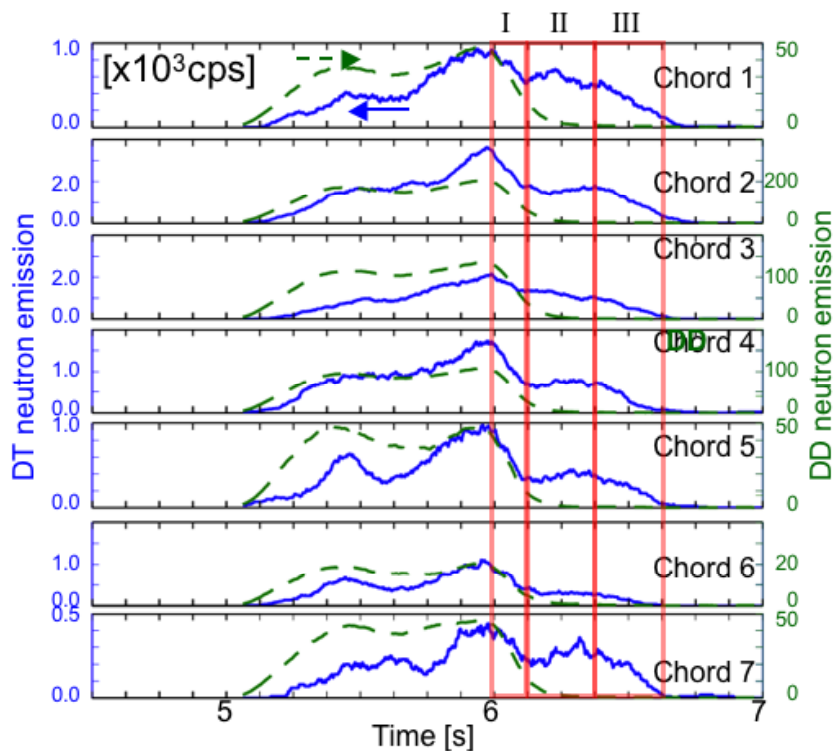


Fig.6 Temporal evolution of DD neutron emission (dashed curve, right axis) and DT neutron emission (solid curve, left axis) for 7 chords depicted in Fig.1. The right axis is for DD neutron, the left axis for DT neutron. Three different decay phase I, II, III were observed.

6.7 Study of Ion Cyclotron Emissions due to DD Fusion Product Ions on JT-60U

M.Ichimura¹⁾, M.Katano¹⁾, Y.Yamaguchi¹⁾, S.Sato¹⁾, Y.Motegi¹⁾, H.Muro¹⁾, T.Ouchi¹⁾, S.Moriyama, M.Ishikawa, K.Shinohara, Y.Sakamoto, A.Kojima, T.Kobayashi, T.Watanabe²⁾

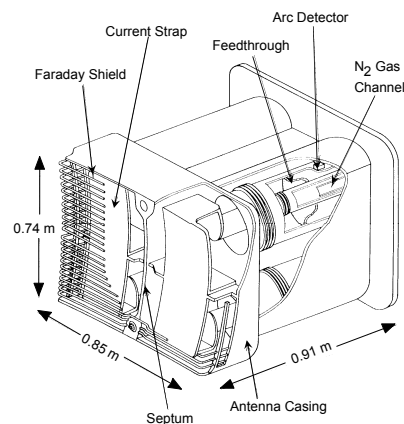
¹⁾ Plasma Research Center, University of Tsukuba

²⁾ National Institute for Fusion Science

1. Introduction

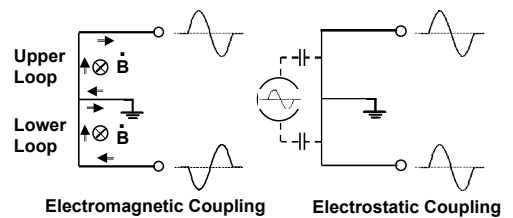
In high-beta plasma experiments, fluctuations in the ion cyclotron range of frequency (ICRF) have been observed due to the anisotropy of energy distribution and the presence of non-thermal ion components. The Alfvén-ion-cyclotron (AIC) mode is one of the typical micro-instabilities excited in the mirror plasmas with the strong temperature anisotropy [1-3]. On the other hand, ion cyclotron emissions (ICEs), of which frequencies are the ion cyclotron frequency and its higher harmonics for the magnetic field strength of the outermost magnetic surface at the outer plasma edge, have been reported in a decade from 1990 on JET, TFTR and JT-60U [4-8]. The high-energy fusion-product (FP) ions are trapped in the local mirror configuration and undergo large excursion orbits from the plasma center to the plasma edge. Such high-energy FP-ions form the non-thermal ion distribution near the plasma edge. The excitation of the fast Alfvén waves is considered to be the most probable origin of ICEs due to FP-ions [5]. On the neutral-beam (NB) injection heated deuterium (D) plasmas in JT-60U, ICEs due to injected D-ions and FP ³He and T-ions have been analyzed by using ICRF antennas as pickup loops [9].

The main motivation of this work is to study spontaneously excited waves in ICRF and the basic physics in the magnetically confined plasmas with non-thermal energy distribution. Recently, ICE due to FP P-ions is also identified. To use ICEs as a significant diagnostic tool for fusion reactions, it is necessary to understand the precise mechanism of the wave excitation



2. Experimental Setup

Conventional positive-ion based neutral beams (P-NBs), of which energy is 80 keV, and negative-ion based neutral beams (N-NBs), of which energy is 300 keV, are normally used for the high performance D-plasma operation on JT-60U [10]. Deuterium-deuterium (DD) fusion neutrons are detected and confirm the realization of DD fusion reactions and production of DD FP-³He, T and P-ions. Two ICRF antennas installed on the outer midplane of the vacuum vessel are used as pickup loops for detecting electrostatic and/or



Electromagnetic Coupling Electrostatic Coupling
 Fig.1 Schematic drawing of ICRF antenna: four current loops are arrayed in two columns and two rows. Schematic drawing of loops for electromagnetic and electrostatic coupling schemes is indicated including the flow direction of induced current for the electromagnetic coupling and induced voltage for the electrostatic coupling.

electromagnetic fluctuations. Two straps (separated with 0.44 m in the toroidal direction) are arrayed in each ICRF antenna. Straps are grounded at the center and both ends of each strap are connected to the output of rf generators through the vacuum feed-through, the matching components and the transmission lines. Then, four loops in two columns and two rows are set for each ICRF antenna as shown in Fig.1. The width of each strap is 0.19 m. Single layer Faraday shield is used and a good coupling for the rf field is expected electro-statically and/or electro-magnetically. The current in both loops on each strap induced by the time derivative of the magnetic field component has the opposite sign because of their opposite loop direction. On the other hand, electric potentials are detected when the plasma and antenna couples electro-statically. The voltage signals on both loops due to the electric field component have the same sign as indicated in the figure. Two sets of ICRF antennas, which are installed with the distance of 1.67 m in the toroidal direction, are used in this experiment and the toroidal wave number can be evaluated due to the small pitch angle of the toroidal magnetic field line.

3. Observations of ICEs due to ^3He and T-ions

By using ICRF antennas as pickup loops, the electromagnetic fluctuations have been clearly detected and their toroidal structures have been evaluated from the phase differences between two antenna straps arrayed in the toroidal direction. Figure 2 shows the temporal evolution of (a) NB powers and (b) plasma parameters (line averaged density and diamagnetic signal). A typical intensity plot of the temporal evolution of the frequency spectrum is indicated in Fig.2(c). The temporal evolution of the amplitude of each frequency peak and the signal of fusion neutrons are also indicated in Fig.2(d). Two sharp peaks, of which frequencies are corresponding to the 2nd harmonic cyclotron frequency of ^3He -ions, ICE(^3He), and a fundamental cyclotron frequency of T-ions, ICE(T), near the outer plasma edge, are clearly observed. The relatively broad peaks are ICEs due to injected D-ions, ICE(D). The amplitude of the second harmonic ICE(^3He) becomes weak when the density and the signal of fusion neutrons start to increase and becomes strong again at the end of the discharge. The amplitude of ICE(T) is almost proportional to the signal of fusion neutrons. As shown in Fig.2(a), several break-downs occur on N-NB and the signal of fusion neutrons follows the N-NB power and also ICE(T) has quick response to the N-NB power.

The wave numbers of both excited waves are determined from the measurement of phase differences among three different antenna straps in the same discharge and those of the second harmonic ICE(^3He) and the

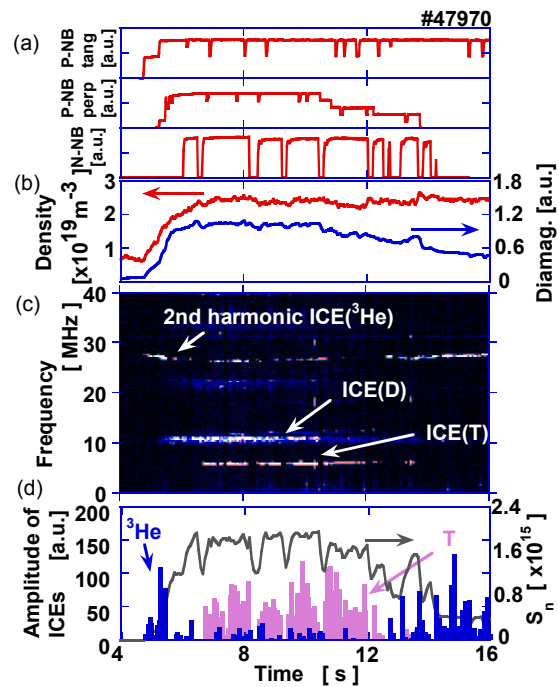


Fig.2 A discharge in which both the second harmonic ICE(^3He) and ICE(T) are detected at the same time. Temporal evolution of (a) NB powers, (b) line averaged density and diamagnetism, (c) frequency spectrum of excited waves, (d) amplitude of excited waves and neutron signal is indicated.

fundamental ICE(T) in this discharge are determined to be around 4 and 8 m^{-1} , respectively.

Recently, ICE due to P-ions, ICE(P), is identified in relatively high density plasmas as shown in Fig.3. In the discharge, the magnetic field strength at the outermost magnetic surface of the outer plasma edge is 1.82 T and the fundamental cyclotron frequency of D-ions is 13.9 MHz. The second harmonic ICE(D) is detected as the broad frequency peak near 28 MHz. Higher harmonic ICEs(D) are sometimes observed as such broad frequency peaks. A relatively sharp peak is observed just below the second harmonic ICE(D). ICEs due to FP-ions

are always excited with the sharp frequency peaks in comparison with ICE(D). The observed frequencies of ICE(D) are just on the cyclotron frequency and higher harmonic frequencies at the plasma edge. On the other hand, the frequencies of ICE due to FP-ions are always detected as lower frequencies at the plasma edge as mentioned in reference 11. Most obvious difference between ICEs(D) and ICEs due to FP-ion is the wave number in the toroidal direction [9]. ICEs due to FP-ions have finite wave numbers and can propagate in the toroidal direction. It is confirmed the sharp peak just below the second harmonic ICE(D) has a finite wave number in the toroidal direction and is identified as ICE(P). In the figure, the second harmonic ICE(^3He) is also observed from 15 s, where the density becomes lower than the former duration from 5 s to 13 s.

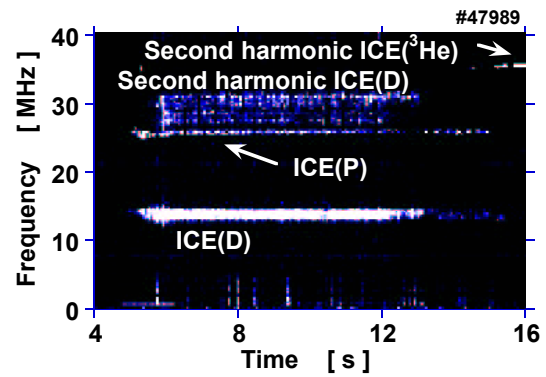


Fig.3 The intensity plot of the temporal evolution of the frequency spectrum in which ICE(P) is clearly observed. From 13 s of the discharge, the density decreases and the second harmonic ICE(^3He) appears.

4. Discussions

In the previous section, experimental observations related to ICEs on JT-60U are presented. In this section, the characteristics and interpretation of FP-ICEs in DD fusion plasmas on JT-60U are discussed. In the previous manuscript [9], the obvious difference between ICEs due to FP-ions and ICEs(D) is described to be that of the toroidal wave numbers. The excitation of obliquely propagating fast Alfvén waves (magneto-acoustic waves) is the possible mechanism for ICE(^3He) [5]. The dispersion relation of the fast Alfvén waves in D-plasmas with minority ^3He -ions is shown in Fig.4(a). Here, the simple dispersion relation of two ion components with Maxwellian distributions is solved. The realistic dispersion relation including the distribution of energetic FP-ions and quantitative evaluations for the experimental observations are under investigation. Branches of ion-Bernstein waves due to ^3He -ions intersect with a branch of fast Alfvén wave in D-plasma.

As measured in the same discharge shown in Fig.2, the toroidal wave number of ICE(T) is larger than that of the second harmonic ICE(^3He). This experimental fact indicates ICE(T) is no longer on the same branch of the fast Alfvén wave and ICE(T) may be on the branch of slow Alfvén wave as indicated in Fig.4(a). The dispersion relation of the slow Alfvén waves in D-plasmas with minority T-ions is shown in Fig.4(b). A new cut-off and a new hybrid resonance appear near the cyclotron frequency of T-ions. As also pointed out in the previous report [9], the frequency of ICE(T) is much lower than the cyclotron frequency of T-ions near

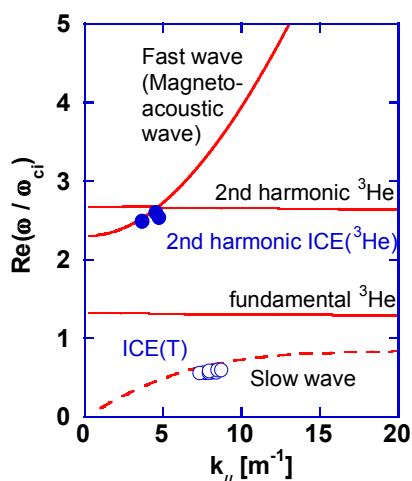


Fig.4(a) Schematic dispersion relation in D-plasmas with minority ^3He -ions. Ion Bernstein waves due to minority ions intersect with the fast Alfvén wave.

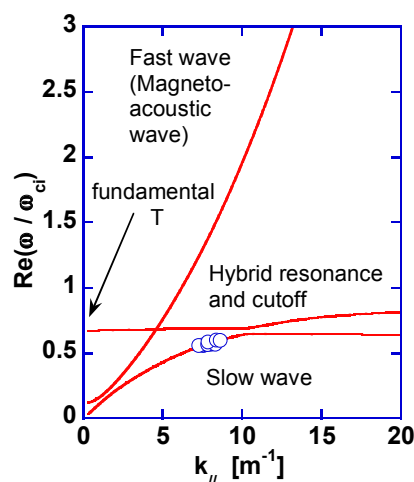


Fig.4(b) Schematic dispersion relation in D-plasmas with minority T-ions. A new cutoff and hybrid resonance appears near the cyclotron frequency of T-ions

the outermost magnetic surface at the outer plasma edge. It is consistent with the experimental observations that the frequency of ICE(T) is somewhat lower than the cyclotron frequency of T-ions as indicated in Fig.4(b). The slow Alfvén wave is well-known to be unstable due to the temperature anisotropy as in the case of AIC-modes. The slow wave branch can be unstable when the minority of T-ions with the temperature anisotropy is included in the calculation.

5. Summary

In this section, ion cyclotron emissions due to deuterium-deuterium fusion-product ^3He , T and P-ions on JT-60U are described. The electromagnetic waves are measured by using ion cyclotron range of frequency antennas. The toroidal wave numbers are evaluated from the phase differences between two antenna straps arrayed in the toroidal direction. The excitation of the fast Alfvén waves (magneto-acoustic waves) for ICEs due to ^3He and P-ions, ICE(^3He) and ICE(P), is consistent with those in the previous JET and TFTR experiments. The density dependence of the excitation of ICE(^3He) is obtained. The anisotropy of the FP T-ions at the outer plasma edge is suggested.

References

- [1] Davidson, R.C., and Ogden, J.M., Phys. Fluids, **18**, 1045 (1975).
- [2] Smith, G. R., Casper, T. A., Gerver, M. J., Nuclear Fusion **23**, 1381 (1983).
- [3] Ichimura, M., et al., Phys. Rev. Lett., **70**, 2734 (1993).
- [4] Cottrell, G.A., et al., Nuclear Fusion, **33**, 1365 (1993).
- [5] Dendy, R.O., et al., Phys. Plasmas, **1**, 1918 (1994).
- [6] Cauffman, S. and Majeski, R., Rev. Sci. Instrum., **66**, 817 (1995).
- [7] Dendy, R.O., et al., Nuclear Fusion, **35**, 1733 (1995).
- [8] Kimura, H., et al., Nuclear Fusion, **38**, 1303 (1998).
- [9] Ichimura, M., et al., Nuclear Fusion, **48** (2008)035012.
- [10] Oyama, N. and JT-60 Team, Fusion Energy 2008, OV/1-3.
- [11] Cauffman, S., et al., Nuclear Fusion, **35**, 1597 (1995).

6.8 Study of Current Decay Time during Disruption in JT-60U Tokamak

Y.Shibata¹⁾, M.Okamoto²⁾, K.Y.Watanabe³⁾, N.Ohno¹⁾, A.Isayama, K.Kurihara, T.Nakano, N.Oyama, Y.Kawano, G.Matsunaga, S.Sakakibara³⁾, M.Sugihara⁴⁾, Y.Kamada and the JT-60 team

¹⁾ Nagoya University, ²⁾ Ishikawa National College of Technology, ³⁾ National Institute for Fusion Science, ⁴⁾ ITER Organization,

1. Introduction

In order to predict the electromagnetic force acting on in-vessel components during disruption, the precise estimation of plasma current decay time τ is important. The database for ITER [1] is established by using the τ normalized by the plasma cross-sectional area S . The area-normalized τ is derived from the L/R model based on a simple series circuit of the plasma resistance R_p and inductance L_p , where τ can be described by L_p/R_p . In this model, the area-normalized τ can be represented by $(L_p/2\pi R_0)/\eta_p$, which has a weak dependence on the device size and a strong dependence on the electron temperature T_e and effective charge Z_{eff} . Here, R_0 and η_p are the plasma major radius and resistivity, respectively. In the ITER database, the lower boundary on area-normalized τ , which is taken as 1.7 ms/m^2 [2], is used as the criterion value for design of ITER. The value is corresponding to $T_e \sim 5\text{eV}$ when $Z_{\text{eff}}=3$ is assumed. In order to verify the L/R model in the existing experimental devices, it is necessary to measure T_e and Z_{eff} of the plasma during disruption in the range from a few eV to tens of eV. However, in mid- and large size tokamak devices, it is difficult to measure the T_e at several eV by using conventional measurement systems with high time evolution. In DIII-D, T_e and Z_{eff} during the current quench have been estimated with collisional radiative analysis in recombining helium plasma [3, 4]. However, the systematic analysis of relation between the τ and T_e during current quench has not been reported yet.

In this paper, we analyze the radiation induced disruptive plasma discharges with massive neon gas puffing in JT-60U, and T_e profile during current quench is estimated by ECE diagnostic system and measurement of He I emission intensity ratios. We investigated the validity of the L/R model during the initial phase of current quench. The measurement of T_e using ECE diagnostic system in a plasma core region is available during the initial phase of relatively slow current decay disruption with $\tau/S = 5 \sim 40 \text{ ms/m}^2$. In the edge region, T_e can be measured by He I emission intensity ratios. In addition, the time evolution of plasma inductance during current quench is focused, and the relationship between τ and L_p is evaluated. MHD equilibrium parameters are evaluated by CCS(Cauchy-Condition Surface) method [5] and MCCP (Maximum Correlation Coefficient Product) method[6] to estimate the L_p .

2. The evaluation method of the plasma inductance using CCS method

Evaluation of the current decay time based on the circuit equation requires the plasma

inductance. The plasma inductance, L_p , is expressed as the following by the internal inductance, l_i , the major radius of plasma, R_0 , and the plasma minor radius, a , for torus plasmas,

$$L_p = L_e + L_i, \quad (1) \quad L_e = \mu_0 R_0 \left(\ln \frac{8R_0}{a} - 2 \right), \quad L_i = \mu_0 R_0 \frac{l_i}{2}, \quad (2)$$

Here L_e and L_i are the external and internal plasma inductance, respectively. In this paper, l_i and a are evaluated by the CCS method using the magnetic sensor signals. R_0 is evaluated as the toroidal current centroid, R_j , which is evaluated by the MCCP method. In the MCCP method, the correlation between the magnetic sensor signal observed in experiment and that by the single filament current source virtually located in vacuum vessel is calculated, and the location of a virtual filament, which has the largest correlation with the experimental signals, is recognized as the center of the toroidal current centroid R_j .

3. Experimental Result

The radiation-induced disruption experiment by massive neon gas puffing was carried out in order to investigate the mechanism of current decay time. After neon gas puffing, the current quench with a rapid increase of \bar{n}_e was observed. In this study, 9 disruptive plasma shots were analyzed. Typical parameters just before the current quench are as follows: the safety factor of plasma surface q_{surf} , varies in the range 5-10, toroidal magnetic field strength B_t , is in the range 1.5-3.8 T. The plasma volume and the major radius are maintained almost constant, 58 m³ and 3.22 m, respectively. We focus on the current decay during the initial phase of the current quench shown by the region enclosed by dotted line in figure 1, where I_p drops by 10%, because the measurement of T_e using ECE diagnostic system in plasma core region is available. In the edge region, T_e can be estimated by He I emission intensity ratio. Figure 1 shows the time evolution of I_p , T_e by ECE and T_e by He I line intensity ratios during the current quench. In figure 1, thermal quench occurs at 12.089 sec and current quench starts at 12.092 sec. After the thermal quench occurs, the plasma current has a peak, which is a typical behaviour of the disruptive discharge. It is found in figure 1(b) that T_e profile becomes flat just after thermal quench occurs, and then returns to a peaked profile in the initial phase at current quench. In this phase, T_e in the core region is about 400 eV. Since the optical thickness is small at $T_e < 100$ eV under the present experimental condition, the sensitivity of ECE diagnostic systems decreases and T_e at normalized minor radius $\rho > 0.4$ cannot be measured by ECE diagnostic system. Then, the T_e at edge region was obtained from the He I emission intensity ratio method. The He I emission intensity is measured from the outer divertor region though the edge region of $\rho > 0.7$. Figures 1(c) shows the

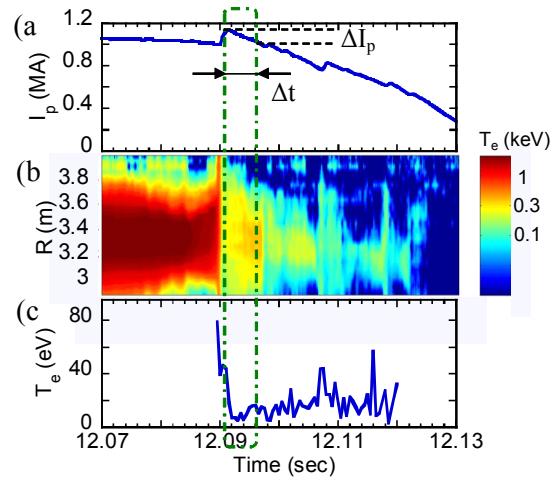


Figure 1. The time evolution of (a) the plasma current I_p , (b) T_e profile by using ECE diagnostic system, (c) electron temperature by using He I emission Intensity ratios.

measured T_e by using He I emission intensity ratio method. Since the He I emission intensity is the integrated value along the line of sight, it is difficult to identify the measurement position of T_e estimated by He I emission intensity ratio. In our analysis, the measurement position is assumed to be $\rho = 0.7$ because He I emission intensity could be strong around $\rho = 0.7$, which is the nearest position from the plasma center to the line of sight. Figure 2 shows the T_e profile measured with ECE diagnostic and He I emission intensity ratios method at $t = 12.094$ sec. The T_e at $\rho = 0.4 - 0.7$ and $0.7 - 1$ is interpolated by a linear function. The ionic fraction of neon calculated by Arnaud and Rothenflug [7] was used to estimate the Z_{eff} . Plasma resistivity η_p is also calculated by classical Spitzer formula with the calculated Z_{eff} . In order to investigate the relation between area-normalized τ and plasma resistivity, the area-averaged $\overline{\eta_p}$ is calculated. The relation between area-normalized τ and area-averaged $\overline{\eta_p}$ is shown in figure 3. Here the experimental current decay time during the initial phase of current quench, $\tau_{100-90\%}$, is defined by the following equation,

$$\tau_{100-90\%} = I_{p0} / (\Delta I_p / \Delta t), \quad (3)$$

where I_{p0} is the plasma current at the maximum of the plasma current after the thermal quench, ΔI_p is 10% of the I_{p0} , and Δt is the time interval between I_{p0} and $0.9 \times I_{p0}$. It is clearly found from figure 3 that $\tau_{100-90\%}/S$ obtained in the experiments has a very weak dependence of $\overline{\eta_p}$. This result suggests that the L/R model cannot be applied to this dataset. One major reason is that L_p changes in time during the initial phase of the current quench.

We apply the CCS method using magnetic sensor signals to evaluate the temporal evolution of plasma inductance and plasma shape. Figure 4 shows the time evolution of the plasma inductance, the poloidal cross-section area and the major radius of the plasma current center, which are evaluated by the CCS and MCCP method. Figure 4(d) shows that R_0 is constant and S changes a little in the initial phase of current quench. As shown in figure 4(b), the current profile could be flat at thermal quench because i_l decreases rapidly around $t = 12.089$ sec. After that, the current density profile could be peaked because i_l increases. L_i and L_e are calculated by eq. (2) in figure 4(c). It should be noted that time derivative of L_i is much larger than that of L_e and time

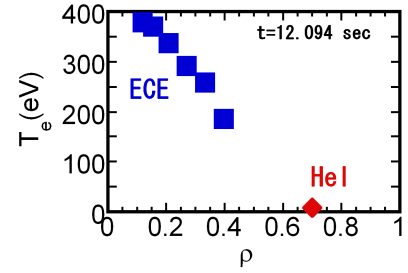


Figure 2. Profile of electron temperature measured by ECE diagnostic and He I emission intensity ratios method at $t = 12.094$ sec.

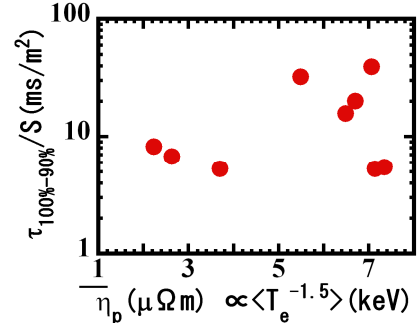


Figure 3. The area-normalized current decay time as a function the area-averaged η_p .

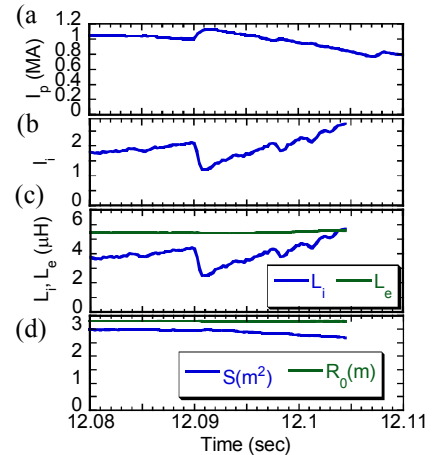


Figure 4. The time evolution of (a) the plasma current, (b) the internal inductance, (c) the plasma internal and external inductance, (d) plasma cross-section and major radius evaluated by CCS method.

derivative of L_p is mainly determined by that of L_i . Figure 5 shows the time averaged value of R_p , L_p and time derivative of L_p , which is denoted by $\Delta L_p/2\Delta t$, in the initial phase of current quench as a function of inverse of the current decay time $\tau_{100-90\%}$. The R_p and L_p are calculated by $R_p = 2\pi R_0 \eta_p/S$ and $L_p = L_i + L_e$, respectively. It is found that the time derivative of L_p is about 10 times as large as R_p in the small region of $\tau_{100-90\%}$. The time derivative of L_p increases dramatically with an inverse of the $\tau_{100-90\%}$. The fact suggests that the time derivative of L_p should be taken into account in the circuit equation in order to accurately predict the current decay time in the initial phase of current quench. When the time derivative of L_p cannot be neglected, an improved model of current decay time[8], $\tau_{L/(R+dL/dt)}$, can be represented by

$$\tau_{L/(R+dL/dt)} = \frac{L_p}{\Delta L_p / 2\Delta t + R_p}, \quad (4)$$

Figure 6 shows a plot of $\tau_{L/R}$ and $\tau_{L/(R+dL/dt)}$ as a function of $\tau_{100-90\%}$. As shown in figure 6, although $\tau_{L/R}$ is about 10 times as large as the $\tau_{100-90\%}$ in the shorter decay time region (the area-normalized current decay time $\tau_{100-90\%}/S < 10\text{ms/m}^2$), $\tau_{L/(R+dL/dt)}$ is considerably consistent with the $\tau_{100-90\%}$. The time evolution of L_p is almost determined by the derivative of L_i . The above result indicates that the time derivative of the plasma internal inductance associated with current profile plays a key role to predict the precise current decay time during initial phase of current quench in the JT-60U radiation induced disruptive plasmas.

References

- [1] Progress in the ITER Physical Basis, Nuclear Fusion **47**, S171 (2007).
- [2] Wesley J.C., Hyatt A.W., Strait E. J. and Schissel D. P. *et al.*, Proceedings of 21st IAEA Fusion Energy Conference, Chengdu, 16-21 Oct. (2006) IT/P1-21.
- [3] Whyte D.G., Humphreys D.A. and Taylor P. L., Phys. Plasma **19**, 4052 (2000).
- [4] Humphreys D.A. and Whyte D.G., Phys. Plasma **19**, 4057 (2000).
- [5] Kurihara K., Fusion Eng. Des., **51-52**, 1049 (2000).
- [6] Kurihara K., Kawamata Y., Sueoka M., Hosoyama H., Yonekawa I., Suzuki T., Oikawa T., Ide S., Fusion Eng. Des., **74**, 527-536(2005).
- [7] Arnaud M., Rothenflug R., Astron. Astrophys. Suppl. Ser. **60**, 425 (1985).
- [8] Shibata Y., Watanabe K.Y., Okamoto M., Ohno N., Isayama A., *et al.*, Nuclear Fusion submitted.

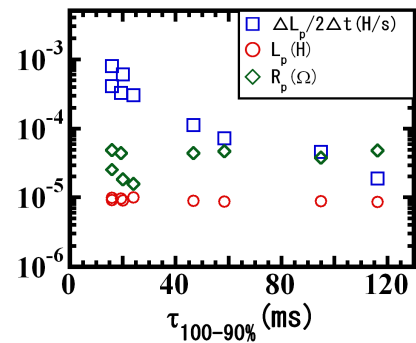


Figure 5. The plasma resistance R_p , the plasma inductance L_p and the time derivative of the plasma inductance as a function of current decay time.

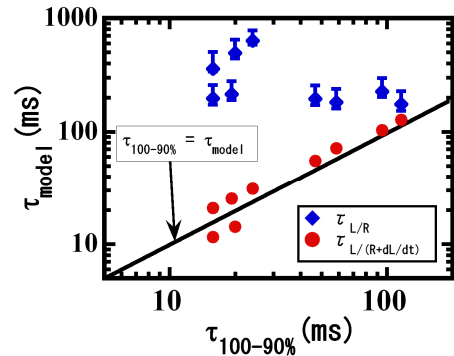


Figure 6. The comparison of the experimental value and predicted current decay time by improved model in initial phase of current quench.

7 Plasma Control and Heating/Current Drive Physics

7.1 Integrated Plasma Control using Real-Time Measurements and Control Systems

M. Yoshida, Y. Sakamoto, M. Sueoka, Y. Kawamata, N. Oyama, T. Suzuki, Y. Kamada,
and the JT-60 Team

1. Introduction

A major target of the large tokamak research is to sustain high beta plasmas with high bootstrap current fraction (f_{BS}) in steady state. In such high performance plasmas, pressure, rotation and current profiles play critical roles in determining transport and MHD stability interacting with each other. Therefore, development of real-time control systems for these parameters is essentially important in sustaining the high performance plasmas. Toward the steady-state operation with high β and high thermal energy confinement, the real-time measurement and feedback control systems have been developed.

For the real-time measurements of the ion temperature (T_i) and the toroidal rotation velocity (V_t) profiles, development of a new charge exchange recombination spectroscopy (CXRS) system was needed. Concerning the logic for T_i control, an integral term is newly installed in addition to the proportional and differential terms, and the proportional gain has been improved to be a function of plasma parameters such as T_i in order to treat temperature dependence of thermal conductivity. Using the real-time CXRS system and the feedback control logic, real-time controls of the T_i gradient at high beta plasmas ($\beta_N \sim 1.6-2.8$) and V_t in ELMy H-mode plasmas have been demonstrated. In addition, real-time control of pressure gradient has been performed in high f_{BS} reversed magnetic shear plasmas.

2. Control Schemes

The schematic diagram of the feedback system and the off-line system is shown in Fig. 1. For the purpose of real-time measurement and feedback control of T_i and V_t , the fast CXRS system has been developed [1]. The charge-coupled device (CCD) is controlled by windows XP acquisition software. The CXR spectra from JT-60U plasma are measured, and then T_i and V_t are calculated by the real-time analysis in the windows PC. The calculated T_i and V_t are sent to the JT-60 plasma control system via a reflective memory network for fast real-time communication, and the NB heating power is controlled by the JT-60 plasma control system so that the measured value agrees with the reference one. The control interval for the NB system is 10 ms. The 30-channel data are also analyzed with Gaussian curve-fitting in off-line system after the discharge, and the calculated T_i and V_t are transferred to the JT-60U database [2]. The difference in T_i between two spatial positions is defined as T_d in keV in this report.

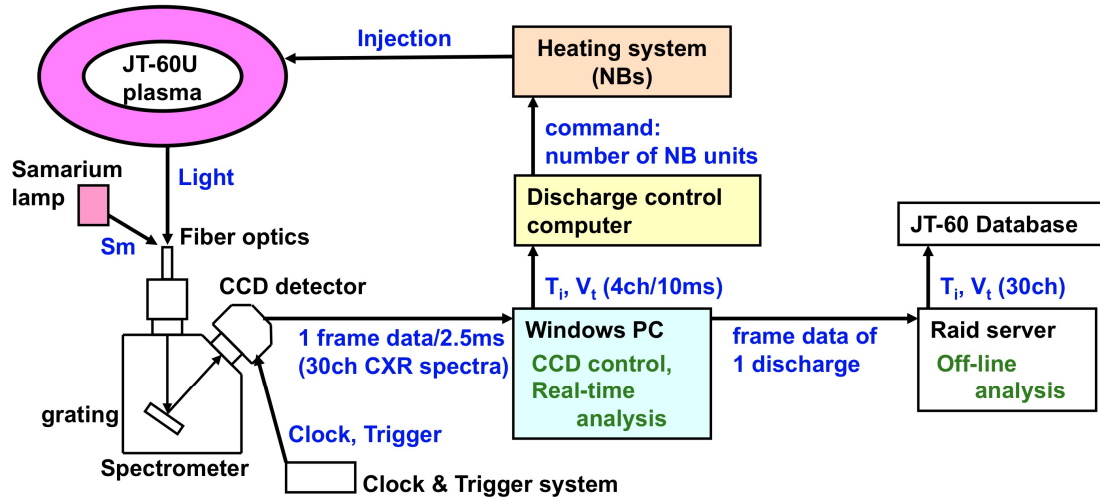


Fig. 1. Schematic diagram of the feedback system.

Concerning the T_d feedback control, the number of NB units for feedback control (U) is determined as,

$$U^{core} = U_{offset}^{core} + G_P^{core} \Delta T_d(t) + G_D^{core} \frac{\Delta T_d(t) - \Delta T_d(t - \Delta t)}{\Delta t} + G_I^{core} \sum \Delta T_d(t) \Delta t, \quad (1)$$

$$U^{edge} = U_{offset}^{edge} + G_P^{edge} \Delta T_d(t) + G_D^{edge} \frac{\Delta T_d(t) - \Delta T_d(t - \Delta t)}{\Delta t} + G_I^{edge} \sum \Delta T_d(t) \Delta t, \quad (2)$$

where U_{offset} , G_P , G_D , G_I and ΔT_d in keV represent the offset in the number of NB units, proportional gain, differential gain, integral gain and the difference between the reference value of T_d (T_d^{ref}) and the observed one (T_d^{obs}), i.e. $\Delta T_d = T_d^{ref} - T_d^{obs}$, respectively. The cycle time of the real-time feedback (Δt) is 10 ms. The superscripts of “core” and “edge” mean the core (on-axis) and edge (off-axis) NB heating units, respectively. The second term of the equations determines the response (the number of NB units) to the current error from the reference value. The third term determines the response to the rate at which the error has been changing. The fourth term determines the response based on the sum of recent errors.

Prior to the feedback control experiment of T_d , the target range of T_d from the power scan is investigated. In order to form a strong ITB, we carried out the experiment at low density ($n_e \sim 1.8\text{--}2.2 \times 10^{19} \text{ m}^{-3}$ at $r/a \sim 0.2$) and high toroidal magnetic field ($I_p = 1 \text{ MA}$, $B_T = 3.0 \text{ T}$). The relation between the achievable T_d and the

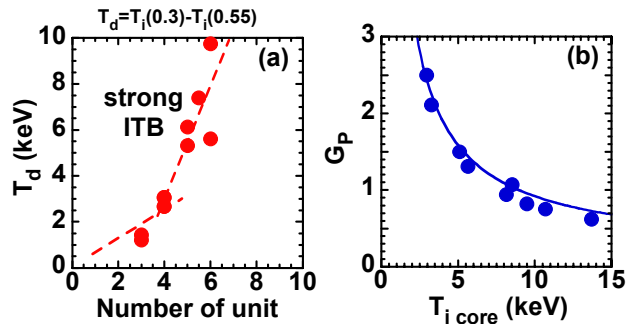


Fig. 2. (a) Dependence of the $T_d = T_i(0.3) - T_i(0.55)$ on the number of core heating NB units. (b) Dependence of proportional gain (G_P) on T_i at $r/a \sim 0.3$ ($T_{i \text{ core}}$).

number of NB units in the strong ITB plasma is shown in Fig. 2(a). The slope ($T_d/\text{NB unit}$) significantly increases from 4 units of NBs in spite of the fact that the electron density increases with increasing the number of NB units. This means the ITB becomes stronger. Roughly speaking, because the horizontal axis implies the heat flux (Q), the slope means the inverse of the ion heat diffusivity (χ_i) from the power balance for steady states $Q = -\chi_i n_i \nabla(T_i)$. The slope indicates the proportional gain as mentioned above, therefore, the slope (G_p) means the quality of energy confinement, and the energy confinement could change with T_i and density and so on. As shown in Fig. 2(b), we found that the slope can be well described as a function of T_i at $r/a \sim 0.3$ ($T_{i \text{ core}}$) for each data point in Fig. 2(a). From this data, we introduced the functional form of G_p as $G_p(1+A T_{i \text{ core}}^B)$, where G_p , A , and B are the time constant values and fitted as 0.124, 48.5 and -0.878 , respectively.

3. Ion temperature gradient control in high beta positive shear plasmas

A result of feedback control experiment ($I_p=1 \text{ MA}$, $B_T=3.5 \text{ T}$) is illustrated in Fig. 3. The feedback control starts at $t=5.0 \text{ s}$, and the reference value of the T_d (dashed line in Fig. 3(a)) was pre-programmed to be in the range from 3 to 5 keV at the measurement positions between $r/a=0.3$ and 0.55. While the toroidal magnetic field is increased about 17%, we use the proportional gain shown in Fig. 2(b) ($G_p(1+A T_{i \text{ core}}^B)$, $G_p=0.124$, $A=48.5$ and $B=-0.878$). The values of G_D and G_I are set at zero to examine the effect of the proportional gain alone. The T_d^{obs} (solid line in Fig. 3(a)) follows to T_d^{ref} within the error $1/G_p$ (hatched region in Fig. 3(a)). Through the discharge, G_p varies from ~ 1.8 to ~ 1.1 according to the change in T_i at the core region ($r/a=0.3$) as shown in Fig. 3(b). Waveform of NB power is shown in Fig. 3(c). Moreover, the real-time control of V_t has been demonstrated from counter to co-direction. Then the ELM behavior changed by controlling the V_t [1].

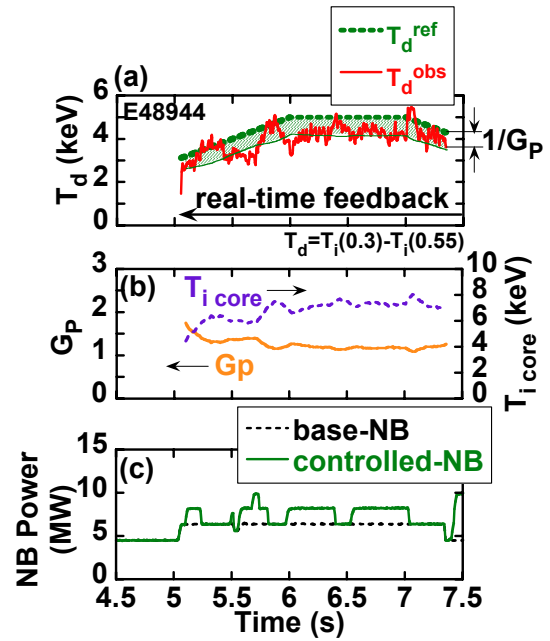


Fig.3. Real-time feedback control of the T_d experiment with G_p as a function of T_i at $r/a \sim 0.3$. (a) Reference T_d and measured T_d . (b) G_p and T_i at $r/a \sim 0.3$. (c) NB power.

4. Ion pressure gradient control in high f_{BS} reversed shear plasmas with low q_{95}

High f_{BS} plasmas are characterized as a self-regulating system or a self-organized

system, where the linkage between pressure and current profiles are strengthened. Therefore development of simultaneous feedback control scheme of pressure and current profiles is important for the steady sustainment of high f_{BS} plasmas. Although the real-time measurement of pressure profile is unavailable at present, it is confirmed that the product of $n_e l \cdot T_d$ is applicable to the indicator of pressure gradient at the ITB. Here $n_e l$ is the line-integrated electron density, and T_d is the difference in T_i between $r/a \sim 0.5$ and 0.7 (CXRS 18ch and 24ch). Then we improved the control logic: “ $\Delta T_d = T_d^{\text{ref}} - T_d^{\text{obs}}$ ” in equations (1) and (2) is replaced by “ $\Delta T_d = (n_e l \cdot T_d)^{\text{ref}} - (n_e l \cdot T_d)^{\text{obs}}$ ”. In addition, control of current profile is set to keep q_{min} constant [3]. The simultaneous control of pressure and current profiles has been attempted in the experiment for the reversed shear plasma above no-wall beta limit ($I_p = 0.85$ MA, $B_T = 2.35$ T, $q_{95} \sim 5.3$, $f_{BS} > 70\%$). Figure 4(a) shows the waveforms of the measured $n_e l \cdot T_d$, and the reference ($G_p = 0.7$, $G_D = 0.03$, $G_I = 1$ and $U_{\text{offset}} = 3$). The feedback control starts at $t = 5.0$ s. The reference of $n_e l \cdot T_d$ is proportionally increased from 30 to 35 ($10^{19} \text{ m}^{-2} \text{ keV}$) during $t = 5.0 - 5.5$ s and increased from 35 to 65 ($10^{19} \text{ m}^{-2} \text{ keV}$) during $t = 5.5 - 6.0$ s. The plasma disrupted at $t = 6.0$ s due to destabilization of RWM. In order to avoid the disruption, the slope of the reference of $n_e l \cdot T_d$ is decreased as shown by dashed line in Fig. 4(b). We also optimized the control gains as $G_p = 0.233$, $G_D = 0.01$ and $G_I = 0.333$. The measured $n_e l \cdot T_d$ follows the reference without disruption and was kept constant from $t = 6.5$ s to 7.0 s. However, we could not demonstrate the current profile control simultaneously because LH conditioning and optimization of plasma configuration were not enough to achieve good coupling conditions, as shown in Fig. 4(c) where the inter-lock of LH system works due to large reflected power.

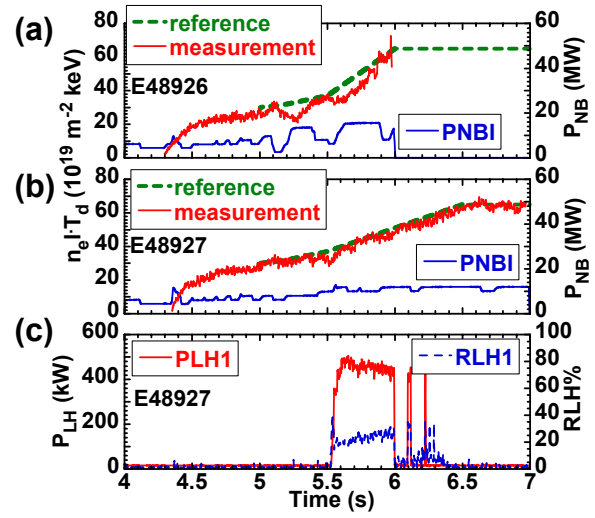


Fig.4. Waveforms for the real-time feedback control of the $n_e l \cdot T_d$ experiment in high f_{BS} reversed shear plasmas. (a) Reference $n_e l \cdot T_d$ (dashed line), measured $n_e l \cdot T_d$ (solid line) and NB power. (b) Those of the optimized case. (c) LH injection power and the ratio of reflected power to injection power.

replaced by “ $\Delta T_d = (n_e l \cdot T_d)^{\text{ref}} - (n_e l \cdot T_d)^{\text{obs}}$ ”. In addition, control of current profile is set to keep q_{min} constant [3]. The simultaneous control of pressure and current profiles has been attempted in the experiment for the reversed shear plasma above no-wall beta limit ($I_p = 0.85$ MA, $B_T = 2.35$ T, $q_{95} \sim 5.3$, $f_{BS} > 70\%$). Figure 4(a) shows the waveforms of the measured $n_e l \cdot T_d$, and the reference ($G_p = 0.7$, $G_D = 0.03$, $G_I = 1$ and $U_{\text{offset}} = 3$). The feedback control starts at $t = 5.0$ s. The reference of $n_e l \cdot T_d$ is proportionally increased from 30 to 35 ($10^{19} \text{ m}^{-2} \text{ keV}$) during $t = 5.0 - 5.5$ s and increased from 35 to 65 ($10^{19} \text{ m}^{-2} \text{ keV}$) during $t = 5.5 - 6.0$ s. The plasma disrupted at $t = 6.0$ s due to destabilization of RWM. In order to avoid the disruption, the slope of the reference of $n_e l \cdot T_d$ is decreased as shown by dashed line in Fig. 4(b). We also optimized the control gains as $G_p = 0.233$, $G_D = 0.01$ and $G_I = 0.333$. The measured $n_e l \cdot T_d$ follows the reference without disruption and was kept constant from $t = 6.5$ s to 7.0 s. However, we could not demonstrate the current profile control simultaneously because LH conditioning and optimization of plasma configuration were not enough to achieve good coupling conditions, as shown in Fig. 4(c) where the inter-lock of LH system works due to large reflected power.

References

- [1] Yoshida M., *et al.*, accepted in Fusion Engineering and Design.
- [2] Sakamoto Y., *et al.*, Section 10.8 in this JAEA-Review.
- [3] Suzuki, T., *et al.*, Nucl. Fusion **48** 045002 (2008).

7.2 Simultaneous Real-time Control of Current and Pressure Profiles

T. Suzuki, M. Yoshida, M. Sueoka, H. Hosoyama, Y. Kawamata

N. Oyama, A. Isayama, and Y. Kamada

1. Introduction

From the start of operation, JT-60U developed various real-time control systems in order to achieve and sustain high performance plasma, e.g. feedback control of stored energy using NB heating. Recently, real-time control systems controlling spatial profiles of current [1] or pressure [2] were realized and demonstrated, separately. It is well known that current profile, and its equivalent q profile, is essential to plasma confinement and stability. Especially rational- q surface having low- q is responsible to appearance of MHD instability (e.g. neoclassical tearing mode (NTM)) that limits attainable plasma pressure. From the viewpoint of avoiding such MHD instability, the minimum of the safety factor profile (q_{\min}) is related to the existence of such rational- q surface having low- q , and hence, the real-time control of q_{\min} was demonstrated [1]. Concerning to the pressure profile, pressure gradient at core region is essential parameter from the viewpoint of stability especially at the internal transport barrier (ITB) required for higher confinement. Since the temperature gradient is a part of the pressure gradient ($\nabla p = n\nabla T + T\nabla n$), and since the ion temperature and its gradient are usually larger than those of electrons in neutral beam (NB) heated tokamaks, control of ion temperature gradient ∇T_i was demonstrated [2]. In this way, real-time controls of current profile and pressure profile were demonstrated, separately. However, since both of them in close cooperation with each other affect stability and confinement, simultaneous control is inevitable to explore optimized operation regime on current and pressure profiles for development and optimization of advanced tokamak (AT) operation scenarios in view of ITER and DEMO. Thus, here we have simultaneously applied the real-time control of q_{\min} and ∇T_i that are characterizing current and pressure profiles, respectively. In this simultaneous control, q_{\min} and ∇T_i are controlled independently, where we assume that q_{\min} and ∇T_i weakly depend on each other in the controlled plasma. This assumption is discussed in the last section (Summary and Discussion).

2. Control Schemes

Safety factor profile is evaluated using motional Stark effect (MSE) diagnostics at 30 spatial channels at 3 optical systems. One of the 3 optical systems having 17 spatial channels has the highest spatial resolution and accuracy (measurement points indicated as squares in Fig. 1). Eleven channels are used for real-time evaluation of safety factor profile in this experiment. The minimum of safety factor profile is calculated as the quadratic minimum of the 3 lowest q of the 11 channels. That is, q profile is adjusted to function $q(\rho) = C(\rho - \rho_{q_{\min}})^2 + q_{\min}$ and $\rho = r/a$ by three parameters C , $\rho_{q_{\min}}$ and q_{\min} using the 3 lowest q data. If the parameter C is negative (q_{\min} is not the minimum but the maximum), q_{\min} is set to the lowest q of the 3 channels. This q_{\min} is controlled by power of off-axis LHCD via PI controller in this

experiment. Since q_{\min} is raised by an increase in off-axis LHCD current in the positive shear plasma, the LHCD power P_{LH} is controlled according to the following equation:

$$P_{LH}(t) = P_{LH}(t_0) - G_p^q \Delta q_{\min}(t) - G_I^q \int_{t_0}^t \Delta q_{\min}(t') dt', \quad (1)$$

where $\Delta q_{\min}(t) \equiv q_{\min}(t) - q_{\min,ref}(t)$.

Two constants of control G_p^q and G_I^q are the proportional and integral gains for q_{\min} control, respectively. The control system including q_{\min} evaluation works in 10 ms cycles.

Ion temperature profile is evaluated using charge exchange recombination spectroscopy (CXRS) diagnostics at 30 spatial channels. The ion temperature at 4 channels out of the 30 CXRS channels can be evaluated in real-time, and 2 of the 4 real-time T_i data are used for evaluation of ∇T_i . Instead of directly controlling the ∇T_i , its equivalent quantity $T_d \equiv -\nabla T_i dr$ is controlled, where dr is the distance between the two CXRS channels. This T_d is a difference of ion temperatures at the two CXRS channels. Since T_i is raised by an increase in the NB heating power, on-axis perpendicular NB heating is used as an actuator; see Fig. 1. This NB is injected almost perpendicular to the toroidal direction so that this NB has little effect in current drive. JT-60U has 4 units of this on-axis perpendicular NB. Since one of these 4 NBs is the diagnostic beam for CXRS diagnostics, the rest 3 NBs are allocated for control. The control system is a PID controller and the number of NB units (U) is calculated according to the following equation:

$$U(t) = U(t_0) - G_p^{Td} \Delta T_d(t) - G_D^{Td} \frac{d}{dt} \Delta T_d(t) - G_I^{Td} \int_{t_0}^t \Delta T_d(t') dt', \quad (2)$$

where $\Delta T_d(t) \equiv T_d(t) - T_{d,ref}(t)$ in keV unit. Control constants G_p^{Td} , G_D^{Td} , G_I^{Td} are the proportional, differential, and integral gains for T_d control, respectively. The control system including the CXRS system works in 10 ms cycles.

3. Experimental Results

The two real-time control systems have been applied to a high-bp ELMy H-mode plasma at $I_p=0.8$ MA, $B_t=2.2$ T ($q_{95}=5.2$). As shown in Fig. 1, a large volume plasma is used in order to obtain good coupling of LH waves to plasma. Magnetic axis is placed on diagnostic beam of MSE diagnostic in order to measure q profile in the whole plasma region. Diagnostic beam for CXRS is also placed as close to the magnetic axis. For T_d control, we selected two CXRS channels at $r/a \sim 0.3$ and $r/a \sim 0.57$ indicated by filled circles as shown in Fig. 1. Hatched region in Fig. 1 indicates the region where the T_d is controlled and where the on-axis perpendicular NBs deposit their power. During the T_d control, power of NBs other

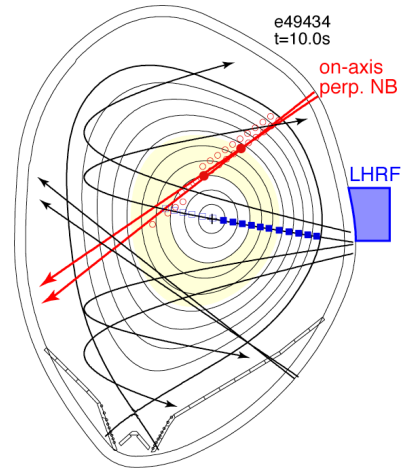


Fig. 1 Configuration of plasma with NB trajectories. CXRS and MSE channels are shown in circles and squares, respectively. CXRS and MSE channels used for real-time control are indicated in filled circles and filled squares, respectively. The hatched region indicates the region where ion temperature gradient was controlled.

than these 3 on-axis perpendicular NBs are fixed as shown by base in Fig. 2 (c). Control gains are set to: $G_p^q=1$ MW and $G_I^q=2$ MW/s $G_p^{Td}=20$ units/keV, $G_D^{Td}=0$ unit s/keV, $G_I^{Td}=10$ units/s keV (integration time of 0.5 s). Thus, both q_{\min} and T_d are controlled via PI controllers. Optimization of these control gains could not be performed due to limitation in machine time. The reference of q_{\min} is set to 1.5. The reference of T_d is set to 1 keV during $t=7-9$ s and is proportionally increased to 1.8 keV during $t=9-10.5$ s. The LH power and the number of NBs at the start of each control are $P_{\text{LH}}(5.5\text{s})\sim 0.8$ MW and $U(7\text{s})=1$ unit. Parallel refractive index N_{\parallel} of the LH waves is 1.9 at phase difference between adjacent antenna modules of 120° .

Figure 2 shows the waveforms of the discharge. Flattop of plasma current starts at $t=5.4$ s in this discharge. Injection of LH waves starts from $t=5.0$ s and the real-time control of q_{\min} starts from $t=5.5$ s, where q_{\min} is decreasing due to the current penetration just after the I_p ramp-up; see Fig. 2 (d). Since q_{\min} is larger than its reference at $t=5.5$ s, LH power decreases due mainly to the integration term in the control equation (1). At $t=6.2$ s, since q_{\min} becomes smaller than its reference, LH power starts increasing to raise q_{\min} , although q_{\min} continues decreasing until $t\sim 7.2$ s. Then, after $t=7.2$ s, q_{\min} starts increasing. Some part of this increase in q_{\min} can be attributed to an increase in off-axis bootstrap current caused by an increased pressure gradient for T_d control, as shown in Fig. 2 (b). Since the difference between q_{\min} and its reference gradually decreases after $t=7.2$ s, LH power gradually decreases due mainly to decrease in proportional term, according to the control equation (1). Finally, q_{\min} approached to its reference value (1.5) at $t\sim 10.3$ s, as shown in Fig. 2 (d).

Here, we examine the T_d control that starts at $t=7$ s as shown in Fig. 2. Figure 2 (a) shows the measured T_i at two spatial channels located at $r/a\sim 0.3$ and 0.57 . Figure 2 (b) shows the corresponding T_d and its reference. Due to the T_d control, T_d is maintained about 1 keV during $t=7-9$ s by the control of on-axis NB heating power as shown in Fig. 2 (c), while T_d is about 0.7 keV at the start of control. Although there is a small oscillation in T_d about its reference value by less than ± 0.1 keV, this is as expected from the choice of the proportional gain ($1/G_p^{Td}=0.05$ keV/unit) and ~ 50 ms delay of NB injection system. During $t=9-10.5$ s,

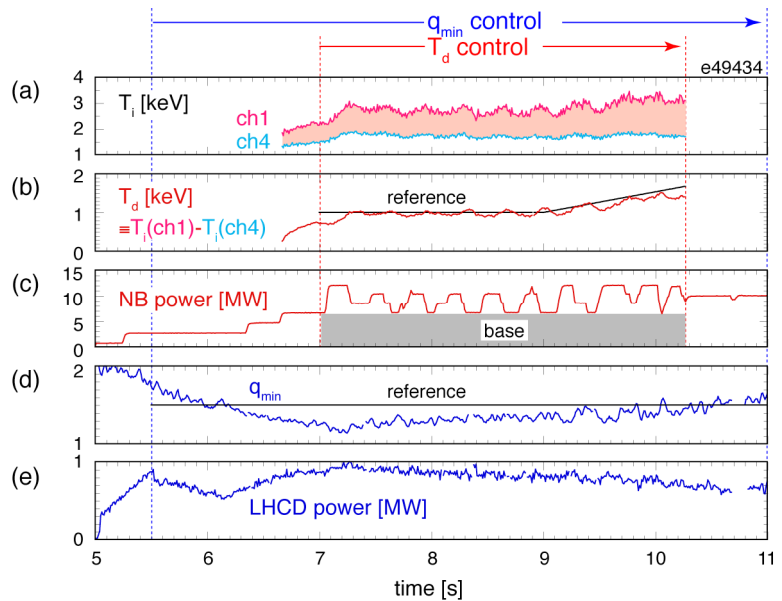


Fig. 2 Waveforms of discharge for simultaneous real-time control of T_d ($t=7-10.3$ s) and q_{\min} ($t=5.5-11$ s). (a) Ion temperature at two channels (ch1: $r/a\sim 0.3$, ch4: $r/a\sim 0.57$) used by real-time control. T_i measurement was terminated at $t\sim 10.3$ s due to the stop of diagnostic NB due to interlock on temperature of NB facing tiles. (b) Difference of ion temperature T_d (hatched in Fig. 2(a)) and its reference value ($T_{d,ref}$). (c) total NB heating power controlling T_d . Hatched part of the total NB power is the fixed base component. (d) q_{\min} and its reference value ($q_{\min,ref}=1.5$). (e) LHCD power controlling q_{\min} .

reference value of T_d is raised from 1 keV to 1.8 keV. According to this increase in $T_{d,ref}$, T_d increases by the increase in effective NB heating power as shown in Fig. 2 (c). This T_d control unexpectedly stopped at $t \sim 10.3$ s due to stop of the diagnostic NB for CXRS by interlock on NB-facing-tile temperature.

Figure 3 (a) shows the ion temperature profiles at the start of control ($t=7$ s) and during control ($t=8$ s and 10 s). ITB structure having steep pressure gradient is observed in $r/a \sim 0.3-0.5$ at $t=10$ s ($T_d=1.5$ keV, $\nabla T_i=5.5$ keV/m along the direction of CXRS diagnostic NB), and is controlled by the system. Figure 3 (b) shows q profile during the control, where q_{min} locates at $r/a \sim 0.15$ (MSE channel 11) as described in section 2. Although change in q_{min} is small, q at $r/a \sim 0.2-0.5$ clearly increases due to the controlled LHCD and the increase in bootstrap current. The ACCOME calculations show that the LH driven current is 0.14 MA ($\sim 17\%$ of I_p) at $t=8.0$ s and that the bootstrap current increases by 0.05 MA from 0.21 MA ($\sim 26\%$) at $t=8.0$ s to 0.26 MA ($\sim 32\%$) at $t=10.0$ s.

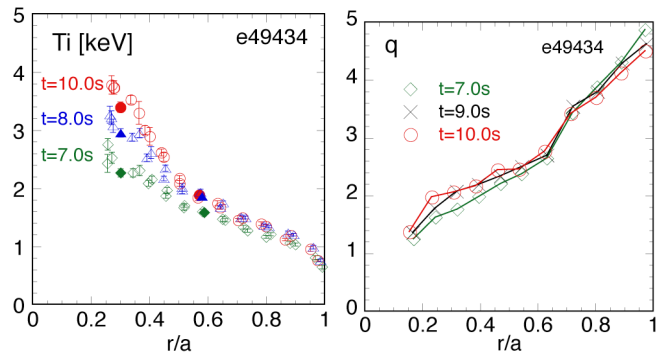


Fig. 3 (a) Ion temperature profile at $t=7.0$ s, 8.0 s, and 10.0 s. Two CXRS channels used by real-time control are shown by filled symbols. (b) Safety factor profile at $t=7.0$ s, 9.0 s, and 10.0 s. Real-time control used 11 MSE channels in order to evaluate q_{min} .

4. Summary and Discussion

Here, simultaneous real-time control of current and pressure profiles has been demonstrated. The minimum of the safety factor profile representing current profile evaluated by MSE diagnostics has been controlled by the off-axis LHCD power. The difference in ion temperature at two spatial location measured by CXRS diagnostics has been controlled by the on-axis heating power. One of reasons of successful control by this system could be attributed to the fact that the actuators are almost orthogonal in their functions (heating, current drive, and momentum input), as schematically described in Fig. 4. Since the functions of perpendicular NB and LHRF are not strongly coupled, independent application of two controls worked fine without taking into account of non-orthogonal term in control matrix, e.g. heating effect of current driver. Another reason would be that self-regulations on pressure and current profiles through bootstrap current are not strong in this plasma. However, strong self-regulations are expected AT operation scenarios in ITER and DEMO so that control of such plasma must be studied and realized in JT-60SA in advance to ITER and DEMO.

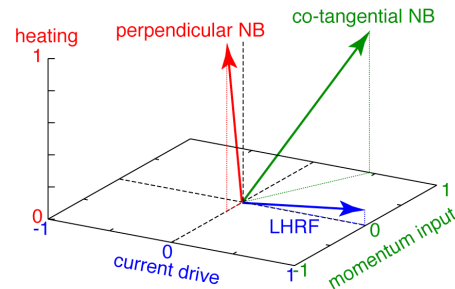


Fig. 4 Schematic image of function of actuators in this study. the functions of perpendicular NB and LHRF are not strongly coupled with each other.

References

- [1] Suzuki, T., et al., Nucl. Fusion **48** (2008) 045002
- [2] Yoshida, M., et al., accepted for publication in Fusion Eng. Des.

7.3 Particle Control Study in JT-60U towards Burning Plasma Control [1]

H. Takenaga and the JT-60 Team

Particle control study has been conducted in JT-60U to expand understanding of burning plasma controllability. In order to understand controllability of density profiles, mechanisms for regulating the density profile was investigated. The density peaking factor increased with decreasing the effective collisionality, which is consistent with ITG/TEM turbulence theory. This dependence indicates that a density profile in ITER should be peaked and also indicates that an increase in density reduces the density profile peakedness. Since fusion gain (Q_{DT}) significantly decreases with decrease of pressure profile peakedness [2], the reduction of the density profile peakedness associated with a density increase could modify the density dependence of Q_{DT} from the square of density. The evidence for existence of dependence of the density peaking factor on other parameters such as toroidal rotation, i.e. density peaking factor increased with counter-rotation, suggests possibility of density profile control in a fusion reactor. Tungsten impurity accumulation was observed with peaked density profiles, while light impurity accumulation was not observed even with peaked density profiles. Heavy impurity accumulation is one of the large concerns with peaked density profiles. In order to improve the controllability, supersonic molecular beam injection (SMBI) was installed in collaboration with CEA-Cadarache [3], which was expected as a faster response actuator for fuelling compared with gas-puffing. Confinement degraded with SMBI as well as gas-puffing, while it was kept constant with HFS shallow pellets, indicating flexible control using combined fuelling as accelerator and brake. Optimization of SMBI conditions to attain high confinement at high density is future issue for expanding the controllability of SMBI. The dynamic plasma-wall interaction experimentally observed was modeled using the 2-D divertor simulation code UEDGE. The simulations suggested that dynamic plasma-wall interaction makes the plasma responses to divertor pumping smaller and slower. By using the burning plasma simulation scheme [2], responses of burning plasmas to fuelling were investigated. It was demonstrated to reduce the simulated fusion gain for keeping the control margin with SMBI due to confinement degradation and flattening of pressure profile. In future, it is important to establish an effective particle control scenario using various fuelling methods and divertor pumping for burning plasma control considering the plasma responses highlighted in this study.

Reference

- [1] Takenaga H. and the JT-60 Team, J. Nucl. Mater. **390-391** (2009) 869.
- [2] Takenaga H., *et al.*, Nucl. Fusion **48** (2008) 035011.
- [3] Takenaga H., *et al.*, Section 4.4 in this JAEA-Review.

7.4 Demonstration of Real Time Control in Burning Plasma Simulation Experiments

H. Takenaga, M. Yoshida, M. Sueoka, Y. Kawamata, Y. Miyo

1. Introduction

In tokamak plasmas, “self-regulating” system is spontaneously formed due to strong linkages among various plasma parameters such as density, temperature, current density and rotation even in a DD non-burning phase. In a DT burning phase, self-heating due to alpha particle heating induces a new linkage, where a heating profile is determined by the pressure profile and the pressure profile is affected by the heating profile, in addition to the above linkages. Consequently, degree of the self-regulating system becomes higher in DT burning plasmas than in present DD non-burning plasmas. Burn control has to be performed under these linkages involving various physics in a fusion reactor. A burning plasma simulation (BPS) scheme has been developed in JT-60U [1], in order to experimentally introduce in DD non-burning plasmas the linkage between pressure and heating profiles similar to the alpha particle heating in DT burning plasmas. In this report, burn controllability was investigated using external heating and fuelling with the BPS scheme.

2. Analysis Results using 1.5D Transport Code

Since density is one of a few controllable parameters for burn control in a fusion reactor, density dependence of the fusion gain (Q_{DT}) is discussed in this section based on the results calculated using the 1.5 dimension transport code TOPICS. In the TOPICS calculation, the plasma parameters similar to the ITER baseline scenario were used, i.e. a plasma current of $I_p = 15$ MA, a toroidal magnetic field of $B_T = 5.3$ T, a major radius of $R = 6.2$ m and a minor radius of $a = 2$ m. The pressure profiles used in these analyses are shown in Fig. 1. A peaked profile shown by solid line in Fig. 1 was assumed with a ratio of $p(r/a=0)/p(r/a=0.7) \sim 2.5$. In order to investigate effect of the pressure profile, a more peaked profile with $p(r/a=0)/p(r/a=0.7) \sim 5$ was also used. Dependence of Q_{DT} on the density was calculated by assuming the fixed density and temperature profiles with constant ion temperature or constant confinement improvement factor over the IPB98(y,2) ELMy H-mode scaling ($HH_{98(y,2)}$). The ratio of deuterium density to tritium density was assumed to be 1:1. The central ion temperature ($T_i(0)$) was assumed in the range of 10-25 keV, where the DT fusion reaction rate is almost proportional to square of T_i . The external heating power and the density range were assumed to be 40 MW and $0.8-1.2n_{GW}$. Here, n_{GW} is the Greenwald density.

In the case of the pressure profile at $p(r/a=0)/p(r/a=0.7) \sim 2.5$, the value of Q_{DT} varied as $\sim n^2$ with a constant temperature as shown by solid lines in Fig. 2. In this figure, Q_{DT} is plotted as a function of volume averaged density normalized by the Greenwald density. The strong temperature dependence was observed in this $T_i(0)$ range. When the density was increased with a constant $HH_{98(y,2)}$, the dependence of Q_{DT} on the density became weaker than

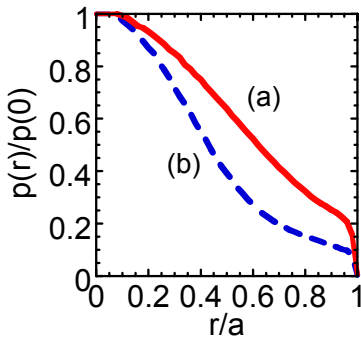


Fig. 1 Pressure profiles used in the analyses. Solid and dashed lines show the (a) peaked and (b) more peaked cases, respectively.

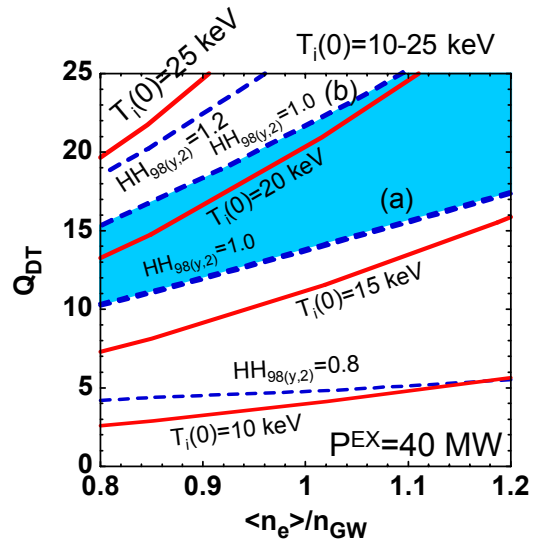


Fig. 2 Density dependence of Q_{DT} . Solid and dashed lines show the data with constant T_i and constant $HH_{98(y,2)}$, respectively. Hatched region indicates pressure profile effect (lower boundary : (a) peaked case and upper boundary : (b) more peaked case).

$\sim n^2$ as shown by dashed lines in Fig. 2. In the case with the more peaked pressure profile ($p(r/a=0)/p(r/a=0.7) \sim 5$), the value of Q_{DT} increased by 50-70% with the constant $HH_{98(y,2)}$ of 1.0 as shown by hatched region in Fig. 2. These results indicate that Q_{DT} strongly depends on not only the density but also confinement time and pressure profile due to T_i dependence of the DT fusion reaction rate. Therefore, it is important to incorporate the T_i dependence of the DT fusion reaction rate into the BPS scheme.

3. Burning Plasma Simulation Scheme

The BPS scheme has been developed using 2 groups of NBs, where one simulates alpha particle heating (P^α) and the other simulates external heating (P^{EX}), as shown in Fig. 3. JT-60U has 11 positive-ion-based NB units with the beam energy of 80-85 keV and the injection power of 2-2.2 MW/unit. In this scheme, the heating power for the simulation of alpha particle heating is changed stepwise, because NB power is controlled by the number of NB units. The control interval for the NB system is 10 ms and there is a delay time of 30 ms for the NB injection. The value of P^α was calculated as $n_e^2 f(T_i)$, where n_e is a line averaged electron density and f is a function for consideration of T_i dependence of the DT fusion reaction rate. Here, f is assumed to be proportional to T_i^2 . The line averaged electron density used here was measured in real-time with CO₂ laser interferometer with the tangential beam line passing through the central region. The central ion

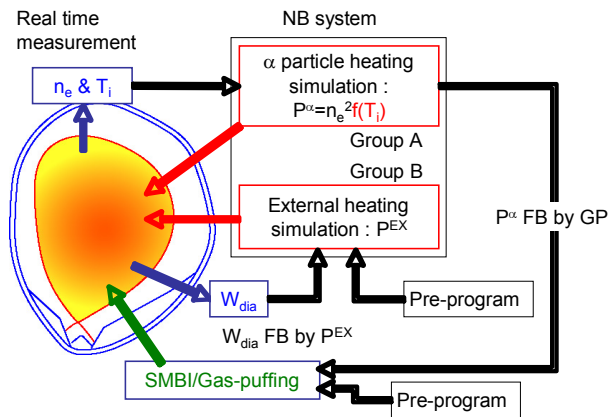


Fig. 3 Schematic drawing of the BPS scheme.

temperature at $r/a \sim 0.3$ was also measured in real-time with the fast charge exchange recombination spectroscopy system [2]. The value of P^{EX} was determined by pre-program or feedback (FB) control systems for stored energy (W_{dia}). Supersonic molecular beam injection (SMBI) [3] installed in collaboration with CEA-Cadarache and gas-puffing were used for fuelling. Feedback control of P^{α} using gas-puffing was also installed into the scheme. Gas-puffing was used for reducing P^{α} due to confinement degradation and flattening of the pressure profile rather than for increasing P^{α} in according to the density dependence shown in Fig. 2. The simulated fusion gain was defined here as $Q^{\text{sim}} = 5P^{\alpha}/P^{\text{EX}}$.

4. Burn Control using External Heating

The BPS experiments were first performed with the W_{dia} FB control in ELMy H-mode plasmas [4], where SMBI was used for investigation of fuelling effect. In the discharge without SMBI, W_{dia} was well controlled at a constant value by reducing P^{EX} against the increase in P^{α} . The value of Q^{sim} increased from 3.7 to 40 with relatively small change in $HH_{98(y,2)}$ from 0.87 to 0.83 and pressure profile peaking factor $\varepsilon = p(r/a=0.2)/p(r/a=0.8)$ from 8.5 to 9.8. SMBI decreased Q^{sim} from 24 to 5.1 due to confinement degradation ($HH_{98(y,2)} = 0.89$ to 0.72) and flattening of pressure profile ($\varepsilon = 9.1$ to 7.9).

Next, the BPS experiments were performed in reversed shear (RS) plasmas with $I_p = 1$ MA and $B_T = 3.7$ T. Figure 4 shows time evolution of the discharge, where the W_{dia} FB control was applied from $t = 4.3$ s and the BPS scheme was applied during $t = 5.5$ -8 s. The W_{dia} was sustained at constant value even in the discharge with strong internal transport barrier, where the linkage becomes stronger. In the BPS phase, oscillation of P^{EX} for keeping constant W_{dia} (constant ITB strength) seems to be large compared with that after $t = 8$ s due to stronger linkage induced by the BPS scheme. The value of Q^{sim} varied from ~ 10 ($t \sim 6.5$ s) to ~ 27 ($t \sim 6.8$ s) in this discharge. The oscillation of P^{EX} in the BPS scheme also seems to be larger in RS plasmas than in ELMy H-mode plasmas. In the previous scheme, where the alpha particle heating power was proportional to the DD neutron yield rate, larger oscillation of P^{EX} was observed in the RS plasma compared with that in the ELMy H-mode plasma [5]. The analysis using the TOPICS code indicated that the larger oscillation of P^{EX} in the RS plasma cannot be explained by the difference of the thermal diffusivity profiles or their temperature dependence. The quick change in the thermal diffusivity related to the change in the heating power could trigger the larger oscillation of P^{EX} in the RS plasma.

5. Burn Control using Gas-puffing

Based on the confinement degradation and flattening of the pressure profile with fuelling, the P^{α} FB control was developed using gas-puffing. In this FB control, the gas-puffing rate proportional to difference between reference and measurement of P^{α} was applied. In ELMy H-mode plasmas with $I_p = 1$ MA and $B_T = 2.1$ T, the P^{α} FB control was demonstrated with constant P^{EX} as shown in Fig. 5. Although time delay existed, P^{α} was

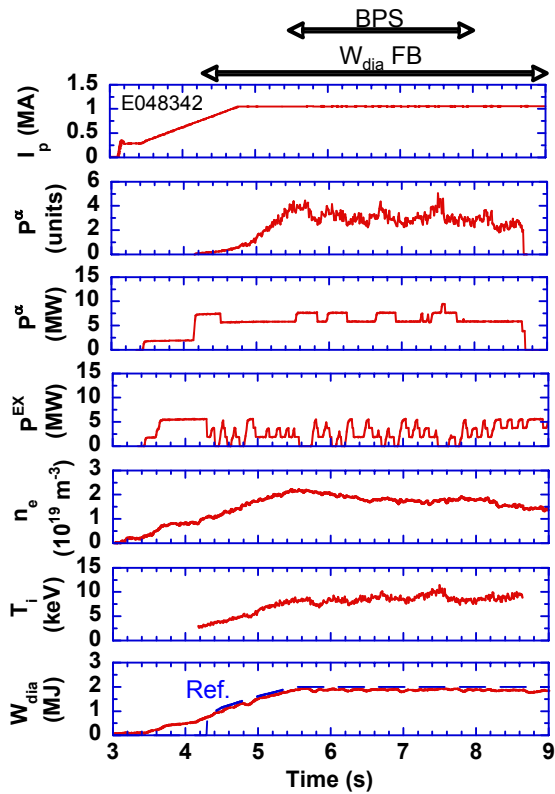


Fig. 4 Waveforms of the BPS experiment in the RS plasma with W_{dia} FB control using P^{EX} .

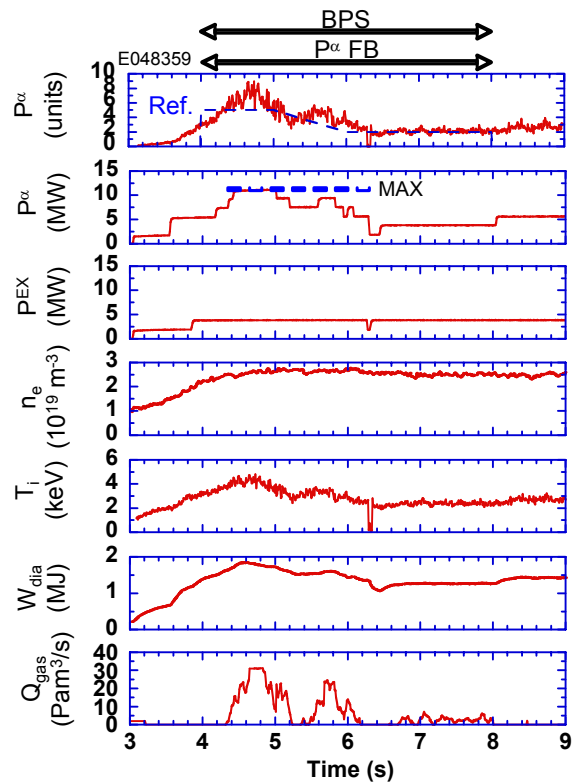


Fig. 5 Waveforms of the BPS experiment in the ELMy H-mode plasma with P^α FB control using gas-puffing.

decreased as reference due to confinement degradation and flattening of pressure profile induced by gas-puffing. Fast response actuator such as SMBI has to be developed for the FB control in future for improving the feedback control system.

6. Summary

The BPS scheme has been developed in JT-60U. The heating power for the simulation of alpha particle heating was calculated with consideration for temperature dependence of the DT fusion reaction rate using real-time measurements of density and ion temperature. In the BPS scheme, good controllability was demonstrated based on the FB control using external heating or gas-puffing. In future, it is important to demonstrate the flexible control by combining pellet injections (to keep confinement) and SMBI (to degrade confinement).

References

- [1] Takenaga H., *et al.*, Nucl. Fusion **48** (2008) 035011.
- [2] Yoshida M., *et al.*, Section 7.1 in this JAEA-Review.
- [3] Takenaga H., *et al.*, Section 4.4 in this JAEA-Review.
- [4] Takenaga H. and the JT-60 Team, J. Nucl. Mater. **390-391** (2009) 869.
- [5] Shimomura K., *et al.*, Fus. Eng. Des. **82** (2007) 953.

7.5 Off-axis NBCD Measurement

T. Suzuki, J. Hobirk ¹⁾, M. Murakami ²⁾, J. M. Park ²⁾, K. Shinohara,

T. Fujita, T. Oikawa, K. Hamamatsu, O. Naito

1) Max Planck Institute for Plasma Physics, Garching, Germany

2) Oak Ridge National Laboratory, Oak Ridge, U. S. A.

1. Introduction and Background

Neutral beam current drive (NBCD) is an important tool not only to sustain plasma current but also to tailor current profile for establishing advanced tokamak operation scenarios in tokamak plasmas. Especially optimization of current profile using off-axis NBCD is envisaged in ITER and JT-60SA. In spite of the importance of the off-axis NBCD, its driven current profile has not been fully recognized yet. This issue was first raised by ASDEX Upgrade (AUG), where disagreement in MSE pitch angles between the experimental measurement and theoretical prediction was observed, in a certain condition (strong heating in low triangularity plasma) [1]. (*Recently, this disagreement in AUG can be recognized by a hypothesis of fast ion transport (redistribution)* [2].) Considering the importance of the off-axis NBCD, off-axis NBCD measurement was conducted in 2006 in JT-60U. In the experiment, we found the following facts [3].

- (1) Spatially localized off-axis NBCD is measured, for the first time, by motional Stark effect (MSE) diagnostics using both loop-voltage-profile analysis, and direct analysis of MSE pitch angle change.
- (2) The NBCD location by MSE diagnostics was consistent with neutron emission profile diagnostics [4].
- (3) Integrated off-axis NBCD current using MSE diagnostics was consistent with both ACCOME calculation and measured change in loop voltage.
- (4) However, the measured NBCD location was outside (by about 0.15 in r/a) than the calculated one by the ACCOME code.
- (5) Off-axis NBCD measurements at different I_p (0.8MA and 1.2MA) were done, but the similar results were obtained. In both I_p cases, no MHD activity (such as sawtooth) except ELM was observed.

Based on the above backgrounds, and on the importance of the off-axis NBCD in ITER, joint experiment SSO-6 (now IOS-5.1) started under ITPA SSO (now IOS) topical group activity from 2007. The off-axis NBCD measurement reported here is conducted as a part of this activity on May 2008, as well as to clarify the unresolved issue (item (4) above) in the 2006 campaign. J. Hobirk from AUG participated this experiment on site, and M. Murakami and J. M. Park remotely from DIII-D. In this report, result of analysis on the item (4), the NBCD location, is mainly described.

2. Experimental Results

In this campaign, systematic scans were carried out on (i) NBCD location (on-axis, slightly off-axis, and off-axis), (ii) beam energy ($E_b \sim 85$ keV using P-NB and ~ 350 keV using N-NB), (iii) NB heating power affecting plasma beta and (iv) plasma triangularity ($\delta = 0.25$ and 0.45). The scanned parameters are summarized in Table 1 and Figure 1, where two parameters, NBCD location and beam energy, are not fully separated. Figure 2 shows the magnetic configurations at different triangularity ($\delta = 0.25$ and 0.45), with superimposed on NB trajectories. In this experiment, high power NB mode (~ 2.5 MW/unit but for 10 s period) is selected in order to maximize NBCD current. Within this 10 s period, toroidal magnetic field (3.7T) is set as high as possible in order to avoid sawtooth instability. Plasma current (1.2MA) is set as large as possible (under $\delta = 0.45$ configuration), in order to minimize the shift of the drift surface. As a result, q_{95} is 5.6-5.8 for both high and low δ cases ($q_{95} \sim 5.4$ at $I_p = 1.2$ MA, $\delta \sim 0.35$ in 2006 campaign). Line averaged electron density varies in a range 1.2 - $2.3 \times 10^{19} \text{m}^{-3}$ (c.f. $2.2 \times 10^{19} \text{m}^{-3}$ in 2006), and is higher in higher heating power cases. It should be noted that configuration with smaller minor radius was employed in 2006 than in 2008 (as shown in Fig. 2) in order to investigate far off-axis NBCD.

| | $E_b \sim 85 \text{keV}$ | $E_b \sim 350 \text{keV}$ |
|--------------------------------------|--------------------------|---------------------------|
| on-axis ($r/a \sim 0$) | P-NB#9 | - |
| slightly off-axis ($r/a \sim 0.3$) | - | N-NB(U) |
| off-axis ($r/a \sim 0.5$) | P-NB#10 | - |

Table 1 Scanned parameter regime on NBCD location (on-axis, slightly off-axis and off-axis) and beam energy (E_b).

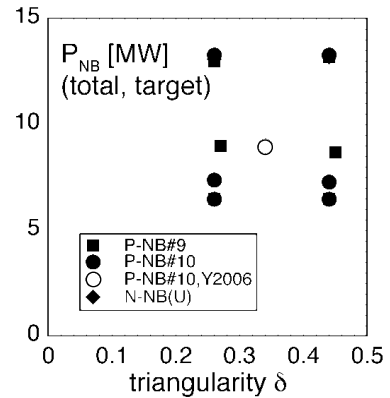


Fig. 1 Scanned parameter regime on P_{NB} and δ , using various NBCD shown in Table 1.

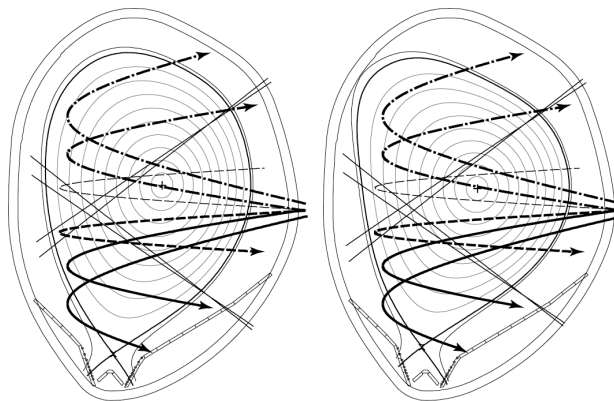


Fig. 2 magnetic configurations (left: $\delta = 0.25$, right: $\delta = 0.45$) with NB trajectories (dot-dashed curves: on-axis NBCD using P-NB#9, thick dashed curve: slightly off-axis NBCD using N-NB(U), and thick solid curves: off-axis NBCD using P-NB#10).

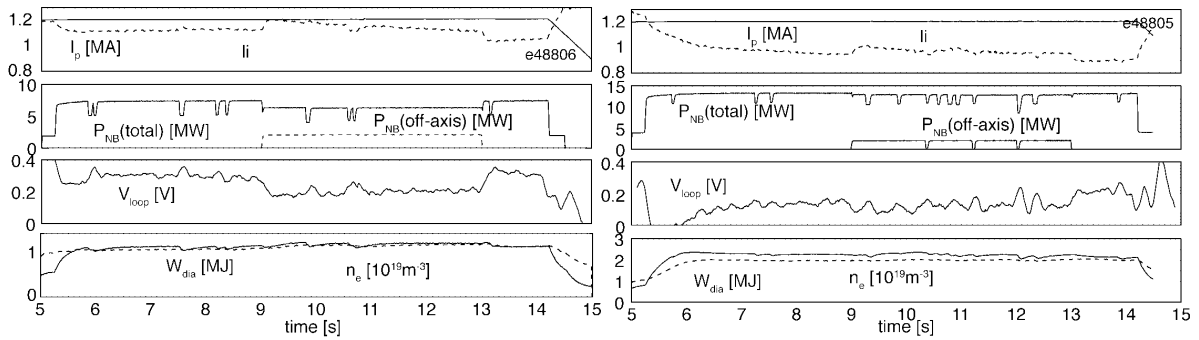


Fig. 3 Waveforms of two discharges at low triangularity ($\delta=0.25$) for low power case (left) and high power case (right). From the top to the bottom: plasma current I_p (solid curve), internal inductance li (dotted curve), total heating power $P_{NB}(\text{total})$ (solid curve), NBCD power $P_{NB}(\text{off-axis})$ (dotted curve), loop voltage V_{loop} , diamagnetic stored energy W_{dia} (solid curve), line average electron density n_e (dotted curve).

Figure 3 shows typical waveforms of discharges for off-axis NBCD measurement. Left figures are for low power at low triangularity, while right figures for high power. Application of NBCD starts at $t=9.0$ s sufficiently after the start of I_p flattop ($t=3.0$ s) in order to minimize effect of current penetration on current profile change. During the NBCD, one or two units of NBs almost perpendicularly injected to the toroidal field are stopped in order to minimize change in the bootstrap current through change in the plasma pressure. Thus, as shown in Fig. 3, diamagnetic stored energy W_{dia} and electron density n_e are kept unchanged. Therefore, decrease in loop voltage V_{loop} shown in Fig. 3 and change in total current profile measured by the MSE diagnostics (described hereafter) are mainly caused by the application of the NBCD itself. Drop in V_{loop} during NBCD is larger in the low power case than in the high power case, since n_e is lower and NB driven current is larger in the low power case. Figures 4 (a) and (b) show temporal evolution of current density and safety factor profiles measured using MSE diagnostics, respectively. Increase in current density around $r/a \sim 0.4$ is observed during the off-axis NBCD application. With this change in current profile, the safety factor (q) outside $r/a \sim 0.4$ becomes smaller and the q profile broadens. This broadening of q profile brings about increase in internal inductance ($li(1)$), as shown in Fig. 3. Corresponding NB driven current

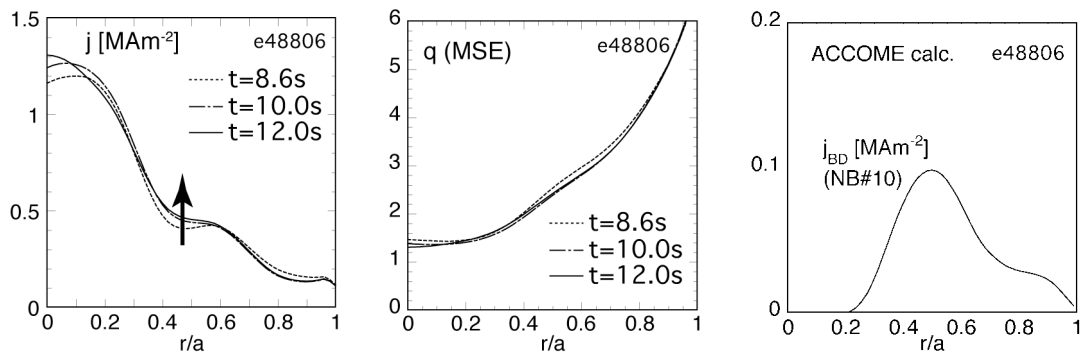


Fig. 4 (a) change in current density profile and (b) safety factor profile measured using MSE diagnostics in low power, low δ case (E048806, left of Fig. 3); $t=8.6$ s: just before the start of off-axis NBCD, $t=10.0$ s: after 1 s of the start of off-axis NBCD, $t=12.0$ s: after 3 s of the start of off-axis NBCD. (c) NB driven current profile calculated using the ACCOME code.

profile calculated using the ACCOME code is shown in Fig. 4 (c), where the peak in driven current is $r/a \sim 0.5$.

This change in current profile is more clearly observed, when we plot change in current density profile (dj) with respect to that at $t=8.6$ s just before the start of NBCD. Figure 5 shows increase in j with light color and decrease in dark color. Increase in j at $r/a \sim 0.4$ only during the NBCD ($t=9-13$ s) is clearly observed, which is a result of off-axis NBCD. However, slight increase in j at $r/a \sim 0.8$ during $t \sim 11-14$ s in Fig. 5 has not been recognized yet. This spatiotemporal change is deduced directly from the MSE

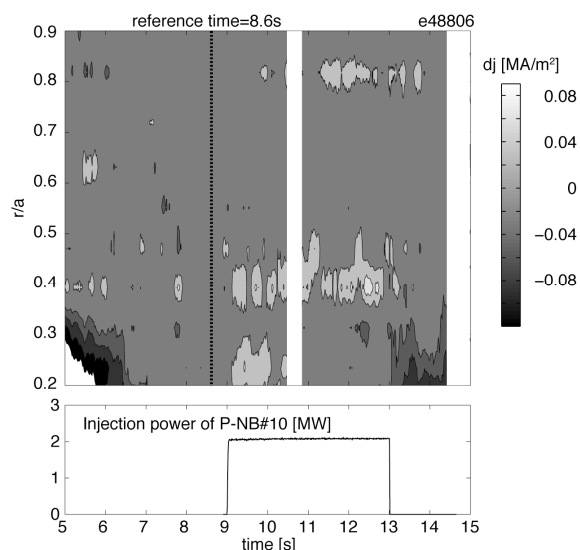


Fig. 5 Spatiotemporal change in current density with respect to the current density profile at $t=8.60$ s shown as dotted curve in Fig. 4 (a) for off-axis NBCD at low power and low δ case.

signal, and small change in j can be detected. To be noted here is that this increment in j (dj) is not the NB driven current but the change in total current due to the application of NBCD, however, peak in dj will be a good measure of NBCD location. To investigate relation between measured NBCD location and the calculated one, the peak location of the total current profile change (dj) and the peak of the calculated NB current density by ACCOME are plotted in Fig. 6. Results on off-axis NBCD using P-NB#10 and slightly off-axis NBCD using N-NB(U) are included in Fig. 6. Both the measurement and the calculation roughly agrees, but some of them (e.g. N-NB(U) at high δ and high power case) still scatter, as well as a result in 2006. Under the current analysis, it is difficult to come to some conclusion. Further analysis is ongoing to evaluate NBCD profile itself using the loop-voltage-profile analysis, not only the change in total current profile. Crosscheck using neutron emission profile diagnostics [4] representing beam population will also be done.

References

- [1] Hobirk, J., et al., Proc. 30th EPS Conf. vol. **27A** (2003) O-4.1B; Günter, S., et al., Proc. 31st EPS Conf. vol. **28G** (2004) O-1.02; Günter, S., et al., Proc. 32nd EPS Conf. vol. **29C** (2005) P-4.075.
- [2] Günter, S., et al., Nucl. Fusion **47** (2007) 920.
- [3] Suzuki, T., et al., Nucl. Fusion **48** (2008) 045002.
- [4] Ishikawa, M., et al., Rev. Sci. Instrum. **73** (2002) 4237.

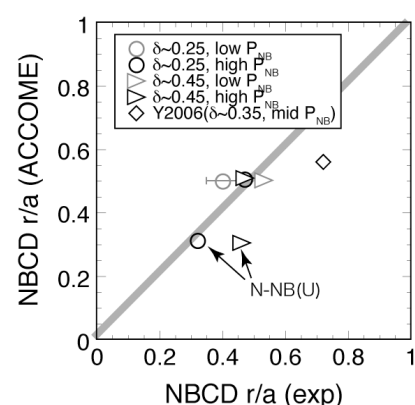


Fig. 6 Comparison of measured NBCD location determined from the change in total current as shown in Fig. 5 and calculated NBCD location evaluated using the ACCOME code at different conditions on P_{NB} and δ . A result in 2006 using similar analysis is shown by a square.

7.6 Plasma Current Start-up Experiment by ECH

T. Maekawa¹⁾, H. Tanaka¹⁾, M. Uchida¹⁾, S.Nishi¹⁾, Y.Takase²⁾, K. Hanada³⁾, S.Ide

1) Kyoto University, 2) The University of Tokyo, 3)Kyushu University

1. Introduction

Removal of the central solenoid (CS) from tokamak reactors is an attractive option to simplify the central structure of reactors. However, we need alternative methods to start-up the plasma current. ECH/ECCD is potentially an attractive candidate for this purpose since plasma initiation and current start-up and ramp-up could be realized simultaneously by an injection of microwave power from a small launcher remote from the plasma. It is also beneficial for future superconducting tokamak reactors even if plasma current can be started up to a level only sufficient for production of initial closed flux surface without the induction from CS. While a number of experiments in small devices have been done and successful in production of closed flux surfaces [1-3], it is highly required to demonstrate its feasibility for reactors in large devices such as JT-60U. Previously, we attempted ECH start-up experiments on JT-60U, where we used VT and VR coils for vertical fields B_v and examined various combinations of currents of these coils as well as various locations of electron cyclotron resonance (ECR) layers. We found that combination of the VT-out coil (no use of inboard VT coil) and the VR coil and the ECR location around $R=2.8\text{m}$ gave relatively good results of $I_p=17\text{ kA}$ [4]. In this experimental campaign we have attempted again an ECH start-up experiment under the same combination of the coils, in which some new observations have been obtained and analyses have been conducted as follows.

2. Experimental Results

Figure 1 shows a typical discharge in which I_p reaches 21 kA by the microwave pulses of the oblique O-mode polarization from four 110 GHz gyrotrons (0.3-0.8 MW for each tube and 2-4 seconds duration). Plasma images on the CCD camera shows that discharge takes place at the ECR layer immediately after ECH is turned on and the plasma expands toward the lower field side and reaches the outboard wall in 0.1 second after discharge initiation. The radial position of the current center (R_j) in figure 1 shows that plasma current initiates near the ECR layer and then moves quickly toward the outboard wall in accordance with the expansion of plasma as observed on the CCD images. The current position then moves toward the ECR layer as I_p increases. When I_p reaches 21 kA a flash appears suddenly on the top wall as shown by an arrow in the plasma image at $t=2.08\text{ s}$. The flash point is near the top of the current profile. The flash disappears in the next frame of the CCD camera images (The framing speed is 30 frames per second), and then I_p quickly decreases. In these times the CCD

image shows that the plasma shrinks towards ECR layer as shown in the plasma image at $t=2.28$ s. Finally I_p disappears. Oblique X-mode injection was also examined with the same discharge condition except for the injection mode. The maximum current was $I_p=13$ kA, which was significantly lower compared with the oblique O-mode case.

3. Analyses and Discussions

Wave theory predicts that in the case of oblique X-mode injection, the wave power is reflected at the right-hand cyclotron cutoff layer before arriving at the ECR layer, while in the case of oblique O-mode injection, almost injection power remains after passing through the ECR layer and reaches the inboard wall since in this mode very small ECR absorption is expected in the present low temperature plasma. The optical depths of both modes upon passing through the ECR layer are estimated to be $T_O \sim 1.3T_e$ and $T_X \sim 400T_e$, respectively, where T_e is in keV and $n_e=10^{19} \text{ m}^{-3}$ is assumed, showing that absorption of X-mode is quite large even if T_e is as low as $T_e=0.01$ keV, while O-mode absorption is negligible. Upon mirror reflection on the inboard wall with the present injection angle (~ 20 degrees from perpendicular direction to the toroidal field at the injection points to the drift direction of the expected current carrying electrons), $\sim 80\%$ of the remained O wave power is mode converted into X wave power. The linear theory predicts that this reflected X-wave can reach the ECR layer and is strongly absorbed. The discharge may be maintained by this absorption.

The flash event quenched the discharge, suggesting the ejection of a large amount of impurities from the wall by a strong bombardment of energetic electrons. While interaction between the wall and the plasma always takes place at the ECR layer as observed in the top photo in figure 1, the plasma current still increases, indicating that the interaction is due to the thermal particles and not fatal. Although the field structure is still open near the time of the flash event, it is deformed significantly from the vacuum field. Therefore, these energetic electrons might be mirror-trapped at the local mirror fields and heated via the EC resonance at the Doppler shifted frequencies. The resonance condition predicts that such heating is possible for the mirror trapped energetic electrons at ~ 100 keV and the pitch angles of $\theta \sim 70^\circ$ when the wave parallel refractive index is $N_{\parallel} > 0.8$. Such high N_{\parallel} waves might be generated after random reflections at complicated wall structures of the vacuum vessel. Some portion of the current may be carried by the toroidal precession of these energetic electrons.

Figure 2 shows the evolution of equilibrium characteristics of the plasma loop in figure 1 as compared with the extended Shafranov formula [5];

$$B_V = (\mu_0 I_p / 4\pi R) \{ G(R/a, \kappa, l_i) + \beta_p \}, \quad \beta_p = 8\pi S \langle P \rangle / \mu_0 I_p^2$$

$$[G(R/a, \kappa, l_i) = \ln(8R/a) + l_i/2 - 3/2, \text{ in the case of Shafranov formula}].$$

While this figure shows that the B_V level for the control of plasma loop is still appropriate,

somewhat smaller B_v level might be more advantageous to prevent the flash event via earlier closure of field line at a smaller current level where energetic electrons are also fewer. Once a closed flux surface is formed direct bombardment may not take place.

References

- [1] Yoshinaga, T. et al., Phys. Rev. Letters Vol.96 (2006) 125005.
- [2] Tanaka, H. et al., IAEA Fusion Energy Conf. (Chengdu 2006), IAEA-CN-149, EX/P6-6.
- [3] Ejili, A., Nucl. Fusion Vol.46 (2006) 709.
- [4] Maekawa, T. et al. JAEA-Review (Review of JT-60U Experimental Results in 2005 and 2006)55.
- [5] Hirshman, S.P. and Neilson, G.H. Physics of Fluids Vol.29 (1986) 790.

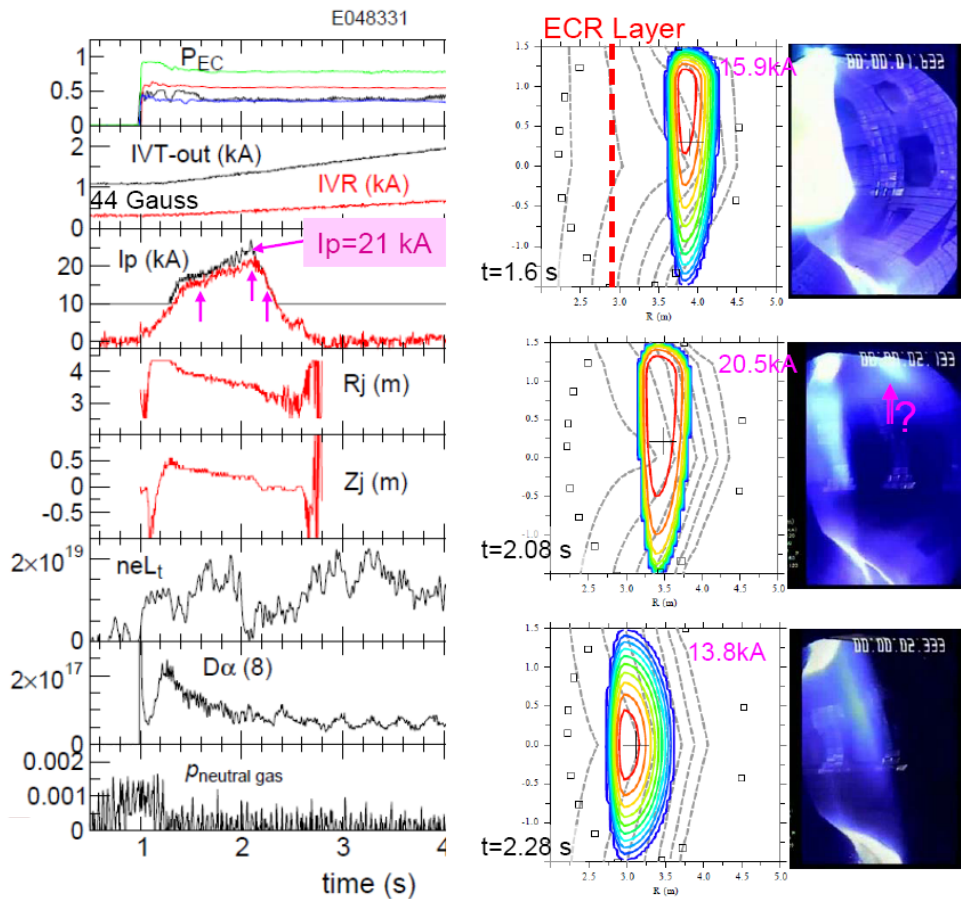


Fig. 1. Time evolutions of ECH power (P_{EC}), VT-out and VR coil currents, plasma current, radial and horizontal locations of the plasma current center (R_j and Z_j), line density along tangential chord on the mid-plane (neL_t), D-alpha emission and deuterium gas pressure. Current profiles (the center is denoted by +) with poloidal projections of field lines and plasma images at the times of $t=1.6s$, $2.08s$ and $2.28s$ are also shown.

$$RB_V = \frac{\mu_0}{4\pi} G(R/a, \kappa, \ell_i) I_P + \frac{2S\langle P \rangle}{I_P}$$

Current loop expanding term + Pressure ballooning term

$$RB_V [10^{-4} m \cdot T] = G(R/a, \kappa, \ell_i) \cdot I_P [kA] + \frac{2S\langle P \rangle [0.1 m^2 \cdot Pa]}{I_P [kA]}$$

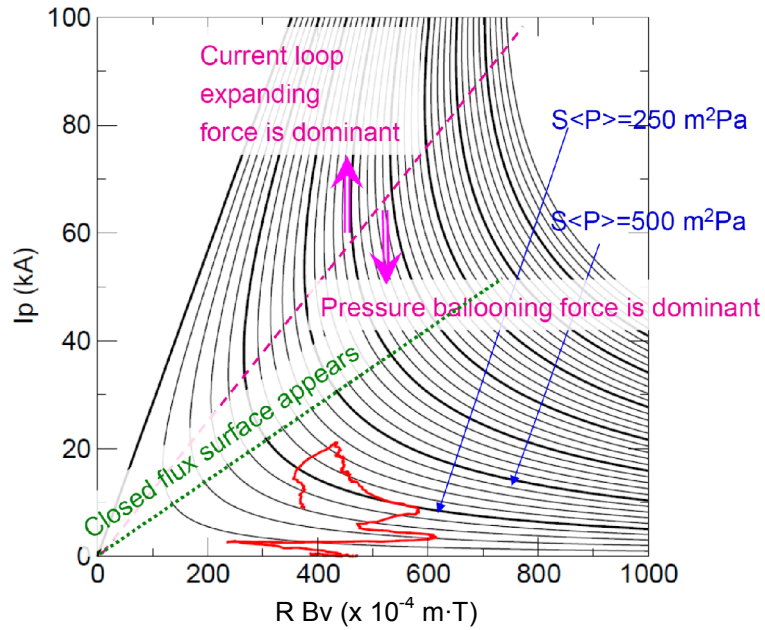


Fig. 2. Comparison of equilibrium characteristics of plasma loop with the extended Shafranov formula for the discharge in figure 1. Contours show the product of the plasma cross section and the averaged plasma pressure. The horizontal axis shows the product of the radial coordinate of plasma current center and the external vertical field B_v at this location. $G=3.5$

7.7 ECH Wall Conditioning Discharges in JT-60U [1]

K. Itami, N. Asakura, H. Tamai, S. Moriyama, A. Kaminaga

In order to reduce impurity influx to the core plasmas and to control particle recycling level, first wall conditioning by the hydrogen and helium discharges, such as glow discharge cleaning (GDC) and Taylor discharge cleaning (TDC) are widely used in fusion devices [2]. For the control of the recycling level, He TDC plasmas with $I_p = 50$ kA, $B_T = 0.7$ T and $t_{\text{pulse}} = 20$ ms are applied for 3 – 7 minutes after disruptive discharges in JT-60U.

However, GDC cannot be utilized due to the stationary toroidal field in superconducting tokamaks, such as ITER and DEMO. There is also restriction on the applicable voltage on the superconducting poloidal coils and the toroidal electric field must be below 0.3 V/m. TDC plasmas won't break down in such low electric field conditions.

In order to address these issues, wall conditioning discharges under high $B_T = 3.6$ T were investigated by using the 110 GHz ECRF system of JT-60U in 2000. Homogeneous He plasmas for wall conditioning were reproducibly obtained with the fundamental ECH when the horizontal field (0.5 % of B_T strength) was applied. It was found that $2.4 \text{ Pa}\cdot\text{m}^3$ of He gas puff was optimum in terms of homogeneous plasma and the maximum H_2 outgas amount with $P_{\text{ECRF}} = 0.59$ MW and $t_{\text{pulse}} = 1$ s. With $P_{\text{ECRF}} = 1.27$ MW and $t_{\text{pulse}} = 1$ s, the efficiency of H_2 outgas in a minute was found to be as large as 79 % of that in He TDC, which had been routinely used in JT-60U.

In 2008, additional experiment was carried out to investigate the horizontal field effect with reduced horizontal field (0.3 % of B_T strength) and enhanced P_{ECRF} . It was found that the horizontal field is crucially important to expand He plasma toward the high field side from the fundamental ECH resonant surface.

The ECH wall conditioning discharge with $P_{\text{ECRF}} = 2.5$ MW and $t_{\text{pulse}} = 1.5$ s was applied after the plasma disruption with $W = 3.3$ MJ. The following experimental plasma was successfully started up with 0.5 V/m of ohmic electric field by applying ECH pre-ionization. While this start-up field is slightly higher than that required for ITER, 0.3 V/m, ECH start-up assist with 0.26 V/m has been successful in JT-60U [3]. Therefore we expect that the wall recovery by the ECH wall conditioning discharges is a promising technique for the fusion reactors. Further studies, including ECH power scan, will be necessary to improve accuracy for assessment of this technique for ITER and DEMO.

References

- [1] Itami, K., et al., J. Nucl. Mater. **390-391**, 983 (2009).
- [2] Winter, J., Nucl. Mater., **161**, 265 (1989).
- [3] Kajiwara, K., et al. Nucl. Fusion, **45**, 694 (2005).

8. Divertor and SOL Plasmas

8.1 Balance of Ionization and Recombination of Carbon Ions in High Density Peripheral Plasmas of the JT-60U Tokamak [1]

T. Nakano, H. Kubo, N. Asakura and K. Shimizu

In a fusion reactor, heat and particles exhausted from the main plasma are transported predominantly along the magnetic field lines through the peripheral plasma and finally into the divertor plasma. In order to suppress the damage of the target plates, the divertor plasma is required to be cooled sufficiently. One of the most straightforward methods is radiative cooling, in particular, by impurities. It has been found that the line-radiation from C^{3+} is one of the dominant energy loss processes in a tokamak divertor with carbon target plates. However, the source of C^{3+} has not been investigated. In the present work, the ionization flux of C^{2+} into C^{3+} and the recombination flux of C^{4+} into C^{3+} were compared to determine the C^{3+} source. Further the contribution of C^{2+} and C^{3+} to the total radiation power was determined.

The spectra from the radiative zone of the divertor plasma of an L-mode discharge with a plasma current of 1.0 MA, a toroidal magnetic field of 3.5 T, an NB heating power of 4.5 MW and a line-averaged electron density of the main plasma of $3.0 \times 10^{19} \text{ m}^{-3}$ were observed with a vacuum-ultra-violet spectrometer and a visible spectrometer with absolutely calibrated sensitivities. The intensity ratio of C III (C^{2+}) lines was analyzed with a collisional-radiative model, and indicated that the C III line emission was due predominantly to the ionizing plasma component (an excited state originates from the ground state, and is finally lost through ionization by an electron impact) with an electron temperature and density of 7.8 eV and $1.0 \times 10^{20} \text{ m}^{-3}$, respectively. Similar analysis for C IV (C^{3+}) indicated that the C IV line emission from $n \leq 4$ levels (n : principal quantum number) were due to the ionizing plasma component and that from $n \geq 5$ levels the recombining plasma component (an excited state is produced by volume recombination, and finally de-excites to the ground state) with an electron temperature and density of 6.3 eV and $7.8 \times 10^{20} \text{ m}^{-3}$. The difference of the evaluated electron temperature and density presumably resulted from the difference of the spatial distribution of the C III and the C IV emission in the observation volume of the VUV spectrometer (~ 12 cm on the poloidal cross-section).

From the above results, the balance of the ionization and the recombination fluxes and the radiation power were determined and the results are summarized in Fig. 1. The C^{3+} production flux, *i.e.*, the recombination flux of C^{4+} into C^{3+} and the ionization flux of C^{2+} into C^{3+} were, respectively, $2.2 \times 10^{20} \text{ m}^{-2} \text{ s}^{-1}$ and $1.8 \times 10^{20} \text{ m}^{-2} \text{ s}^{-1}$. In contrast, the C^{3+} loss flux, *i.e.*, the recombination flux of C^{3+} into C^{2+} was not detected and the ionization flux of C^{3+} into C^{4+} was $0.02 \times 10^{20} \text{ m}^{-2} \text{ s}^{-1}$. Hence the C^{3+} production flux was higher by two orders of magnitude than C^{3+} loss flux, suggesting

significant transport loss of C^{3+} from the radiative zone. The line-radiation power from the ionizing plasma component of C^{2+} and C^{3+} were evaluated to be, respectively 30% and 60% of the total radiation power, measured by a bolometer, while the line-radiation power from the recombining plasma component is only a few percent.

In conclusion, the dominant radiator, C^{3+} , is produced by ionization of C^{2+} and recombination of C^{4+} at similar rates around the radiative zone, and that C^{2+} is the second dominant radiator. Further the transport loss of C^{3+} will be investigated by an impurity transport code (IMPMC), in addition to comparison of the radiation power and atomic processes.

References

[1] Nakano, T. *et al.*, *J. Nucl. Mater.* **390-391**, 255 (2009).

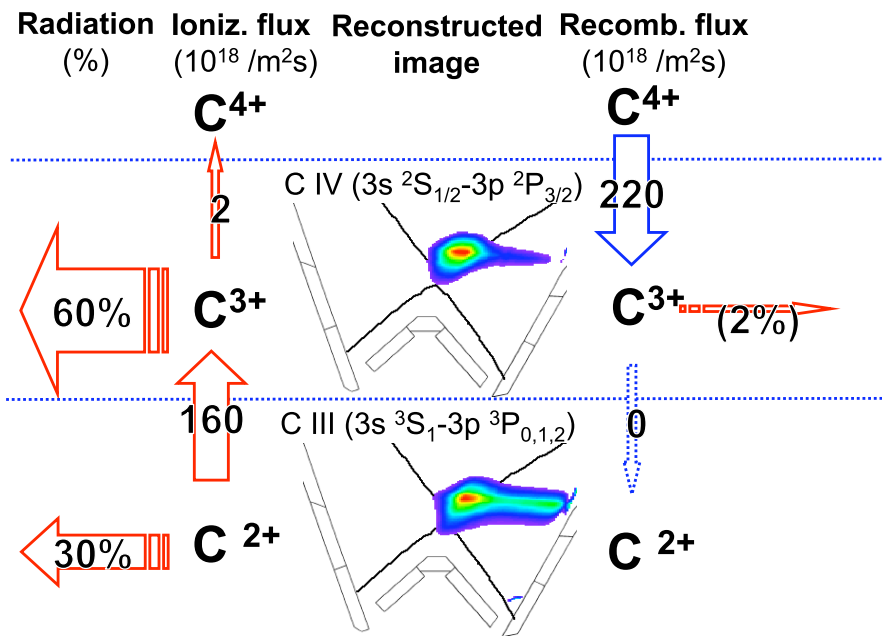


Fig. 1: From the left, the radiation power from the ionizing plasma component, the ionization flux, the reconstructed spatial distribution of the emissivity, the recombination flux, and the radiation power from the recombining plasma component of C^{3+} (upper) and C^{2+} (lower).

8.2 Fluctuation Characteristics of the L-mode and H-mode SOL Plasmas

H. Tanaka¹⁾, N. Ohno¹⁾, N. Asakura, Y. Tsuji¹⁾, H. Kawashima, S. Takamura²⁾, Y. Uesugi³⁾

1) Nagoya University, 2) Aichi Institute of Technology, 3) Kanazawa University

1. Introduction

Intermittent convective plasma transport, so-called “plasma blobs”, have been reported in scrape off layers (SOLs) of several tokamak devices by using Langmuir probe and imaging measurements. This non-diffusive transport is thought to play a key role for cross-field transport making a density profile in SOL much flatter, and so it has strong influence on the recycling flux and impurity generation from a first wall. Characteristics of blobby plasma transport was investigated by application of statistical methods to time series of ion saturation current because the positive spikes appear in the electrostatic fluctuation when plasma blobs pass by the probe electrode.

Theory [1] predicts that plasma blobs in tokamak devices move toward the first wall at the low-field-side (LFS) due to $\mathbf{E} \times \mathbf{B}$ drift, where the charge separation in the blobs is driven by gradient and curvature of magnetic fields. Hence, the characteristic of blobby plasma transport at the high-field-side (HFS) SOL is expected to be quite different with that at the LFS SOL. Therefore, the comparison of electrostatic fluctuations between the LFS and HFS SOLs is important for understanding of generation and propagation of the plasma blobs. The measurements of the electrostatic fluctuation at the HFS were reported only in Alcator C-Mod [2], T-10 tokamak [3].

We report the detailed comparison between intermittent fluctuation characteristics both at the HFS and LFS SOLs in addition to near the X-point in L-mode plasmas and between-ELMs in ELMy H-mode plasma.

2. Experimental Setup

Three reciprocating Mach probes are installed near the LFS midplane, above the HFS baffle and just below the X-point in figure 1(a) [4]. The fluctuation characteristics were

mainly investigated from fast sampling (500 kHz) signals of the ion saturation current (j_s), applying a constant DC voltage of 150–180 V. Each reciprocation probe has 5 electrodes as shown in figure 1(b), and four electrodes are used as two sets of double probe facing upstream

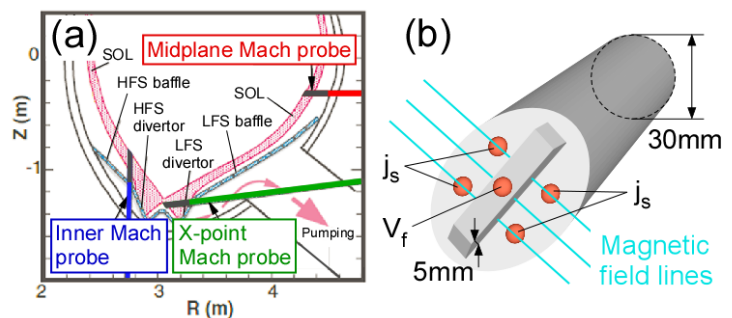


Fig.1. (a) Location of the reciprocating probes and (b) probe structure.

side and downstream side of the magnetic field lines. Here, upstream and downstream sides are defined as the double probe facing the midplane and divertor, respectively. Floating potential V_f is also measured with the electrode at the top.

3. Poloidal Dependence of Fluctuation Characteristics in L-mode Plasmas

Fluctuations of ion saturation currents j_s were measured at the three poloidal locations in L-mode plasmas (shot number #45723 for HFS SOL and LFS SOL, shot number #48473 for X-point as reference). Plasma parameters are given in Table I.

Table I. The list of experimental conditions.

| Shot number | n_e [10^{19}m^{-3}] | I_p [MA] | B_t [T] | P_{NB} [MW] |
|-------------|----------------------------------|------------|-----------|----------------------|
| 45723 | 1.7 | 1.0 | 3.2 | 4.0 |
| 48473 | 2.1 | 1.0 | 3.2 | 3.5 |
| 49819 | 2.0 | 1.0 | 1.8 | 5.2 |

Figure 2 shows radial profiles of the averaged ion saturation currents $\langle j_s \rangle$ and fluctuation amplitude normalized by the averaged value ($\delta j_s / \langle j_s \rangle$). Here, the double probe data at the upstream side is used for this analysis. Δr is a distance from separatrix at the LFS midplane. The each probe positions are mapped to the LFS midplane by the tracing of magnetic field lines. $\delta j_s / \langle j_s \rangle$ at the LFS is much larger than one at the HFS, similarly to the experimental results in the references [2, 3].

Figure 3 shows the probability density functions (PDFs) of j_s at each poloidal position, where Δr is selected to be 40 mm, 40 mm and 10 mm, respectively. The PDF at the LFS SOL is skewed positively, indicating that non-diffusive plasma transport (blobby transport) frequently occurs at the LFS midplane.

Skewness and flatness are defined by the 3rd and 4th moments of PDF, i.e. $S = \langle \tilde{j}_s^3 \rangle / \langle \tilde{j}_s^2 \rangle^{3/2}$ and $F = \langle \tilde{j}_s^4 \rangle / \langle \tilde{j}_s^2 \rangle^2$, respectively. When large positive bursts occur in the fluctuation signal, PDF is positively skewed and becomes flatter compared with the Gaussian distribution, leading to $S > 0$ and $F > 3$. Skewness at the LFS SOL becomes maximum around $\Delta r = 5$ cm and is positive value in wide radii ($\Delta r < 10$ cm) in Fig. 2(c). On the other hand, skewness and flatness of the PDF at the HFS SOL are close to 0 and 3, respectively, in wide radii, meaning that the PDF at the HFS SOL shows Gaussian distribution.

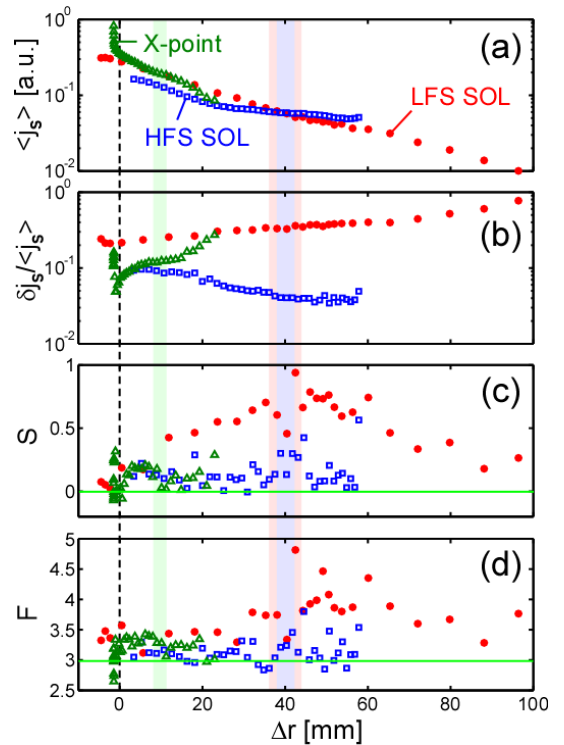


Fig.2. (a) Averaged j_s profiles measured with LFS midplane (circles) and HFS (squares) Mach probes in L-mode. (b) Fluctuation level of j_s , (c) skewness and (d) flatness.

The scaling features of the fluctuation can be studied by mean of Fourier analysis. Figure 4 shows the spectral density $S(f)$ of j_s . The shapes of $S(f)$ allow one to conclude whether the scaling behavior of a time series can be described by power-law dependences, $S(f) \sim f^{-\alpha}$. The power spectrum of turbulent fluctuation quantifies the characteristic of the process. In the LFS SOL, scaling sub-range with respect to the frequency is clearly observed in Fig. 4. The typical value of the scaling exponent α of the power spectrum in the scaling sub-range is 1.5, which is almost same as that observed in several tokamak devices [5]. Some noise peaks are seen in the high-frequency range, which are picked up in the probe measurement circuit.

4. Analysis of positive burst's profile at the LFS SOL in L-mode Plasma

In this section, conditional averaging (CA) method is employed so as to reveal the typical burst's profile at the LFS SOL. This method is standard and useful statistical tool. However, the conventional CA method has some problems, for instance, the burst's detection is not unique, and the high-frequency noise components easily give a strong distortion for the averaged feature.

To obtain the burst's waveform precisely, we apply the VITA (variable-interval time-averaging) method [6], which allows to detect bursty events associated with the sudden variation of the signal in the time domain. In this method, when the localized variance, defined by

$$v_a(t) = \frac{1}{T} \int_{-T/2}^{+T/2} [j_s(t')]^2 dt' - \left[\frac{1}{T} \int_{-T/2}^{+T/2} j_s(t') dt' \right]^2, \quad (1)$$

exceeds the value being k -times as large as the variance of full signal, detection function a_v is set to be 1. Figure 5 shows v_a and a_v , where the time window T and k are $52 \mu\text{s}$ and 1, respectively. The

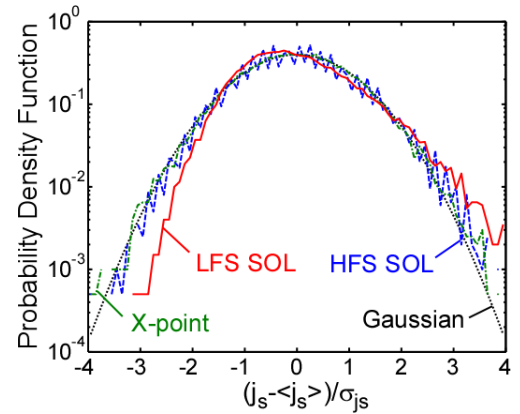


Fig.3. Log-linear plots of probability density function (PDF) of j_s at the LFS (solid line) and HFS SOLs (dashed-dotted line) and X-point (chained line).

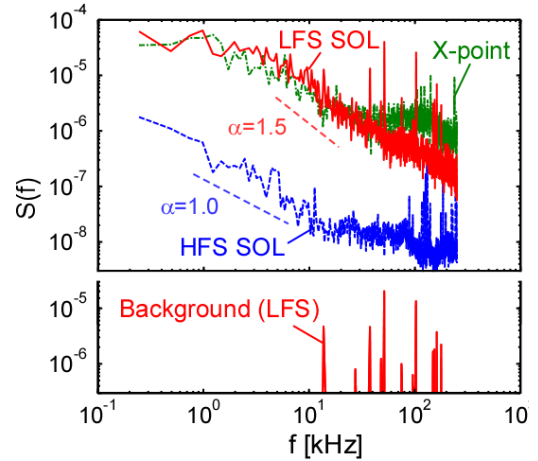


Fig.4. Power spectra of j_s at the three poloidal positions and background power spectrum at the LFS SOL.

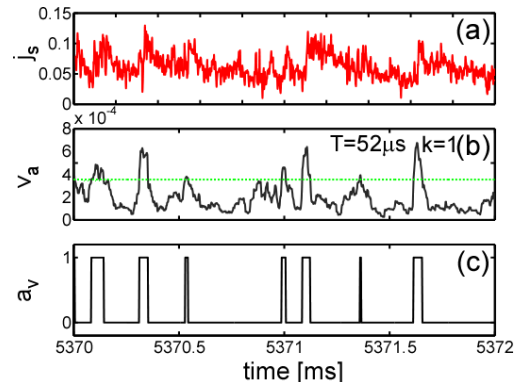


Fig.5. (a) Time evolution of ion saturation current j_s at the LFS SOL, (b) localized variance v_a (solid line) and product of variance multiplied by k (dots). (c) Detection function a_v .

positive burst's profile reconstructed by CA with VITA method provides the precisely feature with fast rump-up and slow decay as shown in Fig. 6.

5. Fluctuation characteristics between ELMs in ELMy H-mode plasma

Fluctuation characteristics of j_s between ELM-spikes in ELMy H-mode plasma (shot number #49819) were analyzed to compare to the L-mode plasmas. The discharge parameters are indicated in Table I. Similarly in the L-mode plasmas, intermittently positive events appear only at the LFS SOL.

Figure 7 shows power spectra of j_s between ELM-spikes in ELMy H-mode plasma at different radial positions at the LFS SOL, which shows that coherent frequency component around 60 kHz appears near the separatrix in the ELMy H-mode. On the other hand, all spectra profile of less than about 10 kHz shows the same tendency in the L-mode plasma.

6. Summary

It is clearly shown that the blobby plasma transport frequently occurs at the LFS midplane in L-mode and ELMy H-mode plasmas. The fluctuation characteristic at the LFS SOL corresponds to that of other devices, and is quite different with that at the HFS SOL. We could reconstruct a precise burst profile of the positive events associated with plasma blobs by using a CA with the VITA method, which can reduce the distortion due to the high-frequency noise components.

References

- [1] Kraheninnikov, S.I., Phys. Lett. A **283**, 368 (2001).
- [2] Terry, J.L., et al., Phys. Plasmas **10**, 1739 (2003).
- [3] Kirnev, G.S., et al., Nucl. Fusion **45**, 2005 (2005).
- [4] Asakura, N., et al., Nucl. Fusion **44**, 503 (2004).
- [5] Antar, G.Y., et al., Phys. Plasmas **10**, 419 (2003).
- [6] Yuan, Y.M., and Mokhtarzadeh-Dehghan, M.R., Phys. Fluids **6**, 2038 (1994).

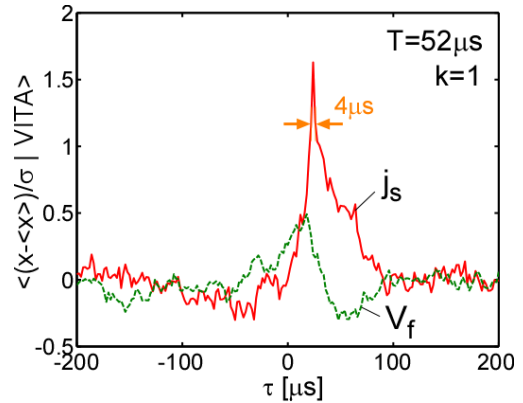


Fig.6. Cross-CA results of j_s (solid line) and floating potential V_f (dashed-dotted line) at the LFS SOL with VITA method.

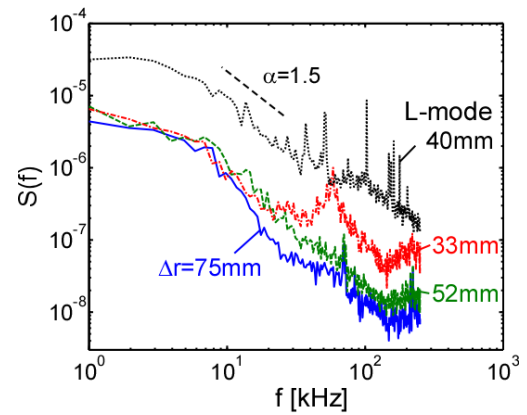


Fig.7. Power spectra at around some radial positions at the LFS SOL in H-mode plasma, and additionally power spectrum in L-mode plasma.

8.3 Fluctuation Characteristics in the Detached Divertor [1]

N. Asakura, N. Ohno¹⁾, H. Tanaka¹⁾, H. Kawashima, T. Nakano

1) Nagoya University

Statistical analysis of a probability distribution function (PDF) and conditional average (CA) was applied to determine intermittent events in fluctuations of ion saturation current (j_s) and floating potential (V_f) measured in the low-field-side (LFS) and high-field-side (HFS) SOLs, using the reciprocating Mach probes. Understanding of SOL fluctuation characteristics, particularly determination of the intermittent events and their temporal scale, has progressed in the L-mode plasmas, where $I_p = 1$ MA, $B_t = 3.2$ T, $P_{NB} = 4$ MW, plasma triangularity (δ) of 0.32, elongation (κ) of 1.4, safety factor at 0.95 ($q_{0.95}$) of 4.7.

For the low to medium densities, i.e. $\bar{n}_e = 1.3\text{-}2.0 \times 10^{19} \text{ m}^{-3}$ ($\bar{n}_e/n^{GW} = 0.31\text{-}0.48$), the fluctuation level ($\delta j_s / \langle j_s \rangle$) was found to be large (20-70%) at the LFS midplane, compared to those near the X-point (4-20%) and at the HFS SOL (4-10%). Characteristics of the fluctuation was represented by the third moment of PDF, normalized by the standard deviation: Skewness is defined as $S = \langle x^3 \rangle / \langle x^2 \rangle^{3/2}$, where Gaussian distribution is characterized by $S = 0$. Large “burst events” were observed at the LFS midplane, and positive $S^{mid} = 0.3\text{-}0.8$ extended over the wide SOL region ($0 < r^{mid} < 10$ cm). Time scale of the “burst events” was determined to be ~ 5 μs by CA, and positive correlation between j_s^{mid} at upstream and downstream sides of the Mach probe suggested either the radial or poloidal transport of the filaments.

For the relatively high density of $\bar{n}_e = 2.4 \times 10^{19} \text{ m}^{-3}$ ($\bar{n}_e/n^{GW} = 0.54$), the plasma detachment extended to the upstream from the outer divertor target and j_s^{xp} near the X-point ($r^{mid} < 0.5$ cm) decreased, resulting in a reduction in the local plasma pressure by a factor of 2 compared to that at the LFS midplane. On the other hand, j_s^{xp} in the attached region ($r^{mid} > 0.6$ cm) increased, and the Mach number of the parallel flow became a sonic level ($M_{//}^{xp} = 0.8\text{-}1$). Here, at the LFS midplane, $\delta j_s^{mid} / \langle j_s^{mid} \rangle$ of 20-40% was comparable to that for the lower \bar{n}_e , and positive S^{mid} was slightly increased to 0.4 - 1.2, and it extended to the far SOL.

Fast sampling of j_s^{xp} showed that large “burst events” appeared near the X-point ($0.5 < r^{mid} < 1.5$ cm) and that radial profiles of $\delta j_s^{xp} / \langle j_s^{xp} \rangle$ and S^{xp} changed significantly. The large “burst events” were observed only at one side of the X-point Mach probe, i.e. facing to the main plasma, suggested that they are transported from the 1ain SOL. Peak j_s^{xp} of the large “burst events” became 2-5 times larger than the averaged value $\langle j_s^{xp} \rangle$, and the waveform was characterized by large positive skewness (S^{xp} up to 1.8) and long time scales of 40-80 μs . They can be considered as a candidate mechanism to enhance the radial transport and the SOL flow towards the divertor.

Reference

[1] Asakura, N., et al., J. Nucl. Mater. **390-391** (2009) 364.

8.4 SOL Flow and Plasma Profiles in High-Field-Side SOL

N. Asakura, T. Nakano, N. Ohno¹⁾, H. Tanaka¹⁾

1) Nagoya University

1. Introduction

Understanding of parallel plasma flow in SOL (SOL flow) has recently progressed due to systematic measurement over several poloidal locations both at High-Field-Side and Low-Field-Side [1]. In particular, Mach number of the SOL flow ($M_{||}$) is increased to a sub-sonic or sonic level (0.5-1) at the HFS SOL. Such fast flow plays an important role on enhancing the friction force with intensive gas puffing into the main SOL, resulting in impurity reduction in the core plasma [2]. The SOL plasma transport at the HFS is also important to determine the wall separation to minimize interaction between the plasma and the first wall. In 2008, SOL characteristics were investigated in the L- and ELMy H-mode plasmas, where the separation from the inner wall was decreased.

2. Measurement of SOL plasma

SOL flow measurement was taken with Mach probes at three different poloidal locations: at LFS midplane, near the null-point (X-point), and above the HFS baffle in two plasma configurations as shown in Fig. 1. Plasma parameters of the L-mode plasmas were $I_p = 1$ MA, $B_t = 3.2$ T with the ion $\mathbf{B} \times \nabla B$ drift direction toward the divertor, $P_{NB} = 4$ MW, and medium \bar{n}_e was increasing from 1.6 to $2.0 \times 10^{19} \text{ m}^{-3}$ ($\bar{n}_e/n^{GW} =$

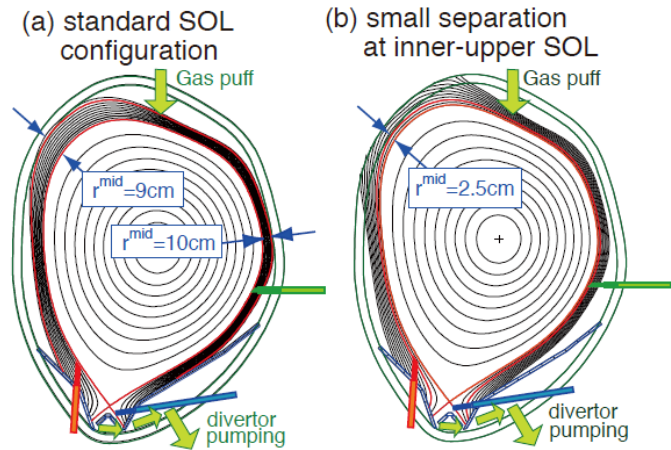


Fig. 1 Plasma configurations and location of the three Mach probes: (a) standard SOL, (b) small separation at the inner-upper SOL.

$0.38-0.47$) during the gas puffing of $15-20 \text{ Pam}^3\text{s}^{-1}$. Corresponding values of n_e near the LFS midplane separatrix were $0.9-1.2 \times 10^{19} \text{ m}^{-3}$. Compared to a standard case as shown in Fig. 1(a), Figure 1(b) was a special configuration with small separation between the upper-inner first wall and the separatrix. For the standard and small separation cases, the magnetic field lines in SOL connected between the HFS and LFS divertors were within 9 and 2.5 cm midplane radii.

Figure 2 shows the radial profiles of electron pressures ($p_e = n_e T_e$) measured at the main plasma side of the Mach probe and $M_{||}$ in the standard plasma configuration. Here, the radial coordinate of profiles is mapped at the LFS midplane (r^{mid}). Positive and negative directions indicate parallel flow toward the HFS and LFS divertors, respectively. Three p_e profiles are

comparable on the magnetic surfaces. In contrast, flow patterns are different: SOL flow away from the LFS divertor (toward the plasma top) occurs in the wide region at the LFS midplane ($r^{\text{mid}} < 5$ cm), and M_{\parallel} becomes subsonic ($M_{\parallel} = 0.3$). The fast SOL flow is continuously toward the HFS SOL, and faster subsonic M_{\parallel} of ~ 0.5 was seen in a wide region at the HFS SOL: the radial location of the fast M_{\parallel} extends to the outer flux surfaces (far SOL). Here, M_{\parallel} in the narrow region near the separatrix shows small flow reversal toward the top ($M_{\parallel} = -0.1$).

It was also found that the SOL flow direction at the LFS midplane reversed for ion $\mathbf{B} \times \nabla B$ drift away from the divertor, i.e., a SOL flow was generated opposite to the ion $\mathbf{B} \times \nabla B$ drift direction, and the SOL flow toward the HFS divertor was enhanced at the HFS. These results suggest that a combination of, at least, two driving mechanisms, i.e. a B_t -independent component of the SOL flow is produced toward the HFS SOL and a B_t -dependent component appears in opposition to the ion $\mathbf{B} \times \nabla B$ drift, forms the complicated SOL flow pattern.

3. HFS plasma and SOL flow

In order to understand the influence of the driving mechanism of the B_t -independent component on the HFS SOL plasma, measurement was performed in the small separation configuration. Profiles of ion saturation current (j_s) and electron temperature (T_e) for the three locations are comparable as shown in Fig. 3. Change in e-folding length of the j_s profile is clearly observed in the separated SOL ($r^{\text{mid}} > 2.5$ cm), and T_e becomes low (1-5 eV) compared to that in the connected SOL (11-18 eV). These observations show that parallel convective and conductive transports of the SOL plasma are dominant compared to

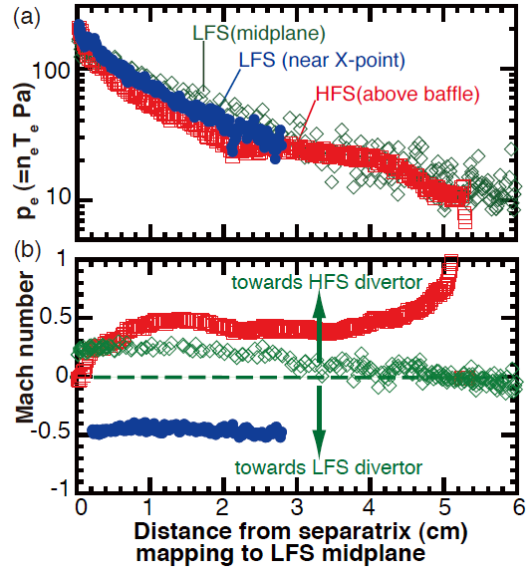


Fig.2 Profiles of (a) electron pressure, (b) Mach number measured by three Mach probes. Positive value presents the SOL flow towards the HFS divertor.

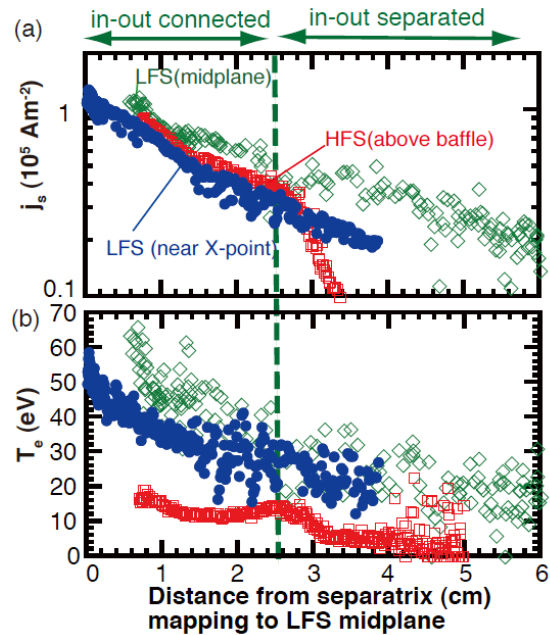


Fig. 3 Profiles of (a) ion flux, (b) electron temperature measured by three Mach probes with small separation between the inner-upper wall and the separatrix ($r^{\text{mid}} = 2.5$ cm).

the radial diffusion. The HFS T_e in the connected SOL is decreased from the LFS T_e (65 eV near the midplane separatrix and 40 eV at $r^{\text{mid}} \sim 2.4$ cm). Influence of the gas puffing at the plasma top on the HFS SOL plasma is significant because the SOL flow is produced from the LFS midplane to the HFS SOL.

Next, Fig. 4(a) shows that profiles of electron pressure ($p_e = n_e T_e$) in the connected SOL are comparable. On the other hand, the HFS p_e in the separated SOL is reduced compared to that at the LFS midplane, where connection lengths from the upper-inner wall to the two Mach probes are comparable, i.e., $L_c = 50$ and 40 m to the HFS and midplane Mach probes, respectively. The sonic level of the HFS $M_{||}$ is also reduced in the separated SOL as shown in Fig. 4(b).

As a result, for the connected SOL in the single null divertor, the convective transport is dominant in the HFS SOL rather than the transverse transport—a large part of the HFS SOL plasma is transported from the LFS SOL. Similar results of in-out asymmetry in the plasma pressure in the separated SOL and stagnation of the SOL flow at HFS were demonstrated in the double null divertor configuration on Alcator C-mod [3]. Generally, in the connected SOL, the static pressure ($n_e T_e + n_i T_i$) plus the dynamic pressure ($m_i n_i [M_{||} C_s]^2$) should be balanced along the field line, assuming no pressure/momentum source nor loss in the SOL. In future, measurements of T_i distribution and the in-out asymmetry in the radial diffusion in SOL will determine the mechanism of the B_t -independent SOL flow component more quantitatively.

4. HFS plasma and SOL flow in ELMy H-mode

Influence of the small separation on the SOL plasma profiles were investigated also in the ELMy H-mode plasma with $I_p = 0.95$ MA, $B_t = 2.0$ T, $P_{\text{NB}} = 5.5$ MW, $\bar{n}_e = 1.75 \times 10^{19} \text{ m}^{-3}$ ($\bar{n}_e/n^{\text{GW}} = 0.43$), and n_e at the LFS midplane separatrix of $0.4 \times 10^{19} \text{ m}^{-3}$. Dynamics of the ELM filaments and the SOL flow was summarized in Ref. 4. In this section, difference in the SOL plasma for the standard ($r^{\text{mid}} = 8$ cm) and small separation cases ($r^{\text{mid}} = 2.6$ cm) is described. Figure 5 shows comparison of the plasma profiles at the HFS SOL such as j_s , T_e , p_e and $M_{||}$. It is noted that j_s (and n_e) in the H-mode SOL is by the factor of 5 lower than that in the L-mode with gas puffing, while \bar{n}_e in the core plasma is comparable. Radial distributions of the large

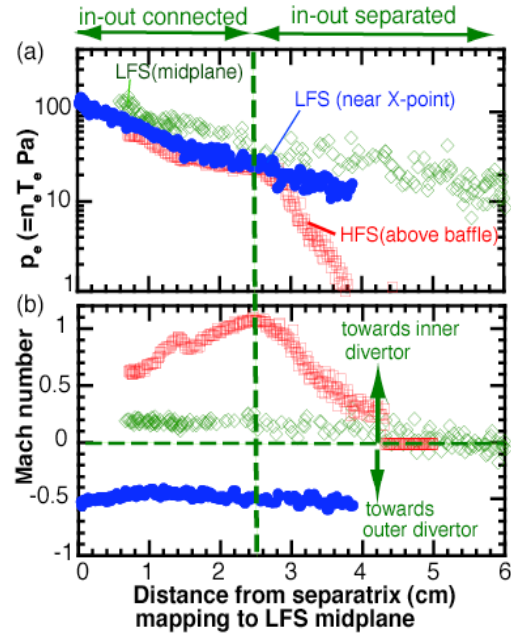


Fig. 4 Profiles of (a) electron pressure, (b) Mach number measured by three Mach probes for the small separation at the upper-inner SOL.

j_s peaks ($j_s^{\text{HFS}}(ELM)$) and corresponding $M_{||}$ values ($M_{||}^{\text{HFS}}(ELM)$) are plotted in Fig. 5(a) and (d), respectively.

For the small separation case, flat $j_s^{\text{HFS}}(ss)$ profile at the far SOL ($r^{\text{mid}} > 3$ cm) disappears, and at the same time, $j_s^{\text{HFS}}(ELM)$ is decreased. Change in $j_s^{\text{HFS}}(ss)$ and $j_s^{\text{HFS}}(ELM)$ distributions is gradual, while T_e is decreased to 1-10 eV at the far SOL ($r^{\text{mid}} > 3$ cm). As a result, change in the j_s^{HFS} and T_e^{HFS} for the small separation is relatively small compared to that in the L-mode with gas puffing. $M_{||}^{\text{HFS}}(ss)$ in the H-mode is generally small (0 -0.25) compared to that in the L-mode (0.5-1).

These results suggest that the radial transport (diffusion or intermittency) appears more than its influence in the L-mode. As shown in Ref. 4, subsonic to sonic $M_{||}^{\text{HFS}}(ELM)$ is seen just near the separatrix, while flow reversal ($M_{||}^{\text{HFS}}(ELM) < 0$) is seen in the outer flux surfaces. Influence of the small separation on $M_{||}^{\text{HFS}}(ELM)$ is not seen.

5. Summary

Change in the SOL plasma characteristics for the small separation was investigated both at HFS and LFS in the L- and H-mode plasmas. Influence of the plasma configuration on the plasma pressure and the SOL flow appeared only at the HFS SOL: reduction in the plasma pressure was seen on the separated field lines at the HFS, which suggested that the parallel convection from the LFS (rather than the transverse transport) is dominant on the connected field lines at the HFS.

References

- [1] Asakura, N., and ITPA SOL and divertor topical group, J. Nucl. Mater. **363-365** 41 (2007).
- [2] Asakura, N., et al., 30th EPS Conf. Contr. Fusion and Plasma Phys., St. Petersburg, ECA **27A** P-2.153 (2003).
- [3] LaBombard, B., et al., Nucl. Fusion **44** 1047 (2004).
- [4] Asakura, N., et al., Journal of Physics: Conference Series **123** 012009 (2008).

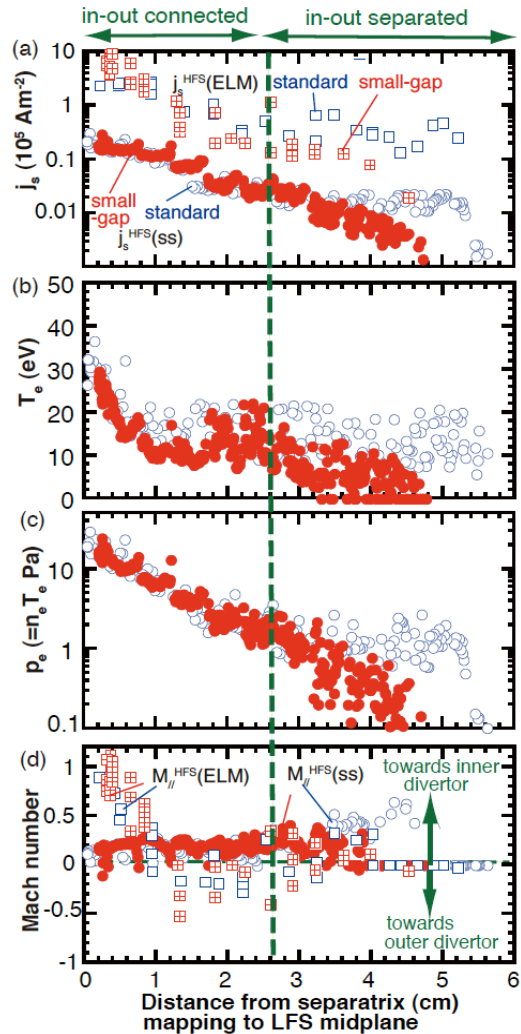


Fig. 5 Radial distributions of (a) j_s^{HFS} peaks (square) and j_s^{HFS} between ELMs (circle) measured at the HFS Mach probe, (b) electron temperature, (c) electron pressure, (d) Mach numbers corresponding to $j_s^{\text{HFS}}(ELM)$ and $j_s^{\text{HFS}}(ss)$. Closed (and plus in square) and open symbols represent the small separation and standard cases, respectively.

8.5 Kinetic Simulation of Impurity Transport in Detached Plasma [1]

K. Shimizu, T. Takizuka, K. Ohya¹, K. Inai¹, T. Nakano, A. Takayama²,
H. Kawashima, K Hoshino

1) Tokushima University, 2) National Institute for Fusion Science

To investigate the power and particle control method by the divertor, 2D multi-fluid divertor codes have been developed, where the impurities are treated usually as fluid species. The fluid modelling for the impurity transport contains the insufficient descriptions; (1) assumption of instantaneous thermalization of impurity ions, (2) neglecting the kinetic effect on the thermal force and (3) simplification for the complicated dissociation process of hydrocarbons. The MC approach is suitable as modellings for such effects, i.e. interactions between impurities and walls/divertor related to gyro-motion, and kinetic effects and methane breakup processes. The MC approach has flexibility in modelling, at the same time, it contains the disadvantage of (i) long computational time, (ii) large MC noise, and (iii) assumption of steady state. Thus, time-evolutional simulation with an MC impurity code coupled self-consistently to a plasma fluid code has not been presented so far.

We solved the problems (i) and (ii) of MC modelling by developing a new diffusion model for scattering process and optimizing on the massively parallel computer. Recently, we solved the problem (iii) by extending the IMPMC (2D impurity Monte-Carlo code) to a time-dependent simulation code, where increasing number of test particles with time is suppressed by a particle reduction scheme. Thereby we have accomplished a coupling of non-steady IMPMC code into a 2D divertor code (SOLDOR: 2D plasma fluid code /NEUT2D: 2D neutral Monte-Carlo code). The integrated divertor code (SONIC) enables us to investigate the details of impurity transport including erosion/redeposition processes on the divertor plates by further coupling of an 3D plasma-surface interaction MC code (EDDY).

The simulation was performed for a JT-60U discharge with NB heating power of $P_{NB}=14\text{MW}$ and a very strong deuterium gas puff of $\Gamma_{\text{puff}}=150\text{Pam}^3/\text{s}$. The dynamic evolution of an X-point MARFE observed in the experiments was reproduced well with the SONIC code. The EDDY/IMPMC code of a full dissociation modelling for hydrocarbons confirmed that the dome with a small sticking coefficient enhanced the contamination of hydrocarbon into the main plasma and that the dissociation process was not able to be simplified down to ionization process of carbon with low energy, especially in the attached divertor plasma. Taking advantage of the MC modeling of IMPMC code, the kinetic thermal force was investigated for JT-60SA detached plasmas. Without the helium recycling at the divertor plates, the kinetic effect improved the helium compression, compared with the conventional (fluid) evaluation. This effect was, however, masked by the helium recycling. Further simulation studies are required for various flow patterns.

Reference

[1] Shimizu, K., Takizuka, T., et al., Nucl. Fusion **49**, 065028 (2009).

9. Plasma-Wall Interactions

9.1 Particle Balance of Long-Pulse Discharges

T. Nakano and N. Asakura

1 Introduction

One of the issues in steady-state devices is tritium inventory. In ITER, an administrative limit of the tritium inventory is 700g by safety reasons. On the assumption that all the plasma facing-components of ITER are made of carbon, the tritium inventory is predicted to reach 700g in about 75 pulses [1]. Thus, wall-pumping, which is effective to control plasma density in short-pulse discharges, should be suppressed.

The wall-pumping is ascribed predominantly to surface absorption, permeation deep into the wall and co-deposition with impurities such as carbon. The surface absorption is expected to saturate in limited time period and the permeation reduces with ion fluence [2]. In contrast, the co-deposition neither saturates nor reduces unlike the above two processes. Hence with increasing pulse-length, the contribution of the co-deposition to the wall-pumping increases compared to those of the surface absorption and the permeation. Therefore, suppression of the co-deposition leads to reduction of particle inventory in steady-state devices.

The amount of retained particles in carbon depends on the temperature of the carbon [3]: at a temperature lower than 420 K, the limit is constant at a ratio of deuterium to carbon of 0.4, and it decreases with increasing temperature down to a very low level at 1000 K. Hence studies on the dependence of the particle inventory on wall temperature is of significance to predict the particle inventory in future devices.

In JT-60U, the baking temperature could be set at lower and higher than the temperature (420 K) at which the particle retention starts to decrease with increasing temperature. Thus, it is possible to investigate the dependence of the particle inventory on the wall temperature. For this purpose, particle balance studies in 30s-H-mode discharges were performed at three baking-temperatures around 420 K.

2 Experimental

In the present study, a particle balance analysis was performed for long-pulse H-mode discharges with a low X-point configuration as shown

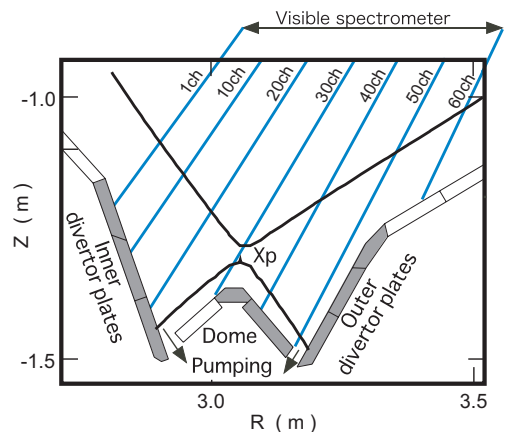


Fig. 1: The divertor structure, the magnetic configuration, and the viewing chord for the visible spectrometer.

in Fig. 1. The discharge conditions were as follows; a plasma current of 1.2 MA, a toroidal magnetic field of 2.3 T, a neutral beam (NB) heating power of 8 MW, a volume-averaged electron density of $2.3 - 3.8 \times 10^{19} \text{ m}^{-3}$, and a baking temperature of 350 K, 420 K and 550 K. A discharge with a volume-averaged electron density of $2.3 \times 10^{19} \text{ m}^{-3}$ ($n_e/n_e^{\text{GW}} \sim 0.55$) was repeated by about 10 pulses, and then the electron density was raised pulse-by-pulse up to $3.8 \times 10^{19} \text{ m}^{-3}$ ($n_e/n_e^{\text{GW}} \sim 0.9$). In total, about 20 long-pulse discharges were repeated at each baking temperature.

Three pumping systems were available: the divertor-pumping, the main pumping and the NB pumping system. The pumping speed of the divertor-pumping system was evaluated to be $28 \text{ m}^3\text{s}^{-1}$ for a pressure measured by a penning gauge at the U2 lower port with a gas flow test. Similarly the pumping speed of the main pumping system was evaluated to be $14 \text{ m}^3\text{s}^{-1}$ for a pressure measured by an ion gauge at the manifold from a decay rate of the pressure inside the vacuum vessel (167 m^3). The cryopumps in the tangential NB chamber worked as a pump for the JT-60U vacuum vessel because the gate valves for these beam lines were not closed after the NB injection. The pumping speed of the NB pumping system was evaluated to be $31 \text{ m}^3\text{s}^{-1}$ for a pressure measured by an ion gauge at the drift tube of the beam line.

3 Analysis

The equation used for the particle balance analysis is expressed as

$$\frac{d}{dt} (N_{\text{ion}}(t) + N_{\text{neutral}}(t)) = \Gamma_{\text{NB}}(t) + \Gamma_{\text{gaspuff}}(t) - \Gamma_{\text{div}}(t) - \Gamma_{\text{NBcryo}}(t) - \Gamma_{\text{turbo}}(t) - \Gamma_{\text{wall}}(t). \quad (1)$$

Here, $N_{\text{ion}}(t)$, $N_{\text{neutral}}(t)$, Γ_{NB} , Γ_{gaspuff} , Γ_{div} , Γ_{NBcryo} , Γ_{turbo} and Γ_{wall} indicate the number of deuterium ions, the number of neutral deuterium atoms, the particle-fueling rate of NB, the gas-puffing rate, the divertor-pumping rate, the NB-pumping rate, the main pumping rate, and the wall-pumping rate, respectively. The first and the second term of the left hand side can be ignored in the case that the steady-state plasma is analyzed. The divertor-pumping rate, the NB-pumping rate and the main pumping rate can be measured with the pumping speeds described above. The NB fueling rate and the gas-puffing rate are known. Then, the wall-pumping rate during a discharge can be evaluated from Eq.(1). Given that Γ_{NB} and Γ_{gaspuff} are zero in Eq. (1) between discharges, the wall-pumping rate, which is usually negative between discharges, can be evaluated with the same equation. The wall inventory is calculated by integrating the wall-pumping rate from the start time of a discharge to that of the next discharge.

4 Results and discussion

Figure 2 shows waveforms of a long-pulse discharge with a Greenwald density fraction of 50%. During a constant NB power injection, the line-averaged electron density

was controlled by a feed-back control technique of the gas-puffing rate, which gradually decreased and reached a very low level at the latter half of the discharge. In contrast, the divertor-pumping rate gradually increased and became nearly constant. The wall-pumping rate, calculated with Eq.(1), finally became negative, indicating deuteriums were released from the walls, *i.e.*, outgassing. Under the outgassing condition, the plasma stored energy and the ELM activity were maintained as shown in Fig. 2.

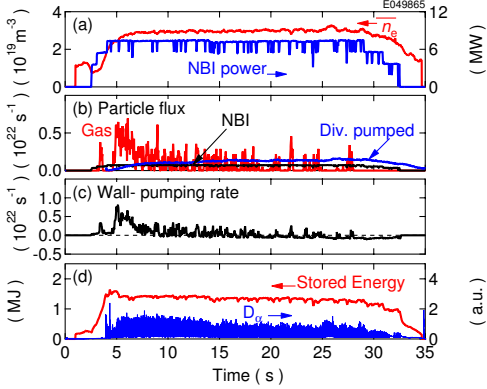


Fig. 2: Waveforms of (a) line-averaged electron density, NB heating power, (b) gas-puffing rate, NB fueling rate, divertor-pumping rate, (c) wall-pumping rate, (d) stored energy and D_α intensity from the outer divertor.

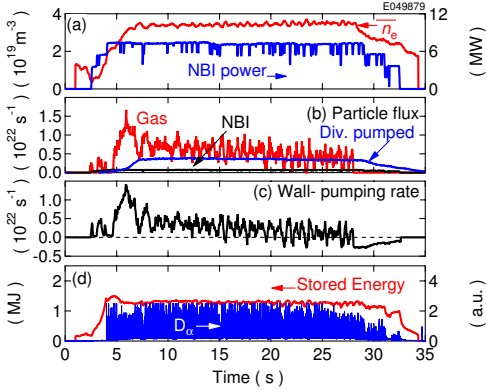


Fig. 3: Waveforms of parameters similar to Fig. 2. Note the scale of Fig. (b) is different from that of Fig. 2 (b).

Hence, it is considered that the difference of the changes of the wall inventory is due to the difference of deuterium absorption in the main chamber wall.

In contrast, in discharges with both the inner and the outer divertor detached (a

Figure 3 shows waveforms of a long-pulse discharge with a Greenwald density fraction of 70%. As shown in Fig. 3 (c), the wall-pumping rate was positive even at the latter half of the discharge. This discharge was performed after the discharge shown in Fig. 2, where the wall pumping was no more effective. Nonetheless, the wall-pumping rate of this discharge was positive. This effect is discussed later.

Figure 4 compares the deuterium inventory at three baking temperatures. In discharges with the inner and the outer divertor detached and attached, respectively, (a Greenwald density fraction of 50%), the deuterium inventory decreased with pulse at 570 K. In contrast, at 420 K, the deuterium inventory decreased more gradually compared to that at 570 K, and the deuterium inventory did not change at 350 K. Possible interpretation is as follows; due to increase of the temperature at the strike point of the outer divertor, the outgassing from the outer divertor plates were expected. The temperature rise of the main chamber wall was so small that the main chamber wall could still absorb deuteriums at a baking temperature of 350 K. In contrast, at 570 K, it is interpreted that the absorption at the main chamber wall was not effective and that the outgassed number of deuterium was larger than the absorbed, resulting in the decrease of the deuterium inventory. The absorption of deuterium at 420 K seems intermediate between those at 350 K and 570 K.

Greenwald density fraction of $\geq 70\%$), the deuterium inventory at the three baking temperatures increased. This is due probably to the co-deposition of deuterium with carbon; as shown in Fig. 5, the CD_4 generation, which was determined from the spectroscopic measurement with viewing chords shown in Fig. 1, does not correlate with the deuterium retention in the discharges with the outer divertor attached. In contrast, the CD_4 generation increased in particular in the outer divertor with increasing deuterium retention in the discharges with the outer divertor detached. This suggests that the deuterium retention is due predominantly to a process which depends on impurity amount such as co-deposition. On the assumption that the fraction of deuterium to carbon in the co-deposition layer is 0.4 and that the net-deposition rate of the co-deposition layer is 80%, the co-deposition can explain all deuterium retention.

In the discharges with the outer divertor detached at 420 K, $^{13}CH_4$ was injected from the outer divertor. Post mortem analyses are planned to evaluate the number of deuteriums included in the co-deposition layer with $^{13}CH_4$. This provides a direct comparison of the deuterium retention evaluated by the particle balance analysis and the post mortem analysis.

5 Summary

In the 30s-H-mode discharges, the changes of the wall inventory were compared at three baking temperatures. In discharges with the outer divertor attached, the absorption at the main chamber wall, which temperature rise was small, seemed to affect the wall inventory. In contrast, in discharges with both the divertor detached, the co-deposition of deuterium with carbon became a dominant contributor to the wall inventory. The contribution of the co-deposition to the wall inventory would be confirmed by planned post mortem analyses.

References

- [1] Roth J. *et al.*, *Plasma Phys. Control. Fusion* **50**, 103001 (2008).
- [2] Roth J. *et al.*, *J. Nucl. Mater.* **363-365**, 822 (2007).
- [3] Moller W.J. *Appl. Phys.* **64**, 4860 (1988).

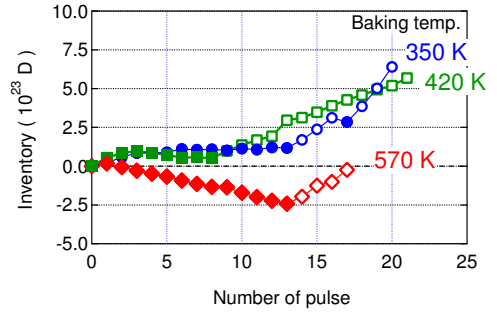


Fig. 4: A change of D inventory as a function of pulse number. Closed and open symbols indicate discharges with the outer divertor plasma attached and detached, respectively.

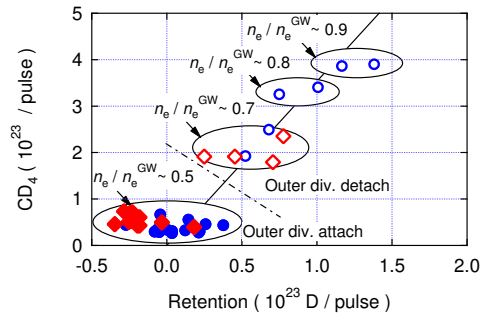


Fig. 5: CD_4 generation as a function of D retention. The meanings of the symbols are the same as in Fig. 4.

9.2 Deuterium Depth Profiling in Graphite Tiles not Exposed to Hydrogen Discharges before Air Ventilation [1]

T. Hayashi, K. Sugiyama¹⁾, M. Mayer¹⁾, K. Krieger¹⁾, K. Masaki, T. Tanabe²⁾ and M. Sato

1) Max-Planck-Institut für Plasmaphysik, Germany, 2) Kyushu Univ.

Depth profiles of deuterium trapped in graphite tiles of the W-shaped divertor not exposed to hydrogen discharges just before air ventilation were determined by the $D(^3\text{He,p})^4\text{He}$ resonant nuclear reaction analysis. The analyzed depth was 16.4 μm , which is deeper than that of the previous work [2].

The highest concentration was found in the inner divertor area, and the D concentration at the surface is 19 at.%, which was higher than that exposed to H discharges at the same location (1.2 at.% [3]). This indicates that the H discharges removed 94% of the trapped D due to isotope exchange only at the very surface, assuming that the D concentration before H discharges was same as that of the tile not exposed to H discharges, even though the experimental period and plasma conditions were different each other. In the outer divertor, the D concentration was relatively low (2.6 at.%) even in the surface, because the surface temperature of the outer divertor tile was high.

In the deeper region of all samples except dome top sample, D concentrations without H discharges were similar to that with H discharges. These results indicate that the trapped D only in the shallow region was removed by H discharges. The removal depth, where D concentrations of the tiles with and without H discharges were comparable, depends on the sample location. The minimum removal depth was found at the outer divertor and the dome top (0.4 μm). The maximum depth was found at the inner divertor (2.6 μm).

According to the integrated deuterium retention within the analyzed depth (16.4 μm), the highest and the lowest D retention were found in the outer dome wing and the outer divertor, respectively, in the both cases of with and without H discharges. The D retention only for the dome top sample with the H discharges (0.39×10^{22} D atoms/ m^2) was lower than that without H discharges (1.25×10^{22} D atoms/ m^2). Thus, H discharges removed 69% of the trapped D due to isotope exchange, assuming that the D concentration before H discharges was same as that of the tile not exposed to H discharges.

References

- [1] Hayashi, T., et al., J. Nucl. Mater. **390–391**, 667 (2009).
- [2] Hayashi, T., et al., J. Nucl. Mater. **349**, 6 (2006).
- [3] Hayashi, T., et al., J. Nucl. Mater. **363–365**, 904 (2007).

9.3 H+D Retention in the First Wall Graphite Tiles [1]

M. Yoshida¹, K. Sugiyama¹, J. Yagyu, Y. Miyo, T. Hayashi, K. Masaki, M. Sato, T. Tanabe¹
1) Kyushu University

Fuel retention of plasma facing graphite tiles in a fusion reactor is one of the important issues from the viewpoint of tritium safety and economy. Although fuel inventories in redeposited layers on divertor tiles and remote area at rather low temperature regions have been extensively studied, the mass balance among fuel input, output and retention in the vacuum vessel is not consistent. The retention has the largest uncertainty and needs more precise measurements. In particular, the fuel retention in the first wall tiles has not been measured except for few works. Although the first wall is mostly eroded and hydrogen retention has been believed to be small so far, the huge surface area of the first wall could have large contribution on the total fuel retention.

In this work, hydrogen (H) and deuterium (D) retentions and depth profiles in the first wall tiles were analyzed by thermal desorption spectroscopy (TDS) and secondary ion mass spectroscopy (SIMS), and compared with those of the divertor tiles [2]. The first wall tiles measured here were exposed to about 18000 DD discharges in the period from Jun. 1992 to Nov. 2004. During the exposure, the vacuum vessel was kept at 573 K (1992-2002) and 423 K (2003-2004), and the temperatures of the first wall tiles must be higher to some extent. Several hundred HH discharges were performed before the air ventilation to remove tritium produced by the DD discharges. During the period, boronization was performed several times with B₁₀H₁₄ + D₂ mixture gas and B₁₀D₁₄. Accordingly some of the first wall tiles were fully covered by the boronized layers. In this work, we selected eroded tiles without any boronized layers from the outboard first wall tiles.

The measured retentions (H+D) in the eroded first wall tiles and the eroded divertor tiles were nearly the same, in spite of the lower temperature of the first wall. This suggests the saturation of hydrogen isotope retention in the topmost surface layers (>0.1 μ m). Because of isotopic replacement during the HH discharges, the most of D retained at the topmost surface layers during the DD discharges was replaced by H, giving very small deuterium to hydrogen ratio (D/H). The D/H ratio increased with the depth (<1 μ m) and far deeper region (>1 μ m) no more D retention was observed. The D/H in the retention of the eroded first wall tiles was much larger than that for the eroded divertor tiles, indicating isotopic replacement of D by H during the HH discharges was suppressed due to the lower tile temperatures of the first wall. Furthermore D retention in a little deeper region (~0.5 μ m) of the first wall tiles was significantly larger than that of the eroded divertor tiles. This is most probably caused by the injection of high-energy deuterons and neutrals originating from NBI by the orbital and ripple loss mechanisms. Although the flux of the energetic particles onto the first wall tiles must be much smaller than that onto the divertor tiles, the lower D concentration in the deeper regions compared to the topmost surface layers would allow the build-up of deuterium up to a certain level, resulting in significantly higher D/H in the deeper regions (<1 μ m). The injection of high energy hydrogen ions by the orbital and ripple loss mechanisms could not be avoided for metallic walls or even result in larger hydrogen retention owing to rapid hydrogen diffusion into more deep.

References

- [1] Yoshida, M., Tanabe, T. et al, J. Nucl. Mater. **390-391**, 635 (2009).
- [2] Hirohata, Y. et al., J. Nucl. Mater. **363-365**, 854-861(2007).

9.4 Analysis of Residual Gas by High-Resolution Mass Spectrometry during Helium Glow Discharge Cleaning [1]

T. Hayashi, A. Kaminaga, T. Arai and M. Sato

The residual gas analysis has been conducted by high-resolution mass spectrometry in order to investigate the effect of helium glow discharge cleaning (He-GDC). The residual gas species in the vacuum vessel were analyzed by the residual gas analyzer (RGA) connected to the vacuum manifold. A high-resolution quadrupole mass spectrometer was equipped in the RGA. The spectral resolution was determined by a gas puff test with He and D₂. The half width at half maximum (0.018 amu) of deuterium and He peaks is smaller than the difference (0.024 amu) between He peak and D₂ peak. These results indicate that the RGA system has sufficient resolution to distinguish between He and D₂ gas species.

The flow and the pressure of helium gas during He-GDC were $5.5 \times 10^3 \text{ Pa m}^3 \text{ h}^{-1}$ and $\sim 0.27 \text{ Pa}$, respectively. The current and the voltage of glow discharge were 2 A and 180–300 V, respectively. The temperature of vacuum vessel was kept at 423 K. The tokamak discharge just before He-GDC was carried out by deuterium gas, and finished normally without disruption. The He-GDC started in 35 minutes after the final tokamak discharge, and continued for 7 hours. Once the He-GDC started, the partial pressure of D₂ gas increased with time and in 61 s, reached the highest pressure of $3.8 \times 10^{-4} \text{ Pa}$, which was about ten times larger than the D₂ partial pressure ($3.5 \times 10^{-5} \text{ Pa}$) just before starting He-GDC. Then, the pressure of D₂ decreased with time. The total amount of released D₂ during the He-GDC (7 h) was evaluated to be 4.4 Pa m^3 at 423 K, or 1.5×10^{21} deuterium atoms. The average areal density of the released deuterium was $8.4 \times 10^{18} \text{ D atoms m}^{-2}$.

Because the gas puff of He stopped after stopping the He-GDC, the pressure of He decreased. Since the pressure of He decreased, the D₂ gas released again. The pressure of D₂ just after He-GDC was $1.6 \times 10^{-5} \text{ Pa}$, which was significantly lower than that of before He-GDC. Moreover, the D₂ pressure slowly decreased with time and reached $5.7 \times 10^{-6} \text{ Pa}$ at $t = 50,000 \text{ s}$. Therefore, the He-GDC is effective to remove the deuterium from plasma facing components.

References

[1] Hayashi, T., et al., Fusion Eng. Des. **84**, 908 (2009).

9.5 Characterization of Re-deposition Layer with Ferritic Steel

N. Ashikawa¹⁾, J. Yagyū, A. Yoshikawa²⁾, Y. Miyo, M. Yoshida³⁾, Y. Inagaki²⁾, A. Sagara¹⁾,
K. Nishimura¹⁾, K. Tsutsumi, Y. Oya²⁾, K. Okuno²⁾, T. Nakano, K. Itami, M. Sato

1) National Institute for Fusion Science, 2) Shizuoka University, 3) Kyushu University

The plasma facing materials (PFMs) in next generation fusion devices, such as ITER and FFHR [1] will be exposed to severer heat load and neutron flux than those in current devices. Thus, low-radio activate ferritic steel has been developed for PFMs or base materials with high Z coating.

In JT-60U tokamak, graphite tiles had mainly been used for PFMs. In 2005, additional 1122 ferritic steel tiles of 8%Cr, 2%W and 0.2%V, which cover about 9.1% areas of the torus, were installed. Although additional metallic depositions of impurities were observed on in-vessel components, sufficient data of these re-deposition layers was not provided yet.

Material probes made of SS 316L, graphite and Si samples were installed on the outer port inside the vacuum vessel, and were exposed to 1328 deuterium plasma discharges during one experimental campaign. These sample holders were installed at different 5 toroidal positions before and after installation of ferritic tiles, and fresh samples into these holders were set for each campaign. Depth profiles of their impurities on these samples were analyzed using the X-ray Photoelectron Spectroscopy (XPS) [2].

For example, an iron atomic concentration of 45 % was observed after ferritic tile installation at P-15 section, where thick carbon deposition layer was also found before and after ferritic tile installation. At the same depth of 2 nm from the top surface, carbon of 34 %, oxygen of 15 %, boron of 6 % are observed after ferritic tile installation. A thickness of deposition layer is about 12 nm and it is similar on each sample before and after ferrite tile installation at P-15. Results of XPS analysis showed the different atomic concentrations of iron due to erosion of ferritic tiles in every position of the torus.

This ferritic steel tile contains 2% of tungsten in wt and a tungsten coating material was used for the divertor target tiles in this experimental campaign. However tungsten element was not observed from any samples.

From these results, it is shown that deposited layer of iron was found after ferritic tile installation. Initial atomic concentrations of ferritic steel were not kept due probably to long-term erosion/deposition processes. The distribution of thickness of deposition layer after the ferrite tile installation was similar to that before the ferrite tile installation.

References

- [1] Sagara, A. et al., Fusion Eng. Design, **83**, 1690 (2008).
- [2] Ashikawa, N. et al, J. Nucl. Materials **363-365**, 1352 (2007).

9.6 Localized Tungsten Deposition in Divertor Region [1]

Y. Ueda¹⁾, M. Fukumoto¹⁾, J. Watanabe¹⁾, Y. Ohtsuka¹⁾, T. Tanabe²⁾, T. Arai, N. Asakura, T. Nakano, Y. Nobuta, M. Sato, J. Yagyu, K. Ochiai, K. Takakura and JT-60 Team

1) Osaka University, 2) Kyushu University

Tungsten local transport in the divertor region emitted from the outer divertor was studied. Tungsten coated CFC tiles were installed in the outer divertor position (toroidal section P-8), on which outer strike points did not normally stay. This tile array covered about 1/21 toroidal length. The thickness of W coating layer was about 50 μm with Re interlayer between W coating and the base CFC tiles.

A neutron activation method was used for the first time for the absolute measurement of deposited W by the $^{186}\text{W}(n,\gamma)^{187}\text{W}$ reaction by slow neutrons in JAEA/FNS (Fusion Neutrinos Source). Conventional surface analysis methods such as EDX (Energy Dispersive X ray spectrometry) and XPS (X ray photoelectron spectroscopy) were also used. Tungsten deposition on the dome tiles was found only near the top surface (within depth of a few μm), while tungsten on the inner divertor tiles was codeposited with carbon to the depth up to about 60 μm . The neutron activation method can measure tungsten in these thick codeposition layers. Depth profiling by XPS in this thick layer is not appropriate.

Poloidal distribution in the same toroidal section as the W-tiles showed dense W deposition near the inner strike points, the dome top and outer wing of the dome, while W deposition on the inner wing of the dome was much less than those. Tungsten composition ratio in the mixed redeposition layer on the inner divertor tile was about 1%. Considering tungsten tile area (1/21 toroidal length) and low erosion yield (about two orders of magnitude lower than that of CFC), it is suggested that W deposition on the inner divertor emitted from the outer divertor is very localized. Carbon ions by puffing $^{13}\text{CH}_4$ from the outer divertor at the same toroidal position of the W-tiles were also deposited mainly near the inner strike points.

In terms of toroidal distribution of W deposition, tungsten surface density on the inner divertor and the outer wing of the dome was much higher at the toroidal angle of 0 deg (at the center of the W-tile array) than those at 60 deg (toroidal section P-5). Especially in the outer wing, tungsten deposition was less than the detection limit at 60 deg. Detailed measurement of W toroidal distribution on the outer wing showed significant localization near the W-tile array within the toroidal angle of about ± 20 deg. The reason of this significant localization could be attributed to inward drift of W ions or deposition of sputtered W atoms without ionization in the thin private plasma in the case of plasma operation with the outer strike position on the W-tiles. In addition, toroidal asymmetry of W distribution on the outer wing was observed. This toroidal asymmetry could be due to the plasma parallel flow in the divertor plasma.

Reference

[1] Ueda, Y., et al., Nucl. Fusion, **49** 065027 (2009).

9.7 Modeling of Tungsten Impurity Transport Using IMPGYRO Code

K. Hoshino, M. Toma¹⁾, A. Hatayama¹⁾, K. Shimizu, T. Takizuka,
Y. Ueda²⁾, N. Nakano, N. Asakura

1) Keio University, 2) Osaka University

1. Introduction

Tungsten is the most promising candidate for a plasma facing material in future fusion devices. Advantages of tungsten are low sputtering yield, low tritium retention, etc. However, large radiation loss in the core plasma might occur because tungsten is not fully ionized even in the core plasma. Therefore, it is important to understand the transport process of tungsten impurity and estimate the radiation loss in the core plasma.

In JT-60U, tungsten coated tiles were installed in the outer divertor. The position of tungsten (W) tile was upper part of the outer divertor only in P-8 section as shown in Fig.1. After the experimental campaigns, the tungsten deposition profile was measured in the poloidal and toroidal direction [1]. However the effect of transport process on the deposition profile is not clear so far.

The numerical analysis of the deposition mechanism with the IMPGYRO code is in progress. Here the preliminary results are described.

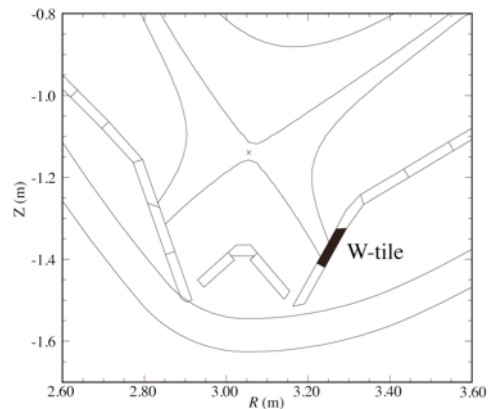


Fig.1 Position of tungsten coated tile

2. Numerical model

The Monte-Carlo transport code IMPGYRO [2] has been developed in order to study a global transport process of high-Z impurity in the whole tokamak plasma and predict the impurity flux penetrating into the main plasma. The code includes important processes for high-Z impurity transport, such as Larmor gyration, Coulomb collisions [3], the thermal force [4] and the multi-step ionization/recombination processes [5]. The three dimensional equation of motion is directly solved in a real tokamak geometry. The plasma-surface interaction, such as a sputtering and a reflection, is taken into account by coupling with the erosion and deposition code “EDDY” [6, 7]. The plasma-surface interaction greatly depends on the incident angle. Therefore in addition to the sheath effect on the incident energy, the change of the incident angle by the sheath acceleration is calculated for each incident particle [8].

The transport process and the deposition profile were analyzed on two magnetic

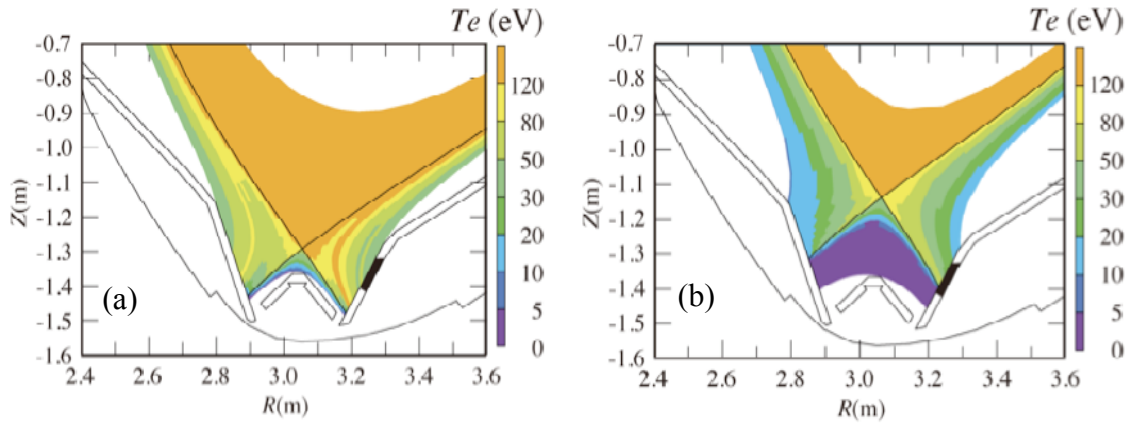


Fig.2 Spatial distribution of electron temperature for (a) the standard configuration and (b) the W experiment configuration.

configurations: (a) standard configuration – the outer strike point is positioned on the lower divertor tile of CFC, and (b) W experiment configuration – the outer strike point is positioned on the W-tile.

The background plasma profiles were calculated by the divertor code SOLPS [9]. The boundary condition at the core interface boundary ($r/a \sim 0.9$) was $n_D = 2.5 \times 10^{19} \text{ m}^{-3}$ and $Q_{in} = 15 \text{ MW}$ for both configurations. The spatial profile of the electron temperature is shown in Fig. 2. The peak of the electron temperature on the outer divertor is higher than 50 eV in both cases.

In the present analysis, the following simple setup has been adopted. As for the initial generation of the tungsten impurities, 10^6 test neutral particles were uniformly launched from the W-tile array with monotonic energy of 10 eV. An absorption condition was set in the main plasma at $r/a \sim 0.995$. The plasma-surface interaction (EDDY) was switched off.

3. Simulation results

The spatial profile of tungsten density is shown in Fig. 3. In the standard configuration, initial generated neutral tungstens are ionized close to the divertor plate. Then tungsten ions

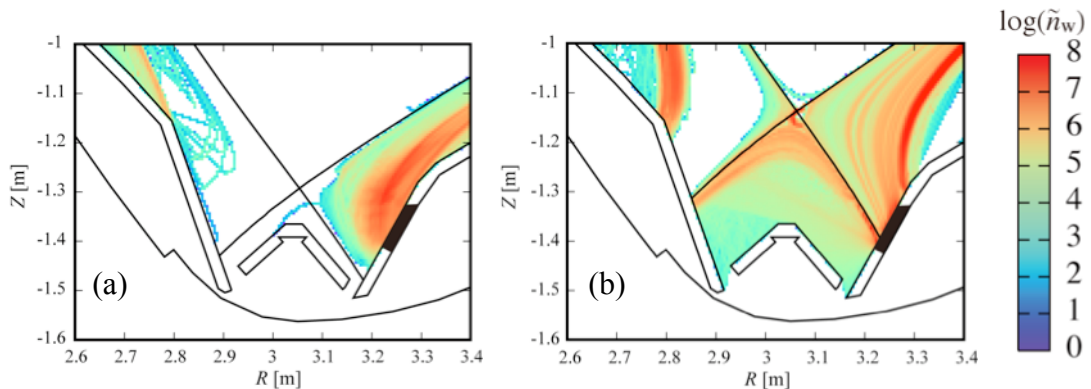


Fig.3 2D profile of W density for (a) standard configuration and (b) W experiment configuration. W density n_w is the sum of all charge states and normalized by the amount of initial generation.

are returned to the outer divertor plate or led toward a SOL plasma top along the magnetic field line by the thermal force. The deposition on the dome or the inner divertor cannot be seen. In the W experiment configuration, the transport of tungsten ions ionized in the divertor region is similar to that in the standard configuration. In the contrast, the tungsten neutrals generated near the separatrix pass through the private region. Some of them are deposited directly on the outer dome wing. The others reach the inner area and are ionized near the inner separatrix. Then they are led to the divertor plate along the magnetic field line.

Figure 4 shows the poloidal profile of the deposited tungsten in the W experiment configuration. The significant deposition on the inner divertor and the outer dome wing can be seen. The features on the outer dome wing agree with the experimental data [1].

In order to investigate the transport process and the deposition profile of tungsten impurities, the analysis with the EDDY code and comparison with the experimental data are in progress.

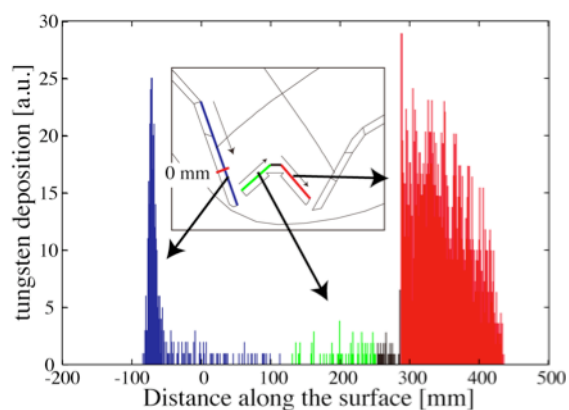


Fig.4 Poloidal distribution of the W deposition. The horizontal axis is the distance along the surface from the inner divertor to the outer dome wing.

References

- [1] Y. Ueda, M. Fukumoto, *et al.*, in Proc. 22nd IAEA-FEC, Geneva, Oct. 2008.
- [2] K. Hoshino, M. Noritake, *et al.*, Contrib. Plasma Phys. **48** (2008) 280.
- [3] T. Takizuka and H. Abe, J. Comp. Phys. **25** (1977) 205.
- [4] J. Neuhauser, W. Schneider, *et al.*, Nucl. Fusion **24** (1984) 39.
- [5] A. Suzuki, T. Takizuka, *et al.*, J. Comp. Phys. **131** (1997) 193.
- [6] K. Ohya, Physica Scripta **T124** (2006) 70.
- [7] M. Toma, K. Hoshino, *et al.*, J. Nucl. Mater. **390-391** (2009) 295.
- [8] K. Hoshino, M. Toma, *et al.*, J. Nucl. Mater. **390-391** (2009) 168.
- [9] R. Schneider, X. Bonnin, *et al.*, Contrib. Plasma Phys. **46** (2006) 3.

9.8 Tungsten Stripe Coatings on the Lower Divertor Plate

T. Nakano, N. Asakura and Y. Ueda.

One CFC plate with tungsten (W) stripe coatings was installed as a lower target of the outer divertor in 2007 for the purpose of investigation on the prompt re-deposition onto the divertor plates. Figure 1 shows the W stripe coatings. Three W stripes with a width of 10 mm and a thickness of $5\ \mu\text{m}$ were coated: One stripe was coated in the poloidal direction and two stripes in the toroidal direction. Because the lower stripe was located below the dome, the outer strike point was not usually put on it. In contrast, on the upper stripe, the outer strike point was often located in various experiments. In that magnetic configuration, intense W emission from the main plasma was occasionally observed.

To identify the source of W, relation between the core W XLVI intensity and the outer-strike-point position during the outer-strike-point sweep around the upper stripe was investigated in an H-mode discharge with a plasma current of 1.0 MA, a toroidal magnetic field of 3.7 T and an NB heating power of 12 MW. As shown in Fig. 2, the W XLVI intensity started to increase when the outer strike point was located just below the upper stripe, and the W XLVI intensity continued to increase with increasing distance from the bottom edge. The W XLVI intensity was kept high when the outer strike point was located above the upper stripe. This is probably due to another W source from the W-coated upper target of the outer divertor by sputtering during ELM.

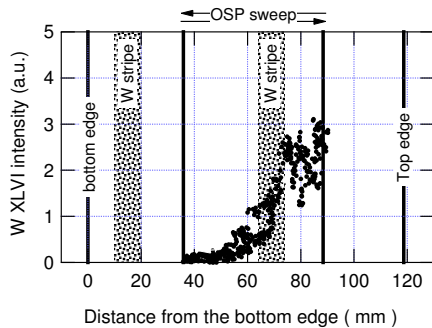


Fig. 2: *W XLVI intensity as a function of the outer-strike-point (OSP) position from the bottom edge of the divertor plates with W stripe coatings.*

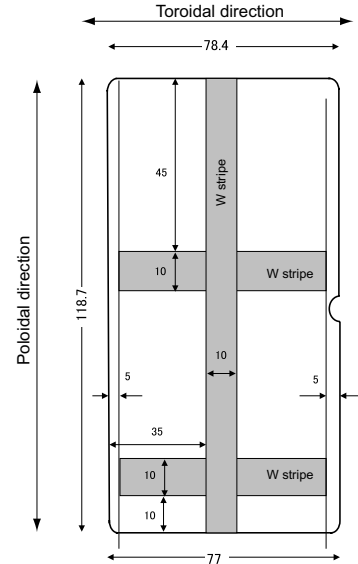


Fig. 1: *Position of W stripe coatings on the lower divertor plates.*

This trend was exactly reproduced during the downward outer-strike-point scan: while the outer strike point was moved downward, the W XLVI intensity started to decrease when the outer strike point was located just above the upper stripe, and then the W XLVI intensity continued to decrease to nearly zero when the outer strike point was located below the upper stripe.

Consequently, it is probable that the source of W in the main plasma was the upper W stripe in the case that the outer strike point was located on the upper W stripe. This plate was removed during the experimental campaign.

10 Diagnostics

10.1 Development of a High-Brightness and Low-Divergence Lithium Neutral Beam for a Zeeman Polarimetry [1]

A. Kojima, K. Kamiya, H. Iguchi¹⁾, T. Fujita, H. Kubo, Y. Kamada and the JT-60 Team

1) National Institute for Fusion Science

A new lithium beam probe (LiBP) has been developed on JT-60U, whose ion beam is characterized by a low-divergence with a high-brightness, for the Zeeman polarimetry to measure the edge current density. The diagnostic system is also utilized for the electron density measurement as a beam emission spectroscopy (BES). So LiBP is a powerful tool to study the H-mode physics, including pedestal and ELMs dynamics. Optimization of the beam injector is essential to improve both higher spatial (~ 1 cm) and temporal resolutions (~ 1 ms for BES and ~ 1 s for Zeeman polarimetry). In the development of the lithium beam on JT-60U, targets of the performances are as follows; Beam energy is required to be relatively low (~ 10 keV) which is the optimum value for the pedestal density range in the H-mode plasma on JT-60U, beam current over 1mA at the plasma edge is required for the good signal-to-noise ratio, and the divergence angle of 0.4 degree for the effective transport and clear separation of the narrow Zeeman-split spectra. In order to obtain the ion beam current over 10 mA, a newly-developed thermionic ion source utilizing a porous tungsten disk with β eucryptite is heated by an electron beam. Moreover, to aim the low-energy and large-extraction simultaneously, the negatively-biased extractor electrode is installed in front of the emission surface of the ion source. The beam optics is designed after detailed numerical simulation taking the space charge effects into account because a low divergence angle of the neutral lithium beam leads to a narrow spectrum of the beam emission. It is also necessary to keep the beam radius small for good spatial resolution due to a long beam line of 6.5 m.

The newly-developed ion gun is operated on a test stand which simulates the diagnostic arrangement on JT-60U, having a 6.5m beam line. Ion beam current of 10mA at beam energy of 10 keV is successfully extracted from the ion source operated at the temperature over 1400 degree Celsius. The ion beam is focused by the optimized Einzel lens. The FWHM (Full Width at Half Maximum) radius of the ion beam at the neutralizer is about 9 mm. A sodium vapor neutralizer neutralizes the collimated ion beam fully at the temperature of 300 degree Celsius. The neutral beam profiles are measured at two locations of the beam line at 2.3 m (corresponding to the beam monitor position) and 6.5 m (corresponding to the plasma region) from the neutralizer, respectively. The FWHM radius of the neutral beam of 52mm and the equivalent beam current of 3 mA with the beam divergence angle of 0.2 degree which is the half-angle divergence has been obtained, achieving the parameter required for the Zeeman polarimetry in addition to the edge BES. Moreover, the long pulse operation up to 50 seconds is demonstrated.

Reference

[1] A. Kojima., et al., , Rev. Sci. Instrum. **79**, 093502 (2006)

10.2 Development and Operation of Lithium Beam Probe

A. Kojima, K. Kamiya, T. Fujita, H. Kubo and the JT-60 Team

1. Introduction

H-mode plasmas are characterized by the pedestal structure and ELM activities in the edge region. The pedestal structure is formed in the narrow region about several cm and the ELM activities have the frequency range up to 1 kHz. Therefore, H-mode study requires the edge diagnostics having the high spatial and temporal resolutions, simultaneously. Toward such requests, Lithium beam probe (LiBP) is one of powerful tools for the edge diagnostic, and is widely utilized at a lot of tokamak devices, such as DIII-D [1], JET [2] and ASDEX-U [3]. In JT-60U, the newly-developed LiBP system with low-energy and high brightness Li injector has been developed and installed in order to measure the time evolution of the edge density profile during ELMs and the edge current profile in H-mode plasmas [4]. The edge current density and electron density measurements have been successfully demonstrated after the beam conditioning and beam axis alignment.

2. LiBP System on JT-60U

LiBP system consists of the Li beam injector and the detectors as shown in Fig. 1. As for the injector, the high-brightness and low-divergence ion gun has been installed in the diagnostic hall. In the beam injection to JT-60U, the leakage magnetic field affects the beam steering seriously. The poloidal coils apply the leakage magnetic field of 10^{-4} T, which is the marginal value to control the beam position within the long and narrow beam line. Therefore, the ion gun has been shielded by the magnetic shield which has the capability to reduce the magnetic field from 3×10^{-2} T to 2×10^{-5} T. The magnetic shield has the three-layer structure and consists of SS400 (40mm) and Permalloy (2mm dual layer). Since the magnetic shield has worked successfully, the beam displacement due

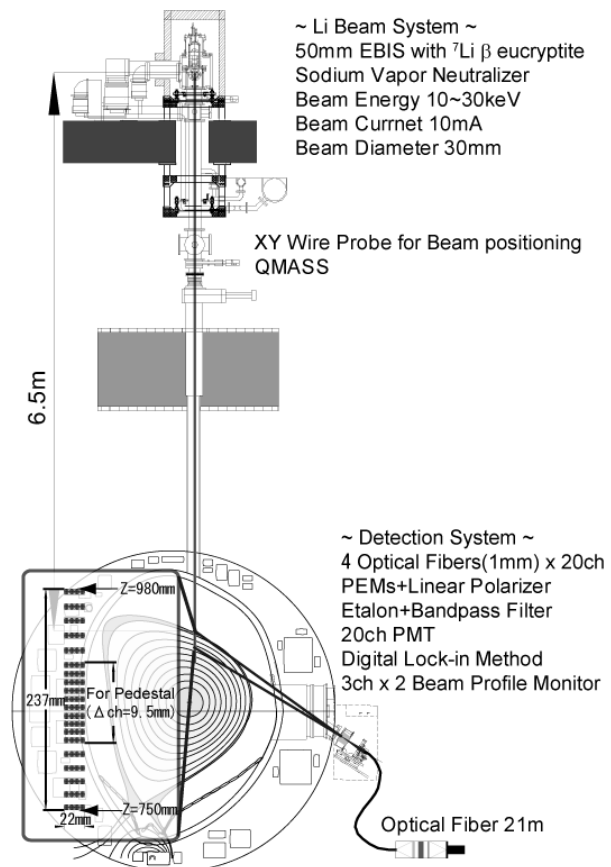


Fig. 1. LiBP system on JT-60U

to the magnetic field has not observed during the beam injection. As for the detectors, the optical system has been installed at the horizontal port of JT-60U. It consists of the optical lens, the photo elastic modulators (PEMs), the linear polarizer and the optical fiber array. The optical lens has the magnification of 0.2 and the effective diameter of 120 mm. S-TIH6 material is utilized for the lens which is the alternative to the low Verdet constant glass SFL6. In front of the lens, the slit is installed to reduce the solid angle to the direction of the beam axis. Optical fiber array has 20 channels for the diagnostics and 3x2 channels for the beam profile and axis monitors. The spatial resolution in the radial direction is 1 cm, depending on the intersection of the beam and the sight line. Four fibers with each core diameter of 1 mm are bundled in each diagnostic channel. The 600 μm fibers are arranged at up- and down-stream for the beam profile monitor, having 3 channels perpendicular to the beam axis. The photo-multipliers with the etalon ($\Delta\lambda\sim 0.1$ nm) and bandpass filters ($\Delta\lambda\sim 1$ nm) detects the Doppler-shifted Li beam emission ($\lambda=670.8$ nm). The high-speed oscilloscopes are utilized for the data-acquisition system.

3. Operation of LiBP

During the experimental campaign, the operation period of LiBP is determined by the short life time of the neutralizer. The life time of the ion source with β eucryptite of 1.5 g is estimated to be 52.5 A sec. In the case of the beam current of 5 mA which is the typical value, the ion source can keep the beam extraction for 10000 seconds corresponding to 200-300 shots. As for the neutralizer, the neutralizer with Na of 1g keeps the effect by 10 hours at the temperature of 300 degree Celsius. Typically, Na of 8g is reserved in the Na reservoir tank. Then, the neutralizer needs to be refilled after 10 operation days. The optimization of the neutralizer configuration or the alternative methods of the charge exchange are issues to improve the life time of the neutralizer.

Injecting Li beam to JT-60U, the beam current is maintained by the PID control of the electron beam (EB) power to the ion source as shown in fig. 2(a). After high voltages are

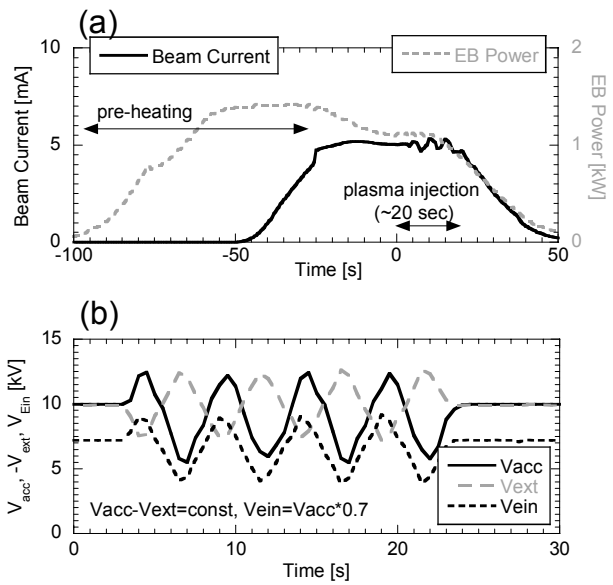


Fig. 2. (a) Operation of the electron heating ion source. (b) Waveforms of the high voltages in the case of the beam energy sweeping.

applied, EB filament current is increased gradually. The relation of the filament power and the EB power are obtained and utilized for the EB power control. After pre-heating of the ion source, the EB power is decreased to maintain the expected beam current. Because it takes several 10 seconds for the temperature profile of the ion source to reach stationary state, the ion source needs to be ready before the beam

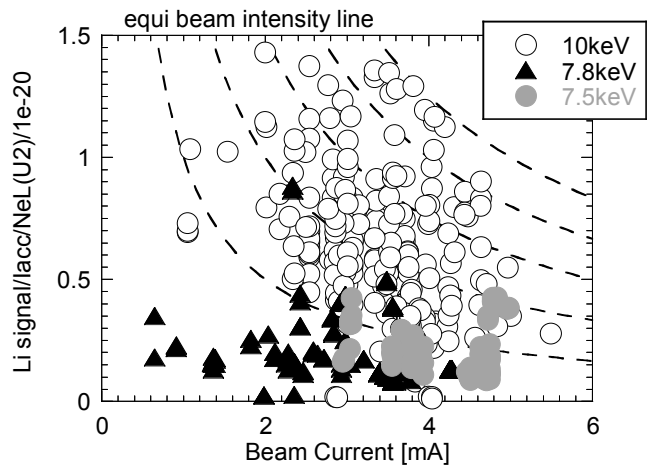


Fig. 3. Progress of the improvement of the beam quality at each beam energy.

injection to the plasma. At the beginning of the plasma injection, the relative sensitivity across the all detectors is carried out by use of the gas injection phase before the plasma ignition in every shot. During the beam injection, the beam chopping by the deflector is used to monitor the background light. To obtain the wavelength characteristic of the etalon filters, the effective method by use of the beam energy sweeping is developed as shown in Fig. 2(b). The acceleration, extraction and Einzel voltages are synchronously scanned to change the beam energy and to keep the beam current in this method.

For the beam axis alignment, the two pairs of high voltages to the XY deflectors are scanned by the high-speed HV amps. And then the Einzel lens voltage is adjusted. The beam position and profile are examined by the XY wire probes (without plasma injection) and the beam profile monitors (with plasma injection). The beam alignment is important for the diagnostic because the beam emission intensity strongly depend on the beam quality corresponding to the beam alignment and focusing as shown in Fig. 3. This figure shows the progress of the beam emission intensity normalized by the beam current and line-integrated electron density. The horizontal axis implies the beam intensity corresponding to

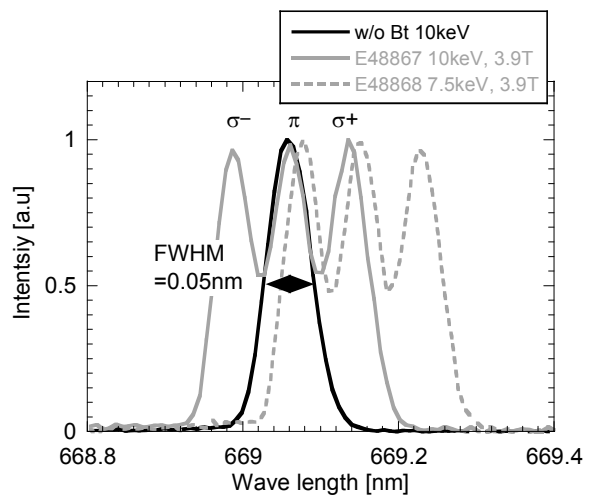


Fig. 4. Beam emission spectra in the cases of the gas injection at 10 keV beam, OH plasma at 10 keV and 7.5 keV beams

the beam quality. Control of low energy and large beam current injections are difficult and require the accurate alignment and repeatability because of the space charge effects. 10 keV injections for the density measurement have been carried out mainly which is the design value of beam energy, and also 7.5 and 7.8 keV injections have been tried to measure the edge current profile; these beam energies correspond to the characteristic of etalon filters. The beam emission spectra are obtained in the gas injection (without toroidal magnetic field) and ohmic heating plasma as shown in Fig. 4. This figure shows that the full width at half maximum of 0.05 nm which is caused by the beam divergence and solid angle of the optical system is small enough to separate each Zeeman splitting spectra.

The density measurement is carried out at beam energy of 10 keV. In the density reconstruction, only the 2s-2p emission is considered and the whole shape of the beam emission profile is estimated from the measured profiles. Including the full atomic process to the reconstruction is the future task. The typical beam emission profiles and the reconstructed electron density are shown in Fig. 5. The background signal is estimated from the beam-off signal of beam chopping method. In the case of the L mode (low density), the beam emission profile is almost identical to the density profile. In the H mode plasma (high density), the beam is fully attenuated within the observation area. Therefore, the penetration length of 10 keV beam is short enough to reconstruct the edge density profile of the JT-60U H mode plasma.

References

- [1] D. M. Thomas, et al., Rev. Sci. Instrum. **61**, 3040 (1990).
- [2] Z. A. Pietrzyk et al., Plasma Phys. Controlled Fusion **35**, 1725 (1993)
- [3] E. Wolfrum, et al., Rev. Sci. Instrum. **77**, 033507 (2006).
- [4] A. Kojima, et al., Rev. Sci. Instrum. **79**, 093502 (2008).

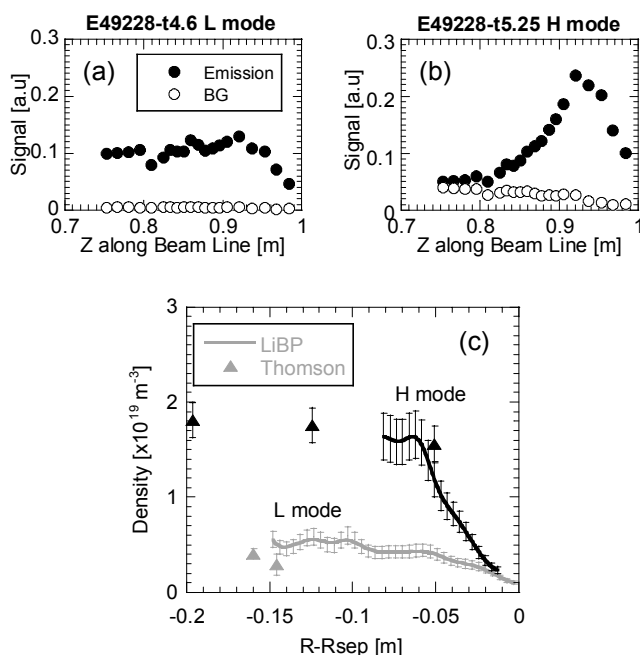


Fig. 5. Beam emission and background signal profiles on (a) L mode and (b) H mode plasmas. (c) Edge density profile on L and H mode plasmas reconstructed by the emission profiles.

10.3 Zeeman Polarimetry Measurement Using Li-beam Probe

K. Kamiya, T. Fujita, A. Kojima and H. Kubo

1. Introduction

It is well known that the edge current density plays an important role for the determination of the edge stability limit according to theory, which affects on the Edge Localized Mode (ELM) behavior and pedestal physics [1]. Recent theoretical studies have pointed out that variations in the ELM characteristics (e.g. Type-I, II and III, including QH-mode and grassy ELMs) could be explained in terms of a low n toroidal mode number MHD model with 2nd stability access (so-called, “peeling-ballooning” model) [2]. The peeling-ballooning instability is driven by pedestal gradients in both pressure and current. In the recent experiments in many tokamaks, the pressure limit in the plasma peripheral region has successfully described with this model. However the edge current density was only inferred from calculations of the edge Pfirsch-Schluter and bootstrap currents using the measured pedestal profiles and neoclassical bootstrap model [3].

A direct measurement of the edge current profiles is very important for understanding the edge MHD stability. Recent experiment on DIII-D, the first direct measurements of the edge poloidal field were made at the outer midplane with a new Li-beam Zeeman polarimetry diagnostic [4], although one of the challenges of this measurement is separating the σ and π components of the Li triplet, which are orthogonally polarized and only ~ 0.03 nm apart for full field operation on DIII-D at ~ 2.1 T [5].

2. Zeeman polarimetry measurement using Li-beam probe

A 10keV Li-beam probing system has been developed on JT-60U for the edge current density measurement using Zeeman polarimetry (ZP), which has 20 channels with spatial resolution of up to 1cm at

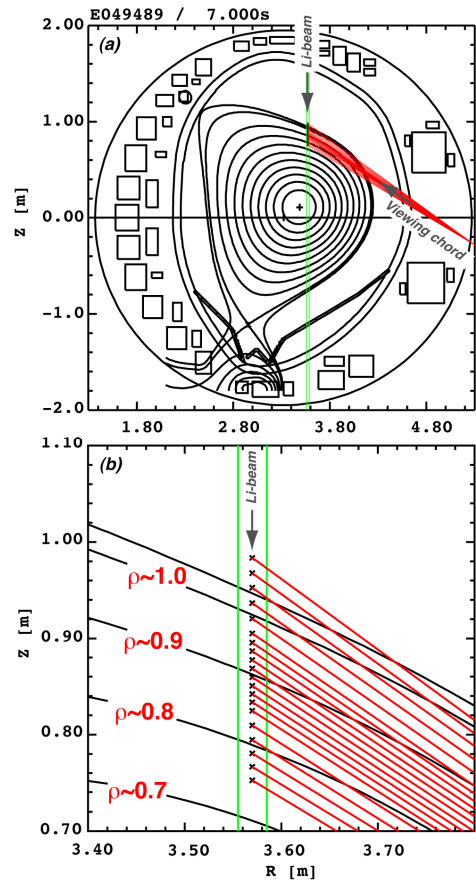


Fig 1. (a) Poloidal cross section for E049489 at 7.0s (elongation $\kappa \sim 1.3$ and triangularity $\delta \sim 0.543$ with plasma volume $V_p \sim 55.8$ m³) showing the lithium beam injection line from the top of the vacuum vessel and the viewing geometry from the outer mid-plane. (b) expanded view of (a).

$r/a \sim 0.8-1$ as shown in figure 1. The diagnostic system makes it possible to measure the electron density and its fluctuation by Beam Emission Spectroscopy BES, simultaneously [6].

In the recent experiment on JT-60U, we have achieved that the Li-beam injection to the NBI heated plasma with beam current of up to ~ 5 mA [7]. An advantage of ZP on JT-60U is higher toroidal magnetic field B_t operation up to ~ 4 T, which enables us to measure the edge current density with high precision due to wider line separation given by the Zeeman effect (0.021 nm per Tesla in the case of lithium for fields greater than about 1 T). Optimization in the beam focusing with electro-static lenses is also important, since each of split line profiles is broadened due to Doppler effects in the beam.

As shown in figure 2, we confirmed that each circular polarized components are fully separated by ± 0.1 nm from linear polarized one at $B_t \sim 4$ T using a high throughput spectrometer CLP-400 (focal-length $f \sim 400$ mm with the F number ~ 2.8). Doppler broadening is also found to be as small as 0.04-0.05 nm. In order to select the σ component of the Zeeman triplet of the Doppler shifted Li emission, the etalon filter having FWHM of $\sim 0.08-0.1$ nm is utilized. This task is not so difficult due to almost fully splitting of π and σ components at the maximum B_t operation on JT-60U (up to ~ 4 T). In this study we have used both temperature and rotational stage tuned fused silica solid etalons, whose parameters are 50.0 mm diameter, 0.5 mm thick, a surface figure of $\lambda/20$, and a reflectivity of 70%. The free spectral range, $FSR = \lambda^2/2nd = 3.1 \text{ \AA}$, where $n=1.45$ is the index of refraction. The reflectivity finesse is given by $F_R = \pi[R/(1-R)]^{1/2} = 8.76$, where $R=0.7$ is the reflectivity. This results in a bandwidth of 0.35 \AA , which would easily resolve the σ component. However, the finesse is reduced by the surface figure of the etalon and the fact that the light is not perfectly collimated. A surface figure finesse $F_{\text{surface}} = s/4.7 = 4.3$, where s is the surface figure given as a fraction of the wavelength (i.e., $s=20$ for $\lambda/20$ surface figure). The pinhole finesse, $F_{\text{pinhole}} = 4\lambda L^2/ndD^2 = 9.3$, where $L=100$ mm is the focal length of the collimating lens and $D=2$ mm is the diameter of the input fiber bundle. The resulting finesse F is estimated to be ~ 3.53 , which is determined from the formula as the following inverse quadrature sum; $1/F^2 = 1/F_R^2 + 1/F_{\text{pinhole}}^2 + 1/F_{\text{surface}}^2$. This results in a bandwidth of $\Delta\lambda_{FWHM} = FSR/F \sim 0.88 \text{ \AA}$, which is consistent with the measured one as shown in figure 2.

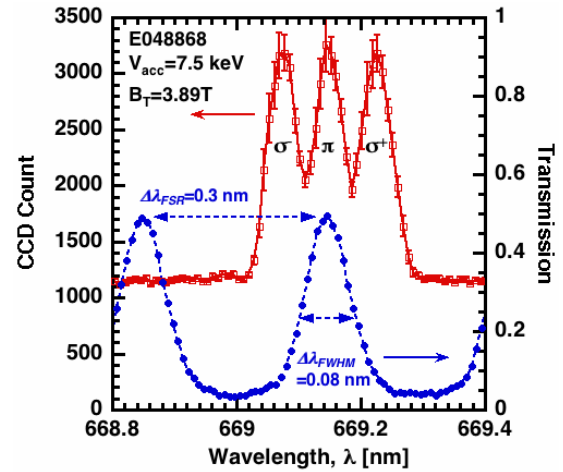


Fig. 2. Measured line profile from CLP-400 spectrometer for E048868 and Etalon transmission when illuminated with white light by the integrated light sphere.

3. Development of a new tuning method of wavelength for etalon.

The pitch angle of the magnetic field is obtained from measurements of the polarization state of a σ^- (or σ) component of the lithium triplet, which is used as a constraint for the MHD equilibrium code to identify the edge current density profile [8]. To accurately determine the ratio of circular to linear polarization using modulation techniques requires lock-in measurements at four different frequencies (fundamental and second harmonic of each of the two PEM resonant frequencies). The most important point to improve the signal to noise ratio is that, the σ (or σ^-) component must be separated as completely as possible not only from the orthogonal linear polarized π component, but also the oppositely handed circularly polarized σ^- (or σ) component. And hence, a fine tuning for the central wavelength of Etalon towards both side direction (namely towards longer and shorter wavelength) is essential, which is possible with the use of both temperature and rotation control systems.

A new tuning method of central wavelength has been demonstrated, scanning the beam acceleration voltage V_{acc} during a single shot as shown in figure 3. During the V_{acc} scan, there is the local *minimum* in the digital lock-in detected signals in the $2f$ (~40 kHz or 46 kHz) component (Linear Polarization, LP) when the $1f$ (~20 kHz) component (Circular Polarization, CP) passes through nearly zero. On the contrary, there are the local *maximum* in the digital lock-in detected signals in the $2f$ (~40 kHz or 46 kHz) component when the $1f$ (~20 kHz) component reaches either *minimum* or *maximum* value. The former V_{acc} (i.e. V_{acc} at the CP component ~ zero) corresponds to the central wavelength of central π component in the Zeeman triplet at the maximum transmitted location of the Etalon. The latter V_{acc} (i.e. V_{acc} at the CP component ~ local *minimum* or *maximum*) corresponds to the central wavelength of the σ^+ or σ^- components in the Zeeman triplet at the maximum transmitted location of the Etalon. It is noted that the sign in the LP components depends on the phase adjustment relatively to the reference signals from PEMs. Once the V_{acc} is known for the central peak in the π or σ components, the location of the optimized wavelength of the Etalon is determined by the conversion of the V_{acc} towards wavelength unit using a calculation of the Doppler-shift $\delta\lambda$ as follows: $\delta\lambda = 670.784(1 - v_{beam}/c)\cos\theta$. Here, $v_{beam} = (2eV_{acc}/m_{Li})^{1/2}$ is velocity of the accelerated Li-neutrals where e is the electron charge and m_{Li} mass of the Li-neutrals, c is the light speed and θ is the angle between the beam line and viewing chords, respectively. It should be noted that each spatial channel has a slightly different wavelength caused by the Doppler shift of the accelerated lithium neutrals due to the variation in viewing angle. As a result, we could tune the central wavelength of the etalon for each channel to the central wavelength of the σ^- component at the $V_{acc}=7.5$ (or 7.8) keV for the edge current measurements and π component at the $V_{acc}=10$ keV for the edge electron density measurements, respectively.

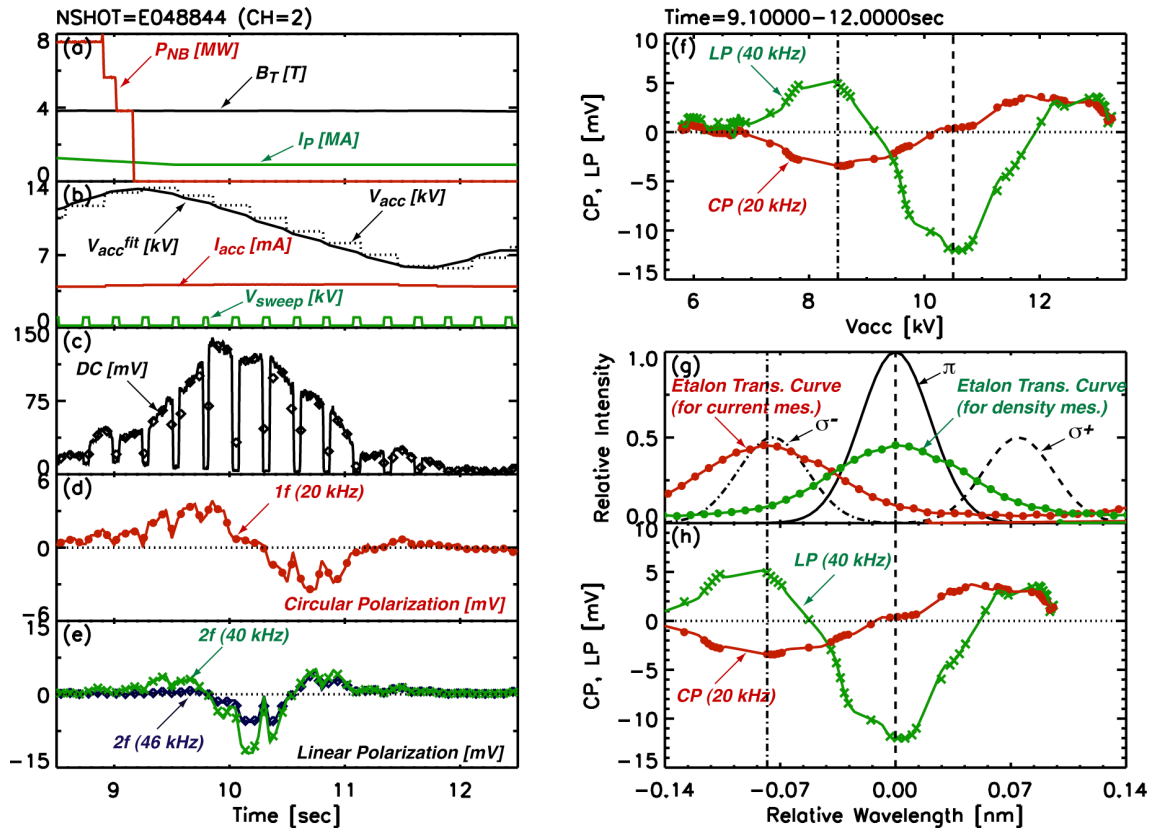


Figure 3. Temporal evolution of (a) toroidal magnetic field B_T , plasma current I_P and NBI power P_{NB} , (b) acceleration voltage V_{acc} , beam extraction current I_{acc} and sweep voltage V_{sweep} , (c) DC, (d) CP and (e) LP components of the phase modulated signals using PEMs. Both CP and LP are detected by the digital lock-in method. In order to check the effect of the background light, the Li-ion beam is electro-statically deflected by the V_{sweep} between the parallel plates equipped in front of the aperture of the neutralizer in the ion-gun. Both CP and LP components plotted against (f) V_{acc} and (h) relative wavelength. (g) Modeling of the σ and π components, broadened to FWHM of 0.05 nm, together with the etalon transmission function whose central wavelength is tuned to the central wavelength of the σ^- and π component for the edge current and density measurements, respectively, are also shown.

References

- [1] Greenfield C. M. *et al.*, Phys. Plasmas **7**, 1959 (2000).
- [2] Snyder P. B. *et al.*, Phys. Plasmas **9**, 2037 (2002).
- [3] Houlberg W.A. *et al.*, Phys. Plasmas **4** 3230 (1997).
- [4] Thomas D. M. *et al.*, Phys. Rev. Lett. **93**, 065003 (2004).
- [5] Carlstrom T. N. *et al.*, Rev. Sci. Instrum. **73**, 1601 (2003).
- [6] Kojima A. *et al.*, Rev. Sci. Instrum. **79**, 093502 (2006).
- [7] Kojima A. *et al.*, this issue, section 10.1 and 10.2.
- [8] Fujita T. *et al.*, this issue, section 10.4

10.4 Equilibrium Reconstruction Using the Lithium Beam Probe Data

T. Fujita, K. Kamiya, A. Kojima and H. Kubo

1. Introduction

A lithium beam probe (LiBP) has been developed for measurement of density and current profiles in the pedestal region with high spatial resolution. The current profile measurement relies on the fact that the fraction of the circular and linear polarizations of the Zeeman split components has information on the orientation of local magnetic field. In this paper, the procedure for evaluating the current profile using the LiBP data and initial results on the current profile measurements are presented.

2. Diagnostics principle and optimization of PEM parameters

In the magnetic field B , the 2S-2P resonance line of a lithium atom is split into a π and two σ lines due to the Zeeman effect. For emission perpendicular to B , the π line and the two σ lines are linearly polarized, parallel and perpendicular to B , respectively. For emission parallel to B , there is no π line and the two σ lines are circularly polarized. Since the sight lines are nearly parallel to the flux surface, as shown in Fig. 1 in [1] for achieving good spatial resolution, the component of B parallel to the sight line is needed for evaluating the pitch angle of B . Hence, it is need to use σ lines and the $\sigma-$ line was used in the experiment. The intensity of circular polarization I_{CL} and that of linear polarization I_{LP} of the σ line are related to the angle α between the local magnetic field and the plane perpendicular to the sight line, as shown in Fig. 1, through the following equation.

$$\frac{I_{CP}}{I_{LP}} = \frac{2\sin\alpha}{\cos^2\alpha} \quad (1)$$

The MHD equilibrium code for analysis of MSE data [2] was modified to calculate the angle α along the lithium beam line for a given equilibrium. The code was used to evaluate change in α caused by a local change in the current density, and it was found that accuracy of $\sim 0.1^\circ$ in α is needed to measure a local current peak with accuracy of $\sim 30\%$ in the edge region for typical conditions ($q_{95} \sim 5$).

A pair of Photo Elastic Modulators (PEMs) with driving frequencies of $f_1 = 20$ kHz and $f_2 = 23$ kHz was employed for polarization measurement. The I_{CP} and I_{LP} are obtained by 1f and 2f components of the signal:

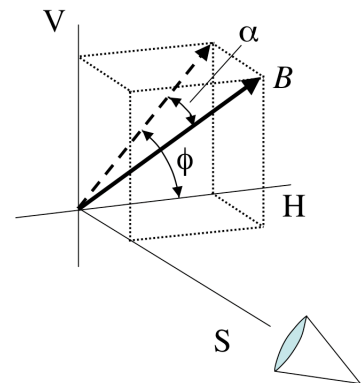


Fig. 1. Definition of angles α and ϕ for denoting orientation of magnetic field B with respect to the sight line S .

$$\frac{I_{CP}}{I_{LP}} = \frac{I_{20}/a(\delta_{20})}{\sqrt{(I_{40}/b(\delta_{20}))^2 + (I_{46}/b(\delta_{23}))^2}}, \quad (2)$$

where I_{20} , I_{40} and I_{46} denote 20 kHz, 40 kHz and 46 kHz Fourier amplitudes, with signs, of the signal, and δ_{20} and δ_{23} denote retardations (in unit of radian) of 20 kHz and 23 kHz PEMs. Though the functions $a(\delta)$ and $b(\delta)$ are given by $J_1(\delta)$ and $J_2(\delta)$, respectively, in theoretical calculation, where J_1 and J_2 being the first and second order Bessel functions, these coefficients need to be calibrated in the real geometry. Though the retardation δ_{20} and δ_{23} are set π [rad] for linear polarization measurement like MSE, this value is not optimum for circular polarization measurement. In the experiment, $\delta_{20} = 0.7\pi$ [rad] and $\delta_{23} = \pi$ [rad] were used, so as to obtain a larger $a(\delta_{20})$ and hence a larger I_{20} for a given I_{CP} , for which $a(\delta_{20})/a(\pi) \sim 1.37$ and $b(\delta_{20})/b(\pi) \sim 0.78$ were obtained in the calibration. Finally, it was found that the effect of background light to be discussed in 3.2 was larger for I_{40} than I_{46} by a factor of 3, and hence I_{LP} was evaluated without using I_{40} but with I_{46} and calculated value of I_{40}/I_{46} , the latter of which is determined by the plasma shape and is not varied by the local current profile.

3. Calibration of polarization measurement and compensation of background light effect

The equation (1) holds only for I_{CP} and I_{LP} of a pure σ line. The intensity obtained from equation (2) in the real experiment, I_{CP}^m/I_{LP}^m , is different because of contamination with (i) undesired π and the other σ lines and (ii) the polarized component of the background light, namely light other than the beam emission. The first effect is determined by conditions of lithium beam operation and etalons, while the second effect depends on the plasma conditions. These two effects will be discussed separately in the following.

3.1. Calibration of polarization measurement

Measurement of beam emission without plasma, namely by injecting the lithium beam into a gas filled torus in a given magnetic field generated by external coils, is an ideal method for the calibration of the polarization measurement. However, it was found that the signal intensity was too weak to obtain calibration data with required accuracy ($<0.1^\circ$) even with the maximum gas (helium and argon) pressure for which the operation of lithium beam injector was possible. As the second method, measurement of the peripheral region of a stationary OH plasma was attempted. It is expected that in the very edge region ($0.93 < \rho < 1$), α can be evaluated within accuracy of 0.1° even without measurement of the current density profile, taking into account reasonable variations in the current density profile. By changing the plasma surface position shot by shot, all of the LiBP channels can be located in $0.93 < \rho < 1$ and thus can be calibrated. However, it was found that the calibration data obtained in a peculiar shot was not valid in other shots. This seems to be because the operation condition of the

lithium beam was not fixed in the experiment but was varied shot by shot in order to improve the beam current and divergence. Finally, the calibration for the measurement on the H-mode was made using the OH or L-mode phase of the same shot. For this calibration, it is needed to assume the current profile at least in the edge region, which causes additional errors. These errors, however, are expected to be small because of absence of an edge current peak in OH and L-mode plasmas.

3.2. Compensation of background light effect

The background (BG) light had a significant fraction of polarization ($\sim 14\%$) and thus affected the measurement of the polarization component as well as that of emission intensity for density measurement [3]. The polarized BG light seems to be generated by reflection of bremsstrahlung light on the first wall. The magnitude of the BG light depended strongly on the location of strike points. Compensating the BG light effect was inevitable in order to measure α with required accuracy of $\sim 0.1^\circ$. In the electron density measurement, the BG component was evaluated by chopping the beam through applying a voltage to the reflector in the ion gun. In the current density measurement, however, this method was not available because averaging the data for a period longer than 1 s was needed to achieve the required accuracy. Instead, we repeated two discharges with and without lithium beam injection and then evaluated net signal caused by the beam emission by their difference. This needs, of course, reproducibility of the BG light. Some of the channels were therefore adjusted not to receive the beam emission at all so as to monitor the BG light for all discharges regardless of lithium beam injection.

Figure 2 shows time evolution of polarization components in repeated discharges. The circular polarized component of BG light was nearly zero as shown in (a), while a nonnegligible amount of linear polarized component of BG light was observed as shown in (b). The BG light was large during the high power heating phase and reproducibility of BG light was quite good as shown in (c).

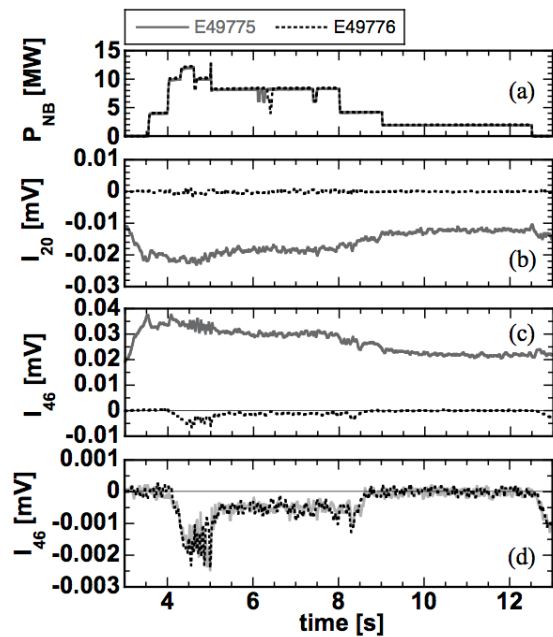


Fig. 2. Polarization components for two repeated discharges for compensating the background light effect. Solid lines denote the discharge with beam injection (E49775) while dotted lines without beam injection (E49776). (a) NB power. (b) 20 kHz component (circular polarization) of CH 10. (c) 46 kHz component (linear polarization) of CH 10. (d) 46 kHz component of CH 8 for monitoring the background light.

4. Evaluation of edge current density profile in an H-mode plasma

The current density profile for an H-mode plasma was evaluated using the data averaged from $t = 5.2$ to 8 s in the shot shown in Fig. 2 (E49775). During this period, small ELMs having mixed grassy and small type-I ELMs (so-called ‘mixture’ ELMs) were maintained with NB power of 8 MW. The plasma parameters were: $I_p = 0.80$ MA, B_t (at the plasma center) = 3.74 T, $q_{95} = 7.9$, $\kappa_{95} = 1.23$, $\delta_{95} = 0.46$, $\beta_p = 1.30$. The calibration was made using the L-mode data in the same shot averaged from $t = 9.5$ to 12.5 s, with NB power of 2 MW, where the BG light component was also compensated. Due to the adiabatic heat capacity (I^2t) of the VT coil used for high triangularity configuration, a plasma shape different from that for the H-mode phase, with $\kappa_{95} = 1.38$ and $\delta_{95} = 0.16$, was employed for the L-mode phase, though the plasma surface position on the lithium beam line was unchanged.

The symbols in Fig. 3 (a) denote α for the H-mode phase from the LiBP measurement calibrated using the L-mode data. The open symbols show the data outside the separatrix or with weak intensity due to beam attenuation. The error bars evaluated from standard deviations during the averaged period were shown in the figure, which was $\sim 0.1^\circ$ for most of the channels. The solid lines in Fig. 3 (a) denote α from the equilibrium code assuming the current density profiles shown in Fig. 3 (b). For the profile without an edge peak shown by a thin solid line, the calculation does not agree with the measurement. For the profile with an edge peak located at $\rho \sim 0.9$, the slope of the line is changed and better agreement to the measurement was obtained. For some of the channels (two around $Z = 0.9$ m and one around $Z = 0.85$ m), the agreement was not obtained, the reason of which is not identified yet. If the channels with solid symbols except for these three are considered, the magnitude of the edge current density peak is found to be around 0.2 MA/m², as shown in the figure. This value will be compared with the bootstrap current evaluated with measured density and temperature profiles.

References

- [1] Kamiya, K., et al., this issue, section 10.3.
- [2] Fujita, T., et al., JAERI-Review 2002-022, section 9.7.
- [3] Kojima, A., et al., this issue, section 10.2.

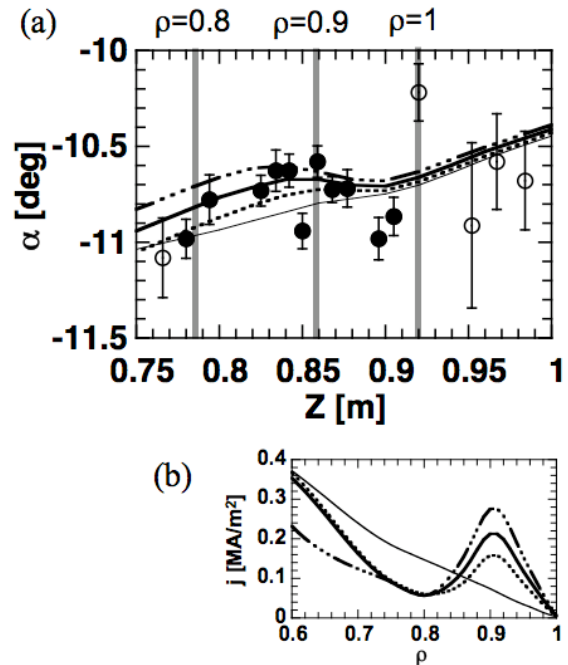


Fig. 3. (a) The angle α as a function of position on the lithium beam line. Symbols are measured values while lines denote calculated values assuming the current density profile shown in (b).

10.5 Development of Doppler Reflectometer and Correlation Reflectometer in JT-60U

N. Oyama, H. Takenaga, T. Suzuki, Y. Sakamoto, A Isayama

1. Introduction

The formation and control of transport barriers in fusion plasmas are essential for the establishment of advanced tokamak plasmas. Transport barriers at the edge and/or core regions, i.e., the edge transport barrier (ETB) and internal transport barrier (ITB), have been observed in many fusion devices. In JT-60U, the Broadband O-mode reflectometer has been developed [1] and applied to the density fluctuation measurement at ETB and ITB [2]. For the further investigation of the transport physics between the anomalous transport and density fluctuations, measurements of the radial electric field (E_r) and the radial correlation of the density fluctuation are important. Therefore, new reflectometer system using synchronized synthesizers, which can sweep the frequency of the incident wave rapidly, has been developed to complement existing three channels fixed O-mode reflectometer for density fluctuation measurements in JT-60U.

2. Doppler reflectometer and correlation reflectometer using synchronized synthesizers

The previous reflectometer system consists of one fixed channel with a frequency of 34 GHz and two selectable frequency channels with frequencies in the range of 36–40 and 48–50 GHz, which correspond to cutoff densities of $1.4 \times 10^{19} \text{ m}^{-3}$, $(1.6\text{--}2.0) \times 10^{19} \text{ m}^{-3}$ and $(2.8\text{--}3.1) \times 10^{19} \text{ m}^{-3}$, respectively. To cover these frequencies in Q-band (33-50 GHz), new reflectometer consists of synchronized synthesizers with the frequency range of 8-12.5GHz and x4 active multiplier (output frequency is 32-50 GHz) as shown in Fig. 1.

Two synthesizers with phase lock loop (PLL) having short time constant to reduce the pull-in time are synchronized to the same reference clock with the frequency of 32 MHz. The typical value of the pull-in time is less than 500 μs . A frequency difference of 32 MHz set

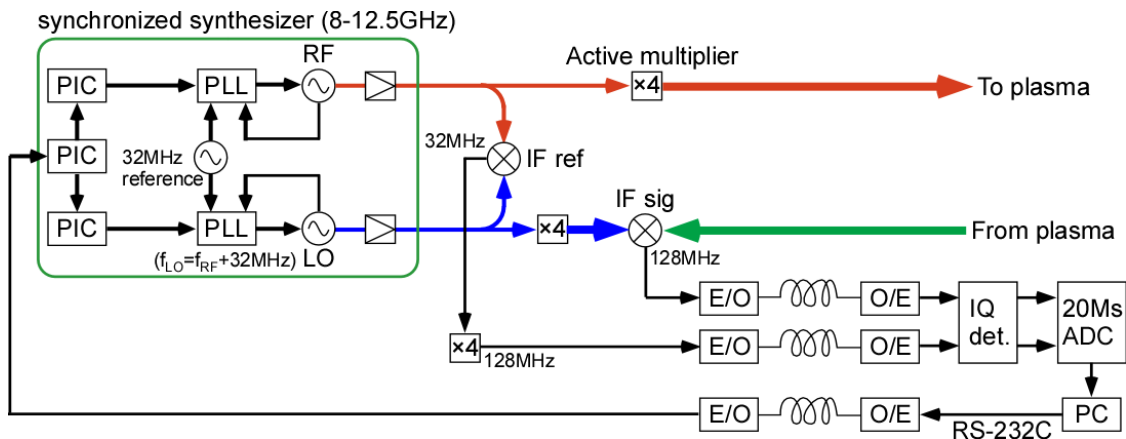


Fig. 1. Schematic of new reflectometer system for Doppler reflectometer and correlation reflectometer.

between two synthesizers used for RF and LO provides 32 MHz intermediate frequency (IF) signal by the heterodyne detection at the mixer. The IF signal is fed to x4 active multiplier to obtain the reference signal with 128 MHz. On the other hand, the main wave branch from two synthesizers are multiplied by 4 using other active multiplier to produce Q-band wave and then fed to plasma as a probe beam or the double balanced mixer as a local wave. The reflected wave at the cutoff density layer is also fed to the double balanced mixer for the heterodyne detection.

The IF signal outputs with the frequency of 128 MHz from two mixers are transferred to the shield-room using the optical fiber link system. The quadrature-type phase detection system (IQ detector) provides sin- and cosine-components of the received signal. The IQ outputs are acquired by a PC-based 14 bit digitizer providing the real time streaming to HDD with the sampling speed of 20 MS/s for 2 channels, providing a longtime data acquisition covering whole plasma duration.

The frequencies and duration of each step of the synthesizer can be preprogrammed up to 20 steps. The parameters for the operation of the synthesizer can be set on the control PC and be downloaded to the synthesizer using RS-232C. In the density fluctuation measurements in JT-60U, 12 different frequencies are cyclically changed with 20 ms duration at each step, which is required for the ensemble averaging.

3. Experimental results

3.1 Evaluation of E_r using Doppler reflectometer

The principle of the Doppler reflectometer is found in ref [3]. In the condition that the incident wave is injected into plasmas with the tilt angle to the mean cut-off layer normal (see Fig. 2), only scattered wave, which satisfies the Bragg condition ($k_f = -2k_0N$, where k_f is the turbulence wavenumber, k_0 is the wavenumber of the incident wave in vacuum and N is the refractive index at the reflection layer.), can be received. Thus, the poloidal rotation speed of the density fluctuation, u_{\perp} , can be evaluated using the relation of $2\pi f_D \sim u_{\perp} k_{\perp}$ assuming $k_{\parallel} \ll k_{\perp}$, where f_D is the Doppler shift.

The f_D is determined by fitting to the Gaussian distribution as shown in Fig. 3. In the configuration shown in Fig. 2, negative Doppler shift corresponds to the poloidal rotation in the direction to the electron diamagnetic drift. Corresponding to the direction of the toroidal

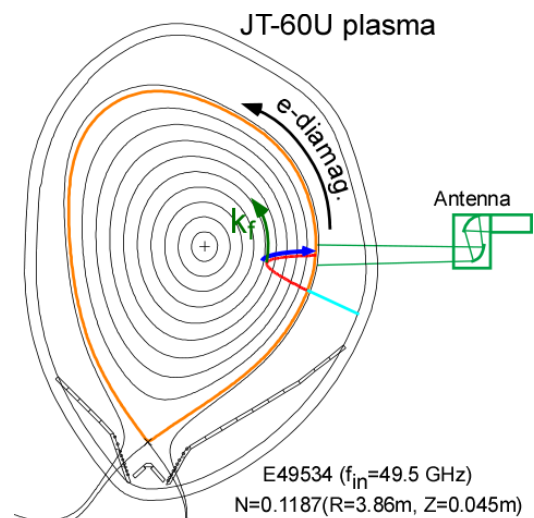


Fig. 2. Schematic of configuration for Doppler reflectometer. Example of ray tracing with $f_0=49.5\text{GHz}$ is also shown.

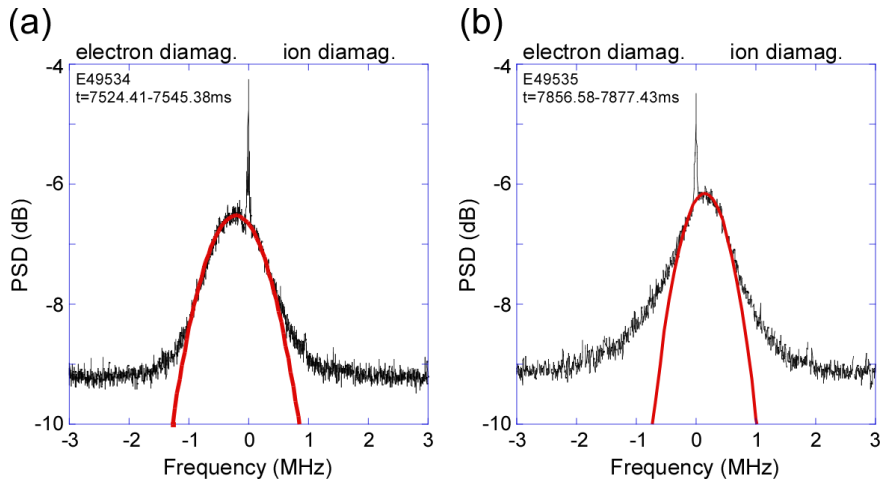


Fig. 3. Frequency spectrum in (a) counter-rotating plasma and (b) co-rotating plasma.

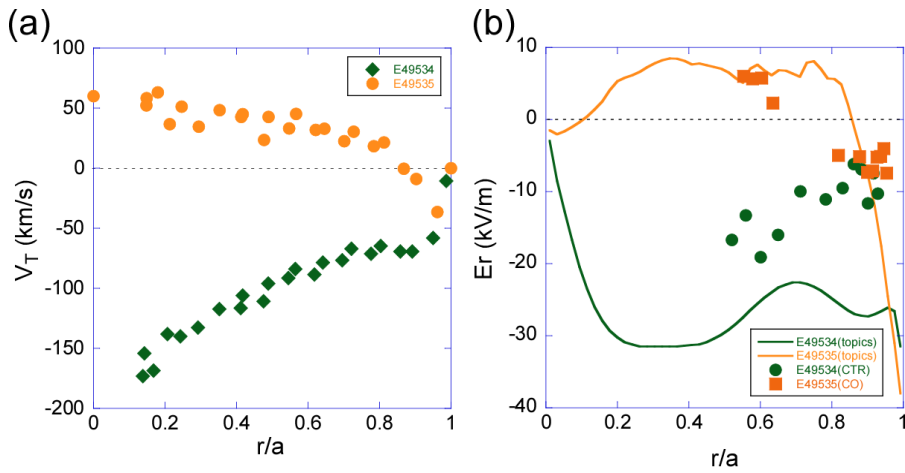


Fig. 4.(a) Toroidal rotation profile. (b) Radial electric field evaluated by topics code (solid lines) and Doppler reflectometer (symbols).

rotation, the sign of the Doppler shift changes. From the series of the same analysis at each incident frequency, the radial profile of the poloidal rotation is obtained. Then, E_r profile shown in Fig. 4(b) can be evaluated from the relation of $E_r = u_{\perp} B_{total}$, where B_{total} is the total magnetic field at the cut-off layer, assuming the phase velocity of the diamagnetic drift is much smaller than $E \times B$ velocity. The comparison of E_r profile deduced from Doppler reflectometer and from the radial force balance equation of carbon ions using TOPICS code assuming neoclassical theory indicated that good agreement in co-rotating plasma and large discrepancy in counter-rotating plasma.

3.2 Change in radial correlation of density fluctuation

When the frequency of the probe beam varies around the frequency of the fixed O-mode reflectometer, the radial correlation of the density fluctuation can be evaluated. This correlation reflectometer has been applied to the density fluctuation measurement at ITB in order to understand the reason of the degradation of ITB with ECH.

Figure 5 compares two discharges, E49780 for ITB degradation case and E48973 for

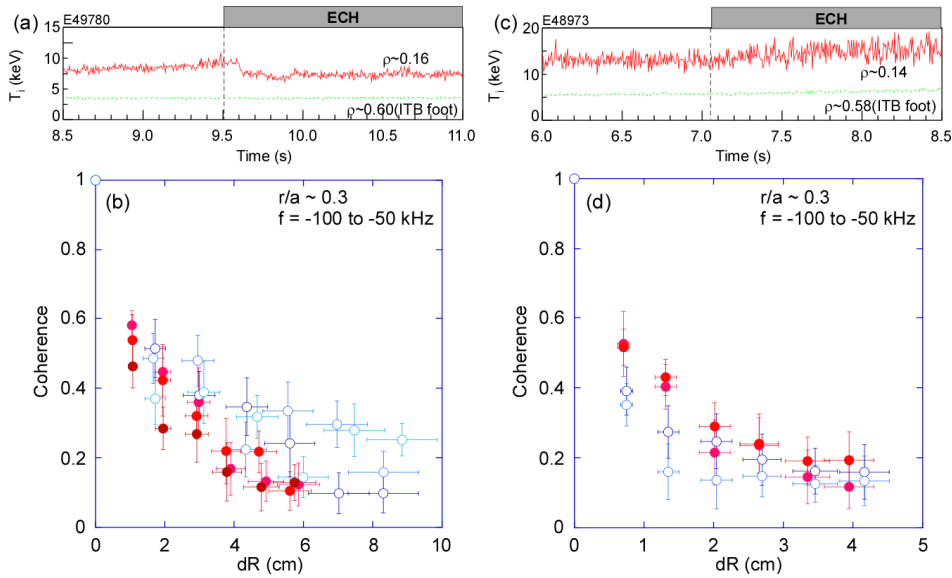


Fig. 5. Comparison of ion temperature and coherence of density fluctuation between two discharges, E49780 for ITB degradation case and E48973 for ITB unchanged case. (a), (c) Time evolution of ion temperature measured at inside ITB and at ITB foot. (b), (d) Coherence of density fluctuation in the frequency range from -100 to -50 kHz. Closed and open symbols show the data without and with ECH, respectively.

ITB unaffected case. The response of the frequency spectrum of density fluctuation seems to be similar between two discharges. However, the coherence in longer distance becomes higher in the T_i -ITB degradation case as shown in Fig. 5(b), suggesting that the longer correlation of the density fluctuation in this case is a possible mechanism for the degradation of T_i -ITB with ECH [4].

4. Summary

The new reflectometer system using the synchronized synthesizers has been developed for Doppler reflectometer and correlation reflectometer in JT-60U. The synchronized synthesizers provide a fast sweep of the frequency of the probe beam, 12 radial points every 250 ms typically. The system has been applied to the density fluctuation measurements and the E_r profile measurement using Doppler reflectometer and the radial correlation measurement using correlation reflectometer are measured. The further analysis in various experimental conditions will provide useful information for the relation between the anomalous transport and density fluctuations.

This work was supported by the Grant-in-Aid for Young Scientists (A) 18686076, Japan Society for the Promotion of Science.

Reference

- [1] Oyama, N. and Shinohara, K., Rev. Sci. Instrum **73**, 1169 (2002).
- [2] Oyama, N., *et al.*, Plasma Phys. Control. Fusion **46**, A355 (2004).
- [3] Conway, G. D. *et al.*, Plasma Phys. Control. Fusion **46**, 951 (2004).
- [4] Takenaga, H. *et al.*, Nucl. Fusion **49**, 075012 (2009); Section 4.3 in this JAEA review.

10.6 Magnetic Fluctuation Profile Measurement Using Optics of Motional Stark Effect Diagnostics in JT-60U [1]

T. Suzuki, A. Isayama, G. Matsunaga, N. Oyama, T. Fujita, and T. Oikawa

Motional Stark effect (MSE) diagnostics in JT-60U works as polarimeter to measure the pitch angle of magnetic field as well as beam-emission-spectroscopy (BES) monochromator simultaneously at 30 spatial channels [2]. Distance between adjacent MSE channels is 6-10 cm. Fluctuation in the BES signal using MSE optics (MSE/BES) contains fluctuations in not only the density but also the pitch angle or the magnetic field. Since the magnetic fluctuation in the tokamak plasma is usually caused by the rotation of deformed magnetic field structure, measurement of magnetic fluctuation profile enables identification of the deformed magnetic field structure, which helps identification and investigation of the magnetohydrodynamic (MHD) activity. Here, we have developed a new method evaluating spatial correlation between the magnetic fluctuations directly measured using the MSE/BES diagnostics.

This correlation analysis of the magnetic fluctuation between two spatial channels of the MSE/BES is applied to high-beta plasma with an MHD activity at frequency of about 0.9 kHz. In the MSE/BES diagnostics, density fluctuation mainly appears in the frequency of the MHD activity f (0.9 kHz here), while the magnetic fluctuation mainly appears in the other frequencies $2f_{\text{PEM}} \pm f$, where f_{PEM} (20.2 kHz or 23.2 kHz) is the modulation frequency of two photoelastic modulators (PEMs) for conventional MSE diagnostics measuring magnetic pitch angle. The complex spectral intensity at frequencies $2f_{\text{PEM}} \pm f$ contains not only the amplitude but also the phase of the magnetic fluctuation. Thus, the special profile of the complex spectral intensity gives the spatial profile of the deformation of the magnetic field line. It has been found, for the first time in this analysis, that the magnetic fluctuation measured by the MSE/BES is spatially localized near the magnetic flux surface having safety factor $q=2$ and that the phase of the magnetic fluctuation is inverted at about the surface, suggesting magnetic island structure by tearing mode. This phase inversion of the fluctuation was also observed in the density fluctuation (at 0.9 kHz) in MSE/BES diagnostics. The phase of the magnetic fluctuation measured by the MSE/BES at outside of the $q = 2$ surface is consistent with that by the pickup coil placed outside the plasma.

This work was partially supported by Grand-in-Aid for Young Scientists B No. 18760650 and Grand-in-Aid for Scientific Research No. 16082209 from MEXT.

References

- [1] Suzuki, T., et al., Rev. Sci. Instrum. **79**, 10F533 (2008).
- [2] Suzuki, T., et al., Rev. Sci. Instrum. **77**, 10E914 (2006).

10.7 Two-dimensional Visible Spectrometer for Divertor Plasmas

T. Nakano, H. Kubo and S. Higashijima

1 Introduction

In divertor plasmas, particularly in low-temperature and high-density plasmas such as a detached plasmas, hydrogen atoms, molecules, ions, electrons and impurities are distributed two-dimensionally. Further these particles receive and release their energy via complicated interaction between them. For investigation of the complicated processes, visible spectroscopy is one of the effective diagnostics. A visible spectrometer can be calibrated with a widely-available standard light source. Thus, the absolute intensities of spectral lines are measured, leading to quantitative evaluation of physical quantities. In addition, spatially-resolved measurement for wide spatial area is possible. This feature is effective to investigate the complicated spatial structure on a reconstructed image by a computer tomography method. This report describes the features of the newly-installed two-dimensional visible spectrometer.

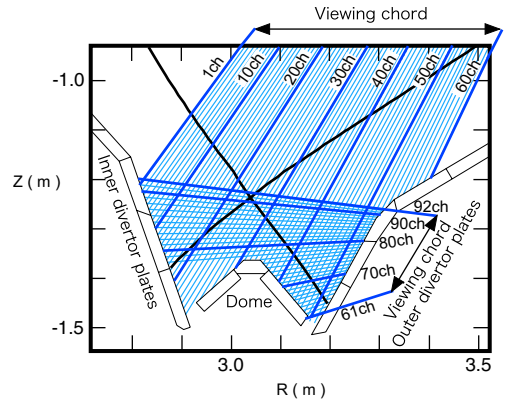


Fig. 1: Viewing chords of the spectrometer.

2 Viewing chords, spectrometer and detector

The viewing chords for the visible spectroscopy for the divertor are shown in Fig. 1. The divertor region is covered with a spatial resolution of ~ 1 cm by 60 vertical and 32 horizontal viewing chords. Emission of light from the divertor plasma is collimated with lenses onto the optical fibers with a core diameter of $200 \mu\text{m}$. Then the light is transmitted to a diagnostic room through the optical fibers with a distance of ~ 300 m. In the diagnostic room, the optical fibers are connected to another optical fibers with a core diameter of $100 \mu\text{m}$, and then to the visible spectrometer. As shown in Fig. 2, in the spectrometer, two camera lenses are built-in to suppress astigmatic images of the optical fibers, leading to a wide imaging area

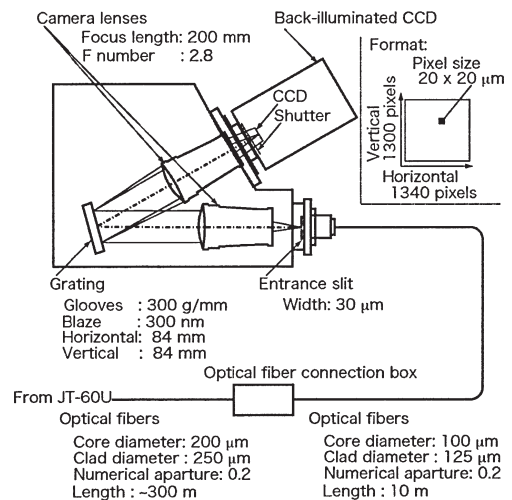


Fig. 2: Schematic diagram of the spectrometer

of $\geq 26 \times 26$ mm. The F number of the camera lenses is 2, and the corresponding numerical aperture ratio (0.25) is higher than that of the optical fiber (0.2). The visible range (350 - 800 nm) is covered with a combination of a grating with 300 grooves / mm and a back-illuminated CCD camera having 1340×1300 pixels with a real size of $20 \times 20 \mu\text{m}$ and a quantum efficiency of $\sim 93\%$ at 550 nm. The entrance slit width is set at $30 \mu\text{m}$, leading to an instrumental width of 0.74 nm on the wavelength scale (= 2.3 pixels). The frame rate of the CCD camera is set at 250 ms or 275 ms (an exposure time of 25 ms or 50 ms, respectively plus a digitization time of 225 ms). The number of accumulated photoelectrons on the CCD are digitized by an analog-digital converter with a resolution of 16 bit, and then saved in a personal computer.

3 Wavelength calibration and dispersion

The absolute wavelength against a pixel number was determined from spectral lines emitted from low-pressure Ne, Ar and Hg lamps. The spectral emission from these lamps were guided to the spectrometer through the optical fibers, and the spectra were recorded on the CCD camera. The central pixel numbers of the spectral lines were determined by fitting with a Gaussian function. In Fig. 3 (a), the absolute wavelengths of the spectral lines in the air are plotted against the determined pixel numbers, and the fitting curve with a fourth-order polynomial is also shown. The poly-nominal is expressed as follows;

$$\begin{aligned} \lambda_{\text{air}}(p) &= 358.8 + 3.167 \times 10^{-1} \times p \\ &+ 1.575 \times 10^{-5} \times p^2 \\ &- 1.712 \times 10^{-8} \times p^3 \\ &+ 4.054 \times 10^{-12} \times p^4 \quad (\text{nm})(1) \end{aligned}$$

Here, p is a pixel number. On the right axis of Fig. 3 (a), difference of the absolute wavelength and the fitting curve is shown. The difference is within ± 0.02 nm, which corresponds to 0.006% and 0.003% at 360 nm and 800 nm, respectively. The inverse linear dispersion is obtained by differentiating the equation (1), and shown in Fig. 3 (b). The highest inverse linear dispersion is 16.1 nm mm^{-1} at the 370 th pixel.

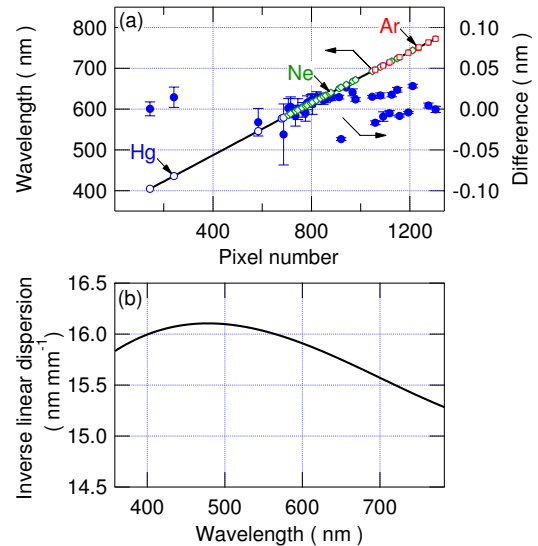


Fig. 3: (a) Wavelengths of spectral lines from Ar, Ne and Hg lamps as a function of pixel number and (b) linear inverse dispersion. The solid curve in Fig. (a) indicate the fitting curve.

4 Instrumental width

The instrumental width was measured from a spectral width of a He-Ne laser. The intensity of the laser was reduced with ND filters, and then the laser light was guided to the spectrometer through the optical fiber. Figure 4 (a) shows the observed spectral profiles of the laser. The full width at half maximum (FWHM) of the laser spectral line was determined by fitting with a Gaussian function. As shown in Fig. 4 (b), the FWHM increases up to 4.2 pixel (= 1.3 nm in the wavelength scale) with increasing slit width up to 140 μm , and the spectral width does not increase further.

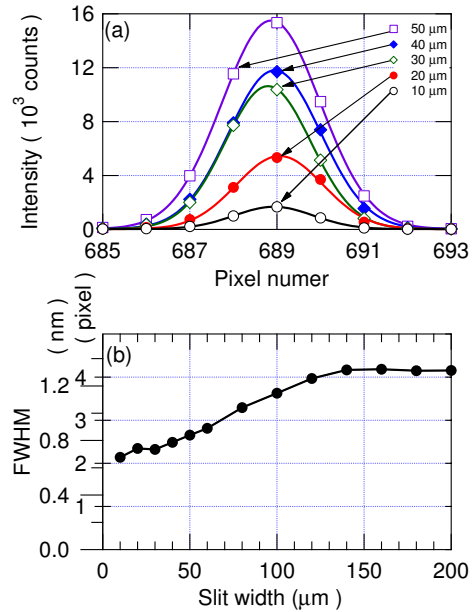


Fig. 4: (a) Spectral profiles of the He-Ne laser and FWHM as a function of the slit width.

5 Absolute sensitivity calibration

The absolute sensitivity of the spectrometer was determined with the integrating sphere, which was placed at the divertor region inside the vacuum vessel. The emission of the integrating sphere was transmitted through the vacuum windows, and focused onto the optical fibers, and then guided to the spectrometer. The calibration factor was determined by the spectral radiance of the integrating sphere divided by the counts measured by the CCD. As shown in Fig. 5, the determined sensitivity is nearly flat in the wavelength range from 550 nm to 700 nm, where the sensitivity was high. But the sensitivity becomes worse with both increasing and decreasing wavelength. On the right axis of Fig. 5, the transmittance of the vacuum window is shown. The transmittance becomes low with decreasing wavelength.

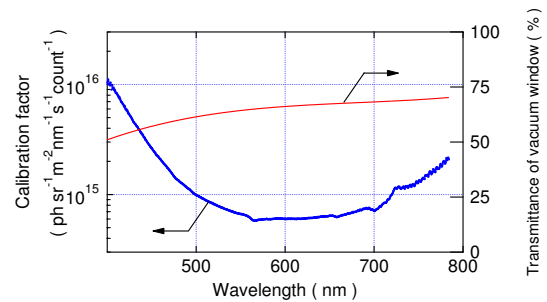


Fig. 5: (left) Calibration factor for 30 ch and (right) transmittance of the vacuum window as a function of wavelength.

6 Statistical error

The statistical error of photoelectrons generation on CCD pixels was estimated. The emission from the integrating sphere was measured 100 times with an exposure time of 50 ms and an digitization frequency of 1 MHz. Then, the measured count at a pixel were converted into the number of photoelectrons with a gain of 0.23 counts per photoelectron, and the average and the standard deviation of the photoelectrons in the 100 measurements were evaluated. This evaluation was performed for all the 1340 pixels. In Fig. 6, the square root of the averaged photoelectrons is compared with the standard deviation of the photoelectron. In the standard deviation range higher than 30, the square root of the averaged photoelectron is close to the standard deviation. This indicates that the statistical error is dominated by the photon shot noise. In contrast, below 30, the standard deviation is higher, showing that another error such as read-out noise (~ 11) becomes dominant.

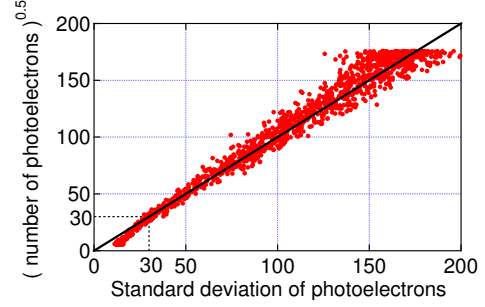


Fig. 6: *The square root of the averaged photoelectrons as a function of the standard deviation photoelectrons.*

7 Linearity

The linearity was investigated from comparison of the number of measured photoelectrons against the spectral radiance from the integrating sphere, which increased gradually. As shown in Fig. 7, the averaged number of measured photoelectron increases with increasing spectral radiance. On the right axis of Fig. 7, the linearity error defined as a following equation is shown.

$$L_{1300B}^{CCD}(L_e) = \frac{N_e^{ave}(L_e) - N_e^{fit}(L_e)}{N_e^{fit}(L_e)} \times 100 \quad (\%) \quad (2)$$

Here, $N_e^{ave}(L_e)$ is the averaged number of measured photoelectrons and $N_e^{fit}(L_e)$ the calculated photoelectron from the fitted line. It is proved that the linearity error is within $\sim 0.5\%$.

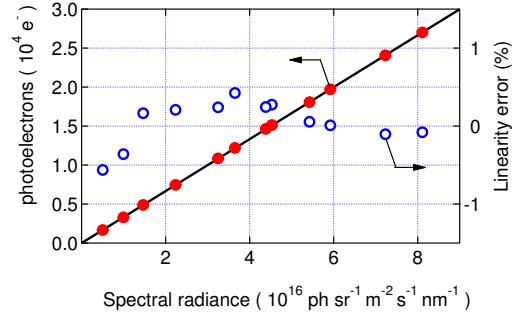


Fig. 7: *(left) The averaged number of photoelectrons and (right) the linearity error as a function of spectral radiance of the integrating sphere. The solid line indicates the fitting result with a line.*

10.8 Upgraded Charge Exchange Recombination Spectroscopy on JT-60U

Y. Sakamoto, K. Ida¹⁾, M. Yoshida, M. Yoshinuma¹⁾

1) NIFS

1. Introduction

Charge exchange recombination spectroscopy (CXRS) is widely used to measure the radial profiles of ion temperature, toroidal and poloidal rotation velocities and density of impurities in the plasma, which enables us to evaluate radial electric field from the radial force balance equation. Therefore the CXRS is one of the essential diagnostics to study transport physics and MHD dynamics. The CXRS system on JT-60U is composed of toroidal and poloidal viewing systems, which have 59 spatial points (23 toroidal and 36 poloidal) [1]. The charge exchange recombination line of fully ionized carbon CVI (529.05 nm, $\Delta n=8-7$) is typically used in JT-60U. In 2006, we have developed the modulation CXRS with high spatial resolution [2]. For the 2007-2008 experimental campaign, we replaced the conventional spectrometer and the image-intensified charge-coupled device with a large throughput spectrometer and an advanced charge-coupled device. As a result, we have achieved a faster time resolution of up to 2.5 ms (factor ~ 7 over the previous system) with high accuracy.

2. Charge exchange recombination spectroscopy setup

Figure 1 shows the bird-eye view photograph of the upgraded CXRS system including the Czerny-Turner spectrometers (Bunkou-Keiki CLP-300), the back illuminated electron multiplying charge coupled device (EMCCD) camera (Andor iXon DV897D-CSO-#BV) as a detector, incident fiber bundles and so on. The characteristics of the Czerny-Turner spectrometer with camera lens (the focal length of 300 mm, F number of 2.8) are 2160g/mm

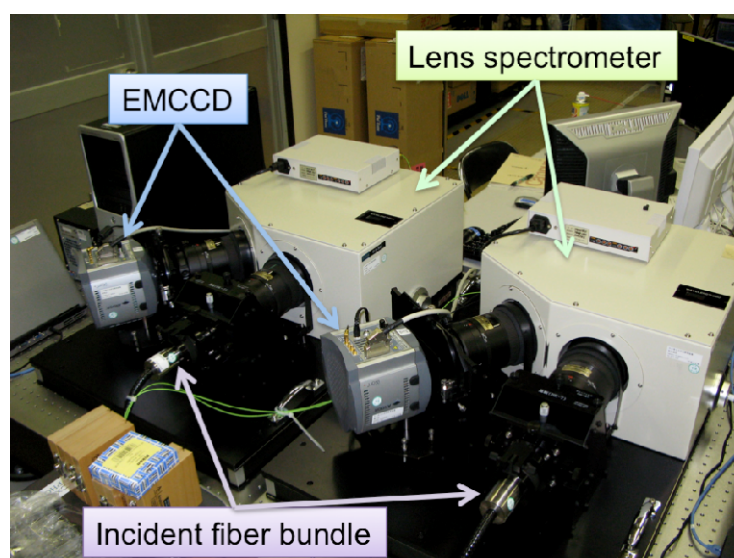


Fig. 1 Bird-eye view photograph of the upgraded CXRS for toroidal and poloidal systems showing the main components such as the lens spectrometers, the EMCCD cameras and the incident fiber bundles.

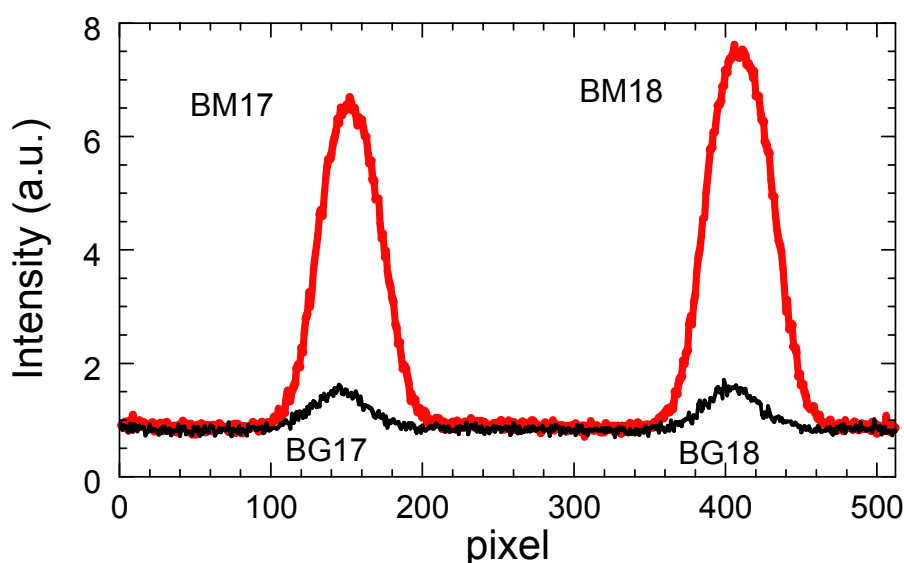


Fig. 2 Spectra on sample stripes for neutral beam viewing chords and the background viewing chords.

grating, its active region of $154 \times 128 \text{ mm}^2$, blaze wavelength of 500 nm. This spectrometer provides superb image quality and very flat image planes. The characteristics of EMCCD camera are 512×512 pixel ($16 \times 16 \text{ }\mu\text{m}^2$), high quantum efficiency of $>90\%$ at the central wavelength of 529.05 nm, high-speed readout of 10 MHz and low dark current due to cooling operation up to -85°C . The wavelength resolution of this system is $\sim 0.023 \text{ nm}$ full width at half maximum (FWHM). The width of measuring wavelength is $\sim 7.9 \text{ nm}$ at the central wavelength of 529.05 nm. The incident fiber array has 64 optical fibers (32 strips in horizontal and 2 lines in vertical). Since the diameter of each optical fiber is $200 \text{ }\mu\text{m}$ in core and $250 \text{ }\mu\text{m}$ in cladding, the optical fiber array is arranged at the slit with a pitch control of $256 \pm 20 \text{ }\mu\text{m}$ in order to match the image of the optical fiber into the strip width of $256 \text{ }\mu\text{m}$ ($16 \text{ }\mu\text{m} \times 16 \text{ pixel}$). Then 64 spectra can be obtained with a high frame rate of 400 Hz in case of 16 pixel vertical binning. The number of frames taken per shot is usually 12000 corresponding to 30 sec.

In order to precisely measure CXR spectra from on the neutral beam line, the background emission mainly from the charge exchange reaction between the fully ionized carbon and the thermal neutrals near the plasma edge region is measured using the other set of viewing chords without neutral beam line. The CXR spectra on the neutral beam line are extracted by subtracting the background emission. The 30 channels are allocated to the emission from viewing chords with neutral beam. The 30 channels are allocated to the background viewing chords. The 2 channels are connected to a samarium lamp for wavelength calibration. The rest 2 channels are the spares. Figure 2 shows the spectra on

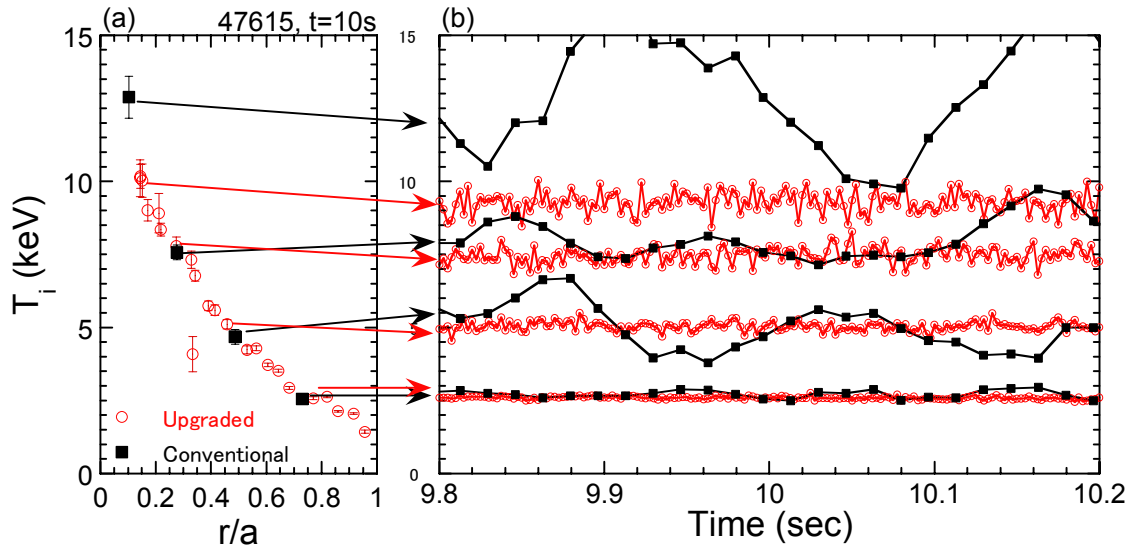


Fig. 3 (a) Radial profile and (b) temporal evolution of ion temperatures obtained in both upgraded and conventional toroidal CXRS systems.

sample stripes for neutral beam viewing chords and the background viewing chords. As mentioned above, two spectra can be obtained in each stripe.

3. Experimental results

Figure 3 shows the radial profile and temporal evolution of ion temperatures obtained in both upgraded and conventional toroidal CXRS systems during quasi-steady state phase of ELMy H-mode plasma. Here only four viewing chords were connected to conventional toroidal CXRS system for the comparison. The consistent radial profile is obtained as shown in the figure. While the temporal evolutions of ion temperature measured by the conventional system with time resolution of 60Hz are fluctuating, those by the upgraded system with high time resolution of 400Hz are very steady with small scatter.

Figure 4 shows the radial profiles of ion temperatures and plasma rotation velocities

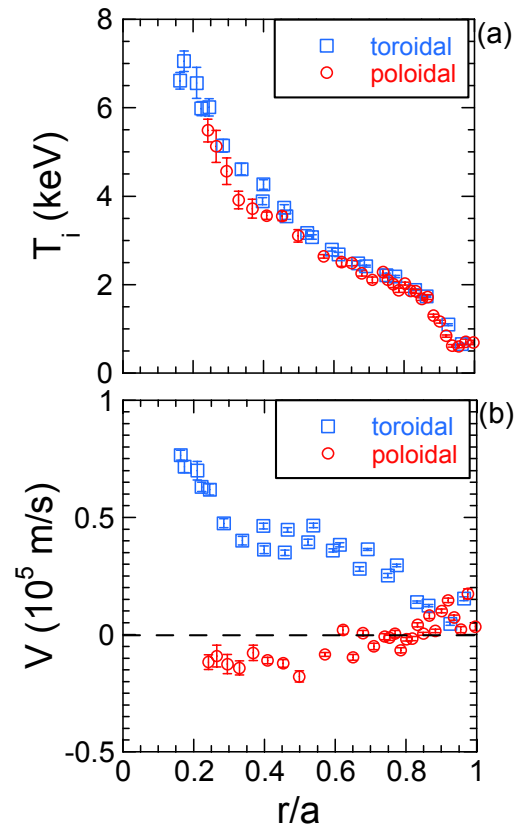


Fig. 3 Radial profiles of (a) ion temperatures and (b) plasma rotation velocities obtained in toroidal and poloidal systems.

obtained in both toroidal and poloidal systems with time resolution of 400 Hz. Similar ion temperature is measured in both systems. Note that the poloidal rotation velocity shown here has not taken into account the various atomic physics corrections [3].

Many results based on temporal evolution of ion temperature and plasma rotation velocity with high time resolution and high accuracy are also discussed in this issues, such as studies of RWM, ELM and ITB.

3. Summary

We have successfully upgraded JT-60U CXRS diagnostics for both toroidal and poloidal systems. By installing the high throughput spectrometer and the high-speed EMCCD camera, the time-resolved profiles at 400 Hz are routinely available for many discharges with the injection of the neutral beam for CXRS measurement.

References

- [1] Koide, Y., et al., Rev. Sci. Instrum. **72** 119, (2001).
- [2] Ida, K., et al., Rev. Sci. Instrum. **79** 053506, (2008).
- [3] Bell, R. E., Synakowski, E. J., AIP Conf. Proc. **547**, 39 (2000).

10.9 Measurements of Carbon Dust by Fast TV Camera and Laser Scattering

N. Asakura, T. Hatae, H. Kawashima, T. Nakano

1. Introduction

Generation and dynamics of dust in fusion devices are focused in terms of potential tritium reservoir and impurity source. Understanding of the dust transport in the plasma as well as determination of where it grows up or it is deposited are important to predict the tritium retention and plasma performance in a fusion reactor. Carbon dust distribution in vacuum vessel of the JT-60U was investigated after 2002 experiment campaign [1]. Measurement of visible images emitted during their surface ablation started since 2006, using a fast TV camera located at a tangential port. Ejection of carbon dust from the inner divertor plate was often observed just after ELM event, and the fast movement towards the toroidal direction (0.3-0.5 km/s) was evaluated [2]. In 2008, YAG Thomson scattering system [3] was applied for the detection of dust scattering light, and number and distribution of the scattering event in the vacuum chamber were investigated. In particular, dust number was significantly increased in the following discharge after disruptions. Preliminary result is presented.

2. YAG scattering and fast TV camera measurements

Thomson scattering diagnostic was applied for measurement of the dust scattering (“Mie scattering”) light, which was produced by Nd-YAG laser (Energy > 2 J, pulse width of 20 ns, wavelength of 1064 nm). Pulse repetition is 50 Hz, and 14 spatial channels cover from the core to SOL area as shown in Fig. 1. Since intensity of the scattered light by a dust particle is much larger than the weak signal produced by the Thomson scattering and the APD (Avalanche photodiode) detector is very sensitive for photon signal, gain of the amplifier is reduced to 1/5 or neutral density (ND) filter with transmission of 0.1-5% is inserted in front of the polychrometer.

Scope of the digital TV camera system (Photoron FastCAM II with full 6.5Gbyte memory) is installed at horizontal tangential port (P-17), where a plasma monitor camera is also installed. Figure 2 shows a typical image of the plasma and inside view of the vacuum chamber from the plasma monitor camera. Typical viewing area of the fast camera measurement is presented by a circle in Fig. 2, where a scope with a wide (42°) viewing angle and the camera setting with 512x512 pixel/frame (6 kHz) are used. Optical image of the

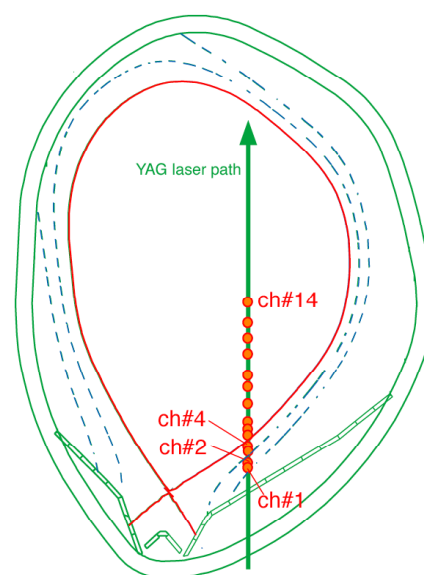


Fig.1 Plasma configuration and 14 locations of the YAG laser scattering measurement.

plasma is transferred to the fast camera, using 15 m fiber-optics bundle consisting of 30000 quartz fibers. Transmission of the light guide is ~ 0.1 , which can be amplified by the image intensifier and spatial resolution is 1.2 cm at the focal distance (2.5-3 m). For the dust measurement, frame rate and size of the fast camera changed from 2 kHz for 1024x1024 pixels/fr. to 8 kHz for 256x256 pixels/fr.

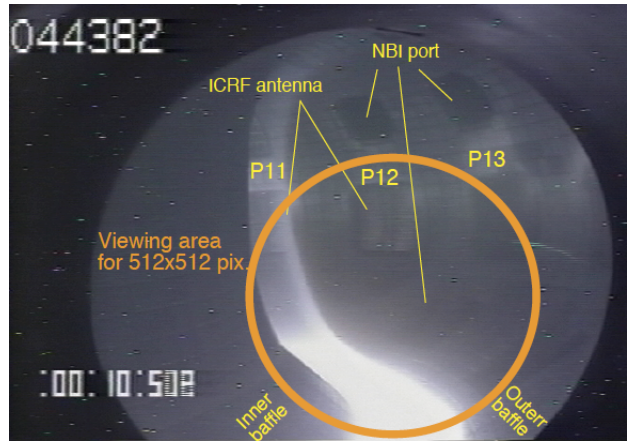


Fig. 2 Plasma monitor (CCD camera) image of JT-60U L-mode plasma, viewing from the same tangential port as the fast camera.

3. Dust in the main chamber

Dust in fusion plasma is generally charged negatively ($Z \sim 10^3-10^4$), and the movement ($M_d dV_d/dt = F$) is determined by friction force from the parallel SOL flow and drift flow (F_{fric}), Coulomb scattering (F_C), electro-static force by potential (F_E), gravitational force (F_g) and rocket force during ablation (F_{roc}). Dust mass (M_d) is decreasing during dust ablation ($T_d > 2000-3000K$) in the SOL and edge plasmas. Dust movement is influenced by geometry of Plasma Facing Component such as the first wall and divertor as well as background plasma.

The dust was measured by the fast camera as a bright spot image of line emission produced from the carbon and hydrogen ions. Generally speaking, appearance of the dust emission was very few in the routine operations even for high power NB injection. On the

other hand, numbers of dust emission were observed in the specific discharges particularly after major disruptions of high I_p plasmas (a few MJ energy to the divertor and first wall). Figure 3 shows six images in the typical discharge (No.69530, $I_p=1.6MA$, $P_{NBI} =16MW$, the plasma configuration is shown in Fig. 1, where the inner and

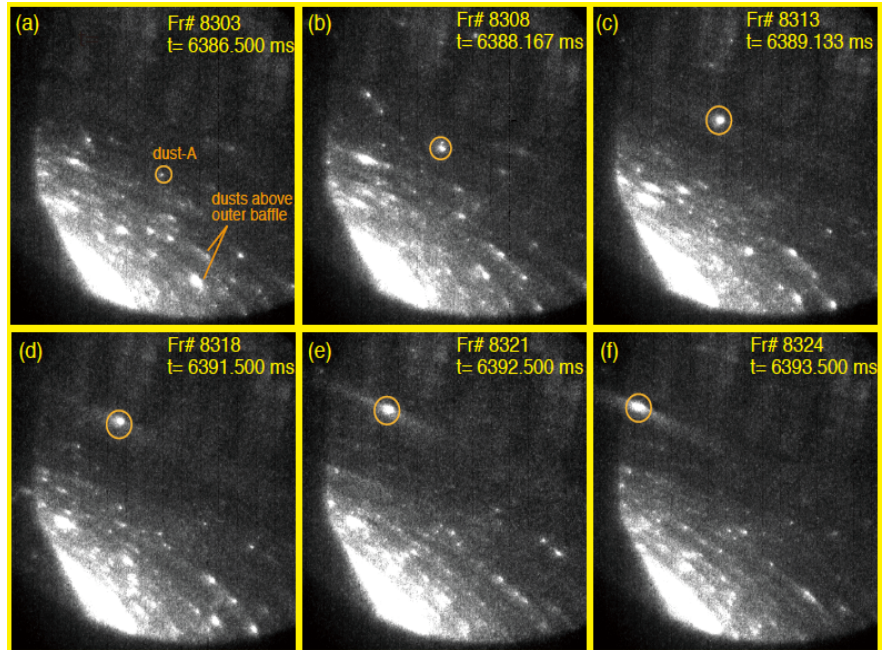


Fig. 3 Fast camera images (6kHz frame rate, 512x512 pixel/frame) for ELMy H-mode plasma E069530. Numbers of dust appear during NBI. Dust-A is moving up from the outer baffle/divertor to the main edge. Plume of the ionization is seen after $t = 6391.5$ ms.

outer strike-points at the divertor target are higher than normal operations. The previous shot (No.69529) was disrupted at $t = 8$ s, and He-TDCs (7 and 5 min.) were repeated. Numbers of dust appear in the divertor and main edge during NBI (ELMy H-mode), and they are moving poloidally from the outer divertor/baffle towards the main plasma edge, at the same time, toroidally towards the co-direction. One example of the large size of emission is marked by dust-A, which appears above the outer baffle at P-12 toroidal section and is moving up and toroidally towards P-18 section (the toroidal direction is consistent with the SOL flow). During the movement in 7 ms, the average velocity is estimated to be 0.4 km/s

Time evolution of the plasma parameters and laser scattering signals in SOL are shown in Fig.4. Calibrated photon factor for each channel is included, but absolute intensity factor for the Mie scattering is not included. Here, each event and the signal intensity correspond to a dust particle in the scattering volume and relative size (assuming a spherical shape), respectively. Gain for the APD amplifier is 0.2. Many dust events are seen particularly in the SOL region during NBI, and some are saturated (corresponding to 2000 counts). Total number of events in the discharge is decreased from 55 at far SOL (ch.1) to 8 (ch.4) near the separatrix.

Distributions of the total event number and medium intensity in four similar discharges are summarized in Fig. 5: three shots of 49530, 49533 and 49536 are just after disruption, and shot 49537 is the second shot after the disruption. Three distributions just after disruptions are similar, where event number particularly in the far SOL increases significantly (10 times) compared to that for the second shot after the disruption. Distance of ch.1 and ch.2 from the separatrix is 14-18 cm.

Intensity of the laser scattering signal is investigated by the Probability Distribution Function (PDF) as shown in Fig. 6, where events in the three discharges are integrated. As mentioned above, significant numbers of dust are transported at the far SOL (ch.1). The PDF for the far SOL is distributed to the high intensity compared to those for other channels. Both

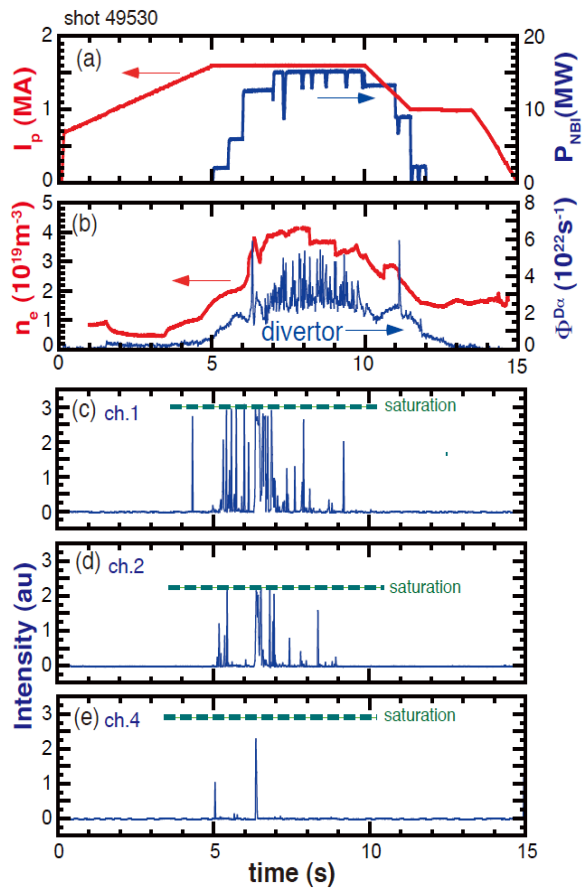


Fig. 4 Time evolution of I_p , P_{NBI} , electron density and recycling flux in the divertor for the ELMy H-mode plasma just after disruption. Laser scattering signals in the SOL (ch.1, 2 and 4) are presented.

the size and the number of dust are decreased near the separatrix, suggesting that ablation or sublimation becomes dominant even in SOL. Here, event number for ch.8 is systematically larger than other channel in the main plasma, which is now under investigation.

From the laser scattering results, the dust images in the fast camera movie (Fig. 3) would be light emitted at the far SOL rather than in the confined plasma edge. Measurement of the laser scattering was also carried out during the disruption. Numbers of events (mostly saturated) appeared at the central channels as well as at the edge and SOL channels within 1s just after the current quench. Dust transport just after the disruption is also important.

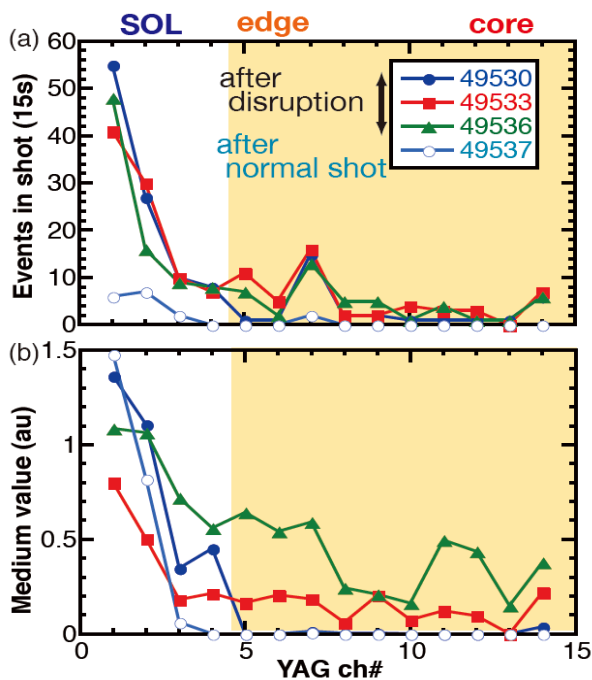


Fig. 5 Distributions of (a) total event number, (b) medium value of the intensity in discharges just after disruption (49530, 49533, 49536). The following shot (49537) is also shown for comparison.

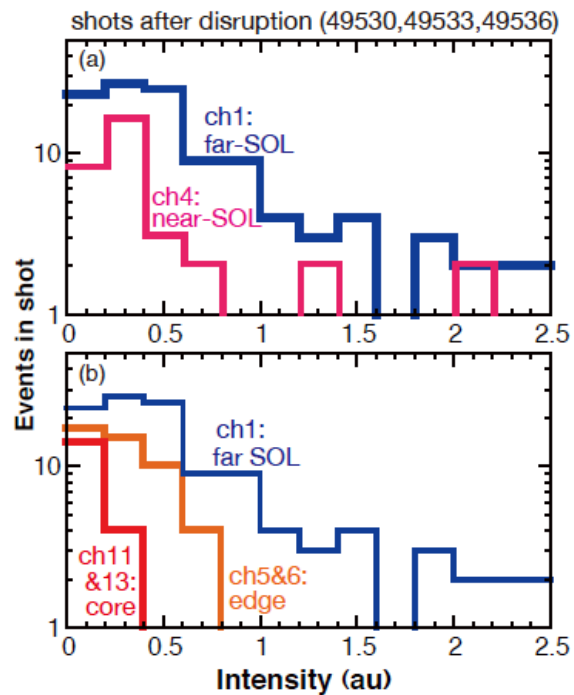


Fig. 6 Probability Distribution Functions of intensity in the far SOL (ch.1), near SOL(ch.4), edge (ch.5 and ch.6) and core (ch.11 and ch.13).

Summary

YAG laser scattering system was applied for the detection of dust scattering light, and event number and its distribution in plasmas were investigated. Significant numbers of dust appeared in discharges just after disruptions, and the location in the plasma was determined, i.e. localized at the far SOL. Dust size as well as number density are decreased near the separatrix, suggesting that ablation becomes dominant near the separatrix.

This research was partly supported by Grant-in-Aid for Scientific Researches on Priority Areas for “Tritium for Fusion” (No.20049011) from MEXT.

References

- [1] Masaki, K., et al., J. Nucl. Mater. **337-339**, 553 (2005).
- [2] Asakura, N., et al., Sec. 10.7 in JAEA-Review 2008-045 (2008) 126-129.
- [3] Hatae, T., et al., Rev. Sci. Instrum. **70**, 772 (1999).

10.10 Development of Polarization Interferometer for Thomson Scattering Diagnostics in JT-60U [1]

T. Hatae, J. Howard¹⁾, N. Ebizuka²⁾, Y. Hirano³⁾, H. Koguchi³⁾,
S. Kitamura, T. Sakuma, T. Hamano

1) Australian National University, 2) Konan University, 3) National Institute of Advanced Industrial Science and Technology

Recently, the use of a polarization interferometer based on Fourier transform spectroscopy for Thomson scattering diagnostics has been proposed [2]. It is possible that this method alleviate some of the disadvantages of conventional grating spectrometers. Furthermore, this method delivers a simple and compact system. We have been developing the polarization interferometer for Thomson scattering diagnostics to demonstrate the proof-of-principle. The polarization interferometer is composed of a birefringent plate having fixed optical delay sandwiched between two polarizers. For thermal electrons, the optical contrast of the interferogram with the Thomson scattered light at an appropriately chosen optical path delay, is a unique function of T_e and n_e using the polarization interferometer. At the first stage, a dual channel polarization interferometer employing a fixed-thickness birefringent plate was developed to prove the principle of this method. Proof-of-principle tests were carried out in TPE-RX reversed field pinch (RFP) device. The pulsed poloidal current drive (PPCD) operation which is one of the good confinement operation conditions in RFP was applied to produce high T_e , n_e ($T_e \sim 1\text{keV}$, $n_e \sim 1 \times 10^{19}\text{m}^{-3}$) plasmas. The existing Thomson scattering system is utilized for this test. The electron temperature of one spatial point at the plasma center was measured employing the polarization interferometer and the existing filter polychromator alternately. Similar T_e values within data variation and error bar ranges were successfully measured by both the polarization interferometer and an existing filter polychromator. Therefore, the validity of the dual channel polarization interferometer was proved from this result. As the second stage, a multichannel polarization interferometer using a Wollaston prism was developed to evaluate the availability for the Thomson scattering diagnostics in JT-60U. Interferograms of three kinds of monochromatic light sources were measured by the multichannel polarization interferometer, and those spectra was reconstructed by Fourier transform. It seems that the utilization of the multichannel polarization interferometer is promising for Thomson scattering diagnostics. As a future plan, we will conduct the electron temperature measurement using the multichannel polarization interferometer for Thomson scattering diagnostics.

References

- [1] Hatae, T., et al., to be published in Plasma Fusion Res. (2009).
[2] Howard, J., Plasma Phys. Control. Fusion **48**, 777 (2006).

10.11 A 160 ps Pulse Generation by Stimulated Brillouin Scattering - Phase Conjugation Mirror for advanced Thomson Scattering Diagnostics [1]

H. Yoshida¹⁾, T. Hatae, H. Fujita¹⁾, M. Nakatsuka¹⁾, S. Kitamura
1) Institute of Laser Engineering (ILE), Osaka University

A stimulated Brillouin scattering-phase conjugation mirror (SBS-PCM) in various liquids, gases and solids is a useful tool for improving the beam quality of high-peak-power laser systems. A SBS compressor enhances the peak intensity of pulses while maintaining their high energy, and compresses the laser pulse duration within 1 ns[2]. This method is very simple and can be used to achieve high brightness. In order to obtain pico-second pulse, mode locking with regenerative amplifier is used. This scheme generally requires complicated optical configuration. An SBS pulse compressor is similar to SBS-PCM, but consists of a long SBS cell (or plural long SBS-cells). In the magnetic confinement fusion devices, both T_e and n_e profiles are routinely obtained by means of Thomson scattering using high-power pulsed laser beam. A LIDAR (Light Detection and Ranging) Thomson scattering which is one of the incoherent Thomson scattering techniques has an advantage that only one port is enough for the laser injection and the observation. Therefore the LIDAR is suitable for a burning plasma measurement from viewpoint of a radiation shield. Since pulse width of laser corresponds to spatial resolution in the LIDAR Thomson scattering diagnostics, the pulse width must be 300 ps or less to obtain spatial resolution of 10 cm. As for the SBS pulse compressor, although there is a room for further investigation, it seems to be promising method to obtain a shorter pulse for advanced Thomson scattering diagnostics (e.g. LIDAR in ITER) with an appropriate SBS medium. We have fabricated two long cells for liquid phase conjugation mirror of length 1.5 m and diameter 4 cm at ILE under the collaboration of JAEA. These cells were filled up with heavy fluorocarbon FC-40 liquid. FC-40 having fast relaxation time of about 200 ps was selected from a lot of heavy fluorocarbon. A maximum SBS reflectivity of over 80% using a $f=750$ mm and $f=1000$ mm focal lengths were obtained at an incident energy of over 1 J. At an input energy of about 100 mJ, the compressed pulse duration used in focal length of $f=750$ mm and $f=1000$ mm were 1.2 ns and 0.8 ns, respectively. In the case of a focal length of 1000 mm, the minimum compressed pulse width near 160 ps was achieved at an incident energy of 1 J.

Reference

- [1] Yoshida, H, Hatae, T., et al., to be published in Opt. Exp. (2009).
[2] Mitra, A., et al., Jpn. J. App. Phys. **45**, 1607 (2006).

10.12 Imaging Bolometer Upgrade on JT-60U [1]

B. J. Peterson¹⁾, S. Konoshima²⁾, H. Kawashima²⁾, H. Parchamy¹⁾, A. Yu. Kostryukov³⁾,
I. V. Miroshnikov³⁾, N. Ashikawa¹⁾, D. C. Seo⁴⁾

1) National Institute for Fusion Science, 2) JAEA, 3) St. Petersburg State Tech. Univ.,
4) National Fusion Research Institute

Plasma radiation plays an important role in cooling the plasma and therefore its measurement is essential to the study of the magnetic confinement of plasma. Imaging bolometers using an infrared (IR) video camera measure the change in temperature of a thin foil exposed to the plasma radiation [2]. This avoids the problems in a reactor environment of conventional resistive bolometers [3] related to electric cabling and vacuum feedthroughs. A prototype of the InfraRed imaging Video Bolometer (IRVB) [4] has been installed and operated on the JT-60U tokamak demonstrating its applicability to a reactor environment [5] and its ability to provide two dimensional (2D) measurements of the radiation emissivity in a poloidal cross-section [6]. An upgraded version of this IRVB has been installed on JT-60U. This upgrade uses a state-of-the-art IR camera (FLIR/Indigo Phoenix-InSb) (3-5 microns, 256 x 360 pixels, 345 Hz, 11 mK) mounted in a neutron/gamma/magnetic shield to view a thin foil (7 cm x 9 cm x 5 micron tantalum) through a 3.6 m IR periscope consisting of a sapphire IR vacuum window, CaF₂ optics and an aluminum mirror. The sensitivity of the imaging bolometer due to the camera is improved by a factor of 100 over that of the previously used Omega IR camera. In the new design the aperture size is decreased to 2 mm (vertical) x 2.5 mm (horizontal) to increase the number of channels and therefore the spatial resolution. With 40 x 24 channels and a time response of 10 ms a noise equivalent power density of 300 $\mu\text{W}/\text{cm}^2$ is achieved or 23 $\mu\text{W}/\text{cm}^2$ for 16 x 12 channels and a time response of 33 ms. This is 30 times better than the previous version of the IRVB on JT-60U. Also, with the faster IR camera, a time resolution of 3 ms (33 ms previously) is available.

This research is supported by MEXT Grant-in-Aid # 16082207.

References

- [1] Peterson, B. J. et al., Rev. Sci. Instrum. **79**, 10E301 (2008).
- [2] Wurden, G. A. and Peterson, B. J., Rev. Sci. Instrum. **70** 255 (1999).
- [3] Mast, K. F. et al., Rev. Sci. Instrum. **62**, 744 (1991).
- [4] Peterson, B. J. et al., Rev. Sci. Instrum. **74**, 2040 (2003).
- [5] Peterson, B. J. et al., J. Nucl. Mater. **363-365**, 412(2007).
- [6] Liu, Y. et al., Plasma Fusion Res. **2**, S1124 (2007).

10.13 Radiation Temperature of ECE in Bi-Maxwellian Tokamak Plasma [1,2]

M. Sato and A. Isayama

For the measurement of electron temperature profile, the 2nd harmonic extraordinary mode (X mode) of electron cyclotron emission (ECE) in magnetically confined plasmas is usually observed in perpendicular to the magnetic field (B) along the equatorial plane. The ECE spectra are changed by the relativistic, Doppler, absorption and refraction effects. The characteristics of ECE spectra are also changed by the electron distribution function [$f_e(p)$]. When electron cyclotron heating (ECH) is applied to JT-60U plasma, the supra-thermal electron produced by ECH may affect on the electron temperature measurement from ECE. Here, the effect of supra-thermal electron on the radiation temperature (T_e^{rad}) from ECE is evaluated in the case of relativistic bi-Maxwellian. In the relativistic bi-Maxwellian, the thermal and supra-thermal parts of distribution function are represented to be average and high energy part, respectively [1,2]. The computational model in bi-Maxwellian is almost the same as ref. 3 basically except for emissivity. The emissivity is calculated using the Trubnikov's formula [4].

The effect of supra-thermal electron on the T_e^{rad} from ECE, that is obtained from fundamental O mode and 2nd harmonic X mode, is evaluated in the case of the relativistic bi-Maxwellian. The small amount of supra-thermal electron [$n_e^{\text{sp}}(0)/n_e^{\text{th}}(0) \sim 1\%$] affects on the T_e^{rad} . The deviation from $T_e^{\text{rad}}(\text{Max})$ is evaluated. The deviation of T_e^{rad} between the bi-Maxwellian and the Maxwellian is defined: $\Delta T_e \equiv T_e^{\text{rad}}(\text{bi-Max}) - T_e^{\text{rad}}(\text{Max})$, where $T_e^{\text{rad}}(\text{bi-Max})$ and $T_e^{\text{rad}}(\text{Max})$ are T_e^{rad} in bi-Maxwellian and Maxwellian, respectively. The small amount of supra-thermal electron affects the T_e^{rad} . The n_e^{sp} in the case of $\Delta T_e/T_e = 10\%$, $n_e^{\text{sp}10\%}$, for the 2nd harmonic X mode and fundamental O mode are estimated where T_e is $T_e^{\text{true}}(\text{Max})$. The n_e^{sp} is uniform profile. For $T_e^{\text{sp}} = 50$ keV, the estimated $n_e^{\text{sp}10\%}$ in the case of the T_e^{rad} from the 2nd harmonic X mode is smaller than that in the case of the T_e^{rad} from fundamental O mode. For $T_e^{\text{sp}} = 150$ keV, the estimated $n_e^{\text{sp}10\%}$ in the case of the T_e^{rad} from the 2nd harmonic X mode is comparable to that in the case of the T_e^{rad} from fundamental O mode.

The general expression of radiation temperature is evaluated in the case of bi-Maxwellian [5]. The parameter dependences of the deviation on T_e^{sp} and modes are interpreted by the following two effects. One is the relativistic effect of supra-thermal electron of the mode used for T_e^{rad} measurement on the thermal electron of the same mode used. The other is the relativistic effect of supra-thermal electron of the higher harmonic used mode on the thermal electron of the same mode used.

References

- [1] Sato, M. and Isayama, A., *Proc. 15th Joint Workshop on ECE and ECH*, Yosemite National Park USA, p263 (2008).
- [2] Sato, M. and Isayama, A., *Proc. 35th EPS Conf. on Plasma Physics*, Greece, P2 092 (2008).
- [3] Sato, M., Ishida S. and Isei, N., *J. Phys. Soc. Jpn.* **62**, 3106 (1993).
- [4] Trubnikov, B. A., 'Magnetic Emission of High-Temperature Plasma', Thesis, Institute of Atomic Energy, Moscow, 1958.[English translation: AEC-tr-4073 June 1960].
- [5] Tribaldos, V. and Krivenski, V., *8th Joint Workshop on ECE and ECH*, Gut Ising Germany, 1992, p123.

10.14 Fast-Ion Measurement with the Doppler Shifted D-alpha Light on JT-60U

M.Osakabe¹⁾, K.Ida¹⁾, M.Yoshinuma¹⁾, Y.Sakamoto, and K.Shinohara

1) National Institute for Fusion Science

1. Introduction

Evaluation of fast-ion confinement properties is one of the most important physics issues in the magnetically confined fusion devices, since the achievement of good confinement of fusion-born alphas is necessary in realizing fusion reactors. Recently, a new fast-ion diagnostic method of using charge exchange recombination spectroscopy was proposed to evaluate fast-ion confinement and demonstrated by Heidbrink, *et.al.*, at DIII-D[1]. In his method, the Doppler shifted deuterium Balmer-alpha light(D_α), which is created as a result of the charge exchange recombination processes between fast-ions and injected Neutral Beams(NB), are utilized as the signals of fast-ions. Compared to the conventional fast-ion diagnostics, e.g. neutron diagnostics and fast neutral particle diagnostics, their method has an advantage in obtaining the spatial information of the fast-ion energy spectra. Since the energy spectra of fast-ions are strongly affected by their confinement properties, this method is expected to bring us the detailed information of fast-ion confinement in plasmas. On the other hand, this measurement is difficult since the D_α -emission is usually weak compared to the other emission from plasmas around their wavelength, i.e., the direct Beam Emission Spectral (BES) light from NB, D_α -lights from the plasma periphery and the continuum spectra of Brems.-radiations. Thus, it is useful to compare the results of this measurement with those of the conventional fast-ion diagnostics to clarify the applicability of this measurement. On JT-60U, six channel collimated neutron detector arrays are installed and are under operation [2] and the Fast Ion D-Alpha (FIDA) measurement can be applied by using the measurement systems for Charge eXchange Recombination Spectroscopy (CXRS) for the bulk ion temperature measurement. Thus, this machine is a good platform to prove the validation of this method.

2. Experimental set-up

In Fig.1, the geometry of the diagnostic and the location of the measured points are shown. The 26 channels of fiber optics for Modulated-CXRS (MCXRS) are utilized for the FIDA measurements on JT-60U. As an active source of charge exchange neutrals, NB#4 is used. Unlike the FIDA geometry demonstrated by Heidbrink on DIII-D, the tangential view was chosen for the measurement. On JT-60U, there were two candidates for FIDA sight lines. One was the use of perpendicular sight lines for the Poloidal- CXRS (PCXRS) measurement. The other is tangential sight lines for the Toroidal-CXRS(TCXRS) or the MCXRS. The latter was

chosen because the measurement using perpendicular sight lines with perpendicular-NB is expected to be difficult from the analysis on the FIDA sight lines by the one of the authors[3].

One of the biggest difficulties of this diagnostic is the isolation of the FIDA signals from the BES-components from the NBs. Since the BES-components of NB#4 can be seen as red-shifted D_α light with MCXRS sight lines, the blue-shifted components of the D_α light are chosen for the FIDA measurement. The NB#7 and #8 interfere with the MCXRS sight lines, but their BES-components can be avoided since they are red-shifted. The operation of NB#2 must be prohibited during FIDA measurements since its BES-component is expected to be seen in the blue shifted region and its intensity will exceed the FIDA-signals.

3. Experimental Results

Figure 2(a) shows the typical spectra obtained by the FIDA measurements with the fiber of channel #7. The measured spectra are ranging between 649[nm] and 653[nm] in wavelength. The D_α -lights from the bulk-plasma components (656.1[nm]) are out of the range and are not shown in the figure. The intense peaks at 650[nm] correspond to the characteristic-lines from the oxygen impurity (650.04[nm]). The black dashed lines indicate the expected wavelengths for Doppler shifted D_α -lights from 80- and 40-keV deuterium neutrals, which are flying toward the view-port of the measurement. Since the blue shifted D_α spectra are chosen to be measured, the signals by lower energy ions appear in the longer wavelength region in the figure and their wavelength approaches 656.1[nm] as the energy of the ion decreases.

In Fig. 2(a), the spectrum shown by green dashed-lines with open squares is obtained during the NB#4 injection and corresponds to the background spectra. In the figure, the spectrum shown by the solid-lines with open circles is for the additional co-directed tangential-NB (#9 and #10) injection, while the lines with closed squares show that for the additional perpendicular-NB (#6 and #13) injection. As shown in this figure, significant

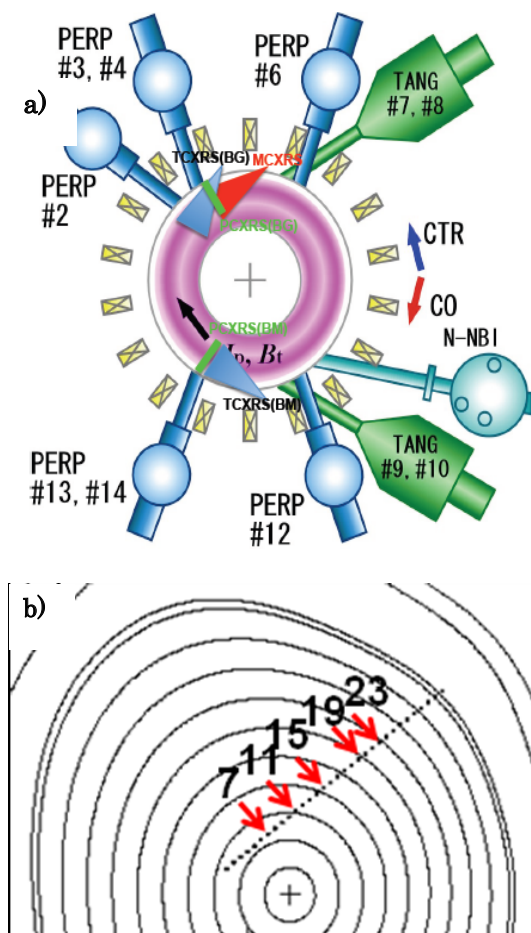


Fig. 1 (a) Geometries of FIDA measurement and NB-injection on JT-60U. (b) Schematic drawings of FIDA-measurement points in the poloidal cross section of JT-60U.

changes of the spectra are observed in the wavelength above 650[nm] with the injections of additional tangential- NBs and perpendicular-NBs. Since these NBs were not injected on the MCXRS sight lines, these spectra are considered to be due to the fast-ions being produced by these NBs. This confirms the fact that these spectra are created by the charge exchange processes between the confined fast deuterium ions and the beam injected neutrals from NB#4.

In Fig. 2(b), the background spectrum is subtracted from each of latter two spectra. As shown in this figure, the intensity of the FIDA spectra by tangential-beams starts to increase at above 650[nm]. This wavelength corresponds to that of the Doppler shifted D_{α} -light from the deuterium neutrals at the beam injection energy. On the other hand, the increase of the spectra are observed above 651[nm] for the perpendicular-NBs, although their injection energies are similar to the tangential-NBs. This discrepancy in the wavelength comes from the difference in the beam injection angles. Since the fast-ions produced by the perpendicular- NBs have less velocity parallel to the magnetic field lines than those by the tangential-NBs, the amount of Doppler shift becomes less.

By integrating the spectra above 650.5[nm](hatched area) in Fig.2(a), the time trace of FIDA-components are evaluated and are shown in Fig. 3. As shown in this figure, the integrated signals have good correlation with the injection of both tangential-NBs and perpendicular-NBs. This also confirms that the measured spectra in the range over

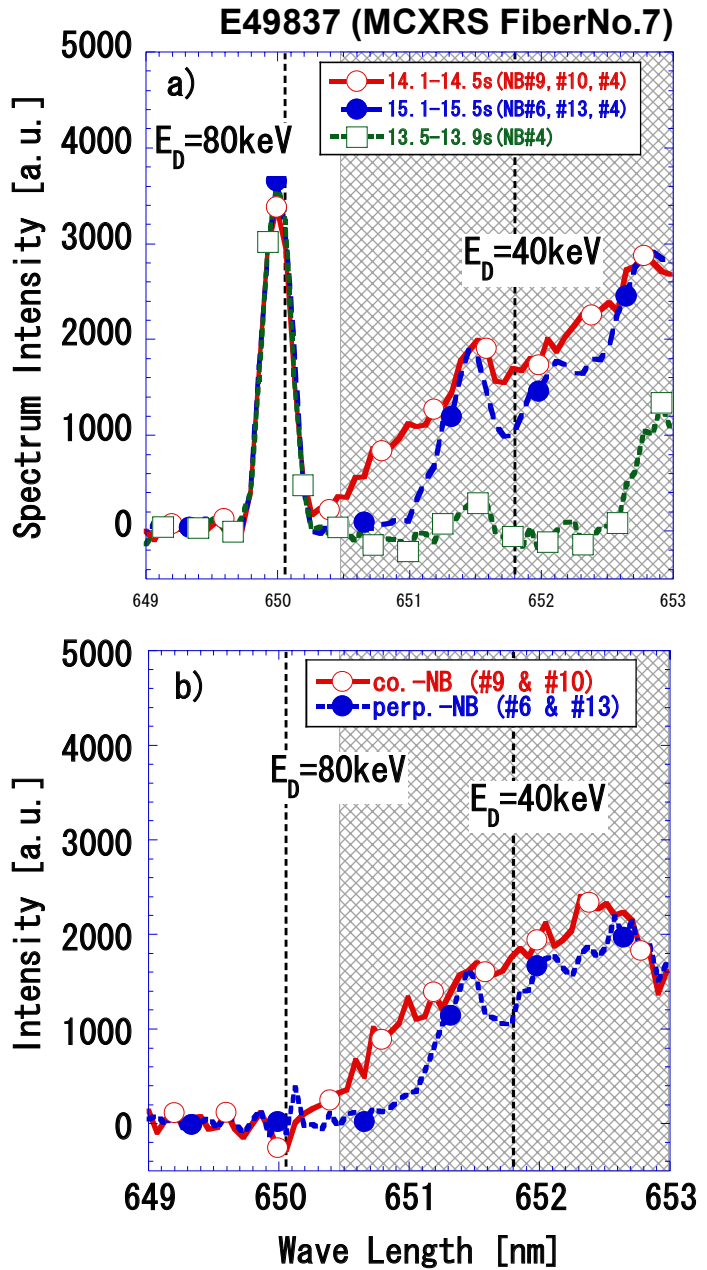


Fig. 2 (a) Typical FIDA-spectra are shown for the tangential-NB injection (red lines with open circles), the perpendicular-NB injection (line with closed circles) and background(dashed lines with open squares). (b) FIDA-sepectra without background. Lines with open circles are for tangential-NB injections and lines with closed circles are for perpendicular-NB injection.

650.5[nm] is the D_{α} -lights due to the confined fast-ions in JT-60U plasmas. Compared to the FIDA signals by the tangential-NBs, those by the perpendicular-NB are small although the injected NB power is larger. This might be due to the poor confinement property of perpendicularly injected particles compared to the tangential ones.

4. Summary

Using the measurement system of MCXRS diagnostic, the FIDA measurements were tried on JT-60U. To avoid the interference by the BES components of the NB on the sight lines, the blue-shifted D_{α} -lights were utilized for the measurement. The FIDA signals are obtained for the fast-ions being produced by the co.-directed tangential NBs and perpendicularly injected NBs. To evaluate the fast-ion spectra from these FIDA signals, the intensity of NB#4 and the contribution of background neutrals must be considered. These evaluations and the detailed analysis on the spectra will be a future work in 2009.

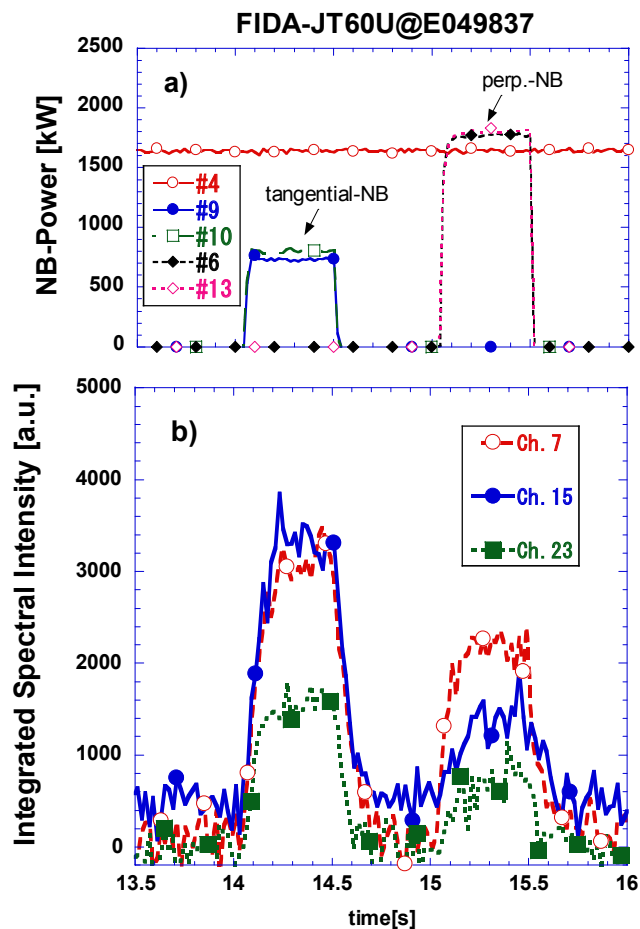


Fig.3 (a) Waveforms for NB-injection power and (b) the time traces of FIDA-signals.

References

- [1] W.W.Heidbrink, *et.al.*, Plasma Phys. and Control Fusion, **46**(2004)1855
- [2] M. Ishikawa, *et.al.*, Rev. Sci. Instrum. **73**(2002) 4237
- [3] M. Osakabe, *et.al.*, Rev. Sci. Instrum. **79**(2008) 10E519

10.15 Absolute Calibration of Microfission Chamber [1]

T. Hayashi, T. Nishitani, A. M. Sukegawa, M. Ishikawa and K. Shinohara

An absolute calibration of a micro fission chamber (MFC [2]) was carried out by both Cf-252 neutron source and real deuterium plasmas in JT-60U. The MFC was installed between the vacuum vessel and the toroidal field coils, whose detector employs both pulse counting and Campbelling (mean square voltage) modes in the electronics to cover wide dynamic range of the neutron source strength. The pulse counting and Campbelling modes were calibrated by Cf-252 and deuterium plasmas, respectively. Point efficiencies (namely, counts per neutron from a point at a single angle) were measured for the neutron point source at 27 locations in the calibrations scanning the toroidal locations. The radial location (port section) of MFC and the nearest neutron monitor were 5.22 m (P-9) and 6.45 m (P-7), respectively.

The toroidal angle for the distribution of the point efficiency for the MFC and the nearest neutron monitor is defined by the relative angle to the center of the port for each detector. The distributions of point efficiency of MFC are basically similar with neutron monitor, even though the radial locations were different. However, in some detail, the point efficiency was influenced by surrounding component such as a protection plate for high heat flux from NBI installed in the port box in front of the MFC, which consists of 25 mm-thick graphite and 10 mm-thick Inconel alloy. The point efficiencies can be integrated and averaged with angle to provide toroidal line efficiencies. The line efficiencies of MFC and the nearest neutron monitor were estimated to be 5.38×10^{-9} and 1.77×10^{-8} , respectively.

In Campbelling mode, the amplifier of the MFC has three outputs to meet wide dynamic range, namely high, middle and low gains. The maximum voltage of the output in each mode is 10 V. The neutron emission was evaluated by the polynomial function in square voltage of the output. The calibration for Campbelling mode was also performed with the real deuterium plasma emitting 2.45 MeV neutrons. The MFC has an excellent linearity with neutron monitor through the plasma discharge, excepting for noise signals. In MFC measurement, noise signals were observed at the time of almost all NBI breakdowns, due probably to long wiring from the detector to the preamplifier. The detector was connected to the preamplifier by both MI cable with 5 meters long and coaxial cable with 10 meters long. The detection efficiency in Campbelling mode was about three-tenth of the nearest neutron monitor, which is consistent with the calibration result obtained by the Cf-252 neutron source for pulse counting mode.

References

- [1] Hayashi, T., et al., Rev. Sci. Instrum. **79**, 10E506 (2008).
- [2] Hayashi, T., et al., Rev. Sci. Instrum. **75**, 3575 (2004).

11 Heating Systems

11.1 Development and Achievements on High Power ECRF and LHRF System in JT-60U

S. Moriyama, T. Kobayashi, A. Isayama, M. Terakado, M. Sawahata, S. Suzuki, K. Yokokura, M. Shimono, K. Hasegawa, S. Hiranai, K. Igarashi, F. Sato, T. Suzuki, K. Wada, S. Shinozaki, M. Seki, A. Kasugai, K. Takahashi, K. Kajiwara, K. Sakamoto and T. Fujii

In JT-60U, the ECRF system started its operation in 1999, and the full system employing four 1 MW gyrotrons and two antennas completed in 2001 [1]. The designed specifications were 1 MW for 5 s at 110 GHz of power output from a triode gyrotron, 80% of transmission line efficiency. The JT-60U ECRF system has completed its full operation in August of 2008. Operation of the system in the last two years was very fruitful. In the high power gyrotron development, 1.5 MW for 1s was recorded [2]. It is the world highest power oscillation > 1 s as shown in Fig. 1. In addition to the carefully designed cavity and collector in view of thermal stress, an RF shield for the adjustment bellows, and a low-dielectric-loss

DC break enabled this achievement. The time trace of the cavity temperature became saturated below the boiling temperature (~150°C) and the temperature has not reached the limit of 1.5 MW for 1 s to date. The time constant of ~ 10 s and the spatial distribution of the collector temperature indicate the possibility of 1.5 MW output power of longer duration.

Power modulation up to 10 kHz was achieved by improvement of anode modulation circuit. The history of the modulation frequency is shown in Fig. 2. Using this technique, modulated and phase controlled ECCD up to 7 kHz synchronizing with NTM was performed to investigate the effectiveness of NTM stabilization. The synchronization system was newly and quickly developed to maintain the required

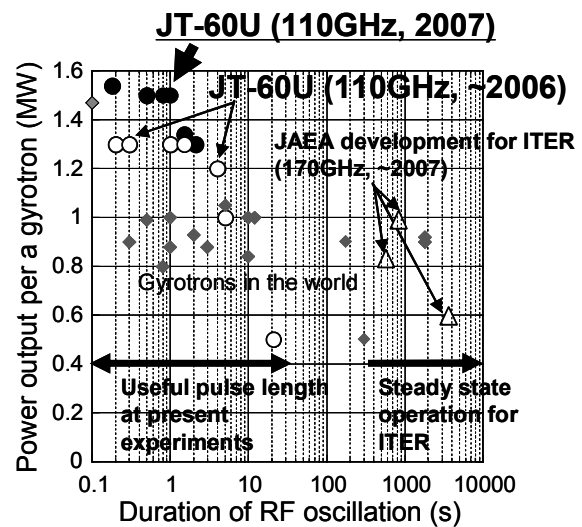


Fig. 1. Gyrotron output power achievements in the world for the pulse length of 0.1 s or over.

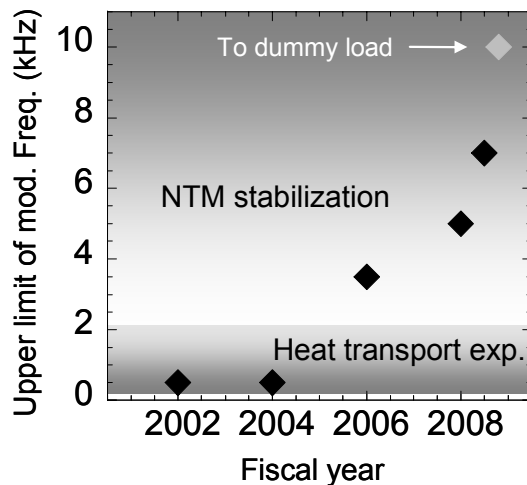


Fig. 2 Progress of power modulation frequency. Realization of 5 kHz modulation enables NTM stabilization experiments by modulated ECCD from 2008.

phasing between NTM and modulated EC power by monitoring the frequency of perturbation of the magnetic probe signal and taking into account of the transition of the oscillation characteristics of the gyrotron during the EC pulse [3].

Total power of 2.9 MW was injected to the plasma with 4 gyrotrons for 5 s, which is the full specification of the ECRF system. The history of injected power and pulse width is shown in Fig. 3. Improvement of conditioning scheme of the diamond window contributed to this improvement of high power injection. As for the long pulse development, the gyrotron, the transmission line, and the antenna showed reliable performance at 0.4 MW for 30 s using one gyrotron with pre-programmed control of anode/cathode-heater.

In addition to the development on the ECRF system in JT-60U, an innovative antenna having wide range of beam steering capability with linearly-moving-mirror concept has been designed for long pulse operation in JT-60SA.

The antenna eliminates need for the flexible tube that supplies the coolant and link mechanism in the vacuum vessel and will reduce the risk of water leakages and the frequency of maintenance. Beam profile and mechanical strength analyses shows the feasibility of the antenna [4].

The LHRF launcher had damage in the launcher mouth in 2004 because of a trouble in the arc detection system and a problem of an electrical contact between the grill and carbon protector grill. Six out of 8 waveguides except two heavily damaged ones were used for some years, but one of the damaged waveguides was repaired in 2007 using a newly developed torch for welding. In 2007-2008 operation, 2.1 MW injection for > 1 s was achieved. It was 1.3 of the maximum power (1.6 MW) in 2006, and exceeded the expectation from the repair ($7/6=1.17$).

Reference

- [1] Ikeda, Y., et al., Fusion Sci. Technol. **42**, 435 (2002).
- [2] Kobayashi, T., et al., Plasma Fusion Res. **3**, 014 (2008).
- [3] Kobayashi, T., et al., Plasma Fusion Res., **4**, 037 (2009).
- [4] Moriyama, S. et al., Nucl. Fusion, **49**, 085001 (2009).

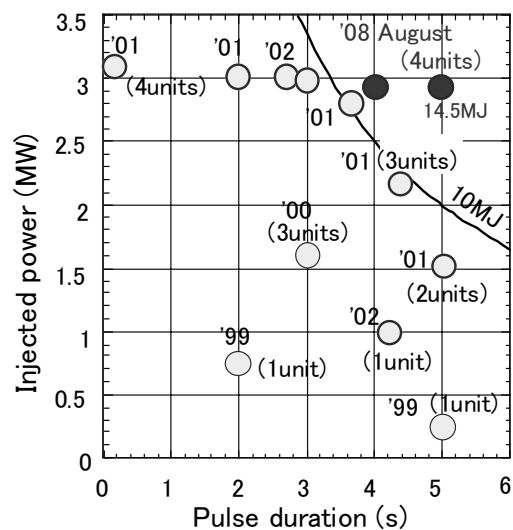


Fig. 3. Injected RF power and pulse duration of JT-60 ECRF system. Simultaneous operation of all 4 gyrotrons at 1 MW for 5 s enabled 2.9 MW (14.5 MJ) injection.

11.2 Development of Long Pulse Neutral Beam Injector on JT-60U [1]

M. Hanada, Y. Ikeda, M. Kamada, K. Kobayashi, N. Umeda, N. Akino, N. Ebisawa, T. Inoue, A. Honda, M. Kawai, M. Kazawa, K. Kikuchi, M. Komata, K. Mogaki, K. Noto, K. Oasa, K. Oshima, S. Sasaki, T. Simizu, T. Takenouchi, Y. Tanai, K. Usui, K. Watanabe

In the campaign of 2007-2008 on JT-60U, significant progress has been made in the long pulse injection of neutral beams. Three positive NBI units were newly upgraded by modifying the power supplies to extend the injection pulse length from 10 s to 30 s in addition to the five P-NBI units upgraded in 2003. The pulse length of the newly upgraded units was extended to 17-25 s at 2 MW depending on the progress in the conditioning of the injection port. By this extension, sum of the injection energy from individual positive NBI units achieved 480 MJ, which is 1.5 times higher than that in 2003 .

The modification for the long pulse injection was also done in negative-ion-based NBI, where the grid power loading in the ion source was reduced to an allowable level. To reduce the direct interception of the D^- ions by acceleration grids, the steering angle of outermost beamlets was tuned by modifying a field shaping plate (FSP). The modified FSP succeeds in the reduction of the highest grid power loading from 7% to 5% of the accelerated beam power. This power loading is an allowable level for the full power injection on JT-60SA. The modification of N-NBI allowed to extend the pulse length to 30 s at an injection power of 3 MW and the beam energy of 340 keV as shown in Fig. 1. The achieved injection energy was 80 MJ, and 1.4 times higher than that in 2003 [1].

These modifications of the positive and negative NBI units increased a simultaneous injection energy up to 450 MJ. This high injection energy significantly contributed to a long pulse production (28 s) of high beta plasma with $\beta_N=2.6$ that is comparable to the beta value in the ITER hybrid scenario.

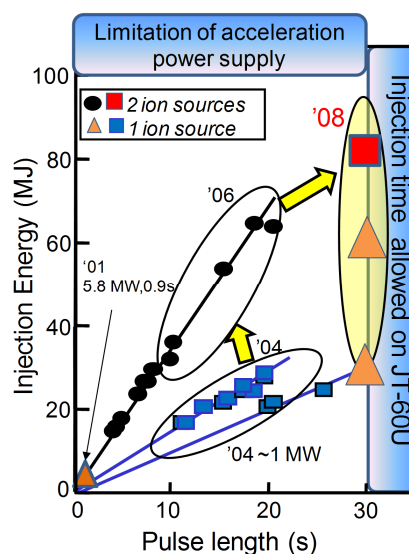


Fig. 1. Injection energy of N-NBI as a function of beam pulse length.

Reference

- [1] Hanada, M. et al., 'Development of Long Pulse Neutral Beam Injector on JT-60U for JT-60SA', Proceedings of the 22nd IAEA Fusion Energy Conference, FTP2-27, Geneva, 2008; submitted to Nuclear Fusion.

Acknowledgments

The authors wish to acknowledge dedicated efforts of the member of Japan Atomic Energy Agency in support of the JT-60 program. They also wish to express their gratitude for domestic and international collaborations for the JT-60 experiments.

This is a blank page.

国際単位系 (SI)

表1. SI基本単位

| 基本量 | SI基本単位 | |
|-------|--------|-----|
| | 名称 | 記号 |
| 長さ | メートル | m |
| 質量 | キログラム | kg |
| 時間 | 秒 | s |
| 電流 | アンペア | A |
| 熱力学温度 | ケルビン | K |
| 物質の量 | モル | mol |
| 光度 | カンデラ | cd |

表2. 基本単位を用いて表されるSI組立単位の例

| 組立量 | SI基本単位 | |
|-------------------------|--------------|--------------------|
| | 名称 | 記号 |
| 面積 | 平方メートル | m ² |
| 体積 | 立方メートル | m ³ |
| 速度 | メートル毎秒 | m/s |
| 加速度 | メートル毎秒毎秒 | m/s ² |
| 波数 | 毎メートル | m ⁻¹ |
| 密度, 質量密度 | キログラム毎立方メートル | kg/m ³ |
| 面積密度 | キログラム毎平方メートル | kg/m ² |
| 比体積 | 立方メートル毎キログラム | m ³ /kg |
| 電流密度 | アンペア毎平方メートル | A/m ² |
| 磁界の強さ | アンペア毎メートル | A/m |
| 量濃度 ^(a) , 濃度 | モル毎立方メートル | mol/m ³ |
| 質量濃度 | キログラム毎立方メートル | kg/m ³ |
| 輝度 | カンデラ毎平方メートル | cd/m ² |
| 屈折率 ^(b) | (数字の) | 1 |
| 比透磁率 ^(b) | (数字の) | 1 |

(a) 量濃度 (amount concentration) は臨床化学の分野では物質濃度 (substance concentration) とよばれる。
 (b) これらは無次元量あるいは次元1をもつ量であるが、そのことを表す単位記号である数字の1は通常は表記しない。

表3. 固有の名称と記号で表されるSI組立単位

| 組立量 | SI組立単位 | | | |
|---------------------------------|-----------------------|-------------------|----------------------|--|
| | 名称 | 記号 | 他のSI単位による表し方 | SI基本単位による表し方 |
| 平面角 | ラジアン ^(b) | rad | 1 ^(b) | m/m |
| 立体角 | ステラジアン ^(b) | sr ^(e) | 1 ^(b) | m ² /m ² |
| 周波数 | ヘルツ ^(d) | Hz | | s ⁻¹ |
| 力 | ニュートン | N | | m kg s ⁻² |
| 圧力, 応力 | パスカル | Pa | N/m ² | m ⁻¹ kg s ⁻² |
| エネルギー, 仕事, 熱量 | ジュール | J | N m | m ² kg s ⁻² |
| 仕事率, 工率, 放射束 | ワット | W | J/s | m ² kg s ⁻³ |
| 電荷, 電気量 | クーロン | C | | s A |
| 電位差 (電圧), 起電力 | ボルト | V | W/A | m ² kg s ⁻³ A ⁻¹ |
| 静電容量 | ファラド | F | C/V | m ² kg ⁻¹ s ⁴ A ² |
| 電気抵抗 | オーム | Ω | V/A | m ² kg s ⁻³ A ⁻² |
| コンダクタンス | ジーメンズ | S | A/V | m ⁻² kg ⁻¹ s ³ A ² |
| 磁束 | ウェーバ | Wb | Vs | m ² kg s ⁻² A ⁻¹ |
| 磁束密度 | テスラ | T | Wb/m ² | kg s ⁻² A ⁻¹ |
| インダクタンス | ヘンリー | H | Wb/A | m ² kg s ⁻² A ⁻² |
| セルシウス温度 | セルシウス度 ^(e) | °C | | K |
| 光照射度 | ルーメン | lm | cd sr ^(e) | cd |
| 放射線量 | グレイ | Gy | J/kg | m ² s ⁻² |
| 放射線量当量, 周辺線量当量, 方向性線量当量, 個人線量当量 | シーベルト ^(g) | Sv | J/kg | m ² s ⁻² |
| 酸素活性 | カタール | kat | | s ⁻¹ mol |

(a) SI接頭語は固有の名称と記号を持つ組立単位と組み合わせても使用できる。しかし接頭語を付した単位はもはやコヒーレントではない。
 (b) ラジアンとステラジアンは数字の1に対する単位の特別な名称で、量についての情報をつたえるために使われる。実際には、使用する時には記号rad及びsrが用いられるが、習慣として組立単位としての記号である数字の1は明示されない。
 (c) 測光学ではステラジアンという名称と記号srを単位の表し方の中に、そのまま維持している。
 (d) ヘルツは周期現象についてのみ、ベクレルは放射性核種の統計的過程についてのみ使用される。
 (e) セルシウス度はケルビンの特別な名称で、セルシウス温度を表すために使用される。セルシウス度とケルビンの単位の大きさは同一である。したがって、温度差や温度間隔を表す数値はどちらの単位で表しても同じである。
 (f) 放射性核種の放射能 (activity referred to a radionuclide) は、しばしば誤った用語で"radioactivity"と記される。
 (g) 単位シーベルト (PV.2002.70.205) についてはCIPM勧告2 (CI-2002) を参照。

表4. 単位の中に固有の名称と記号を含むSI組立単位の例

| 組立量 | SI組立単位 | | |
|-----------------|-------------------|-----------------------|--|
| | 名称 | 記号 | SI基本単位による表し方 |
| 粘り度 | パスカル秒 | Pa s | m ⁻¹ kg s ⁻¹ |
| 力のモーメント | ニュートンメートル | N m | m ² kg s ⁻² |
| 表面張力 | ニュートン毎メートル | N/m | kg s ⁻² |
| 角速度 | ラジアン毎秒 | rad/s | m m ⁻¹ s ⁻¹ =s ⁻¹ |
| 角加速度 | ラジアン毎秒毎秒 | rad/s ² | m m ⁻¹ s ⁻² =s ⁻² |
| 熱流密度, 放射照度 | ワット毎平方メートル | W/m ² | kg s ⁻³ |
| 熱容量, エントロピー | ジュール毎ケルビン | J/K | m ² kg s ⁻² K ⁻¹ |
| 比熱容量, 比エントロピー | ジュール毎キログラム毎ケルビン | J/(kg K) | m ² s ⁻² K ⁻¹ |
| 比エネルギー | ジュール毎キログラム | J/kg | m ² s ⁻² |
| 熱伝導率 | ワット毎メートル毎ケルビン | W/(m K) | m kg s ⁻³ K ⁻¹ |
| 体積エネルギー | ジュール毎立方メートル | J/m ³ | m ⁻¹ kg s ⁻² |
| 電界の強さ | ボルト毎メートル | V/m | m kg s ⁻³ A ⁻¹ |
| 電荷密度 | クーロン毎立方メートル | C/m ³ | m ⁻³ s A |
| 表面電荷 | クーロン毎平方メートル | C/m ² | m ⁻² s A |
| 電束密度, 電気変位 | クーロン毎平方メートル | C/m ² | m ⁻² s A |
| 誘電率 | ファラド毎メートル | F/m | m ⁻³ kg ⁻¹ s ⁴ A ² |
| 透磁率 | ヘンリー毎メートル | H/m | m kg s ⁻² A ⁻² |
| モルエネルギー | ジュール毎モル | J/mol | m ² kg s ⁻² mol ⁻¹ |
| モルエントロピー, モル熱容量 | ジュール毎モル毎ケルビン | J/(mol K) | m ² kg s ⁻² K ⁻¹ mol ⁻¹ |
| 照射線量 (X線及びγ線) | クーロン毎キログラム | C/kg | kg ⁻¹ s A |
| 吸収線量率 | グレイ毎秒 | Gy/s | m ² s ⁻³ |
| 放射線強度 | ワット毎ステラジアン | W/sr | m ³ m ⁻² kg s ⁻³ =m ² kg s ⁻³ |
| 放射輝度 | ワット毎平方メートル毎ステラジアン | W/(m ² sr) | m ² m ⁻² kg s ⁻³ =kg s ⁻³ |
| 酵素活性濃度 | カタール毎立方メートル | kat/m ³ | m ⁻³ s ⁻¹ mol |

表5. SI接頭語

| 乗数 | 接頭語 | 記号 | 乗数 | 接頭語 | 記号 |
|------------------|-----|----|-------------------|------|----|
| 10 ²⁴ | ヨクタ | Y | 10 ⁻¹ | デシ | d |
| 10 ²¹ | ゼタ | Z | 10 ⁻² | センチ | c |
| 10 ¹⁸ | エクサ | E | 10 ⁻³ | ミリ | m |
| 10 ¹⁵ | ペタ | P | 10 ⁻⁶ | マイクロ | μ |
| 10 ¹² | テラ | T | 10 ⁻⁹ | ナノ | n |
| 10 ⁹ | ギガ | G | 10 ⁻¹² | ピコ | p |
| 10 ⁶ | メガ | M | 10 ⁻¹⁵ | フェムト | f |
| 10 ³ | キロ | k | 10 ⁻¹⁸ | アト | a |
| 10 ² | ヘクト | h | 10 ⁻²¹ | ゼプト | z |
| 10 ¹ | デカ | da | 10 ⁻²⁴ | ヨクト | y |

表6. SIに属さないが、SIと併用される単位

| 名称 | 記号 | SI単位による値 |
|-------|------|--|
| 分 | min | 1 min=60s |
| 時 | h | 1h=60 min=3600 s |
| 日 | d | 1 d=24 h=86 400 s |
| 度 | ° | 1°=(π/180) rad |
| 分 | ' | 1'=(1/60)°=(π/10800) rad |
| 秒 | " | 1"=(1/60)'=(π/648000) rad |
| ヘクタール | ha | 1ha=1hm ² =10 ⁴ m ² |
| リットル | L, l | 1L=1l=1dm ³ =10 ³ cm ³ =10 ⁻³ m ³ |
| トン | t | 1t=10 ³ kg |

表7. SIに属さないが、SIと併用される単位で、SI単位で表される数値が実験的に得られるもの

| 名称 | 記号 | SI単位で表される数値 |
|----------|----|--|
| 電子ボルト | eV | 1eV=1.602 176 53(14)×10 ⁻¹⁹ J |
| ダルトン | Da | 1Da=1.660 538 86(28)×10 ⁻²⁷ kg |
| 統一原子質量単位 | u | 1u=1 Da |
| 天文単位 | ua | 1ua=1.495 978 706 91(6)×10 ¹¹ m |

表8. SIに属さないが、SIと併用されるその他の単位

| 名称 | 記号 | SI単位で表される数値 |
|-----------|------|---|
| バール | bar | 1 bar=0.1MPa=100kPa=10 ⁵ Pa |
| 水銀柱ミリメートル | mmHg | 1mmHg=133.322Pa |
| オングストローム | Å | 1 Å=0.1nm=100pm=10 ⁻¹⁰ m |
| 海里 | M | 1 M=1852m |
| バイン | b | 1 b=100fm ² =10 ⁻¹² cm ² =10 ⁻²⁸ m ² |
| ノット | kn | 1 kn=(1852/3600)m/s |
| ネーパ | Np | SI単位との数値的な関係は、 対数量の定義に依存。 |
| ベベル | B | |
| デジベル | dB | |

表9. 固有の名称をもつCGS組立単位

| 名称 | 記号 | SI単位で表される数値 |
|------------|-----|--|
| エルグ | erg | 1 erg=10 ⁻⁷ J |
| ダイン | dyn | 1 dyn=10 ⁻⁵ N |
| ポアズ | P | 1 P=1 dyn s cm ⁻² =0.1Pa s |
| ストークス | St | 1 St=1cm ² s ⁻¹ =10 ⁻⁴ m ² s ⁻¹ |
| スチルブ | sb | 1 sb=1cd cm ⁻² =10 ⁴ cd m ⁻² |
| フット | ph | 1 ph=1cd sr cm ⁻² 10 ⁴ lx |
| ガリ | Gal | 1 Gal=1cm s ⁻² =10 ⁻² ms ⁻² |
| マクスウェル | Mx | 1 Mx=1G cm ² =10 ⁻⁸ Wb |
| ガウス | G | 1 G=1Mx cm ⁻² =10 ⁴ T |
| エルステッド (c) | Oe | 1 Oe≐ (10 ³ /4π)A m ⁻¹ |

(c) 3元素のCGS単位系とSIでは直接比較できないため、等号「≐」は対応関係を示すものである。

表10. SIに属さないその他の単位の例

| 名称 | 記号 | SI単位で表される数値 |
|-----------|------|---|
| キュリー | Ci | 1 Ci=3.7×10 ¹⁰ Bq |
| レントゲン | R | 1 R=2.58×10 ⁻⁴ C/kg |
| ラド | rad | 1 rad=1cGy=10 ⁻² Gy |
| レム | rem | 1 rem=1 cSv=10 ⁻² Sv |
| ガンマ | γ | 1 γ=1 nT=10 ⁻⁹ T |
| フェルミ | f | 1フェルミ=1 fm=10 ⁻¹⁵ m |
| メートル系カラット | | 1メートル系カラット=200 mg=2×10 ⁻⁴ kg |
| トル | Torr | 1 Torr=(101 325/760) Pa |
| 標準大気圧 | atm | 1 atm=101 325 Pa |
| カロリ | cal | 1cal=4.1858J (「15°C」カロリ), 4.1868J (「IT」カロリ) 4.184J (「熱化学」カロリ) |
| マイクロン | μ | 1 μ=1μm=10 ⁻⁶ m |

